101 pages

IN-12891

Final Report For
Grant NAG5-196
Entitled

SPECTRORADIOMETRIC CONSIDERATIONS FOR ADVANCED LAND OBSERVING SYSTEMS

AX852975

Philip N. Slater
Principal Investigator
Optical Sciences Center
University of Arizona
Tucson, Arizona 85721

July 1986

Introduction and Summary

This is the final report on grant number NAG5-196 which started on July 1, 1981.

Theses and Dissertation

The grant has provided partial financial support for three MS students and one PhD student. The names of the students and the titles and abstracts of their theses and dissertation are listed below.

D. D. Dyche, MS thesis entitled "Experimental Determination of Atmospheric Scattering Effects on Scanner Edge Response."

> The influence of background radiance from surface areas outside the ground-projected IFOV of an aircraft sensor was experimentally investigated on a 600 x 550 m field, evenly divided between mature cotton and bare soil. An aircraft carrying a multispectral scanner made passes at 1,000, 8,000, and 16,000 ft AGL obtaining radiance data in the 420-450 nm range. Ground reflectances were approximately 0.025 (cotton) and 0.105 (bare soil). At 440 nm the atmospheric extinction coefficient was measured to be 0.297. The data indicate that a boundary effect may exist, where flux reflected from one side of the field is scattered by the atmosphere so as to appear to the sensor to come from the adjacent side. Experimental and theoretical data agreed closely for the cases of total detected radiance changes and border radiance values but not for radiance changes between altitudes. Thus, a boundary effect may be present, but its existence is not clearly proved or disproved.

A. L. Phillips, MS thesis entitled "Absolute Calibration of and Atmospheric Measurements with a Multiband Field Radiometer."

> Three different techniques were employed to calibrate in an absolute sense a multiband field radiometer. The three techniques were a source-based

one using a calibrated standard lamp as a reference, a detector-based one using a collimated monochromatic source, and a detector-based one using an extended uniform source. Because of the optical system of the radiometer, the detector-based technique using the monochromator system was inappropriate for absolute calibration. Based on the uncertainties associated with the other two techniques, the detector-based one using the extended source was preferred. However, the monochromator system was also used to get the shape of the responsivity as a function of wavelength. This technique yielded an absolute calibration with an uncertainty of ±4.5%.

Using the same radiometer, an experiment was conducted to test the influence of "surround spectral reflectance" upon the measured ratio of the diffuse component of solar radiation to the direct component. A comparison was made of the measured ratio to the ratio determined by an atmospheric radiative transfer program. The comparison showed similar trends in 3 visible bands, but showed disagreement in a near infra-red band.

S. L. Witman, MS thesis entitled "Radiometric Calibration of the Thematic Mapper 48-inch Diameter Spherical Integrating Source (48-SIS) Using two Different Calibration Methods."

Two methods are described for calibrating the 48-inch integrating sphere used to radiometrically calibrate the Landsat Thematic Mapper. The output of the sphere was first measured monochromatically by engineers at the Santa Barbara Research Center. The author of this thesis reduced these monochromatic data such that they coincided with the spectral bandpasses of a calibrated radiometer. The second calibration method used this radiometer to measure the output radiance of the sphere. The reduced monochromatic and radiometric data sets were compared. The results show that the radiance of the integrating sphere measured with a monochromator and a radiometer agreed within the limits of the uncertainties of the measurements. The radiometer was calibrated against the same reference standard as used for calibrating the monochromator. In addition, the monochromator versus radiometric sphere calibration results show good agreement with other independent source-based and detector-based calibrations of the radiometer.

C. J. Kastner, PhD dissertation entitled "In-Flight Radiometric Calibration of the Landsat Thematic Mapper."

> The in-flight absolute radiometric calibration of the Thematic Mapper (TM) is being conducted using the results of field measurements at White Sands, New Mexico. These measurements are made to characterize the ground and atmosphere at the time the TM is acquiring an image of White Sands. The data are used as input to a radiative transfer code that computes the radiance at the entrance pupil of the TM. The calibration is obtained by comparing the digital counts associated with the TM image of the measured ground site with the radiative transfer code result. The calibrations discussed here are for the first four visible and near-infrared bands of the TM.
>
> In this dissertation the data reduction for the first calibration attempts on January 3, 1983, and July 8, 1984, is discussed. Included are a review of radiative transfer theory and a discussion of model atmospheric parameters as defined for the White Sands area. These model parameters are used to assess the errors associated with the calibration procedure. Each input parameter to the radiative transfer code is varied from its model value in proportion to the uncertainty with which it can be determined. The effects of these uncertainties on the predicted radiances are determined. It is thought that the optical depth components τ_{Ray}, τ_{Mie}, τ_{oz}, and τ_{H_2O} can be measured to within 10%, 2%, 10%, and 30%, respectively. For the white gypsum sand, surface reflectance uniformity is on the order of 1.5%, and the overall uncertainty in measured reflectance is about 2%. This is due to an uncertainty in the reflectance factor of the calibration plates. The greatest uncertainty in calibration is attributed to our uncertainty in the aerosol parameters, in particular the imaginary component of refractive index. The cumulative effect of these uncertainties is thought to produce an uncertainty in computed radiance of about 5%.

Publications:

Ten publications were also directly supported by the grant. The authors, titles and journals are listed below and the papers themselves have been duplicated to comprise the balance of this final report.

P. N. Slater (1982), "Absolute radiometric calibration of advanced remote sensing systems," International Geoscience and Remote Sensing Symposium, Munich, Germany.

P. N. Slater and R. D. Jackson (1982), "Atmospheric effects on radiation reflected from soil and vegetation as measured by orbiting sensors using various scanning directions," Appl. Opt. 21:3923-3931.

C. J. Kastner and P. N. Slater (1982), "In-flight radiometric calibration of advanced remote sensing systems," Proc. SPIE 356.

P. N. Slater, (1984), "Importance and attainment of accurate absolute radiometric calibration," Proc Vol 475. SPIE Critical Review of Remote Sensing, ed. P. N. Slater pp. 34-40.

N-Z Che, R. D. Jackson, A. L. Phillips, and P. N. Slater (1984), "Field radiometer methods for reflectance and atmospheric measurements," Proc. SPIE 499, pp. 24-33.

P. N. Slater (1984), "Radiometric considerations in remote sensing," invited paper in the Proceedings of the IEEE Vol. 73, No. 6, pp. 997-1011.

S. F. Biggar, C. J. Bruegge, B. A. Capron, K. R. Castle, M. C. Dinguirard, R. G. Holm, R. D. Jackson, L. J. Lingg, Y. Mao, M. S. Moran, J. M. Palmer, A. L. Phillips, R. K. Savage, P. N. Slater, S. L. Witman and B. Yuan (1985), "Absolute calibration of remote sensing instruments," Proc. Third International Colloqium on Spectral Signatures of Objects in Remote Sensing, ESA SP-247, pp.309-314.

P. N. Slater (1985), "Variations in in-flight absolute radiometric calibration," ISLSCP Conference in Rome, Italy.

Ray D. Jackson and Philip N. Slater (1986), "Absolute calibration of field reflectance radiometers," Photogrammetric Engineering and Remote Sensing, Vol 52, pp 189-196.

The grant has been of immense value in providing support for some basic and applied research aimed at improving our ability to determine the in-flight absolute radiometric calibration of advanced land observing systems. In particular it has provided research funding in partial support of our very successful

satellite sensor calibration program at White Sands. We are pleased to say that this grant activity is being continued as part of the Earth Observing System program and wish to express our thanks to NASA for their continued support of the satellite calibration program at the University of Arizona.

Presented at the 1982 International Geoscience and Remote Sensing Symposium,
Munich, Germany, June 1982.

ABSOLUTE RADIOMETRIC CALIBRATION OF ADVANCED REMOTE SENSING SYSTEMS

P. N. Slater

Committee on Remote Sensing
Optical Sciences Center
University of Arizona

ABSTRACT

The distinction between the uses of relative and absolute spectroradiometric calibration of remote sensing systems is discussed. The advantages of detector-based absolute calibration are described, and the categories of relative and absolute system calibrations are listed. The limitations and problems associated with three common methods used for the absolute calibration of remote sensing systems are discussed.

Two methods are proposed for the in-flight absolute calibration of advanced multispectral linear array (MLA) systems. One makes use of a sun-illuminated panel in front of the sensor, the radiance of which is monitored by a spectrally flat pyroelectric radiometer. The other uses a large, uniform, high-radiance reference ground surface. The ground and atmospheric measurements required as input to a radiative transfer program to predict the radiance level at the entrance pupil of the orbital sensor are discussed, and the ground instrumentation is described.

Key words: Radiometry; Calibration; Remote Sensing.

1. SPECTRORADIOMETRIC CALIBRATION--WHO NEEDS IT?

For purposes of this discussion, the community of remote sensing data users can be divided into two groups :

1. Users requiring relative, but not necessarily absolute, spectroradiometric sensor calibration. These include workers in computer-aided scene classification, cartographers, image processors, photointerpreters, and people concerned with composing large mosaics.

2. Users requiring absolute spectroradiometric calibration. These include physical scientists concerned with relating ground-measured parameters and/or atmospheric characteristics to the spectral radiance at the entrance pupil of the space sensor.

The distinction can be drawn that the former are concerned primarily with taking an inventory or compiling a map of ground features. The latter are concerned primarily with understanding and characterizing the physical interactions taking place, usually through models and often with a view to optimizing (for example an irrigation schedule) or to predicting a change in a particular process (for example an agricultural yield). Expressed differently, those concerned with relative calibration use data described in digital counts, while those needing absolute calibration use data referenced in terms of radiance units at the entrance pupil of the sensor (in this case, the radiometric calibration of the sensor is invoked to convert the digital value to spectral radiance). We must emphasize that the radiance value is of no more worth to the average user than the digital value, as both refer to an incident radiance level at the sensor over broad, unequal spectral passbands, over which the spectral reflectance of the feature being observed can change by a significant but unknown amount. However, there are two reasons for converting the digital value to radiance: first, in multitemporal sensing, to account for any documented changes of radiometric calibration with time; second, to test or utilize physical models in which the ground reflectance and atmospheric effects are measured and/or calculated over identical spectral passbands as employed by the space sensor.

Perfect relative radiometric response occurs when the outputs from all detectors in a band are equal or can be adjusted during preprocessing to be equal, when the incident spectral radiance is constant across the sensor's field of view. (Note that the number of detectors in a band can be as few as six for the Multispectral Scanner System (MSS) on Landsat and as many as 18,500 on future MLA systems.) This condition must be met independently of the spectral content of the scene. When this condition is not met, the image appears striped. If it is not scene-dependent, striping often can be completely removed by the histogram equalization method; thus, relative radiometric precision can be high even though the accuracy involved may be low. In this equalization procedure the histogram of each detector output is compared with that of every other detector, after a large number of data samples ($\sim 2 \times 10^5$) have been recorded. It is assumed that, if the scene is spatially and spectrally random, the histograms for a large number of samples will be identical. If the histograms are not identical, adjustments are made during the preprocessing step to make them so. This procedure can be repeated for scenes of different average radiance, and the relative responses can then be equalized over the dynamic range of the detectors. This procedure does not work if the striping is scene-dependent (Ref. 1). Fortunately the design and the spectral band location for the Thematic Mapper and future MLA sensors will not give rise to a scene-dependent

striping problem of the magnitude of that in the MSS.

Inadequately corrected relative detector-to-detector response causes unsightly striping in the imagery. Striping can cause inaccuracies in automated scene classification. In addition, even though the human photointerpreter is usually more forgiving than a computer, if the striping is severe it can cause errors in photointerpretation. Uncorrected striping can be aggravated by the application of some image processing algorithms. Thus, it is important to reduce striping as much as possible for image processing and classification purposes. The relative response of the individual detectors is also important for ratioing purposes. However, once the in-band tolerance has been met, the concern is with the relative stability of response because many applications utilize the comparison of multitemporal band ratios.

The utilization or verification of physical models usually requires the use of data calibrated in an absolute sense. Until recently the highest in-orbit absolute radiometric accuracy has been little better than 10%. This low accuracy has been due to: (a) the fact that the calibration in orbit has often been for the focal plane only, not for the complete system; (b) the loss in accuracy accompanying the transfer of calibration from the standard source at the national laboratory to the factory or laboratory calibration site; (c) the use of source-based calibration procedures.

As described later, the use of detector-based calibration promises to reduce the approximately 10% error to 1%. To what extent we can afford to relax or strive to exceed the 1% potential can best be determined from a set of well-coordinated measurement and modeling exercises conducted as part of an experimental MLA mission. The results of work to date on this subject are in disagreement. On one hand we know that natural or scene variability is seldom less than 1% and we also know from atmospheric modeling work (not yet experimentally verified) that we can expect considerable atmospheric-scatter-induced spectral radiance crosstalk between neighboring ground samples owing to the so-called adjacency or boundary effect (Refs. 2-5). On the other hand, the sensor simulations made to date (Ref. 6) indicate there is an improvement in classification accuracy in going from 6-bit to 8-bit quantization. Eight-bit quantization is available on most future sensors. A purist might contend that, if 8-bit radiometric resolution is really justified, it should, for maximum utility, be associated with commensurate (<0.4%) error in absolute radiometric accuracy!

In summary, we know that spectroradiometric calibration is important and that the need for relative or absolute calibration depends on the application for the data. However, we do not know how accurate the calibrations should be, particularly the absolute calibration. The most encouraging aspect of the situation is that we now have the potential of utilizing 8-bit quantization resolution with commensurate absolute radiometric accuracy in an orbital imager at least over the 400 to 900 nm range. This potential should be exploited as fully as possible as an important component of any system and applications research associated with an experimental land-observing system having an 8- to 10-bit quantization capability.

2. DETECTOR-BASED RADIOMETRIC CALIBRATION

The recent work at the US National Bureau of Standards on self-calibrated photodiodes is described only briefly here. For more details the interested reader is referred to references 7-12.

The calibration of the photodiode is accomplished by either of two differently applied biasing procedures, depending on the wavelength region of interest. At short wavelengths, a negative bias is applied to remove the recombination centers at the Si-SiO interface at the front of the detector. To do this, a contact is made with the front surface using an electrode immersed in a conducting liquid, or the surface can be exposed to a corona discharge. For long wavelengths, a back-bias is applied to extend the depletion region to a depth beyond which incident flux penetrates. The experimental procedure is to irradiate the detector with a constant monochromatic flux level and to increase the bias voltage until further increase no longer gives rise to an increase in output signal. For both the short and the long wavelength ranges, the internal quantum efficiency saturates at a value extremely close to unity, as shown in Fig. 1. Thus the maximum increase in signal output obtained as a result of biasing can be used to determine the internal quantum efficiency of the detector without biasing, as it will be used in practice.

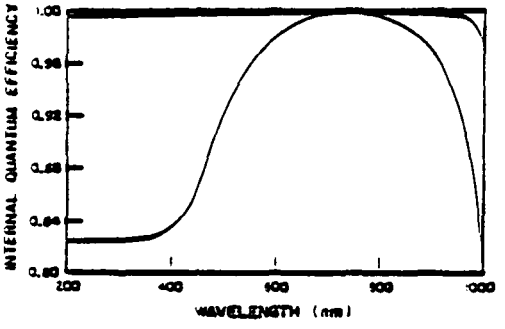

Fig. 1. Typical photodiode internal quantum efficiency without biasing (lower curve) and with biasing (upper curve), reference 9.

The only significant loss in the external quantum efficiency of the photodiode is caused by reflection. This can be reduced to insignificance by making use of three photodiodes according to the geometry sketched in Fig. 2.

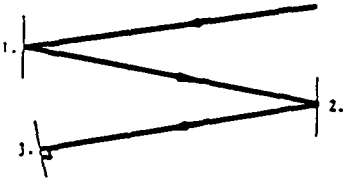

Fig. 2. A three-diode arrangement to minimize specular reflection losses.

The output signals from the three diodes are summed to provide the signal corresponding to a black detector of overall quantum efficiency that

can be assumed to be unity. The second diode reflects the specular reflection from diode 1 to diode 3, which acts as a retroreflector. The incident flux thereby undergoes five reflections, and at a 10% value the final specular reflectance is down to 10^{-5} of the initial incident radiance. It is claimed (Ref. 12) that the diffuse reflectance losses for clean detectors are typically much less than 1%. The photodiodes used in similar calibration facilities at NBS and at the University of Arizona, Optical Sciences Center, are EGG UV 444B.

The discussion at the end of this paper refers to the use of self-calibrating NBS detectors for the spectroradiometric calibration of an MLA system. However, as shown in Fig. 1, the unbiased quantum efficiency is wavelength dependent. Because of possible changes in the passband position of spectral filters during long duration space flights, it may be advisable to use the NBS detectors to calibrate a spectrally flat pyroelectric detector, at the 0.1-0.2% level, and for that to be used in the in-orbit calibration.

3. BROAD CLASSIFICATION OF CALIBRATION PROCEDURES

Some of the most commonly used procedures for the calibration of remote sensing systems are referred to in Fig. 3. The two major divisions in the figure are between relative and absolute calibration and between the static macro-image response and the dynamic micro-image response of the system. Some aspects of relative calibration were discussed in the first part of this paper and together with dynamic micro-image response will not be discussed further, beyond remarking that the dynamic micro-image response is of vital interest in any pixel-by-pixel analysis of remotely collected imagery. The rest of this paper deals with the absolute calibration of remote sensing systems, and only the static macro-image response will be considered in this context, as is usually the case.

The procedures for the absolute calibration of a remote sensing system fall into the three categories shown in the bottom right of Fig. 3:

(1) The absolute calibration of the system is made only before launch. In flight the calibration is checked by irradiating the focal plane with a radiometrically calibrated source and optical system. The drawbacks to this procedure are that any change in the transmission of the image-forming optics of the sensor system, due to the condensation of outgassed contaminants, will be undetected and the on-board calibration system is also assumed to be stable through launch and unaffected by the vacuum, high energy particle irradiation, and zero-g environment at orbital altitudes. The Thematic Mapper and the Multispectral Scanner System on Landsat-D are examples of remote sensing systems calibrated in this manner.

(2) The sun or an on-board calibrated source can be used to irradiate the focal plane through the image-forming optics. The drawbacks to this approach are the uncertainty in the knowledge of (a) the irradiance of the sun above the atmosphere and (b) the output of the calibrated source system, for the reasons mentioned earlier. Furthermore, in examples of the use of this procedure (MSSs 1, 2 and 3 and SPOT), the calibration beam passes through only a small portion of the aperture of the system, thus not simulating the actual operation of the system. When imaging the ground, the system entrance aperture is irradiated over its entire area by flux incident over a roughly three steradian solid angle. In the imaging mode there is much more stray light present in the system and incident on the focal plane. If this additional flux level is unknown, it may introduce a substantial uncertainty into the absolute calibration of the system.

(c) Reference can be made in-flight to a ground area of known spectral radiance. If at the time the sensor system is imaging the known area, measurements are made of the atmospheric conditions, these data can be used with an atmospheric radiative transfer program to predict the spectral radiance at the entrance pupil of the sensor. The main uncertainty in this approach is that of determining the atmospheric aerosol content well enough. The approach is also limited to scenes having large uniform areas of high radiance. For example, although many water bodies are of sufficient size and uniformity, they are not appropriate for calibration purposes because their radiance is too low to provide a calibration of sufficient accuracy or to cover much of the dynamic range of the sensor. Fortunately, some suitable areas do exist, particularly in the arid regions of

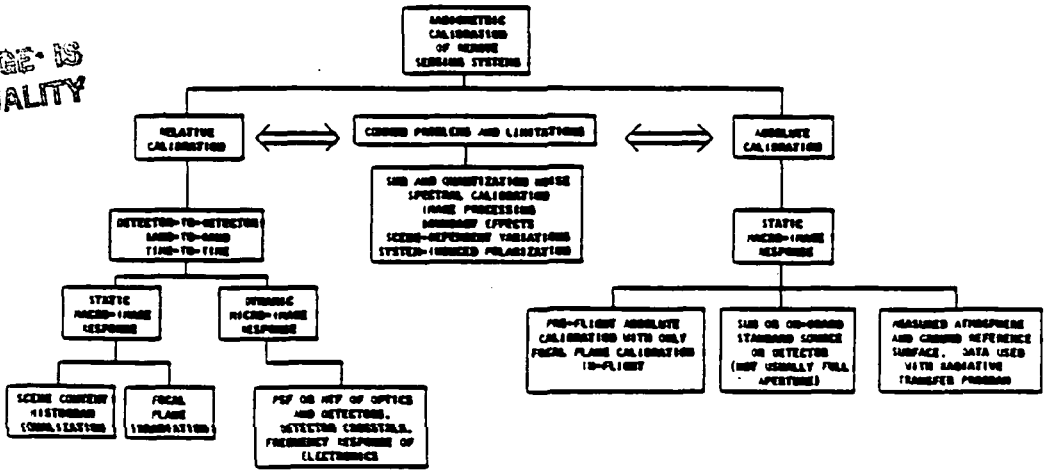

Fig. 3. Classification of radiometric calibration procedures.

the world, for example at White Sands, New Mexico, in the United States.

The rest of this paper is devoted to discussion of the factory and in-flight calibration of an MLA system using the self-calibrated photodiode approach and the use of a ground reference area for calibration purposes.

4. CALIBRATION IN THE FACTORY AND IN ORBIT

The concept proposed for the factory calibration is similar to the proposed orbital procedure, the main difference being that an artificial source is used in the factory and the sun is used in orbit—simply a matter of convenience in the former case and of convenience and reliability in the latter case. In the factory, redundancy is not at a premium and our requirements for a source are simply power, spectral flatness, and stability. We do not need a standard source although an array of standard NBS FEL tungsten halogen lamps could be used, if their polarization characteristics can be tolerated (Ref. 13). A xenon arc selected for minimum arc wander and with a highly stable power supply and a feedback loop would suffice.

The source would be used to irradiate a near-Lambertian, near-unity-reflectance, white-surfaced panel perhaps 1 m x 0.5 m in size in front of the system. (An integrating sphere could be used, but it would have to be very large, and uniformity checks can sometimes themselves introduce non-uniformities.) A self-calibrating NBS-style radiometer, with the incident beam perhaps defined by two or three apertures, and using spectral bandpass filters matching those used in the MLA, would be used to determine the radiance of the panel in each band. The MLA would image the panel out of focus, but being an extended object, its image would have exactly the same irradiance in or out of focus. The arrangement is sketched in Fig. 4.

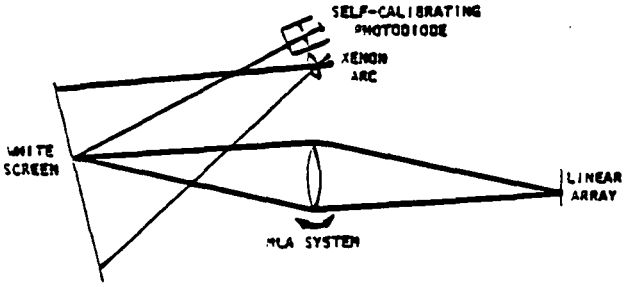

Fig. 4. The factory procedure for absolute spectroradiometric calibration.

To avoid problems due to the nonuniform irradiation of the panel, the MLA should be rotated to sequentially irradiate the focal plane with the image of the same small area that is sampled by the radiometer. The reason for a large panel is to simulate the viewing conditions from space in which, depending on the baffle design, significant out-of-the-field-of-view stray light could be incident on the image plane to modify the calibration. For this reason it would be worthwhile to conduct at least one calibration using a white panel several meters in diameter. To check for linearity of response, several different irradiance levels on the panel should be used. This irradiance level can be changed conveniently by inserting heat-resistant neutral density filters in front of the stabilized xenon arc source.

The profiles of the spectral filters should be measured in a spectrophotometer using the same F/No. beam as the MLA. If they are integral with the array, they should be measured using a double monochromator, again with the MLA F/No., before installation in the focal plane. Care should be taken to cover the whole wavelength sensitivity range of the detectors, the off-band suppression being particularly important for detectors with the wide spectral response of silicon.

The procedure proposed here for in-flight calibration is similar to the panel method sketched in Fig. 4, but it uses the sun as the source. We believe that the irradiance over the panel can then be considered to be uniform and known spectrally to better than 1% absolute. (Several solar measurement programs are currently being conducted with this accuracy as a goal. However, if the uncertainty is thought to be greater than 1%, a pyroelectric detector could be used to measure the direct solar flux in orbit, over the wavelength intervals of interest and at the same time that the system is being calibrated.) The calibration would be carried out in the few minutes while the spacecraft is sun-illuminated but before it images the sun-illuminated earth. The absolute radiometer containing the pyroelectric detector would now be needed only to check for any deterioration in the reflectance of the panel owing to exposure to the space environment and short exposures to unattenuated UV and other high energy radiation from the sun and from space. In this last respect, the panel would usually be stowed in a well-shielded compartment and exposed only during actual calibration checks. Also, when deployed, it would not interfere with normal operation of the system, as it would be viewed by the stereo mirror in one of its extreme positions. In this respect it is fail-safe.

5. WHITE SANDS AS A CALIBRATION REFERENCE

To keep the decription of the theory of the method brief, spectral dependencies are not included in the following discussion. In all cases the spectral dependence is implied, the spectral value having the same wavelength dependence as the spectral response of each band of the sensor being calibrated. The theoretical basis for the calibration method is straightforward.

The radiance at the sensor, L_s, is determined with respect to the ground radiance, L_g, the reduction of this radiance by the upward path through the atmosphere, $\tau'_{ext} \sec\theta$ (where τ'_{ext} is the atmospheric extinction and θ is the nadir scan angle), and $L_{\theta,\phi}$, the atmospheric path radiance (where ϕ is the azimuth angle of the observation). Thus,

$$L_s = L_g \exp(\tau'_{ext} \sec\theta) + L_{\theta,\phi}$$

The path radiance term, $L_{\theta,\phi}$, in the equation is unknown and can be determined only by the use of a radiative transfer calculation. Such calculations require a knowledge of τ'_{ext}, ground reflectance, the irradiance incident at the top of the atmosphere, the aerosol optical depth and phase

function, the optical depth due to ozone and water vapor, the solar zenith angle, the nadir angle of the sensor, and its azimuthal angle with respect to the sun's direction. These radiative transfer calculations assume an infinite, flat, Lambertian reflecting surface with an atmosphere composed of plane homogeneous layers. Although these assumptions are never exactly met, they are closely approximated by the nearly Lambertian flat surface of the gypsum at White Sands and the small field of view of the space sensors.

The quantity τ'_{exp} can be determined from the solar radiometer data in the following way. The solar radiometer records the irradiance E_{θ_z} at the ground as a function of the solar zenith angle during the morning of the overpass. If the atmospheric conditions are steady during that period, the Langley plot of $\ln E_{\theta_z}$ against $\sec\theta$ is a straight line of slope τ'_{ext}. The extrapolation of the line to a $\sec\theta_z$ value of zero gives the value of the irradiance above the atmosphere in the measurement passband. The value of the ground radiance L_g is determined at the time of the overflight by the solar radiometer looking at the ground at the same θ and ϕ angles as that of the space sensor. The ground radiance value can be converted into the reflectance required as input to the radiative transfer program in one of two ways. First, the global irradiance can be measured by the solar radiometer with either a horizontal cosine diffuser or an integrating sphere, with horizontal entrance port, placed over the entrance aperture of the solar radiometer. Or second, the solar radiometer can be pointed down at a horizontal, diffusing, white surface such as $BaSO_4$ or Halon. The cosine diffuser approach is preferred because its small surface can be conveniently stored to minimize contamination. Intercomparisons will be made, during the six monthly recalibrations of the field equipment, between the cosine diffuser global irradiance and the Lambertian white reference surface measurements of the ground reflectance. The nadir angle from the satellite to the ground observation point, the solar zenith angle, and the azimuth of the satellite nadir angle to the sun's direction are all readily determinable. Such quantities as atmospheric pressure, humidity, surface and air temperature, etc., are routinely monitored by the Atmospheric Sciences Laboratory at White Sands. These data will be formatted with the radiation data and telemetered to Wallops Island, Virginia, United States.

The difficult quantities to determine for radiative transfer calculations are the characteristics of the atmospheric aerosols. Fortunately, we can make reasonable assumptions regarding their values based on prior results. For example, 79 aerosol profiles have been measured at White Sands (Ref. 14) to establish an atmospheric model; the effects of aerosol complex refractive index and size distribution on extinction and absorption for the wavelength range 0.55 to 10.6 um for desert atmospheres are reported in reference 15; and reference 16 reports that the imaginary refractive index is 0.007 at 0.6 um and shows little dependence on wavelength over the range 0.3 to 1.1 um.

We intend to investigate some new techniques for determining aerosol chacteristics that are under development and that make use of sky polarization measurements. We also intend to explore methods of monitoring the aerosol size distribution from inversion of the spectral optical depth measurements (Ref. 17) and aureole measurements (Ref. 18). Some of these measurements and analyses, particularly the polarimetric, fall into the research category. They represent attempts to improve the accuracy of the calibration procedure and, because of their untested nature, require validation. However, without them we anticipate an overall accuracy of about ±3% absolute. This represents an improvement over the ±5% value claimed in reference 19, and is due to our anticipated ±1% absolute accuracy of calibration of the ground instrumentation.

The proposed basic design of the instrumentation is similar to that being designed and built at the University of Arizona for the investigation of solar irradiance variations over a 23-year period. It employs a precision alt-azimuth tracking stand, with stepper motors to drive the two axes, so that it can be pointed in almost any direction or be held in alignment with the sun. A microprocessor based computer system will be used to control the motors as well as the data acquisition and processing system. A conceptual view of the instrument is shown in Fig. 5, further details of its design will be presented at the symposium.

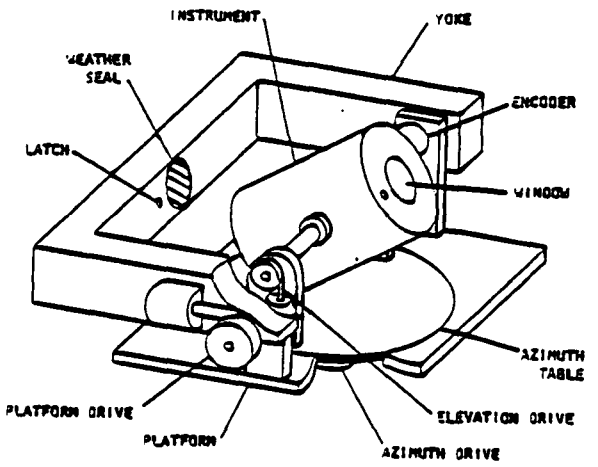

Fig. 5. Conceptual view of spectroradiometer for ground and atmospheric measurements.

6. ACKNOWLEDGEMENTS

I wish to thank J. Geist, S.J. Martinek, J.M. Palmer and E.F. Zalewski for the benefit of useful discussions. This work was supported under grant number NAG 5-196.

7. REFERENCES

1. Slater P N 1980, *Remote Sensing: Optics and Optical Systems*, Reading, Mass., Addison-Wesley, 481-484.

2. NASA Contract NASS-23639 1977, *A study of the effects of the atmosphere on thematic mapper observations*, by Pearce W A.

3. Dave J V 1980, Effect of atmospheric conditions on remote sensing of a surface nonhomogeneity, *Photogram Eng & Remote Sensing* 46(9), 1173-1180.

4. NASA Tech Memo 33818 1981. *The effect of finite field size on classification and atmospheric correction*. by Kaufman Y J & Fraser R S.

5. Tanre D et al 1981. Influence of the background contribution on space measurements of ground reflectance, *Appl Opt.* 20(20), 3676-3684.

6. Environmental Res Inst of Michigan Final Report E77-10057 1976. *Investigation of Landsat follow-on thematic mapper spatial, radiometric and spectral resolution*, by Morgenstern J P et al.

7. Geist J 1979, Quantum efficiency of the p-n junction in silicon as an absolute radiometric standard. *Appl Opt.* 18(6), 760-762.

8. Geist J 1980, Silicon photodiode front region collection efficiency models. *J Appl Phys.* 51(7), 3993-3995.

9. Geist J et al 1979, Spectral response and self-calibration and interpolation of silicon photodiodes, *Appl Opt.* 19(22), 3795-3799.

10. Geist J & Zalewski E F 1979, The quantum yield of silicon in the visible, *Appl Phys Lett.* 35(7), 503-506.

11. Zalewski E F & Geist J 1980, Silicon photodiode absolute spectral response self-calibration, *Appl Opt.* 19(8), 1214-1216.

12. Zalewski E F 1981, private communication.

13. Kostuk R K 1981, Polarization properties of a 1000-W FEL type filament lamp, *Appl Opt.* 20(13), 2181-2184.

14. Air Force Cambridge Research Laboratories Environmental Research Papers No 285 1968, *UV visible and IR attenuation for altitudes to 50 km*. by Elterman L.

15. Jennings S G et al 1978, Effects of particulate complex refractive index and particle size distribution variations on atmospheric extinction and absorption for visible through middle ir wavelengths, *Appl Opt.* 17(24), 3922-3929.

16. Lindberg J D & Laude L S 1974, Measurement of the absorption coefficient of atmospheric dust, *Appl Opt.* 13(8), 1923-1927.

17. King M D et al 1978, Aerosol size distribution obtained by inversion of spectral optical depth measurements, *J Atmos Sci.* 35, 2153.

18. Twitty J T 1975, The inversion of aureole measurements to derive aerosol size distributions, *J Atmos Sci.* 32, 584.

19. Kriebel K T 1981, Calibration of the METEOSTAT-VIS channel by airborne measurements, *Appl Opt.* 20(1), 11-12.

Reprinted from Applied Optics, Vol. 21, page 3923, November 1, 1982.

Atmospheric effects on radiation reflected from soil and vegetation as measured by orbital sensors using various scanning directions

Philip N. Slater and Ray D. Jackson

Ground-measured spectral reflectance data for Avondale loam and drought-stressed and unstressed wheat were converted into digital counts for spectral bands 5 and 7 of the Landsat Multispectral Scanner System (MSS). For dry loam, the differences between ratios of MSS bands 7–5 as determined from space and from ground level measurements were 2.3% for clear and 5.6% for turbid atmospheric conditions. By contrast, for wet loam the differences were 10.4 and 29.5%. We found that atmospheric conditions may cause a delay of from 3 to 7 days in the discrimination between drought-stressed and unstressed wheat. For oblique angle observations the atmospheric modification of ground-measured reflectances increased with angle at a greater rate in the 0/180° azimuth than in the 90/270° azimuth. Implications of this result are discussed for oblique angle Système Probatoire d'Observation de la Terre (SPOT), Mapsat, future multispectral linear array system imagery, and wide-angle imagery collected from scanners in high-altitude aircraft.

I. Introduction

During the first years that Landsat satellites were in orbit there was a paucity of ground-based information on which to base interpretations of satellite imagery. In the past few years a considerable amount of ground-based data has accumulated that describes the spectral reflectance characteristics of earth surface features; a recent colloquium in fact was devoted largely to ground-based measurements of the spectral signatures of soil and vegetation.[1] The reason for using ground-based data is that they can describe the experimental results of different agronomic treatments on numerous small plots. Such experiments can be conveniently conducted repeatedly and rapidly to yield relationships between agronomic variables and remotely sensed parameters.

To permit comparison of ground-based information and satellite data, atmospheric scattering and absorption must be accounted for. Atmospheric scattering has been considered by Chance,[2] Dave,[3,4] Otterman and Fraser,[5] Potter,[6] Richardson *et al.*,[7] Rochon *et al.*,[8] and Turner *et al.*[9] The effect on the Landsat Multispectral Scanner System (MSS) band 7 of atmospheric water vapor absorption at 0.96 μm has been investigated by Pitts *et al.*[10] (Absorption in the thermal IR bands has been studied by several investigators but is not relevant here.)

Philip Slater is with University of Arizona, Optical Sciences Center, Tucson, Arizona 85721; Ray Jackson is with U.S. Department of Agriculture, Agriculture Research Service, Water Conservation Laboratory, Phoenix, Arizona 85040.

Received 13 April 1982.

A recent report by Schnetzler[11] concerning the effect of the atmosphere on the radiance at the sensor for oblique viewing angles is of particular interest. He determined the conditions that allow off-nadir across-track angles to be used so that the radiance difference between nadir and off-nadir is <5%. His variables included three atmospheric conditions, two wavelengths, a range of latitudes from 60° north to 60° south, solstice and equinox dates, two equatorial crossing times, and bidirectional reflectance data for a grass target.[12,13]

Our results complement those of Schnetzler, although fewer variables are considered. Our purpose is to show, through use of ground-based data and an atmospheric radiative transfer model, how satellite data vary with atmospheric conditions. Our data cover a wide range of Lambertian reflectances for bare soil and for drought-stressed and well-watered wheat. Employing the commonly used vegetation index MSS7/MSS5, we illustrate the magnitude of atmospheric effects on the soil line (a fundamental parameter for the physically based model of Kauth and Thomas[14]) and on stressed and nonstressed wheat. The data were calculated in terms of Landsat digital counts and include an example of signal quantization. Two optical depths were considered, and the ranges of nadir and azimuthal look angles were chosen to include the Landsat MSS, Système Probatoire d'Observation de la Terre (SPOT), Mapsat, and future multispectral linear array systems as well as high-altitude aircraft scanners. The specific reflectance data used were the soil line for Avondale loam described by Jackson *et al.*[15] and the discrimination of stressed from unstressed vegetation described by Jackson and Pinter.[16]

II. Geometric and Atmospheric Considerations

Figure 1 is a plot of solar azimuth angle (measured eastward from north) as a function of the variation of solar declination angle throughout the year. The latitude values for the four curves are 55, 30, 15° N, and 0. The longitude values corresponding to the position of a satellite in a 99° inclination orbit are, respectively, 94, 104, 108, and 111° W. Actually this particular orbit is Landsat path 33 in the Worldwide Reference System index map of the U.S.A. compiled by the U.S. Geological Survey and included in the *Landsat Data Users Handbook*.[17] The orbital path crosses the U.S.A. from eastern North Dakota to western Texas with an equatorial crossing time of ~0930 h. Because of the nature of the Landsat orbit, this particular orbit is typical of all others covering this latitude range at the times of year shown in Fig. 1.

The nadir-viewing mode of operation of the proposed Mapsat system, Colvocoresses,[18] and Itek,[19] is geometrically identical to that of the Landsat MSS.

A. Solar Zenith Angle

We used the single solar zenith angle of 45° to minimize the number of costly radiative transfer calculations required. This resulted in introduction of a variation in the time of year with latitude. Thus by reference to Fig. 1, we see that at 55° N the corresponding times of year are late April and mid-August; similarly, 30° N corresponds to mid-March and late September and 15° N to mid-February and late October.

B. Solar Azimuth Angle

The solar azimuth angles, measured eastward from north, corresponding to a solar zenith angle of 45° at latitudes of 55, 30, and 15° N, are roughly 150, 132, and 128°. Taking into account the roughly 99° orbital inclination of the Landsat MSS, the azimuthal angles between the orbital path and the sun's direction become 141, 123, and 119°; for convenience we chose a single value of 120° (see Fig. 2). The MSS scans across a swath perpendicular to the orbital plane. Thus, for the case considered here, the scan direction is at a 30° azimuthal angle to that direction.

C. Nadir Viewing Angle

A 5° angle to nadir was selected. For reference, the maximum angles to nadir for the Landsat MSS and Thematic Mapper are 5.8 and 7.5°, respectively. The MSS scan direction is not perpendicular to the sun–target–sensor plane, so we can expect to obtain different angular distributions of the radiance levels at the sensor on either side of nadir. This is because of nadir angle variations in atmospheric path radiance, depending on whether the nadir angle is 5° to the east or the west of the nadir point. We shall discriminate between these cases by referring to 5° E or 5° W, recalling that these scan positions are at 30° in azimuth to the sun–target–sensor plane.

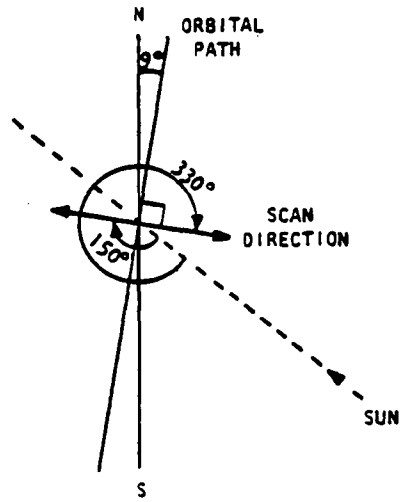

Fig. 2. Irradiance and sensing geometry selected. The solar zenith angle is 45°. The scan directions are at azimuth angles with respect to the sun–target–sensor plane of ϕ = 150 and 330°. For convenience, these directions are designated as westerly (W) and easterly (E), respectively. Thus θ_N = 5° E refers to an angle of view from nadir of 5° in a direction 330° in azimuth (measured in a clockwise sense) from the sun's direction.

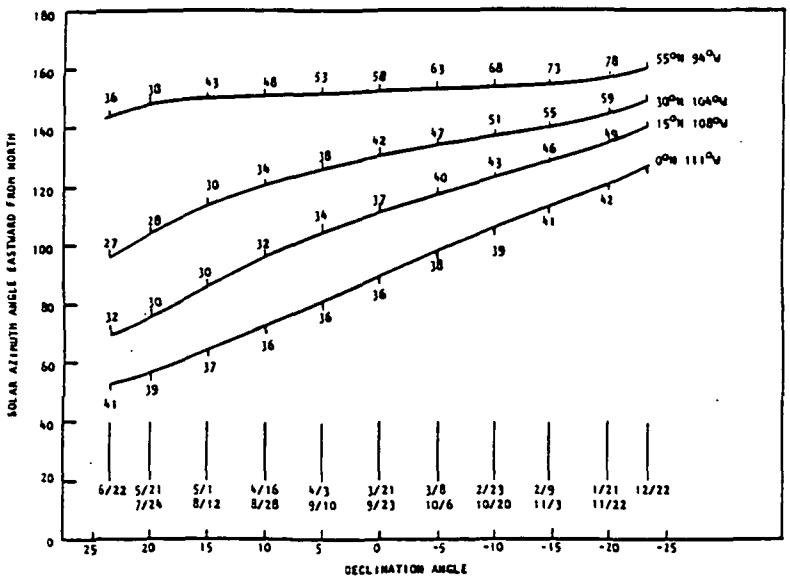

Fig. 1. Plot of solar azimuth angle vs solar declination angle for a typical Landsat orbit. The day and month of the year and the solar zenith angle are marked for 5° increments of declination angle. The latitudes considered are 0, 15, 30, and 55° N.

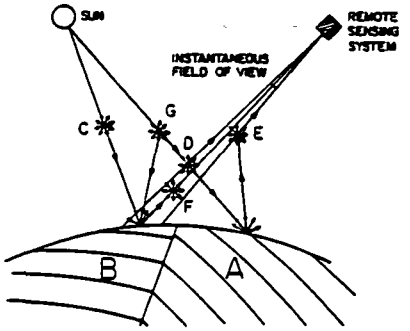

Fig. 3. Role of the atmosphere in attenuating and scattering incident and reflected radiant flux.[20]

D. Atmospheric Considerations

The various ways in which the atmosphere influences remotely sensed data collected from high altitudes can be appreciated by reference to Fig. 3. Solar radiant flux is partially absorbed or scattered as it passes through the atmosphere to the earth's surface. The surface at B is, therefore, irradiated by direct solar flux and by scattered flux from the hemisphere of sky above B. An example of this latter contribution is the scattered flux from G. The ground scene reflects part of the flux incident on it in the direction of the remote sensing system. This reflected flux, passing through the atmosphere, is again absorbed and scattered as shown at F, but to it is added scattered flux from the atmosphere shown at D that has not been reflected from the ground scene. The radiance contribution at the entrance pupil of the system owing to scattering at points such as D provides a major contribution to what is referred to as path radiance. Scattering at point E in Fig. 3 also contributes to path radiance and is accounted for in the radiative transfer calculations. However, we do not consider the case of A having a different reflectance than B.

The primary quantity that determines the influence of the atmosphere on the total radiance L_s at the entrance pupil of an orbital sensor is the atmospheric spectral extinction coefficient or optical depth $\tau'_{ext}(\lambda)$, which is defined in terms of the spectral transmittance $\tau(\lambda)$ along a slant path at a zenith angle θ through the entire atmosphere by

$$\tau(\lambda) = \exp[-\tau'_{ext}(\lambda) \sec\theta]. \quad (1)$$

A change in $\tau'_{ext}(\lambda)$ causes a number of interrelated changes in the ground irradiance and in L_s. Thus with larger $\tau'_{ext}(\lambda)$, we get smaller direct solar irradiance at the ground but a larger component of diffuse downward scattered flux, greater attenuation of the flux reflected from the ground, and greater path radiance. The greater path radiance is important in quantitative studies of imagery collected from high-altitude aircraft or space sensors, because, for low-ground reflectances, short wavelengths, or turbid atmospheres, it is the predominant component of radiance at the entrance pupil of the sensor.

The radiative transfer calculation technique developed by Herman and Browning,[21] used to obtain the results for a simulated atmosphere, and described in the following, assumes a flat earth with an infinite uniform Lambertian surface and a horizontally homogeneous atmosphere. All orders of atmospheric scattering are included. (Polarization effects could have been calculated, but they were not for this analysis.) The atmospheric parameters used as input to the model assumed a Junge size distribution of nonabsorbing particles of refractive index 1.54, which corresponded to a Mie extinction coefficient that varied in inverse proportion to the wavelength. The output from the radiative transfer calculations gave the total radiance emerging from the top of the atmosphere at 5, 15, 25, 35, and 45° to nadir as a function of five ground reflectances (0, 0.1, 0.25, 0.5, and 0.75) for two wavelengths roughly at the centers of MSS5 and MSS7 (0.65 and 0.9 μm), for four azimuthal planes (0/180, 30/210, 60/240, and 90/270°), and for a clear and a turbid atmosphere.

Figure 4 is a plot of spectral extinction coefficient against wavelength for the clear and turbid atmospheres examined and, for reference, for a Rayleigh atmosphere. The extinction coefficients as a function of wavelength are listed in Table I for the Rayleigh and aerosol scattering components. The meteorological range for the clear atmosphere is ~100 km, which is typical of a clear

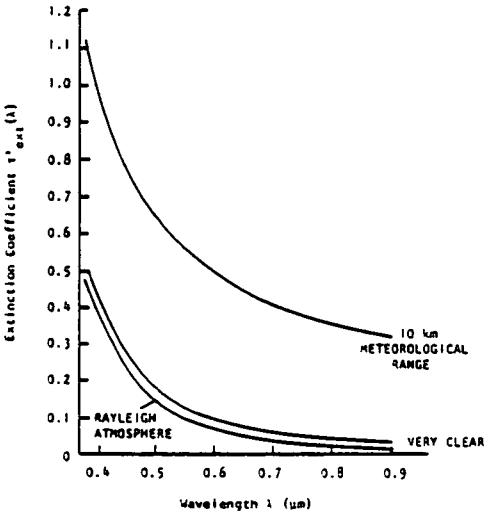

Fig. 4. Atmospheric extinction coefficient as a function of wavelength for various atmospheric conditions.

Table I. Rayleigh, Mie, and Total Extinction Coefficients for the Different Atmospheres Studied

Atmosphere	Wavelength (μm)	Rayleigh	Mie	Total
Clear	0.65	0.048	0.026	0.074
Turbid	0.65	0.048	0.397	0.445
Clear	0.90	0.013	0.020	0.033
Turbid	0.90	0.013	0.300	0.313

day in the desert Southwest of the U.S.A. and many other arid regions of the world. The meteorological range for the turbid atmosphere is 10 km. Flowers *et al.*[22] have found that, for selected urban sites across the U.S.A., on 55% of the days in the year the meteorological range is <10 km; for suburban and rural areas the percentages are 18 and 1%, respectively.

Several assumptions and approximations have been made to simplify the analysis:

(1) Lambertian reflectance has been assumed throughout.

(2) A flat earth has been assumed which means that results for large angles to nadir predict too small an atmospheric effect. The actual slant range (h in meters) can be calculated approximately from

$$h = [R\cos\theta - (R^2\cos^2\theta - 2HR\sin^2\theta)^{1/2}]/\sin^2\theta, \qquad (2)$$

where R = earth radius in meters,
H = sensor altitude in meters, and
θ = slant angle to nadir.

For high-altitude aircraft the difference between the curved and flat earth slant ranges is insignificant, even when $\theta = 45°$. However, for a nadir angle of 25° at an altitude of 700 km, used in a later example, the effective atmospheric path for a curved earth corresponds to a nadir angle of 23.7°.

(3) Square passbands between 0.6 and 0.7 and 0.8 and 1.1 μm, having the atmospheric characteristics of monochromatic wavelengths at 0.65 and 0.9 μm, have been assumed to model the Landsat MSS sensor. In view of the accuracy of the radiative transfer calculation method used, this approximation may seem unnecessarily rough. However, at present, we cannot characterize the atmosphere well enough from measurements on a global scale to merit using more accurate simulations. For example, even for one particular remote sensing measurement, it is difficult to determine whether absorbing aerosols are present and, if they are, what complex indices of refraction to ascribe to them. Furthermore, the adjacency effect described by Pearce[23] has not been experimentally validated and is difficult to account for even for simple scenes.

(4) The effect of atmospheric water vapor was not considered, although it must be in all practical applications of MSS7 data. The reasons for neglecting water vapor absorption were twofold: first, it can be largely accounted for from the results of Pitts *et al.*,[10] who showed that the water absorption band centered at 0.94 μm can reduce the radiance at the sensor by a factor of 0.77; second, later systems such as the Thematic Mapper and SPOT use near-IR passbands that avoid strong water absorption bands.

The following calculations are designed, then, to indicate representative trends rather than predict accurately the influence of specific atmospheric characteristics on the radiance at the sensor. We start by describing the procedure for determining the relationship between the digital counts for MSS5 and MSS7 for the two atmospheric conditions defined and for Avondale loam and wheat (*Triticum durum* Desf. var. Produra).

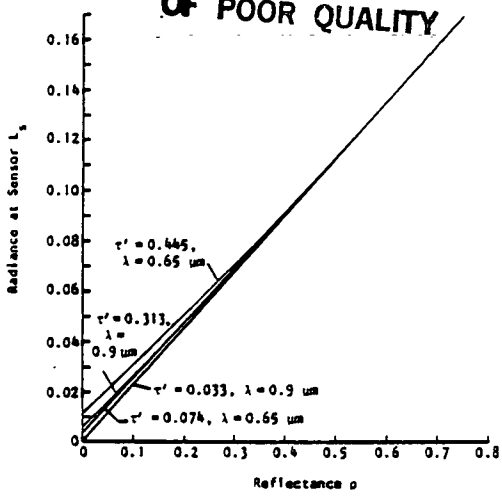

Fig. 5. Radiance at the sensor as a function of Lambertian ground reflectance for clear and turbid atmospheric conditions in bands 5 and 7. Curves are for unity irradiance, normal to the sun's direction at the top of the earth's atmosphere, and a solar zenith angle (θ_z) = 45°.

III. Calculation Procedure for Avondale Loam

(1) Figure 5 was plotted from the results of the radiative transfer model to relate the radiance at the sensor L_s to the ground reflectance ρ. Note that the radiance values correspond to an incident irradiance of unity at the top of the atmosphere. Figure 5 is not at a scale to show differences between the 5° E and 5° W curves, and hence only the four curves for the 5° E case are shown; however, the least-squares fits for all eight cases are listed in Table II.

(2) Using the best fit equation in Fig. 6 for Avondale loam, values for ρ_7 were determined corresponding to ρ_5 values of 0, 0.1, 0.25, 0.5, and 0.75.

(3) The radiances L_5 and L_7 corresponding to the sets of ρ_5 and ρ_7 values were determined by substituting the appropriate reflectance values in Eqs. (3) and (7) listed in Table II. (Later, in plotting the relationship between L_5 and L_7 for low ρ values, all eight equations listed in Table II were used.)

(4) A least-squares equation was determined that related L_5 and L_7.

(5) Steps (3) and (4) were repeated using Eqs. (5) and (9) to yield a least-squares fit for the relationship between L_5 and L_7 for the more turbid atmosphere. The least-squares fits for the two relationships are

$$L_7 = 2.6058 \times 10^{-3} + 1.2363L_5 - 0.17032L_5^2 \qquad (11)$$

for the clear atmosphere,

$$L_7 = -2.4725 \times 10^{-3} + 1.2815L_5 - 0.17685L_5^2 \qquad (12)$$

for the turbid atmosphere.

(6) Four sets of corresponding L_5 and L_7 values from the equations in Table II were converted to digital counts over the low reflectance range $0 < \rho < 0.1$. These were used to determine the change in radiance

Table II. Least-Squares Fits for the Radiance at the Sensor in Terms of Ground Reflectances[a]

λ (μm)	$\tau_{ext}(\lambda)$	Scan azimuth w.r.t. sun[b] (deg)	Eq.	a	b	c
0.65	0.074	30 (E)	(3)	4.545×10^{-3}	0.2106	1.194×10^{-2}
		30 (W)	(4)	4.972×10^{-3}	0.2108	1.155×10^{-2}
	0.445	30 (E)	(5)	1.202×10^{-2}	0.185	3.343×10^{-2}
		30 (W)	(6)	1.270×10^{-2}	0.185	3.343×10^{-2}
0.90	0.033	30 (E)	(7)	1.393×10^{-3}	0.2203	4.641×10^{-3}
		30 (W)	(8)	1.538×10^{-3}	0.2202	4.645×10^{-3}
	0.313	30 (E)	(9)	6.659×10^{-3}	0.1996	2.434×10^{-2}
		30 (W)	(10)	6.989×10^{-3}	0.1999	2.395×10^{-2}

[a] a, b, and c are coefficients in the equation $L_s = a + b\rho + c\rho^2$; nadir angle is 5°.
[b] (E) and (W) refer to easterly and westerly directions; that is, the 5° nadir angle is pointing into the direction of the sun and at 30° to the sun–target–sensor plane in the (E) case and away from the direction of the sun at 30° to the sun–target–sensor plane in the (W) case.

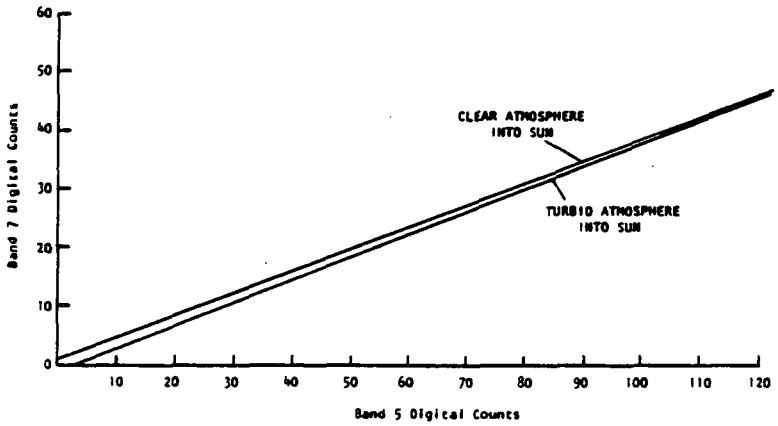

Fig. 7. Plots of digital counts in band 7 vs band 5 for Avondale loam under clear and turbid atmospheric conditions.

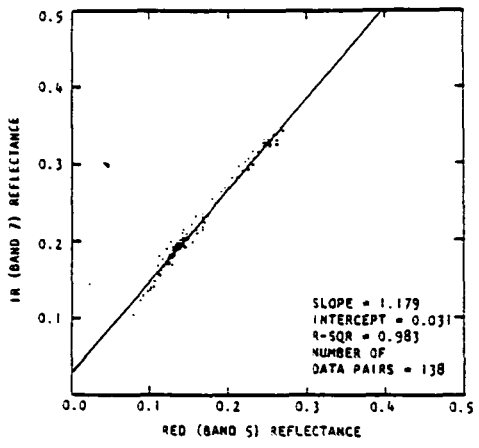

Fig. 6. Band 7 vs band 5 reflectance for Avondale loam, Phoenix, Ariz. The coefficient of determination (R-SQR) was 0.983. Data were taken between 1330 and 1400 h from Nov. 1978 to May 1979.[15]

at the sensor owing to a change in the viewing angle from 5° E to 5° W and to examine the effect of quantization. Results are discussed later and presented in Fig. 8.

The procedure for converting the radiances in Eqs. (11) and (12) to digital counts from the Landsat MSS5 and MSS7 was as follows. First, the actual radiances at the entrance pupil of the MSS in bands 5 and 7 were found by multiplying the normalized radiance values by 15.1 and 25.1. These are the solar irradiances in mW cm^{-2} in bands 5 and 7 as determined from solar spectral irradiance data tabulated by Thekaekara *et al.*[24] Then a range of pairs of MSS5 and MSS7 radiance values was converted to digital counts (DC) by use of the following relationships[25]:

$$\text{Band 5 DCs} = (L_5 - 0.07)/0.0117; \quad (13)$$

$$\text{Band 7 DCs} = (L_7 - 0.14)/0.0637. \quad (14)$$

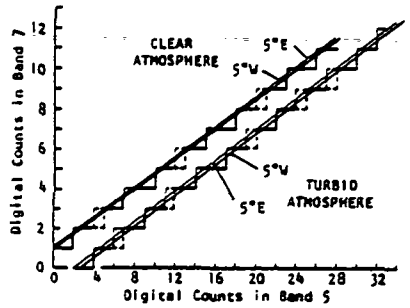

Fig. 8. Digital counts in band 7 vs band 5 for clear and turbid atmospheres for scan positions of ±5° to nadir. The staircases show the effect of Landsat MSS 6-bit quantization.

IV. Results in Terms of Digital Counts

Figure 7 is a plot of the digital counts in band 7 vs the corresponding counts in band 5 for the two atmospheric conditions. Note that the substitution of 127 and 63 counts in Eqs. (13) and (14) yields the levels of entrance pupil radiances (1.56 and 4.15 mW cm^{-2}) that correspond to the onset of detector saturation for the Landsat 2 MSS during the 22 Jan. to 15 July 1975 period.

The digital counts are the consequence, of course, of the quantization of the output signals from the MSS. However, Fig. 7 does not reflect this condition in two respects. First, the straight lines should have a staircase pattern, each step corresponding to one or more counts. Second, band 5, like bands 4 and 6, is initially quantized into 64 steps and later during ground processing expanded to 128 steps. If the initial quantization is linear, not logarithmic, each of the 128 steps has a precision of one part in 64, not one part in 128. If the initial quantization is logarithmic, the precision will vary throughout the dynamic range. The noise equivalent radiance difference detectable by the MSS is approximately half of a digital count in each channel, so with a probability of 95% the radiance error for a single pixel is ±1 count or ±1.6%.

Figure 8 shows the plots of digital counts in bands 5 and 7 for clear and turbid atmospheric conditions and for a nadir look angle of 5° in both the easterly and westerly azimuthal directions. Because of the coarse quantization of the MSS, shown by the uneven staircase patterns, we cannot differentiate in most cases between the 5° E and 5° W results. However, the quantization resolution is quite adequate when related to the standard deviation of data, presented in Fig. 6, for the reflectances of Avondale loam. In this regard it is interesting to note that, when imaging identical ground features, the future systems with their greater quantization resolution of 256 steps will output significantly different digital counts between easterly and westerly scan positions. This is particularly true for systems that operate in a non-nadir viewing mode, as we shall see later.

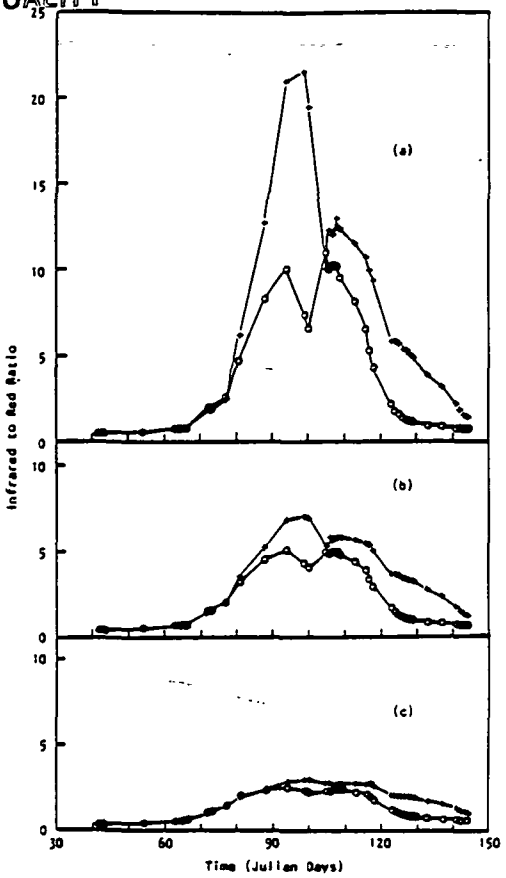

Fig. 9. Effect of the atmosphere on the MSS digital counts from stressed O and unstressed + vegetation. (a) Results of ground-measured reflectance ratios (unmodified by the atmosphere); (b), (c) results using simulated Landsat counts through clear and turbid atmospheric conditions, respectively.

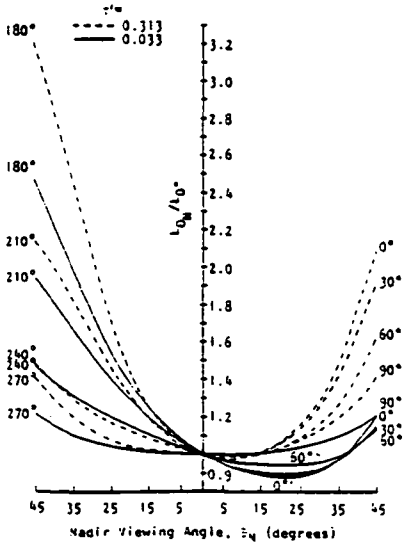

Fig. 10. Normalized values of $L_{\theta N}/L_{0°}$ vs nadir viewing angle for λ = 0.9 μm, ρ = 0.0, and ϕ = 0/180, 30/210, 60/240, 90/270° for clear and turbid atmospheres.

V. Results for Vegetation

Jackson and Pinter[16] have shown that the ratio of band 7 to band 5 reflectances can be used to discriminate water-stressed vegetation. Results of radiative transfer calculations, shown in Fig. 5 and listed in Table II, were applied to the measured values of band 7 and band 5 values reported in Ref. 16 following the procedure outlined earlier for Avondale loam. The resulting curves for the band 7 to band 5 ratios, for high quantization resolution digital counts, are shown in Figs. 9(b) and (c) for clear and turbid conditions. For comparison, Fig. 9(a) is a plot of the ground reflectance ratios for stressed and unstressed vegetation.

Calculations show that the 6-bit quantization of the MSS is sufficient to differentiate between the ratio values in Fig. 9(a) at Julian day 94 at the 95% probability level, but it is insufficient for the same day under clear and turbid atmospheric conditions. The 8-bit quantization of future sensors will differentiate between the ratios in Fig. 9(a) over the entire period of interest from day 77 to day 118. It will also provide differentiation of the ratios at about day 88 under clear conditions [Fig. 9(b)] and at about day 94 under turbid atmospheric conditions [Fig. 9(c)].

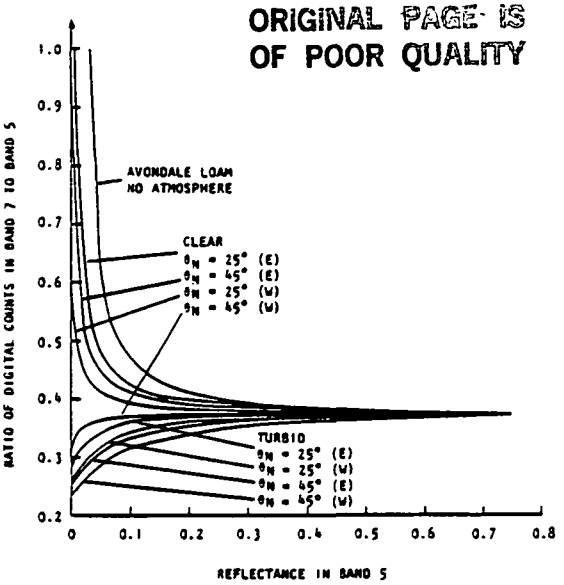

Fig. 11. Ratio of digital counts in band 7 to band 5 for the Landsat MSS as a function of the reflectance in band 5 for Avondale loam. Results are for three atmospheric conditions: no atmosphere and a clear and a turbid atmosphere. The nadir view angles are 25° E, 25° W, 45° E, and 45° W.

VI. Oblique Angle Imagery

The effect of the atmosphere can be illustrated most dramatically by considering the radiance at the entrance pupil of a space sensor that is imaging a region of zero reflectance. This radiance is then entirely path radiance. Figure 10 is a plot of the radiance at the entrance pupil of the high altitude or space sensor as a function of the angle between the scan direction and the nadir (which we call the nadir angle) to that for zero nadir angle. Several nadir angles θ and azimuths, ϕ were considered. (The ϕ = 0/180° azimuth describes the vertical plane containing the sun and the target with ϕ = 0 representing the direction into the sun.) The curves are for a wavelength of 0.9 μm and for the clear and turbid atmospheric conditions described earlier.

The following conclusions can be drawn from Fig. 10. First, the largest variation in the radiance at the entrance pupil of the sensor occurs for the ϕ = 0/180° azimuth, and the least occurs for the symmetrical case of the ϕ = 90/270° azimuth. Second, the variation for the asymmetrical cases is greatest for the direction away from the sun. Third, the variation is greater for a given azimuth the more turbid the atmosphere.

The shapes of the families of corresponding curves for λ = 0.65 μm and/or for $\rho > 0$ are similar to those in Fig. 10; however, the variations are not as pronounced. For example, the uppermost curve in Fig. 10 has maximum values for $L_{\theta N}/L_{0°}$ of 2.1 in the direction into the sun and 3.2 in the direction away from the sun. The corresponding ratios for λ = 0.65 μm and ρ = 0 are 1.8 and 2.7, and those for λ = 0.9 μm and ρ = 0.1 are 1.2 and 1.5, respectively. These general conclusions are apparent in the following specific examples.

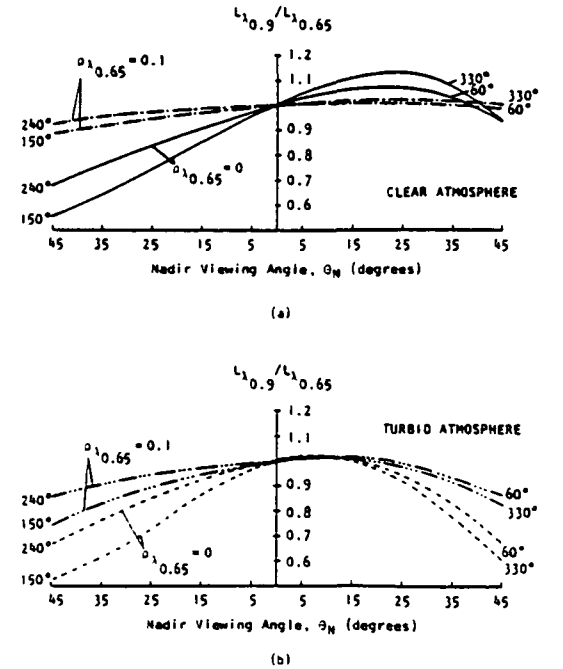

Fig. 12. Normalized values of $L_{\lambda 0.9}/L_{\lambda 0.65}$ vs nadir viewing angle for $\rho_{\lambda 0.65}$ = 0.0 and 0.1, $\rho_{\lambda 0.9}$ = 0.5, ϕ = 150/330, and 60/240° for (a) clear and (b) turbid atmospheres.

Table III. Percentage Differences Between $L_{\lambda_{0.9}}/L_{\lambda_{0.65}}$ at Nadir and at 25°

Atmospheric condition	$\rho_{\lambda_{0.9}} = 0.5, \rho_{\lambda_{0.65}} = 0$ Azimuth angles (deg)				$\rho_{\lambda_{0.9}} = 0.5, \rho_{\lambda_{0.65}} = 0.1$ Azimuth angles (deg)			
	330/150		60/240		330/150		60/240	
Clear	+13	−25	+7	−16	+2	−5	+1	−3
Turbid	−8	−26	−6	−15	−3	−10	−2	−5

Table IV. Percentage Differences Between $L_{\lambda_{0.9}}/L_{\lambda_{0.65}}$ at Nadir and at 45°

Atmospheric condition	$\rho_{\lambda_{0.9}} = 0.5, \rho_{\lambda_{0.65}} = 0$ Azimuth angles (deg)				$\rho_{\lambda_{0.9}} = 0.5, \rho_{\lambda_{0.65}} = 0.1$ Azimuth angles (deg)			
	0/180		90/270		0/180		90/270	
Clear	−7	−51	−17	−17	0	−15	−3	−3
Turbid	−42	−59	−28	−28	−19	−33	−11	−11

Figure 11 is a plot of the ratio of the digital counts in band 7 to band 5 as a function of the reflectance in band 5 for Avondale loam. The results are for no atmosphere and for a clear and turbid atmosphere. Only one azimuth (Fig. 2) is considered; the angles to nadir are 25 and 45°. The 25° case corresponds to an operating mode of Centre National d'Etudes Spatiales' SPOT or NASA's future multispectral linear array (MLA) system, in which imagery can be acquired by pointing the scanner to either side of nadir, orthogonally to the flight path. (In some cases a 35° angle is being considered to increase the frequency of coverage.) The 45° case corresponds to a high-altitude aircraft system, such as the Daedalus scanner, whose extreme scan angle is nearly 45°.

The curves in Fig. 11 show how the atmosphere increasingly modifies the ratio of MSS7 to MSS5 digital counts at the sensor as (1) the ground reflectance decreases, (2) the angle to nadir increases, and (3) the atmosphere becomes more turbid. For wet loam with a band 5 reflectance of 0.1, the band 7 to band 5 ratio, unmodified by the atmosphere, is 0.47. The ratio drops to 0.425 at 25° E and 0.39 at 25° W for a clear atmosphere and to 0.365 and 0.34 for a turbid atmosphere. For 45° E and 45° W, the ratios become 0.415 and 0.37 for the clear and 0.33 and 0.315 for the turbid atmosphere. It is interesting to note that, as the values of the ratio become further removed from the unmodified value, the differences between the values across the scan line become smaller. With reference to Fig. 10, we see that for a clear atmosphere and with respect to a zero nadir angle a change in scan angle of 25° to the east produces a 3.4% change in radiance at the sensor, and one of 25° to the west produces a 5.1% change. These changes are significant when compared with the ~0.5% noise equivalent radiance differences of future sensor systems.

Figure 12 relates for clear and turbid atmospheric conditions, respectively, the normalized ratios of radiances at $\lambda = 0.9$ μm to those at $\lambda = 0.65$ μm as a function of nadir angle for two azimuths $\phi = 150/330°$ and $\phi = 60/240°$ with respect to the sun. (Normalized radiance values were chosen to facilitate the extension of the calculations to the bandpasses at or near 0.65 and 0.9 μm to be used by some future systems.) The $\phi = 60/240°$ azimuth is representative of the plane of the fore and aft viewing directions for in-track stereo scanners such as the proposed Mapsat system. The $\phi = 150/330°$ azimuth is representative of sensors that achieve stereo and/or increased temporal coverage by pointing off-nadir in the across-track direction. Examples are SPOT and MLA.

In Fig. 12 the flatter lines are for ground reflectances of 0.1 in band 5 and 0.5 in band 7; the more curved lines are for ground reflectances of zero in band 5 and again 0.5 in band 7. The region between curves of the same azimuthal angle encompasses many representative vegetation ratios for radiances at 0.9 and 0.65 μm. The values plotted in Fig. 12 are summarized in Table III. From these results it is clear that, from a radiometric standpoint, it is preferable to obtain oblique imagery from a Landsat-type orbit by pointing in the forward in-track direction. Results from Table IV show how desirable it is to collect wide-angle high-altitude aircraft imagery when the flight path is in the sun's direction rather than when the path is perpendicular to that direction.

VII. Conclusions

The results presented here indicate the range over which the atmosphere can be expected to modify band ratio results (MSS7 to MSS5 or L_7 to L_5); the atmospheres considered had meteorological ranges of 100 and 10 km. In all cases considered, the modification was significant primarily because, for the examples chosen, the reflectance at 0.65 μm was lower than at 0.9 μm, and the effect of the atmosphere was, therefore, more pronounced at 0.65 μm.

In the case of Avondale loam imaged by the MSS, the influence of soil moisture is critical. For dry loam, the difference between the band 7 to band 5 ratios as determined from space and as determined from ground-level measurements is 2.3% for clear and 5.6% for turbid

atmospheric conditions. In contrast, for wet loam the differences are 10.4 and 29.5%. Because of the low quantization resolution of the MSS and its small (<5.6°) angle to nadir, the difference between the ratios in the east and west scan directions is hardly detectable even for very low band 5 reflectances, which is indicative of damp loam. This is not the case for a near-nadir high-quantization resolution sensor such as the Thermatic Mapper, and the effects become much more pronounced for oblique viewing systems. For example, the band 7 to band 5 ratio, for Avondale loam of reflectance 0.1, determined from space measurements at a 25° nadir angle, is less than the vertical ground-based measurement by 10% in the east direction and 17% in the west direction for a clear atmosphere and by 23% in the east direction and 28% in the west direction for a turbid atmosphere. Compared to the values of the ratios determined from space measurements at a nadir viewing angle, the increases are −4.4, +3.9, 0, and +6.1%, respectively. The effect of the atmosphere on band ratios for vegetation indicates that atmospheric conditions may delay the discrimination of stressed from unstressed vegetation by 3–7 days.

In general the results indicate that the atmosphere modifies band ratios significantly for low-ground reflectance values. The degree of the modification increases for oblique angle observations, and the path radiance and the change in path radiance are greater in the 0/180° azimuth than in the 90/270° azimuth. The results also indicate that if in-track stereo data are to be used for radiometric purposes, they should be collected in the fore and nadir directions rather than the aft and nadir directions. The more similar radiometric responses between the fore and nadir directions may facilitate the roughly 1-D digital correlation of the two images for stereo purposes.

Results emphasize the need for development of techniques for measurement of atmospheric parameters from space to facilitate the correction of spectral signatures for atmospheric effects. This is particularly true if in the future comparisons are to be made among near-nadir, oblique, and ground-based measurements.

References

1. G. Guyot and M. Verbrugghe, Eds., *Proceedings, International Colloquium, Spectral Signatures of Objects in Remote Sensing, Avignon, France* (Institut National de la Recherche Agronomique, Versailles, France, 1981).
2. J. E. Chance, Int. J. Remote Sensing **2**, 1 (1981).
3. J. V. Dave, Remote Sensing Environ. **10**, 87 (1980).
4. J. V. Dave, IBM J. Res. Dev. **23**, 214 (1979).
5. J. Otterman and R. S. Fraser, Remote Sensing Environ. **5**, 247 (1976).
6. J. F. Potter, Proc. Soc. Photo-Opt. Instrum. Eng. **51**, 78 (1975).
7. A. J. Richardson, D. E. Escobar, H. W. Gausman, and J. H. Everitt, *Machine Processing of Remotely Sensed Data* (Purdue U., Lafayette, Ind., 1980), pp. 88–97.
8. G. Rochon, H. Audirac, F. J. Ahern, and J. Beaubien, in *Proceedings, Twelfth International Symposium on Remote Sensing of Environment* (Environmental Research Institute of Michigan, Ann Arbor, 1978), pp. 1267–1277.
9. R. E. Turner, W. A. Malila, R. F. Nalepka, and F. J. Thomson, Proc. Soc. Photo-Opt. Instrum. Eng. **51**, 101 (1975).
10. D. E. Pitts, W. A. McAllum, and A. E. Dillinger, in *Proceedings, Ninth International Symposium on Remote Sensing of Environment* (Environmental Research Institute of Michigan, Ann Arbor, 1974), Vol. 1, pp. 483–497.
11. C. C. Schnetzler, "On the Use of Off-Nadir Pointing for Increased Temporal Resolution of Earth Observing Satellite Systems," NASA Tech. Memo 82139 (Goddard Space Flight Center, Greenbelt, Md., 1981).
12. J. A. Kirchner, C. C. Schnetzler, and J. A. Smith, Int. J. Remote Sensing **2**, 253 (1981).
13. J. A. Smith, K. J. Ranson, and J. A. Kirchner, Final Contract Report to NASA Goddard Space Flight Center (Operations Research, Inc., 1980).
14. R. J. Kauth and G. S. Thomas, *Proceedings, Symposium on Machine Processing of Remotely Sensed Data* (Purdue U., Lafayette, Ind., 1976), pp. 41–51.
15. R. D. Jackson, P. J. Pinter, Jr., R. J. Reginato, and S. B. Idso, *Hand Held Radiometry* (Agricultural Research Science and Education Administration, USDA, Oakland, Calif., 1980), 66 pp.
16. R. D. Jackson and P. J. Pinter, Jr., *Proceedings, International Colloquium on Spectral Signatures of Objects in Remote Sensing, Avignon, France* (Institut National de la Recherche Agronomique, Versailles, France, 1981).
17. Anon., *Landsat Data Users Handbook* (U.S. Geological Survey, Arlington, Va., 1979), Rev. Ed.
18. A. P. Colvocoresses, Proc. Soc. Photo-Opt. Instrum. Eng. **278**, 60 (1981).
19. Anon., *Conceptual Design of an Automated Mapping Satellite System (MAPSAT)*, Itek, Final Tech. Rept. (Itek Corp., Lexington, Mass., 1981).
20. P. N. Slater, *Remote Sensing: Optics and Optical Systems* (Addison-Wesley, Reading, Mass., 1980).
21. B. M. Herman and S. R. Browning, J. Atmos. Sci. **32**, 1430 (1975).
22. E. E. Flowers, R. A. McCormick, and R. R. Kurfis, J. Appl. Meteorol. **8**, 955 (1969).
23. W. A. Pearce, *A Study of the Effects of the Atmosphere on Thematic Mapper Observations*, Report 004-77 (EG&G/Washington Anal. Serv. Center, Appl. Sys. Dep., Riverdale, Md., 1977), 136 pp.
24. M. P. Thekaekara, R. Kruger, and C. H. Duncan, Appl. Opt. **8**, 1713 (1969).
25. Anon., NASA Landsat Newsletter 15 (NASA Goddard Space Flight Center, Greenbelt, Md., 1977).

P. N. Slater wishes to acknowledge the benefit of discussions with B. M. Herman and S. J. Martinek of the University of Arizona and the use of the radiative transfer model developed by B. M. Herman. The work was supported in part by NASA (grant NAG 5-196), the USDA (broadform contract 12-14-5001-38), and the USGS (P.O. 50987).

Presented at 1982 SPIE Meeting, San Diego, California (Conference 356), Field Measurement and Calibration Using Electro-Optical Equipment: Issues and Requirements

In-flight radiometric calibration of advanced remote sensing systems

C. J. Kastner and P. N. Slater

Optical Sciences Center, University of Arizona, Tucson, AZ 85721

Abstract

Several methods for the in-flight calibration of advanced remote sensing systems are reviewed. Pre-flight and in-flight detector-based calibration are discussed. Calibration by reference to instrumented ground targets is suggested for current systems. Preliminary data are presented on the accuracy and sensitivity required of measurements of ground targets and the atmosphere between the targets and the sensor to achieve an uncertainty in absolute terms of less than ±3% in the calibration of Landsat-4 systems.

Introduction

Many remote sensing applications and studies, particularly those that depend on the modeling of the interaction of radiant flux with the earth's surface and/or atmosphere,[1,2,3] require an accurate conversion of the sensor's output (in digital counts) to the radiance level at the entrance pupil of the sensor. The accuracy of this conversion depends on the suitability and accuracy of the absolute spectroradiometric calibration of the system. Unfortunately, none of the in-flight absolute calibration procedures used for remote sensing systems have been entirely appropriate. They have involved directing a small beam of solar radiation through the optics, while leaving the rest of the entrance pupil dark. When imaging the earth, the entrance pupil is irradiated with a uniform radiance level over its entire area from a field of roughly 3 steradians. This inevitably introduces a level of stray radiation across the image surface that is not accounted for in the calibration procedures used thus far. (The stray radiation is due to scattering off optical surfaces, supporting structures, etc., and can increase dramatically with small amounts of contamination that may accumulate on them in the space environment.)

Although through-the-optics radiometric calibration techniques have been available on the early Landsat Multispectral Scanner Systems (MSSs), they have not been successful and have not been used to any great extent. For the MSS on Landsat-4 the calibration wedge approach[4] will be used to determine "absolute" and relative band-to-band response. Scene content histogramming will be used to monitor detector-to-detector gain and bias to achieve the ±1 quantum level specification. These techniques have worked well for earlier MSSs, but we should remember that histogramming is a relative correction technique, suitable only for removing scene-independent striping,[5,6,7] and the calibration wedge provides only a focal plane calibration. It provides no information on the transmittance of the image-forming system (including scanning mirror). Because the condensation of outgassed contaminants and the presence of high-energy irradiation in the space environment can rapidly change the reflectances of mirrors and the transmittances of refracting elements, a through-the-optics procedure must be used for the absolute calibration of the space remote sensing system to be meaningful. There is no provision for a through-the-optics calibration of the Thematic Mapper (TM) on Landsat-4. A focal plane calibration only will be used, in conjunction with a pre-flight absolute calibration.

The Système Probatoire d'Observation de la Terre, Haute Resolution Visible (SPOT HRV) utilizes a fiber optics arrangement that transfers solar flux from an external surface to a relay system. The main imaging system together with the relay system then focuses an image of the internal ends of the fibers onto the CCD detectors.[8] The absolute radiometric calibration of SPOT HRV is quoted[9] as 10%. Specifications for advanced multispectral linear array systems call for uncertainties in absolute calibration of ±5%,[10] while one detailed design study[11] has estimated that the uncertainty can be as low as ±1.4%.

In this paper we present a brief review of relative and absolute calibration methods for advanced remote sensing systems, pointing out anticipated problems and limitations. We briefly describe the technique for the self-calibration of a photodiode in absolute terms using several laser wavelengths and how this has been extended to calibration in terms of a tungsten source filtered with narrow, well-characterized interference filters. We suggest this detector-based method for the pre-flight and in-flight calibration of future systems. For current systems, where there is no on-board provision for absolute calibration, we discuss absolute calibration with reference to large uniform ground areas instrumented to provide ground spectral reflectance and atmospheric data.

Broad classification of calibration procedures

Some of the most commonly used procedures for the calibration of remote sensing systems are referred to in Figure 1. The two major divisions in the figure are between relative and absolute calibration and between the static macro-image response and the dynamic micro-image response of the system. Relative calibration and dynamic micro-image response will not be discussed further, beyond remarking that the dynamic micro-image response is of vital interest in any pixel-by-pixel analysis of remotely collected imagery and will be studied by several investigators as part of the Landsat-4 image data quality analysis program. The rest of this paper deals with the absolute calibration of remote sensing systems, and only the static macro-image response will be considered in this context, as is usually the case.

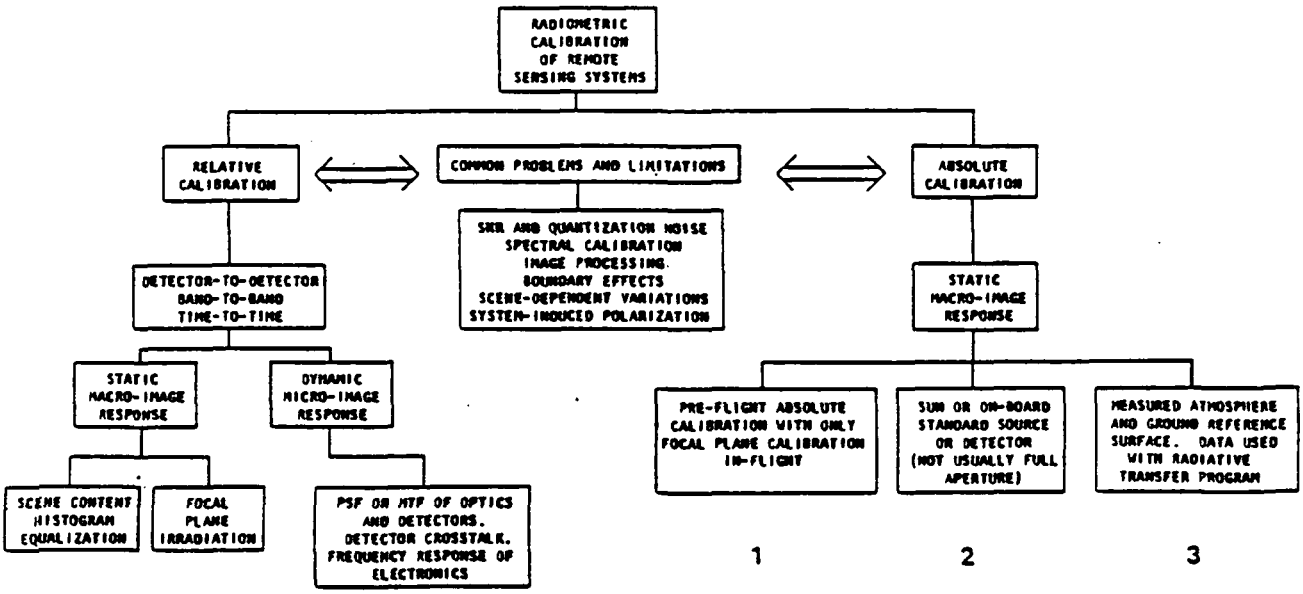

Figure 1. Classification of radiometric calibration procedures.

The procedures for the absolute calibration of a remote sensing system fall into the three categories shown in the bottom right of Figure 1:

(1) The absolute calibration of the system is made only before launch. In flight, the calibration is checked by irradiating the focal plane with a radiometrically calibrated source and optical system. The drawbacks to this procedure are that any change in the transmission of the image-forming optics of the sensor system, due to the condensation of outgassed contaminants, will be undetected and the on-board calibration system is also assumed to be stable through launch and unaffected by the vacuum, high energy particle irradiation, and zero-g environment at orbital altitudes. The Thematic Mapper and the Multispectral Scanner System on Landsat-4 are examples of remote sensing systems calibrated in this manner.

(2) The sun or an on-board calibrated source can be used to irradiate the focal plane through the image-forming optics. The drawbacks to this approach are the uncertainty in the knowledge of (a) the irradiance of the sun above the atmosphere and (b) the output of the calibrated source system, for the reasons mentioned earlier. Furthermore, in examples of the use of this procedure (MSSs 1, 2 and 3 and SPOT), the calibration beam passes through only a small portion of the aperture of the system, thus not simulating the actual operation of the system. When imaging the ground, the system entrance aperture is irradiated over its entire area by flux incident over a roughly three steradian solid angle. In the imaging mode there is much more stray light present in the system and incident on the focal plane. If this additional flux level is unknown, it introduces a substantial uncertainty into the absolute calibration of the system.

(3) Reference can be made in-flight to a ground area of known spectral radiance. If measurements are made of the atmospheric conditions at the time the sensor system is imaging the known area, these data can be used with an atmospheric radiative transfer program to predict the spectral radiance at the entrance pupil of the sensor. The main uncertainty in this approach is that of determining the atmospheric aerosol content well enough. The approach is also limited to scenes having large uniform areas of high radiance. For example, although many water bodies are of sufficient size and uniformity, they are not appropriate for calibration purposes because their radiance is too low to provide a calibration of sufficient accuracy or to cover much of the dynamic range of the sensor. Fortunately, some suitable areas do exist, particularly in the arid regions of the world, for example at White Sands, New Mexico.

The rest of this paper is devoted to a discussion of the factory and in-flight calibration of an MLA system using the self-calibrated photodiode approach and the use of a ground reference area for calibration purposes.

Detector-based radiometric calibration

The recent work at the US National Bureau of Standards on self-calibrated photodiodes is described only briefly here. For more details the interested reader is referred to references 12-16.

The calibration of the photodiode is accomplished by either of two differently applied biasing procedures, depending on the wavelength region of interest. At short wavelengths, a negative bias is applied to remove

the recombination centers at the $Si-SiO_2$ interface at the front of the detector. To do this, a contact is made with the front surface using an electrode immersed in a conducting liquid, or the surface can be exposed to a corona discharge. For long wavelengths, a back-bias is applied to extend the depletion region to a depth beyond which incident flux penetrates. The experimental procedure is to irradiate the detector with a constant monochromatic flux level and to increase the bias voltage until further increase no longer gives rise to an increase in output signal. For both the short and the long wavelength ranges, the internal quantum efficiency saturates at a value extremely close to unity, as shown in Figure 2. Thus the maximum increase in signal output obtained as a result of biasing can be used to determine the internal quantum efficiency of the detector without biasing, as it will be used in practice.

The only significant loss in the external quantum efficiency of the photodiode is caused by reflection. This can be reduced to insignificance by making use of three photodiodes according to the geometry sketched in Figure 3.

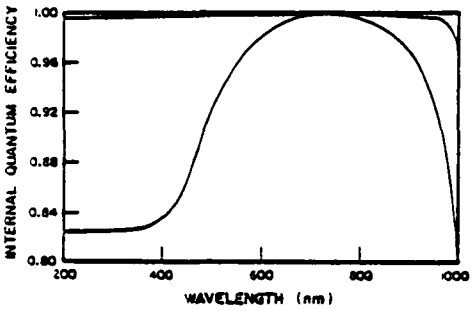

Figure 2. Typical photodiode internal quantum efficiency without biasing (lower curve) and with biasing (upper curve), reference 14.

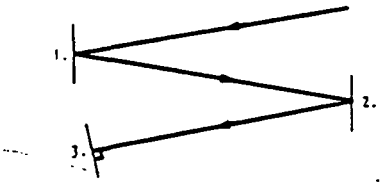

Figure 3. A three-diode arrangement to minimize specular reflection losses.

The output signals from the three diodes are summed to provide the signal corresponding to a black detector of overall quantum efficiency that can be assumed to be unity. The second diode reflects the specular reflection from diode 1 to diode 3, which acts as a retroreflector. The incident flux thereby undergoes five reflections, and at a 10% value the final specular reflectance is down to 10^{-5} of the initial incident radiance. It is claimed[17] that the diffuse reflectance losses for clean detectors are typically much less than 1%. The photodiodes used in similar calibration facilities at NBS and at the University of Arizona, Optical Sciences Center, are EGG UV 444B.

The discussion at the end of this paper refers to the use of self-calibrating NBS detectors for the spectroradiometric calibration of an MLA system. However, as shown in Figure 2, the unbiased quantum efficiency is wavelength dependent. Because of possible changes in the passband position of spectral filters during long duration space flights, it may be advisable to use the NBS detectors to calibrate a spectrally flat pyroelectric detector, at the 0.1-0.2% level, and for that to be used in the in-orbit calibration.

A recent paper[18] shows that photodiode self-calibration using filtered tungsten radiation, in place of laser radiation, can provide an absolute spectral response scale from 0.4 to 0.8 μm with an uncertainty of less than ±1%. The filters used in this work were roughly of 10 nm half-width, which is about a factor of 10 less than those of the MSS and TM. The possibility of extending this filter approach or a monochromator approach[19] to provide a means to calibrate field and flight spectroradiometric instrumentation with an uncertainty in absolute accuracy of the order of ±1% appears then to be close to reality.

Calibration in the factory and in orbit

The concept proposed for the factory calibration is similar to the proposed orbital procedure, the main difference being that an artificial source is used in the factory and the sun is used in orbit—simply a matter of convenience in the former case and of convenience and reliability in the latter case. In the factory, redundancy is not at a premium and our requirements for a source are simply power, spectral flatness, and stability. We do not need a standard source although an array of standard NBS FEL tungsten halogen lamps could be used, if their polarization characteristics can be tolerated[20]. A xenon arc selected for minimum arc wander and with a highly stable power supply and a feedback loop would suffice.

The source would be used to irradiate a near-Lambertian, near-unity-reflectance, white-surfaced panel perhaps 1 m x 0.5 m in size in front of the system. (An integrating sphere could be used, but it would have to be very large, and uniformity checks can sometimes themselves introduce non-uniformities.) A self-calibrating NBS-style radiometer, with the incident beam perhaps defined by two or three apertures, and using spectral bandpass filters matching those used in the MLA, would be used to determine the radiance of the panel in each band. The MLA would image the panel out of focus, but being an extended object, its image would have exactly the same irradiance in or out of focus. The arrangement is sketched in Figure 4.

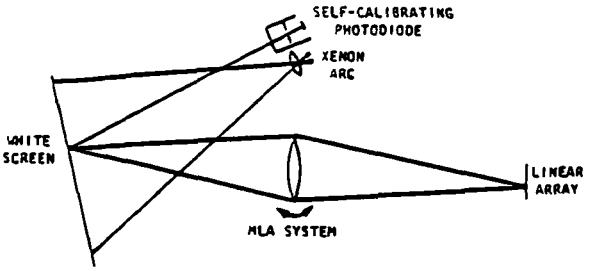

Fig. 4. The factory procedure for absolute spectroradiometric calibration.

To avoid problems due to the nonuniform irradiation of the panel, the MLA should be rotated to sequentially irradiate the focal plane with the image of the same small area that is sampled by the radiometer. The reason for a large panel is to simulate the viewing conditions from space in which, depending on the baffle design, significant out-of-the-field-of-view stray light could be incident on the image plane to modify the calibration. For this reason it would be worthwhile to conduct at least one calibration using a white panel several metres in diameter. To check for linearity of response, several different irradiance levels on the panel should be used. This irradiance level can be changed conveniently by inserting heat-resistant neutral density filters in front of the stabilized xenon arc source.

The profiles of the spectral filters should be measured in a spectrophotometer using the same F-No. beam as that for the MLA. If they are integral with the array, they should be measured using a double monochromator, again with the MLA F-No., before installation in the focal plane. Care should be taken to cover the whole wavelength sensitivity range of the detectors, the off-band suppression being particularly important for detectors with the wide spectral response of silicon.

The procedure proposed here for in-flight calibration is similar to the panel method sketched in Figure 4, but it uses the sun as the source. We believe that the irradiance over the panel can then be considered to be uniform and known spectrally to better than 1% absolute. (Several solar measurement programs are currently being conducted with this accuracy as a goal. However, if the uncertainty is thought to be greater than 1%, a pyroelectric detector could be used to measure the direct solar flux in orbit, over the wavelength intervals of interest and at the same time that the system is being calibrated.) The calibration would be carried out in the few minutes while the spacecraft is sun-illuminated but before it images the sun-illuminated earth. The absolute radiometer containing the pyroelectric detector would now be needed only to check for any deterioration in the reflectance of the panel owing to exposure to the space environment and short exposures to unattenuated UV and other high energy radiation from the sun and from space. In this last respect, the panel would usually be stowed in a well-shielded compartment and exposed only during actual calibration checks. Also, when deployed, it would not interfere with normal operation of the system, as it would be viewed by the stereo mirror in one of its extreme positions. In this respect it is fail-safe.

White Sands as a calibration target

White Sands, New Mexico, has been proposed as a calibration site for the Landsat-4 sensors. This area provides a large uniform target, the reflectance of the gypsum sands is close to Lambertian for the solar angles of interest, and the concentration of atmospheric aerosols under calm wind conditions is low. These properties simplify radiative transfer computations. To compute the radiance at the sensor, a set of ground-based measurements is combined with a proven radiative transfer model.

The sensor radiance, L_s, is given by

$$L_s = E \cdot \exp(-\tau'_{ext} \sec\theta_s) \cdot \frac{\rho}{\pi} + L_p$$

(spectral quantities assumed). Here θ_s is the sensor down look angle (as measured from nadir), ρ the ground reflectance, and E the solar spectral irradiance. A Langley plot of ln E versus sec θ_z (where θ_z is the solar zenith angle) can be drawn from data taken throughout the morning of the Landsat-4 overflight. The slope of this plot is a measure of the total atmospheric extinction (τ'_{ext}), and the exo-atmospheric spectral solar irradiance (denoted E_o) is found by extrapolating to the value of E where $\sec\theta_z = 0$. Path radiance, L_p, is computed from data inputs such as E_o and ρ and from assumptions about the composition of the atmosphere at the time of the Landsat overflight.

Instrumentation

The instrument that is be used at White Sands is similiar to that being built at the University of Arizona for the investigation of solar irradiance variations over a 23-year period. It employs a precision alt-azimuth tracking stand, with stepper motors to drive the two axes, so that it can be pointed in almost any direction or be held in alignment with the sun. A microprocessor-based computer system will be used to control the motors as well as the data acquisition and processing system. A diagram of the optical layout of the instrument is shown as Figure 5a and Figure 5b is an artist's drawing of the instrument and its mounting. The ground-based measurements to be made include ground reflectance, solar irradiance versus time of day, temperature, and relative humidity. However, the high reflectance of White Sands restricts the time of year with which these data can be used for comparison to the actual digital counts registered by the orbital system. Preliminary calculations indicate that some of the sensor bands are saturated from February to November (where a large solar elevation angle is encountered at the time of overflight). These calculations are summarized in Figure 6a for the MSS bands, and Figure 6b for TM. The dashed lines represent saturation levels of the two sensors. This study included only ozone as a molecular absorber, but accounted for desert aerosols and Rayleigh scattering.

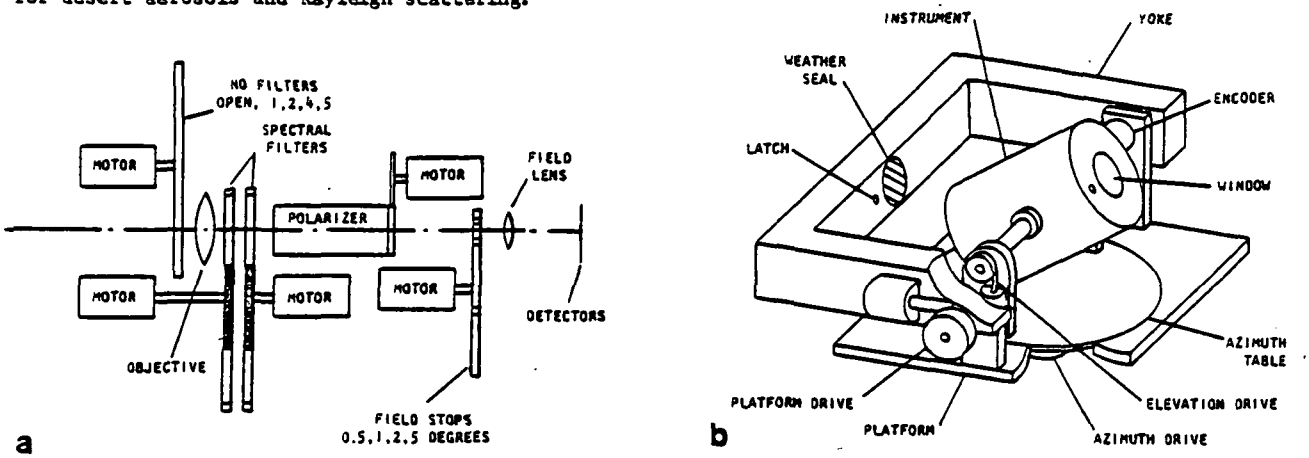

Figure 5. (a) Optical layout of field instrument. (b) Artist's concept of instrument and mounting assembly.

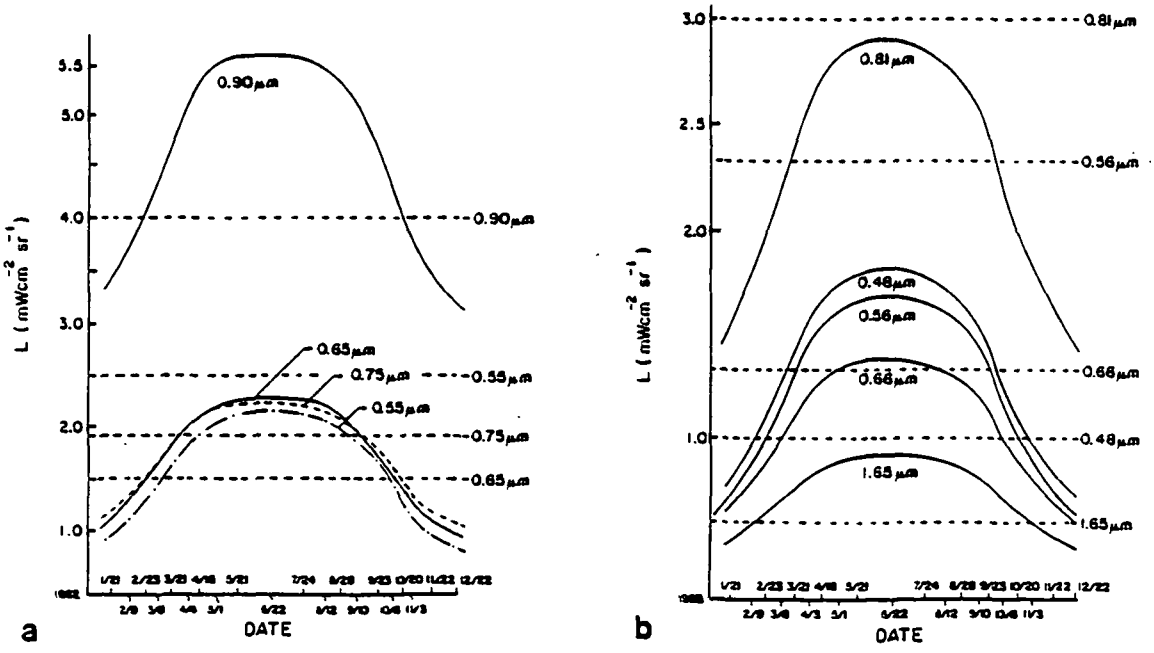

Figure 6. Radiance at sensor for (a) MSS and (b) TM bands as a function of date. Horizontal lines show calculated saturation levels for White Sands.

Sensitivity Analysis

Previous efforts to estimate radiance levels at down-looking orbital sensors have been, at best, at the ±5% uncertainty level,[21] although some comparative studies have shown that much larger uncertainties can exist. For example, the ratio of outputs of the S192 to the S191 experiments on Skylab was 0.79 ± 0.14 when the systems were simultaneously viewing the same ground scene.[22] With improved instrumentation and calibration accuracies (to ±1%), it now seems feasible to use ground-based reference targets for sensor calibration. A sensitivity analysis is required, however, to predict just what this new accuracy might be. This involves a study of the parameters affecting the radiative transfer codes, and their effect on the predicted radiance. Such work has been initiated, and preliminary results are presented here. Currently the radiative transfer codes agree among themselves to within 1% for a given set of input parameters.[23] Problems arise when specific values of these inputs have to be defined so as to represent a given atmosphere. Typically, approximations and seasonal averages are used for parameters relating to aerosols (number density, refractive index, radius distribution, and vertical distribution), ozone, and water vapor concentrations, and molecular gases. Often, however, these parameters vary considerably from their seasonal average values. This is especially true of aerosol and ozone and water vapor concentration. Fortunately, large variations in some of these parameters (10%) often lead to tolerable errors (<1%) in calculations of radiance at the sensor. Table 1 lists those variables that affect the transfer calculations. Comments are included to summarize their expected variability and our preliminary study into the effect each has on overall accuracy. It is seen that other parameters such as the ground reflectance, time of day, and solar spectral irradiance should be known to 0.1%. This is not an unreasonable requirement, given the recent advances in calibration techniques. Our simulation was made by using an average desert aerosol number density, with complex index of n=1.5-0.01i. Published data[24] were used for the ozone optical depth and absorption coefficients. Up to now water vapor variability, which affects the fourth MSS band, has not been analyzed.

Table 1. Preliminary Examination of Input Parameters to Radiative Transfer Codes

Aerosols

Total Number Density and Vertical Distribution. Both variable,[25] with aerosol optical thickness varying by as much as a factor of 2.

Particle Size Distribution. Normalized Junge and Deirmenjian distributions compared. Number of particles at a given radius found to vary by an order of magnitude. Change in output was <0.1%.

Refractive Index. Extinction may vary by an order of magnitude for the various values used to approximate desert aerosols,[26] extinction being more affected by the real part of the refractive index. Our calculations show that a change in index from n=1.5 to 1.5-0.01i varies output by <1%.

Other Parameters

Ozone. Can expect up to 10% daily variation from seasonal mean,[27] this changes output by 1%.

Water vapor. With humidity range of 30% to 90%, and temperature of 4°C to 21°C, water concentration varies from 0.15 to 3 gm cm^{-2} km^{-1}.

Ground reflectance, exo-atmospheric solar spectral irradiance. For negligible output error, need to know these parameters to within 0.1%. With recent detector calibration techniques, this is no longer unreasonable.

Field of view. A study has been done using an infinitesimal target having the reflectance of White Sands (ρ=0.7) and a background of ρ=0.35 and 0.7. The resultant output varied by 2%.

Pressure. A 10% change in pressure changes output by only 0.2%. Negligible error anticipated as pressure can be measured on a continuous basis to high accuracy.

Time of Day. Need to know within 1 second of measurement for Langley plot.[28,29]

Polarization. Studies[30,31] need to be extended to determine the influence of scene and atmosphere induced polarization on the calibration of an orbital sensor. Polarization introduced by the sensor itself needs to be known from pre-flight measurements.

Conclusions

The use of self-calibrated detectors promises the achievement of pre-flight and on-board in-flight absolute calibration of future systems to an uncertainty of less than ±1.5%.

Without appropriate pre-flight and on-board calibration, it now appears possible that present earth resources satellite systems can be radiometrically calibrated in absolute terms with an uncertainty of less than ±3% by reference to ground targets. This conclusion is based on recent advances in the establishment of self-calibrated detectors as accurate absolute radiometric standards together with the development of radiative transfer codes that account for multiple scattering and include all relevant atmospheric parameters. The degree of uncertainty in the calibration procedure depends heavily on our ability to accurately characterize the atmosphere above the target during the sensor overflight. We plan to investigate this matter both theoretically and experimentally during the image data quality analysis phase of the Landsat-4 program.

Acknowledgements

We wish to thank J. Geist, B. M. Herman, S. J. Martinek, J. M. Palmer and E. F. Zalewski for the benefit of useful discussions. This work was supported under NASA grant number NAG 5-196.

References

1. Richardson, A. J., D. E. Escobar, H. W. Gausman, and J. H. Everitt, "Comparison of Landsat-2 and Field Spectrometer Reflectance Signatures of South Texas Rangeland Plant Communities," Proc. Symp. on Machine Processing of Remotely Sensed Data. West Lafayette, Ind., pp. 88-97. 1980.

2. Rochon, G., H. Audriac, F. H. Ahern, and J. Beaubain, "Analysis of a Transformation Model of Satellite Measurements into Reflectances," Proc. 12th Int. Symp. on Remote Sensing of Environment, pp. 1276-1277. 1978.

3. Slater, P. N. and R. D. Jackson, "Atmospheric Effects on Radiation Reflected from Soil and Vegetation as Measured by Orbital Sensors Using Various Scanning Directions," Appl. Opt., 1982 (in press).

4. Horan, J. J., D. S. Schwartz, and J. D. Love, "Partial Performance Degradation of a Remote Sensor in a Space Environment, and Some Probable Causes," Appl. Opt. vol. 13, p. 1230. 1974.

5. Slater, P. N., Remote Sensing, Optics and Optical Systems, Addison-Wesley, Reading, Mass. 1980.

6. Duggin, M. J., P. N. Slater, and S. L. Somers, "A Method for Calibrating Multispectral Scanners to Allow for the Spectral Dependence of the Instrument Response," AIAA Sensor Systems for the 80's Conference, 80-1935-CP, Colorado Springs, 1980.

7. Markham, B. L., and J. L. Barker, "Spectral Characterization of the Landsat-D Multispectral Scanner Subsystems," Technical Memo. 83953, pp. 45, 1982.

8. Dinguirard, M., and J.-M. Maisonneuve, "Dispositif d'etalonnage sur le Soleil de la Camera HRV du Projet SPOT," XXVII Rassegna Internazionale Elettronica ed Aerospaziale, Roma, 7-16 Marzo 1980.

9. Maisonneuve, J.-M., and M. Dinguirard, "Problems et Dispositifs d'etalonnage en vol de la Camera HRV du Projet de Satellite SPOT," XXVII Rassegna Internazionale Elettronica ed Aerospaziale, Roma, 7-16 Marzo 1980.

10. Richard, H. L., "Solid State Instrumentation Concepts for Earth Resource Observation," Twentieth Goddard Memorial Symposium, AAS Publication Office, P.O. Box 28130, San Diego, CA 92128. 1982.

11. Keene, G. T., "An Improved Earth Resources Sensing Instrument," Proc. SPIE Meeting on Advanced Multispectral Remote Sensing and Applications, Arlington, VA. 1982.

12. Geist, J., "Quantum Efficiency of the p-n Junction in Silicon as an Absolute Radiometric Standard," Appl. Opt., vol. 18, pp. 760-762. 1979.

13. Geist, J., "Silicon Photodiode Front Region Collection Efficiency Models," J. Appl. Phys. vol. 51, pp. 3993-3995. 1980.

14. Geist, J., E. F. Zalewski, and A. R. Schaefer, "Spectral Response and Self-calibration and Interpolation of Silicon Photodiodes," Appl. Opt., vol. 19, pp. 3795-3799. 1979.

15. Geist, J., and E. F. Zalewski, "The Quantum Yield of Silicon in the Visible," Appl. Phys. Lett., vol. 35, pp. 503-506. 1979.

16. Zalewski, E. F., and J. Geist, "Silicon Photodiode Absolute Spectral Response Self-calibration," Appl. Opt., vol. 19, pp. 1214-1216. 1980.

17. Zalewski, E. F., personal communication, 1981.

18. Hughes, C. G., III, "Silicon Photodiode Absolute Spectral Response Self-calibration Using a Filtered Tungsten Source," Appl. Opt., vol. 21, pp. 2129-2132. 1982.

19. Palmer, J. M., personal communication, 1982.

20. Kostuk, R. K., "Polarization Properties of a 1000 W FEL Type Filament Lamp," Appl. Opt., vol. 20, pp. 2181-2184. 1981.

21. Kriebel, K. T., "Calibration of the METEOSAT-VIS Channel by Airborne Measurements," Appl. Opt., vol. 20, p. 11. 1981.

22. Kenney, G. P., and W. E. Hensley, "Skylab Program, Earth Resources Experiment Package, Sensor Performance Evaluation, Final Report," Vol. III(S192), NASA-CR-144564. 1975.

23. Ahmad, Z., "A Study of the Relative Accuracy of Two Iterative Radiative Transfer Programs," Report TR-SASC-002, Systems and Applied Science Corp., MD. 1976.

24. Elterman, L., "UV, Visible and IR Attenuation for Altitudes to 50 km, 1968," Environmental Research Papers No. 285, Air Force Cambridge Research Laboratories, Bedford, Mass. 1968.

25. Elterman, L., R. B. Toolin, and J. D. Essex, "Stratospheric Aerosol Measurements with Implications for Global Climate," Appl. Opt., vol. 12, p. 330. 1973.

26. Jennings, S. G., R. G. Pinnick, and H. J. Avermann, "Effects of Particulate Complex Refractive Index and Particle Size Distributions Variations on Atmospheric Extinction and Absorption for Visible through Middle IR Wavelengths," Appl. Opt., vol. 17, pp. 3922-3929. 1978.

27. Craig, R. A., The Upper Atmosphere, Academic Press, New York, 1965.

28. Palmer, J. M., "The Effects of Errors in the Geometrical Determination of Optical Air Mass on the Accuracy of Extraterrestrial Solar Irradiance as Obtained Using the Langley Method," Submitted to Solar Energy, 1982.

29. Herman, B. M., M. A. Box, J. A. Reagan, and C. M. Evans, "Alternate Approach to the Analysis of Solar Photometer Data," Appl. Opt., vol. 20, p. 2925. 1981.

30. Coulson, K. L., "Effects of Reflection Properties of Natural Surfaces in Aerial Photography," Appl. Opt., vol. 5, pp. 905-917. 1966.

31. Koepke, P., and K. T. Kriebel, "Influence of Measured Reflection Properties of Vegetated Surfaces on Atmospheric Radiance and Its Polarization," Appl. Opt., vol. 17, pp. 260-264. 1978.

The importance and attainment of accurate absolute radiometric calibration

Philip N. Slater

Optical Sciences Center, University of Arizona
Tucson, AZ 85721

Abstract

The importance of accurate absolute radiometric calibration is discussed by reference to the needs of those wishing to validate or use models describing the interaction of electromagnetic radiation with the atmosphere and earth surface features. The in-flight calibration methods used for the Landsat Thematic Mapper (TM) and the Système Probatoire d'Observation de la Terre, Haute Résolution Visible (SPOT/HRV) systems are described and their limitations discussed. The questionable stability of in-flight absolute calibration methods suggests the use of a radiative transfer program to predict the apparent radiance, at the entrance pupil of the sensor, of a ground site of measured reflectance imaged through a well characterized atmosphere. The uncertainties of such a method are discussed.

Introduction

The use of satellite-acquired image data in scene models is inextricably dependent on atmospheric correction and sensor absolute radiometric calibration. Unlike automated scene classification, which depends on a statistical analysis of the digital counts in a scene image, usually without correction for the intervening atmosphere, modeling is concerned with determining the radiance of the scene. For this purpose we need to know, first, the output digital counts from the sensor when it is imaging the feature of interest, second, the absolute radiometric calibration of the sensor in order to convert the digital counts to radiance at the entrance pupil of the sensor, and third, the radiance modification introduced by the intervening atmosphere (the atmospheric correction) in order to relate the entrance pupil radiance to the radiance of the ground feature.

The problem divides into three parts: (1) determining to what accuracy we have to know the feature radiance in order to produce satisfactory data from the various models available—not a well understood relationship in many cases, (2) providing a means to make atmospheric corrections to a certainty commensurate with (1) above, preferably using the imaging sensor or a co-located system—even simple ground-based atmospheric measurements are rarely attempted today, and (3) providing in-flight absolute radiometric calibration to a certainty commensurate with (1) and (2)—the estimated ±10% uncertainties of current systems are unlikely to meet these needs.

This paper discusses the need for accurate absolute radiometric calibration in the use of scene radiation models. It then describes calibration methods presently in use and the main limitations and sources of error associated with them. Finally, a method that utilizes simultaneous ground and atmospheric measurements is suggested for the in-flight calibration of the newer sensors.

Use of absolute calibration in scene models

The main reason for developing models is to obtain quantitative and/or diagnostic information regarding specific areas or features or to study global phenomena. Examples of the former are to diagnose the cause of a loss of crop vigor or to determine and map chlorophyll concentration in prospective fisheries. Examples of the latter are global earth-atmosphere-ocean studies such as those envisioned by COSPAR's International Satellite Land Surface Climatology Project and those proposed as part of NASA's Global Habitability program.

A good source of information on the various models developed over the past decade can be found in a recent review by Smith.[1] Most of the models predict an upward radiance, just above the feature, on the basis of certain input values. For example, in the case of a crop canopy, the input values would include the leaf spectral reflectance and canopy geometry (leaf area index, LAI, and leaf orientation), the soil spectral reflectance, and the geometry of illumination and viewing. For many purposes the inverse form of this model is more valuable: Given the radiance and illumination and viewing geometry, what is the constitution (LAI, vigor, etc.) of the canopy? Goel and Strebel[2] have described such a model; however, relatively little other work on inversion models has been reported.

The sensitivity of both direct and inversion models to measurement accuracies and assumptions needs much further exploration. In this respect it is interesting to note how various scientists working with models respond informally to the question "What sensor absolute radiometric calibration uncertainty can you tolerate in using your models?" The answers should represent the model's sensitivity. Some responses are as follows:

0.5% D. G. Goodenough (Canada Centre for Remote Sensing) to provide the correction for change in sensor response with time, necessary for multi-temporal studies.

1% J. L. Barker (Goddard Space Flight Center) in support of his layered concept. For example, the removal of atmospheric effects to obtain BRDFs followed by the use of the BRDF data to interpret subtle texture changes and natural variations.

1% J. Gower (University of British Columbia) for ocean color studies, in particular chlorophyll concentration determination.

3% N. J. J. Bunnik (NLR, the Netherlands) for vegetation and ocean model studies.

3% J. Dozier (UC Santa Barbara) for snowfield model studies.

3% J. A. Smith (Colorado State University) for general model studies and plant canopy models in particular.

5% R. D. Jackson (Agricultural Research Service, Phoenix) for evapotranspiration models.

These responses deserve more detailed study. In particular it is important to determine, for each response: (1) whether absolute radiometric calibration meant a calibration in physical units (radiance) or a stability of relative calibration (in digital counts) with time, (2) whether it was assumed that atmospheric effects had been perfectly corrected, and (3) whether these values were well corroborated and a study had been made to determine information loss as a function of calibration uncertainty.

The literature describing the use of models for the analysis of satellite-acquired digital image data is meager. The works of Aranuvachapun and LeBlond,[3] Doak et al.,[4] Gordon,[5] Kowalik et al.,[6] Otterman and Fraser,[7] and Robinove et al.[8] represent perhaps the most significant contributions. The lack of reported results can be related to (1) the difficulty of making accurate atmospheric corrections, (2) the large uncertainty in sensor absolute radiometric calibration, and (3) the fact that not many models have been developed and their experimental testing and exploitation involves considerable effort.

In-flight calibration

We describe in-flight radiometric calibration by reference to the methods used on the SPOT/HRVs and the TM. The limitations of both methods are also discussed.

Calibration of the HRVs

On the HRVs, two calibration procedures[9,10] are to be used. One provides absolute calibration for a few detectors in each of the four image plane arrays. The other provides relative calibration for all the detectors in the arrays.

Both the absolute and relative methods provide calibration of the complete optical system. The radiation sources for both calibration methods, the internal ends of optical fibers and a lamp, are located in a calibration unit positioned so as to relay radiant flux through the telescope optics to the detector arrays.

The absolute calibration, to be conducted once each month in orbit, is made by reference to the solar irradiance incident on bundles of fibers 3 m long whose external ends are perpendicular or nearly perpendicular to the sun's rays and whose internal ends are located in the calibration unit. To cover the range of solar incidence angles from winter to summer, three sets of fibers are used with gradient refractive index tips manufactured by Selfoc. One fiber in each set emerges from a different port on an external surface at a different angle to the sun. The Selfoc tips provide an output constant to 1% for a solar angle variation of $\pm 60^{\circ}$. The fibers are drawn from doped silica, and tests show they do not discolor in a simulated high-energy-particle space environment.

Because of the possibility of a relative displacement occurring between the calibration unit and the arrays, particularly during launch, and an uncertainty in the angular position of the pointing mirror, the images of the fibers are arranged to follow a staggered line along the arrays. The arrangement of the fibers in the focal plane of the calibration unit is shown in Figure 1. The calibration unit and HRV produce a magnification of about 4.3X, so the diameter of a 250-μm-core fiber, when aligned with the array, covers more than 50 detectors in their 13-μm along-line dimension. The image of the staggered fiber array covers a lateral displacement of about 3.4 mm in the HRV focal plane.

Figure 2 is a schematic of the calibration unit. It shows the internal ends of the fibers imaged, after reflection by a beamsplitter cube, onto the focal plane of the HRV as described above. A Philips Osram 20-W, 12-V helical filament tungsten halogen lamp is used to uniformly irradiate the aperture of lens C. By use of Kohler illumination, this

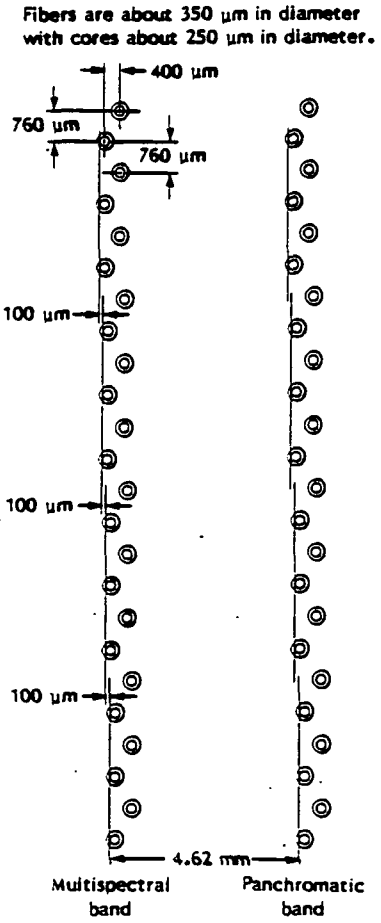

Figure 1. Staggered images of the fibers in the focal plane of the SPOT/HRVs.

aperture is imaged onto the focal plane of the HRV. Thus the entire focal plane is uniformly irradiated with white light. This arrangement can then be used to calibrate the system in a relative sense and thereby transfer the absolute calibration of the detectors calibrated by use of the fibers to all the detectors in each array.

The accuracy of the absolute calibration method is limited by (1) the uncertainty in our knowledge of the exo-atmospheric solar spectral irradiance, (2) the accuracy to which the spectral transmittance of the 3-m-long fibers and the optics in the calibration unit can be measured, (3) the constancy of the transmission of the fiber optics when exposed to the space environment, particularly including any contamination of the external fiber surfaces, and (4) the amount of stray light present in the system in its normal operating mode. We shall return to this last point later.

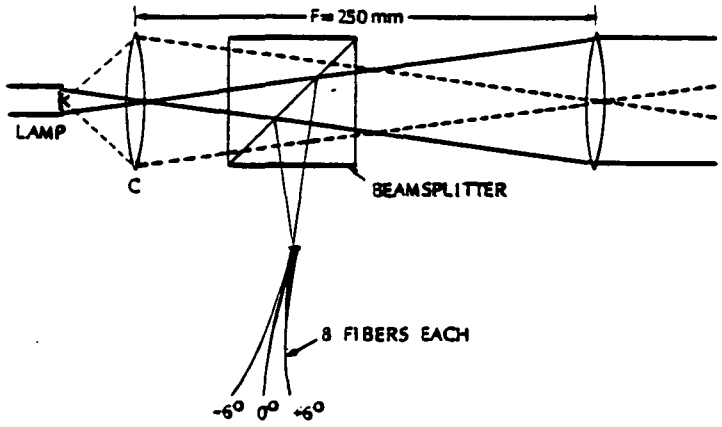

Figure 2. Schematic of the SPOT/HRV calibration unit.

Calibration of the TM

The calibration of all the detectors of the TM is carried out by an opto-mechanical system referred to, because of its action, as a "flag." The flag oscillates back and forth at the same frequency as the scanning mirror. During the 10.7 ms of scan mirror reversal time, the flag blocks the scene radiant flux from the detectors and provides various levels of irradiance for the calibration.

Figure 3 shows the internal calibrator flag. It consists basically of three light sources whose radiant output is transmitted by optical fibers to a prism end lens arrangement that projects radiant flux uniformly onto the 96 detectors in bands 1 to 5 and 7. In addition, a concave a mirror focuses the output from a temperature-controlled blackbody source onto the four detectors in band 6. To minimize inertia, the fiber optics and prism-lens arrangement are on a beryllium support that is suspended from three flex pivots and driven at resonant frequency by a brushless DC motor. The flag is essentially a torsional spring mass system that does not use bearings and gears and therefore needs no lubrication.

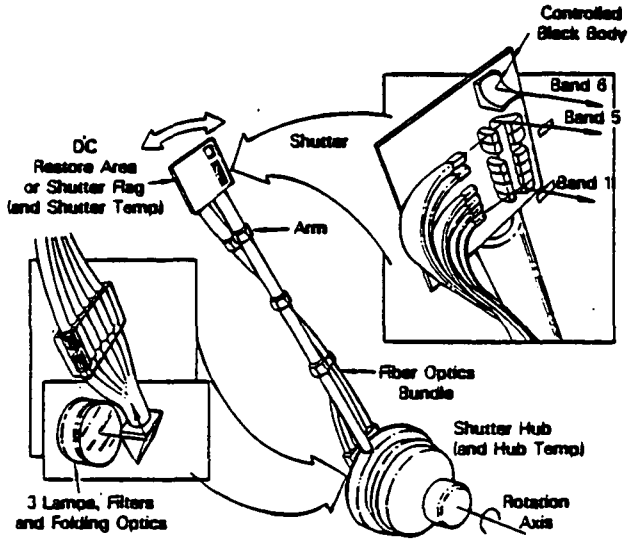

Figure 3. Internal calibrator for the TM.

The illumination system for the internal calibrator is shown in Figure 4. The three stationary, miniature tungsten filament lamps are at 120° intervals about the flag rotation axis. Prisms are used to arrange the images of the three filaments into a delta pattern, as seen in Figure 5a. Attenuating masks, which follow the prisms shown in Figure 5b, modify the outputs of the lamps so that they are in the ratio 2:3:4 on entering the circular fiber bundle. The lower end of the fiber bundle is uniformly irradiated by the radiant flux from each filament. Thus, as the lamps are turned on in different combinations, irradiance levels in the ratio 0:2:3:4:5:6:7:9 can be obtained.

The circular fiber bundle, of diameter 3.3 mm, is divided into six smaller circular bundles, each of diameter 1.35 mm, and each coupled across a short air gap to another bundle, of 1 x 1.5 mm rectangular cross section. Each bundle provides flux to a different TM band. The air gaps can be adjusted to provide small radiometric

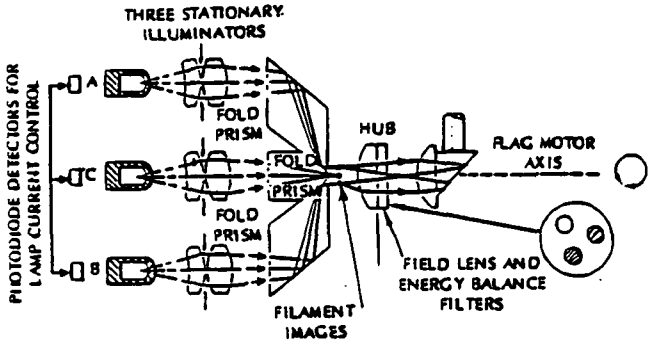

Figure 4. Illuminator optics of the TM internal calibrator.

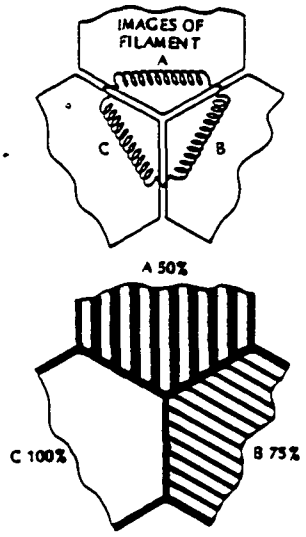

Figure 5. TM internal calibrator lamp attenuators.

corrections in any of the bundles. The top end of each fiber bundle is attached to a solid light pipe, which provides a uniform radiance area to be projected, by the lenses that follow, onto the detector plane. Between the first lens and prism in each band there is an aperture stop whose adjustment provides one way for matching the calibrator output to the selected saturation level for the system. The upper end of the flag also contains a black surface of known temperature that is viewed by all the detectors during the DC restoration step.

Behind each source is a spectral filter and a silicon PIN detector to monitor the source output and thereby control the current input to maintain constant source radiance. This scheme counteracts the reduction in radiance that results from the build-up of tungsten deposited on the inside of the lamp envelope during the life of the lamp. The spectral filter transmittance was chosen to be in the range 0.65 to 0.68 μm, for which Si detectors have essentially zero temperature coefficient of responsivity (±0.01%/°C).

Limitations of the methods

The SPOT/HRV calibration method provides a means for both absolute and relative calibration through the optical system. The condensation of outgassed materials on the external ends of the fibers and the effect of direct high energy solar radiation on these materials could change the response of the absolute calibration system. The relative calibration system does not include a feedback system to ensure stabilized source output. Because the tungsten filament becomes fragile after use, the calibration source will be turned on only briefly for essential calibration purposes before the HRV is in orbit. To minimize the risk of lamp failure, a suggestion was made to assume stability of response of the CCDs from laboratory calibration through launch and orbit insertion and to calibrate the source, at the earliest opportunity in orbit, against the known CCD response.

Perhaps the most serious drawback of the absolute calibration method is that it does not simulate the conditions of image data collection. Only a 100-mm-diameter area of the 330-mm-diameter entrance pupil receives flux from the calibration unit,[9] and the solid angle subtended by the source lens in the calibration unit at the entrance pupil of the HRV is small. In contrast, when the HRV is viewing the earth, the entire entrance pupil is irradiated and the solid angle subtended by the surface of the earth at the HRV is about π steradians. Although the actual field of view of the HRV is much smaller than this (1.3×10^{-3} sr), π sr is a measure of the total angular range of the irradiance on a horizontal plane in front of the HRV. Radiant flux over most of this π sr solid angle is not going to be imaged directly by the HRV, but some of it is going to be reflected and scattered off the front optical elements, their supports, and the barrel of the camera and onto the detectors. Such stray light is typically a few percent in a clean, well designed optical system. However, the percentage can rise dramatically if surfaces become dusty or if a coating of scattering material is deposited on them. Under imaging conditions like this the transmission of the system may actually appear to increase although in reality the signal of interest has decreased a little and this has been more than compensated for by an increase in the DC stray light background level. Thus, the absolute calibration system on the HRVs is probably not sufficiently sensitive to the stray light problem.

The main limitation of the TM calibration method is that it checks the calibration of only the filters, detectors, and electronics although it also includes the relay optics for bands 5, 6, and 7. Thus it does not provide a measure of the change in the transmittance of the image-forming optics and the change in reflectance of the scan mirror and the scan line correction mirrors.

The calibration layout illustrated in Figure 6 shows that the port in the integrating sphere is about the same size as the entrance port to the TM. During calibration they are placed about 5 m apart. This arrangement does not simulate the orbital imaging conditions of the TM, and it can introduce a systematic error into the TM calibration. This type of error was discussed in reference to the SPOT/HRV.

The internal calibration system contains long glass paths and more than 20 glass-vacuum interfaces. To the extent that these are not affected by the condensation of outgassed materials and high energy flux in the space environment, the internal calibrator should prove a stable reference because of its use of stabilized sources. It should then be useful as an accurate reference for relative calibration purposes.

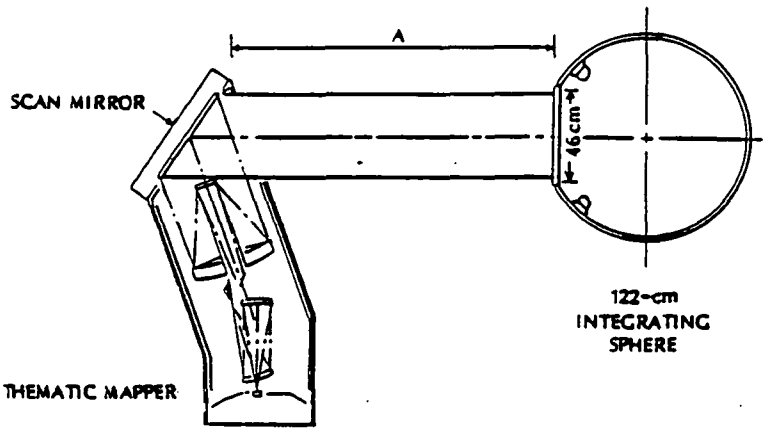

Figure 6. The radiometric test arrangement for the TM.

Because of these potential shortcomings and because in-flight sun calibration systems seem potentially less stable than the systems they are intended to calibrate, both CNES and NASA are exploring the use of a ground reference area for in-flight absolute calibration.[11]

White Sands as a calibration target

White Sands, New Mexico, is being used as a calibration site for the Landsat-4/5 sensors because this area provides a large uniform target, the reflectance of the gypsum sands is close to Lambertian for the solar angles of interest, and the concentration of atmospheric aerosols under calm wind conditions is low. These properties simplify radiative transfer computations. To compute the radiance at the sensor, a set of ground-based measurements is combined with a proven radiative transfer model.

The sensor radiance, L_s, is given by

$$L_s = E \exp(-\tau'_{ext} \sec\theta_s) \frac{\rho}{\pi} + L_p$$

(spectral quantities assumed). Here E is the solar spectral irradiance, τ'_{ext} is the total atmospheric extinction, θ_s is the sensor downlook angle (as measured from nadir), ρ is the ground reflectance, and L_p is the path radiance. A Langley plot of ln E versus $\sec\theta_z$ (where θ_z is the solar zenith angle) can be drawn from data taken throughout the morning of the Landsat-4/5 overflight. The slope of this plot is a measure of τ'_{ext}, and the exo-atmospheric spectral solar irradiance (denoted E_o) is found by extrapolating to the value of E, where $\sec\theta_z = 0$. L_p is computed from data inputs such as E_o and ρ and from assumptions about the composition of the atmosphere at the time of the Landsat overflight.

The instrument that is used at White Sands employs a precision alt-azimuth tracking stand, with stepper motors to drive the two axes, so that it can be pointed in almost any direction or be held in alignment with the sun. A microprocessor-based computer system is used to control the motors as well as the data acquisition and processing system. Figure 7 is a diagram of the optical layout of the instrument. Figure 8 is an artist's drawing of the instrument and its mounting. The ground-based measurements to be made include ground reflectance, solar irradiance versus time of day, temperature, and relative humidity.

Previous efforts to estimate radiance levels at down-looking orbital sensors have been, at best, at the ±5% uncertainty level,[12] although some comparative studies have shown that much larger uncertainties can exist. For example, the ratio of outputs of the S192 to the S191 experiments on Skylab was 0.79 ± 0.14 when the systems were simultaneously viewing the same ground scene.[13] With improved instrumentation and calibration accuracies (to ±1%), it now seems feasible to use ground-based reference targets for sensor calibration. A sensitivity analysis is required, however, to predict just what this new accuracy might be. This involves a study of the parameters affecting the radiative transfer codes, and their effect on the predicted radiance. Such work has been initiated, and preliminary results are presented here. Currently the radiative transfer codes agree among themselves to within 1% for a given set of input parameters.[14] Problems arise when specific values of these inputs have to be defined so as to represent a given atmosphere. Typically, approximations and seasonal averages are used for parameters relating to aerosols (number density, refractive index, radius distribution, and vertical distribution), ozone and water vapor concentrations, and molecular gases. Often, however, these parameters vary considerably from their seasonal average values. This is especially true of aerosol and ozone and water vapor concentration. Fortunately, large variations in some of these parameters (10%) often lead to tolerable errors (<1%) in calculations of radiance at the sensor. Table 1 lists those variables that affect the transfer calculations. Comments are included to summarize their expected variability and our preliminary

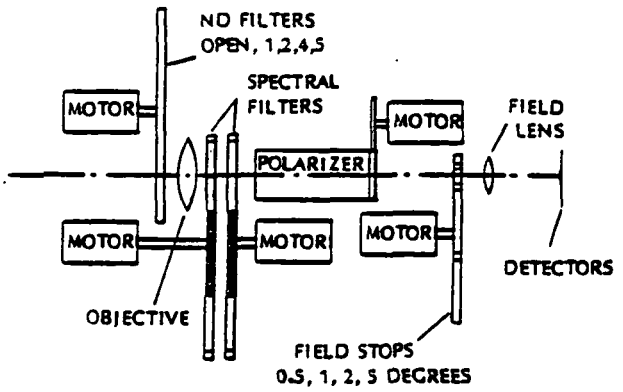

Figure 7. Optical layout of field instrument.

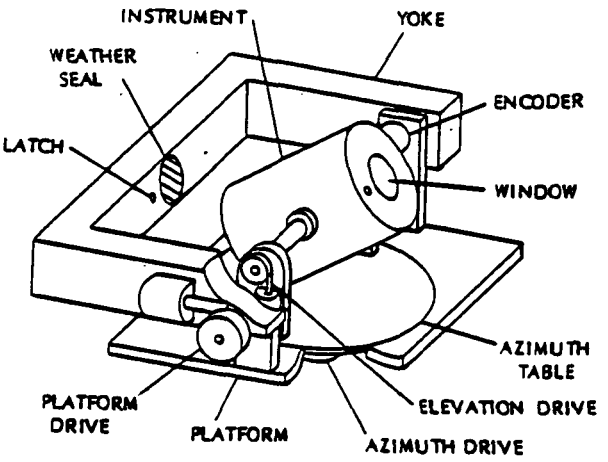

Figure 8. Artist's concept of instrument and mounting assembly.

Table 1. Preliminary Examination of Input Parameters to Radiative Transfer Codes

Aerosols:

Total Number Density and Vertical Distribution. Both variable,[15] with aerosol optical thickness varying by as much as a factor of 2.

Particle Size Distribution. Normalized Junge and Deirmenjian distributions compared. Number of particles at a given radius found to vary by an order of magnitude. Change in output was <0.1%.

Refractive Index. Extinction may vary by an order of magnitude for the various values used to approximate desert aerosols,[16] extinction being more affected by the real part of the refractive index. Our calculations show that a change in index from n = 1.5 to n = 1.5-0.01i changes output by <1%.

Other Parameters:

Ozone. Can expect up to 10% daily variation from seasonal mean;[17] this changes output by 1%.

Water Vapor. With humidity range of 30% to 90%, and temperature of 4°C to 21°C, water concentration varies from 0.15 to 3 gm cm^{-2} km^{-1}.

Ground Reflectance, Exo-Atmospheric Solar Spectral Irradiance. For negligible output error, need to know these parameters to within 0.1%. With recent detector calibration techniques, this is no longer unreasonable.

Field of View. A study has been done using an infinitesimal target having the reflectance of White Sands (ρ = 0.7) and background of ρ = 0.35 and 0.7. The resultant output varied by 2%.

Pressure. A 10% change in pressure changes output by only 0.2%. Negligible error is anticipated, as pressure can be measured on a continuous basis to high accuracy.

Time of Day. Need to know within 1 second of measurement for Langley plot.[18,19]

Polarization. Studies[20,21] need to be extended to determine the influence of scene- and atmosphere-induced polarization on the calibration of an orbital sensor. Polarization introduced by the sensor itself needs to be known from pre-flight measurements.

study into the effect each has on overall accuracy. It is seen that other parameters such as the ground reflectance, time of day, and solar spectral irradiance should be known to 0.1%. This is not an unreasonable requirement, given the recent advances in calibration techniques. Our simulation was made by using an average desert aerosol number density, with complex index of n = 1.5-0.01i. Published data[22] were used for the ozone optical depth and absorption coefficients. Up to now, water vapor variability, which affects the fourth MSS band, has not been analyzed.

Results of the first attempt to make such a calibration for Landsat 4, together with further discussion of the uncertainties involved, can be found in Castle et al.[23]

Conclusions

Without appropriate pre-flight and on-board calibration, it now appears possible that present earth resources satellite systems can be radiometrically calibrated in absolute terms with an uncertainty of less than ±3% by reference to ground targets. This conclusion is based on recent advances in the establishment of self-calibrated detectors as accurate absolute radiometric standards together with the development of radiative transfer codes that account for multiple scattering and include all relevant atmospheric parameters. The degree of uncertainty in the calibration procedure depends heavily on our ability to accurately characterize the atmosphere above the target during the sensor overflight. We are investigating this matter both theoretically and experimentally during the image data quality analysis phase of the Landsat-4/5 program.

Acknowledgments

I wish to thank J. L. Engel of Santa Barbara Research Center, a subsidiary of Hughes Aircraft Company, and J. L. Barker of NASA Goddard Space Flight Center for technical data on the TM, and M. Dinguirard of the Centre d'Etudes et de Recherches de Toulouse for technical data on the SPOT/HRVs.

This study was supported by NASA, grant number NAG 5-196, and the USDA, broadform contract number 12-14-5001-38.

References

1. Smith, J. A., "Matter-Energy Interaction in the Optical Region," Chapter 3 in R. N. Colwell, ed., Manual of Remote Sensing, ed. 2, American Society of Photogrammetry, Falls Church, Va., 1983.
2. Goel, N. S., and D. E. Strebel, "Inversion of Vegetation Canopy Models for Estimating Agronomic Variables. I. Problem Definition and Initial Results Using the Suits' Model," Remote Sensing of Environment, Vol. 13, pp. 487-507. 1984.
3. Aranuvachapun, S., and P. H. LeBlond, "Turbidity of Coastal Water Determined from Landsat," Remote Sensing of Environment, Vol. 11, pp. 113-132. 1981.
4. Doak, E., J. Livisay, D. Lyzenga, J. Ott, and F. Polcyn, "Evaluation of Water Depth Techniques Using Landsat and Aircraft Data," ERIM final report on contract DMA 800-78-6-0060, pp. 207. 1980.
5. Gordon, H. R., "Removal of Atmospheric Effects from Satellite Imagery of the Oceans," Appl. Opt., Vol. 17, pp. 1631-1636. 1978.
6. Kowalik, W. S., R. J. P. Lyon, and P. Switzer, "The Effects of Additive Radiance Terms on Ratios of Landsat Data," Photogramm. Eng. and Remote Sensing, Vol. 49, pp. 659-669. 1983.
7. Otterman, J., and R. S. Fraser, "Earth-Atmosphere System and Surface Reflectivities in Arid Regions from Landsat MSS Data," Remote Sensing of Environment, Vol. 5, pp. 247-266. 1976.
8. Robinove, C. J., P. S. Chavez, Jr., D. Gehring, and R. Holmgren, "Arid Land Monitoring Using Landsat Albedo Difference Images," Remote Sensing of Environment, Vol. 11, pp. 133-156. 1981.
9. Maisonneuve, J.-M., and M. Dinguirard, "Problèmes et dispositifs d'étalonnage en vol de la caméra HRV du projet de satellite SPOT," XXVII Rassegna Internazionale Elettronica Nucleare ed Aerospaziale, Rome, 7-16 March 1980.
10. Dinguirard, M., and J.-M. Maisonneuve, "Dispositif d'étalonnage sur le soleil de la caméra HRV du projet SPOT," Rassegna Internazionale Elettronica Nucleare ed Aerospaziale, Rome, 7-16 March 1980.
11. Kastner, C. J., and P. N. Slater, "In-Flight Radiometric Calibration of Advanced Remote Sensing Systems," Proc. SPIE, Vol. 356, pp. 158-165. 1982.
12. Kriebel, K. T., "Calibration of the METEOSAT-VIS Channel by Airborne Measurements," Appl. Opt., Vol. 20, p. 11. 1981.
13. Kenney, G. P., and W. E. Hensley, "Skylab Program, Earth Resources Experiment Package, Sensor Performance Evaluation, Final Report," Vol. III(S192), NASA-CR-144564. 1975.
14. Ahmad, Z., "A Study of the Relative Accuracy of Two Iterative Radiative Transfer Programs," Report TR-SASC-002, Systems and Applied Science Corp., Md. 1976.
15. Elterman, L., R. B. Toolin, and J. D. Essex, "Stratospheric Aerosol Measurements with Implications for Global Climate," Appl. Opt., Vol. 12, p. 330. 1973.
16. Jennings, S. G., R. G. Pinnick, and H. J. Avermann, "Effects of Particulate Complex Refractive Index and Particle Size Distributions Variations on Atmospheric Extinction and Absorption for Visible Through Middle IR Wavelengths," Appl. Opt., Vol. 17, pp. 3922-3929. 1978.
17. Craig, R. A., The Upper Atmosphere, Academic Press, New York. 1965.
18. Palmer, J. M., "The Effects of Errors in the Geometrical Determination of Optical Air Mass on the Accuracy of Extraterrestrial Solar Irradiance as Obtained Using the Langley Method," Solar Energy. Submitted 1982.
19. Herman, B. M., M. A. Box, J. A. Reagan, and C. M. Evans, "Alternate Approach to the Analysis of Solar Photometer Data," Appl. Opt., Vol. 20, p. 2925. 1981.
20. Coulson, K. L., "Effects of Reflection Properties of Natural Surfaces in Aerial Photography," Appl. Opt., Vol. 5, pp. 905-917. 1966.
21. Koepke, P., and K. T. Kriegel, "Influence of Measured Reflection Properties of Vegetated Surfaces on Atmospheric Radiance and Its Polarization," Appl. Opt., Vol. 17, pp. 260-264. 1978.
22. Elterman, L., "UV, Visible and IR Attenuation for Altitudes to 50 km, 1968," Environmental Research Papers No. 285, Air Force Cambridge Research Laboratories, Bedford, Mass. 1968.
23. Castle, K. R., R. G. Holm, C. J. Kastner, J. M. Palmer, and P. N. Slater, "In-Flight Absolute Radiometric Calibration of the Thematic Mapper," IEEE Geosciences and Remote Sensing, special edition entitled Landsat 4, ed. by V. V. Salomonson. 1984.

The use of field radiometers in reflectance factor and atmospheric measurements

Che Nianzeng
Beijing Institute of Technology, Beijing, China

R. D. Jackson
USDA-ARS, U.S. Water Conservation Laboratory
Phoenix, AZ 85040, U.S.A.

A. L. Phillips and P. N. Slater
Optical Sciences Center, University of Arizona
Tucson, AZ 85721, U.S.A.

Abstract

This paper discusses field radiometer methods for measuring (1) the reflectance factor of a surface, (2) the ratio of atmospherically scattered to direct irradiance (s/d) at the ground, and (3) the atmospheric extinction coefficient.

Calculations show that, under hazy or cloudy conditions, reflectance factor measurements of an unknown surface made in the field with reference to a white panel, both surfaces having nonlambertian characteristics, can differ by up to 6% from laboratory measurements of the unknown surface. This applies to surfaces having reflectance factors greater than 0.05. The error can be reduced to 0.4% if the direct solar component alone is used for the determination.

Measurements of surfaces with reflectance factors from 0.09 to 0.4 showed errors of 10% and 2% respectively when the total radiance of the target was ratioed to that of the reference panel. These errors can be reduced to 4% and less than 1% respectively when the direct solar components are ratioed.

The mid-infrared (mid-IR) bands of a commonly used field radiometer showed a high out-of-field response that gave rise to measurement errors on the order of 20%.

The effect of the reflectance of other surfaces in the neighborhood of the target is demonstrated by determining the ratio of shaded to direct irradiances. Agricultural scenes can show changes of about 5% in the red and 20% in the near IR.

A commonly available field radiometer, in conjunction with a reference panel, can be used reliably to determine the atmospheric extinction coefficients in broad wavelength intervals.

Introduction

Measurement of the reflectance factor of ground features has become a routine procedure by a number of investigators. Multispectral radiometers have been designed especially for such measurements.[1] Reflectance factor data obtained from these instruments are used as "ground truth" for aircraft and satellite experiments and are used to verify models that have been developed to describe the radiation environment of surfaces.

Such radiometers can also be used for atmospheric measurements. The separation of the atmospheric diffuse component from the global component is usually made by using two pyranometers,[2] one exposed to the total global radiation and the other to the diffuse radiation. The attenuation of solar radiation by atmospheric scattering, usually measured with solar radiometers, can also be evaluated with field radiometers by measuring the radiance of a target of known reflectance factor that is alternately sunlit and shaded at a number of solar zenith angles. The atmospheric extinction coefficient can be obtained by the Langley plot method.[3]

It has been pointed out[4,5] that a number of factors should be considered when making field measurements, for example, the variation in solar irradiance with a change in solar zenith angle, the effect of cloud movements on the scattered irradiance during measurements, and the effect on surface irradiance of the proximity of the observer. The errors introduced by assuming uniformly distributed skylight and lambertian reflectance characteristics of the target and reference panel have also been described.[6,7]

This paper develops the equations to: (1) describe the errors in reflectance factor measurements introduced by these assumptions together with the assumption that the radiometer has perfect out-of-field rejection characteristics; (2) determine the influence of the reflectance of the surrounding area on the measurement of the ratio of diffuse to direct irradiance, taking into account the imperfect out-of-field rejection characteristics of the radiometer; (3) determine the correction coefficient needed in the measurement of the ratio of diffuse to direct irradiance to account for the high radiance in the vicinity of the sun, which is shielded from the panel during the measurement of the diffuse component; and (4) determine atmospheric extinction coefficient using a multiband radiometer and horizontal reference panel. Example results are calculated from these equations and compared to the results of field measurements.

Development of Equations

The irradiance at a target surface located in a field environment is composed of three parts: (1) the direct irradiance from the sun, (2) the component scattered by the atmosphere before interaction with the ground, and (3) the component that comprises flux reflected from the ground and scattered by the atmosphere onto the surface to be measured. Figure 1 shows the geometry of a radiometer viewing a reference reflectance panel in a field environment.

The scattered irradiance from the hemispherical sky is

$$E_{sky} = 2\pi \int_0^{\pi/2} L_{sky}(\theta) \sin\theta \cos\theta \, d\theta,$$

where $L_{sky}(\theta)$ is the component of solar flux scattered by the atmosphere and incident on the target without previous interaction with the ground. Then, the scattered irradiance on the surface can be written as

$$E_{dif} = E_{sky} + (E_{dir}\cos\theta_z + E_{sky})P(R_t,R_s), \qquad (1)$$

where $E_{dir}\cos\theta_z$ is the solar irradiance at the surface at a solar zenith angle θ_z, and $P(R_t,R_s)$ is a coefficient representing the irradiance contribution from the ground-reflected flux that has been subsequently scattered downward. $P(R_t,R_s)$ is a function of the surround reflectance and the atmospheric conditions at the time of measurement. R_t and R_s are the reflectance factors of the target and the surround, respectively. By definition, a reflectance factor is the ratio of the radiant flux from a surface to that from an identically irradiated perfectly lambertian surface.

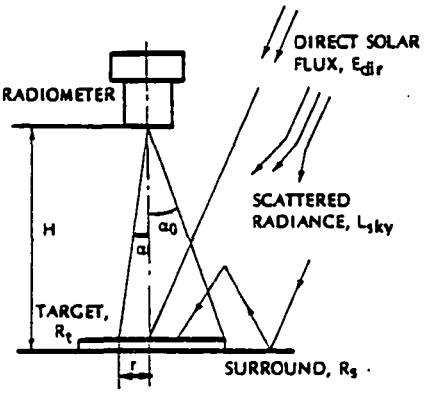

Fig. 1. Measurement geometry with a field spectroradiometer.

We set $Q = (E_{dir}\cos\theta_z + E_{sky})P(R_t,R_s)$, which is the irradiance contribution due to the surround. Noting that this can be taken as a uniform irradiance on the target, and considering the angular reflection characteristics of the target, we can write

$$E_{dif}R_t(\theta) = \left[E_{sky}[1 + \xi_t(\theta)] + Q\right]R_t(\theta)$$

$$= QR_t(\theta) + 2\pi \int_0^{\pi/2} L_{sky}(\theta)\, R_t(\theta) \sin\theta \cos\theta \, d\theta, \qquad (2)$$

where the term $1 + \xi_t(\theta)$ is a reflectance factor correction coefficient, which accounts for the nonlambertian characteristics of the target and the nonuniform hemispheric scattered irradiance on the surface. If the target is perfectly lambertian, then $R_t(\theta) = R_t$ and $\xi_t(\theta) = 0$.

Referring to Fig. 1, we see that the radiometer voltage signal can be written as

$$V_{tot,t}(\theta) = \int_0^{\alpha_0} \left[E_{dir}\cos\theta_z + E_{sky}[1 + \xi_t(\theta)] + Q\right]R_t(\theta)\, r(\alpha)\, K d\Omega$$

$$+ \int_{\alpha_0}^{\infty} \left[E_{dir}\cos\theta_z + E_{sky}[1 + \xi_s(\theta)] + Q\right]R_s(\theta)\, r(\alpha)\, K d\Omega, \qquad (3)$$

where $\xi_s(\theta)$ is a correction coefficient with the same meaning as $\xi_t(\theta)$ except that it applies to the surround, $r(\alpha)$ is the spatial responsivity of the radiometer, K is a constant that includes the diameter of the aperture, the filter factor, and the transmittance of the radiometer, and $d\Omega$ is the solid angle increment, defined as

$$d\Omega = \frac{2\pi r dr}{(H/\cos\alpha)^2} = 2\pi \tan\alpha \, d\alpha.$$

To account for out-of-field-of-view contribution to the radiometer signal, we define

$$K_1 = 2\pi K \int_0^{\alpha_0} r(\alpha) \tan\alpha \, d\alpha \qquad \text{and} \qquad K_2 = 2\pi K \int_{\alpha_0}^{\infty} r(\alpha) \tan\alpha \, d\alpha \qquad (4)$$

where K_1 and K_2 are voltages per unit of reflected radiance from the target and surround, respectively. They can be determined if the spatial responsivity $r(\alpha)$ of the radiometer and the subtended angle α_0 are known. Substituting Eqs. (4) into Eq. (3), we have

$$V_{tot.t}(\theta) = \left[E_{dir}\cos\theta_z + E_{sky}[1 + \xi_t(\theta)] + Q\right]R_t(\theta)\, K_1 + \left[E_{dir}\cos\theta_z + E_{sky}[1 + \xi_s(\theta)] + Q\right]R_s(\theta)\, K_2. \quad (5)$$

In Eq. (5), the first term is the radiometer voltage signal due to the flux reflected from the target. The second term is that due to the flux reflected from the surround; it is detected by the radiometer because of the radiometer's imperfect out-of-field-of-view rejection characteristic.

When the surface measured is shaded from the sun with a shield, the radiometer voltage reading is

$$V_{shad.t}(\theta) = \left[F_1E_{sky}[1 + \xi_t(\theta)] + Q\right]R_t(\theta)\, K_1 + \left[E_{dir}\cos\theta_z + F_2E_{sky}[1 + \xi_s(\theta)] + Q\right]R_s(\theta)\, K_2, \quad (6)$$

where F_1 is the fraction of scattered skylight falling on the target when the shield is in place and F_2 is the corresponding quantity for the surround (Fig. 2). F_2 and F_1 are larger than 0.9 when the shaded solid angle is small. We discuss the F_1 coefficient in a later section. In this case the factor Q is small and the effect of a change in Q with shading is negligible.

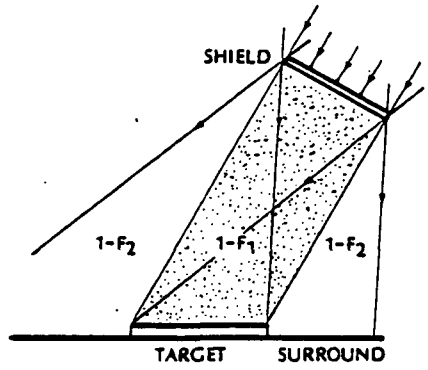

Fig. 2. Shading geometry. Part of the scattered irradiance on both the target and the surround is obstructed.

Subtracting Eq. (6) from Eq. (5), we have

$$V_{dir.t}(\theta) = V_{tot.t}(\theta) - V_{shad.t}(\theta) = \left[E_{dir}\cos\theta_z + (1-F_1)E_{sky}[1 + \xi_t(\theta)]\right]R_t(\theta)K_1 + (1-F_2)E_{sky}[1 + \xi_s(\theta)]R_s(\theta)K_2. \quad (7)$$

We use Eq. (7) in the following description of a technique for measuring the reflectance factor in the field.

Reflectance factor measurement in the field

To measure the reflectance factor, a radiometer is directed alternately at the target surface and at a calibrated reference surface, for example a $BaSO_4$ panel, and the results are ratioed. To eliminate the effect of scattered irradiance on measurement accuracy, readings are recorded when the reference and the target surface are shaded and then again when they are sunlit. Although the change in irradiance during the measurement procedure introduces an error, the error can be compensated for by taking a second shaded reading after the V_{tot} reading and averaging the two V_{shad} readings. To reduce errors, the V_{shad} and V_{tot} readings should be taken in rapid succession. Taking the ratio of the two sets of readings, we have

$$R(\theta) = \frac{V_{tot.t}(\theta) - V_{shad.t}(\theta)}{V_{tot.r}(\theta) - V_{shad.r}(\theta)} = \frac{V_{dir.t}(\theta)}{V_{dir.r}(\theta)} = \frac{\left[E_{dir}\cos\theta_z + (1-F_1)E_{sky}[1 + \xi_t(\theta)]\right]R_t(\theta)K_1 + (1-F_2)E_{sky}[1 + \xi_s(\theta)]R_s(\theta)K_2}{\left[E_{dir}\cos\theta_z + (1-F_1)E_{sky}[1 + \xi_r(\theta)]\right]R_r(\theta)K_1 + (1-F_2)E_{sky}[1 + \xi_s(\theta)]R_s(\theta)K_2}, \quad (8)$$

where $\xi_r(\theta)$ has the same definition as $\xi_t(\theta)$ and $\xi_s(\theta)$ but applies to the reference surface of reflectance factor R_r. Usually in field measurements, $R_t(\theta) = R_s(\theta)$ because the target is a part of the surround, for example in measurements of part of an agricultural field. However, a reference target such as a $BaSO_4$ panel has a reflectance factor considerably different from the surround.

In both the numerator and the denominator the last term is small compared to the first term. In estimating the ratio of the second to the first term in the numerator we refer to Table 1, which lists the spatial responsivity $r(\alpha)$ of a Barnes Model 12-1000 modular multiband radiometer[8] as a function of field of view, and Table 2, which lists the K_2/K_1 values calculated by Eq. (4) for different fields of view.

Table 1. Spatial responsivity of a Barnes radiometer, band 5.

Field of view (deg)	r(α) 15 deg field	r(α) 1 deg field
0	1.000	1.000
4	0.984	0.719
10	0.939	0.167
15	0.208	—
20	0.066	0.001
30	0.002	0.001
40	0.001	—

Table 2. K_2/K_1 values as a function of field of view.

Field of view (deg)	K_2/K_1 15 deg field	K_2/K_1 1 deg field
1	—	2.549
4	—	0.858
10	1.2825	0.053
12	0.6327	—
14	0.1710	—
18	0.0218	—
20	0.0023	0.004
30	—	0.004

If $F_1 = F_2 = 0.95$, $E_{sky} = 0.2E_{dir}\cos\theta_z$, $R_t(\theta) = R_s(\theta)$, $\xi_t(\theta) = \xi_s(\theta) = 0$, and $K_2/K_1 = 0.06$ (15° field of view), then

$$\frac{(1-F_2)E_{sky}R_s(\theta)\,K_2}{[E_{dir}\cos\theta_z + (1-F_1)E_{sky}]R_t(\theta)K_1} = 0.06\%,$$

which is negligible. Thus,

$$R(\theta) = \frac{V_{dir,t}(\theta)}{V_{dir,r}(\theta)} = \frac{\left[E_{dir}\cos\theta_z + (1-F_1)E_{sky}[1 + \xi_t(\theta)]\right]R_t(\theta)}{\left[E_{dir}\cos\theta_z + (1-F_1)E_{sky}[1 + \xi_r(\theta)]\right]R_r(\theta)}. \tag{9}$$

If the measured surface has approximately lambertian characteristics, then $\xi_t(\theta)$ and $\xi_r(\theta)$ are nearly equal, so the reflectance factor of the measured surface is

$$R_t(\theta) = R(\theta) * R_r(\theta). \tag{10}$$

However, when $R_s(\theta)$ is much larger than $R_t(\theta)$, as for example between rows of plants in the near IR, when E_{sky} is very large, or when the out-of-field response of the radiometer is high, the second term in the numerator in Eq. (8) cannot be neglected. The mid-IR bands of the Barnes radiometer provide an example of how a high out-of-field response can give rise to large measurement errors. Previous work[9] on measuring the radiance of the exit port of an integrating sphere from different distances indicated that the out-of-field response was high. Our results, listed in the last column of Table 1, agree with this observation. If we assume severe measurement conditions, for example, $E_{sky}/E_{dir}\cos\theta_z = 0.4$, $R_s(\theta) = 4R_t(\theta)$, and a 1-degree field of view, representing a high out-of-field response ($K_2/K_1 = 2.549$, see Table 2), a measurement error of 20% occurs even if the shaded readings are taken into account.

Analysis of the reflectance factor error

We now discuss the reflectance factor correction coefficient $\xi_t(\theta)$ due to the nonlambertian characteristics of the target surface and reference panel and due to the angular nonuniformity of the diffuse sky irradiance.

From the notation in Eq. (2),

$$1 + \xi_t(\theta) = \frac{\int_0^{\pi/2} L_{sky}(\theta)\,R_t(\theta)\sin\theta\cos\theta\,d\theta}{R_t(\theta)\int_0^{\pi/2} L_{sky}(\theta)\sin\theta\cos\theta\,d\theta}, \tag{11}$$

$\xi_t(\theta)$ can be estimated if the hemispherical distribution of the skylight and the reflectance factor of the target surface as a function of solar zenith angle are known.

To calculate some typical values for $\xi_t(\theta)$, we refer to two atmospheric models, a model for a diffuse panel, and several models for targets. The atmospheric models are those of Dave.[10] The first (Fig. 3) is the Light Haze L model for $\lambda = 0.415$ μm, a scattering optical thickness $\tau_b = 0.1$, and irradiance angle $\theta = 40$ deg. The second (Fig. 4) is the Cloud C1 model for $\lambda = 0.825$ μm, a scattering optical thickness $\tau_b = 0.1$, and irradiance angle $\theta = 40$ deg. For purposes of this calculation, we made some approximations to the distribution curves and also assumed that the curves do not change shape but only translate along the abscissa as the solar

zenith angle changes. Six different normalized reflectance factor models were used to simulate several possible situations (Fig. 5). Model 1 is of a typical painted $BaSO_4$ diffuser and is used here for reference. Models 2 through 6 represent five different possible surface reflection characteristics.

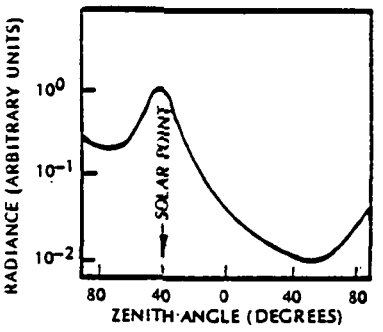

Fig. 3. Downward scattered radiance distribution as a function of solar zenith angle for Dave model Haze L.

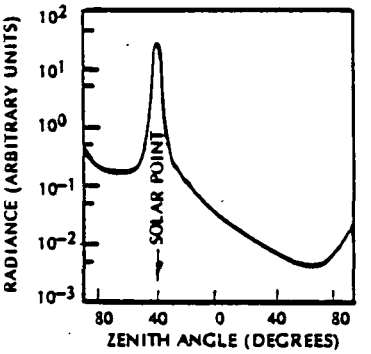

Fig. 4. Downward scattered radiance distribution as a function of solar zenith angle for Dave model Cloud C1.

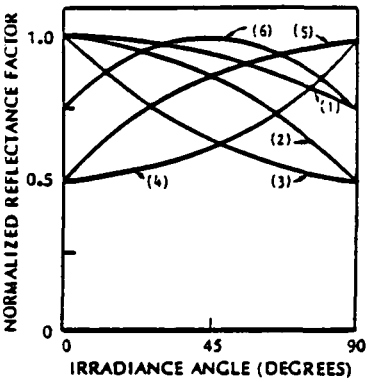

Fig. 5. Six reflectance factor models used for calculation of the reflectance factor error.

We define ΔR_{dir} and ΔR_{tot} as reflectance factor errors due to hemispheric scattered irradiance and nonlambertian characteristics of targets with shaded readings subtracted (ΔR_{dir}) and not subtracted (ΔR_{tot}). Referring to Eq. (9), ideally $R(\theta)$ should be equal to $R_t(\theta)/R_r(\theta)$, which we will refer to as $R_{id}(\theta)$. Now the error will be

$$\Delta R_{dir}(\theta) = \left[\frac{E_{dir}\cos\theta_z + (1-F_1)E_{sky}[1 + \xi_t(\theta)]}{E_{dir}\cos\theta_z + (1-F_1)E_{sky}[1 + \xi_r(\theta)]} - 1\right]R_{id}(\theta) ; \tag{12}$$

referring to Eq. (5),

$$\Delta R_{tot}(\theta) = \left[\frac{\left[E_{dir}\cos\theta_z + E_{sky}[1 + \xi_t(\theta)] + Q\right](K_1 + K_2)}{\left[E_{dir}\cos\theta_z + E_{sky}[1 + \xi_r(\theta)] + Q\right]K_1 + \left[E_{dir}\cos\theta_z + E_{sky}[1 + \xi_t(\theta)] + Q\right]R_{id}(\theta)K_2} - 1\right]R_{id}(\theta). \tag{13}$$

From Eqs. (12) and (13), we see that the magnitude of the errors ΔR_{tot} and ΔR_{dir} is dependent on the ratio of scattered to direct irradiance, the nonlambertian characteristics of the measured surface, the reflectance factor of the target, and the percentage of shaded irradiance, $(1-F_1)$. The ΔR_{dir} should be much smaller than ΔR_{tot} because the effect of scattered irradiance has been significantly reduced.

The reflectance factor errors illustrated in Fig. 6 were determined by setting E_{sky} equal to $0.2E_{dir}\cos\theta_z$. The results show that if the ratio V_{tot} is used to determine the reflectance factor, the error $\Delta R_{tot}/R_{id}$ may be

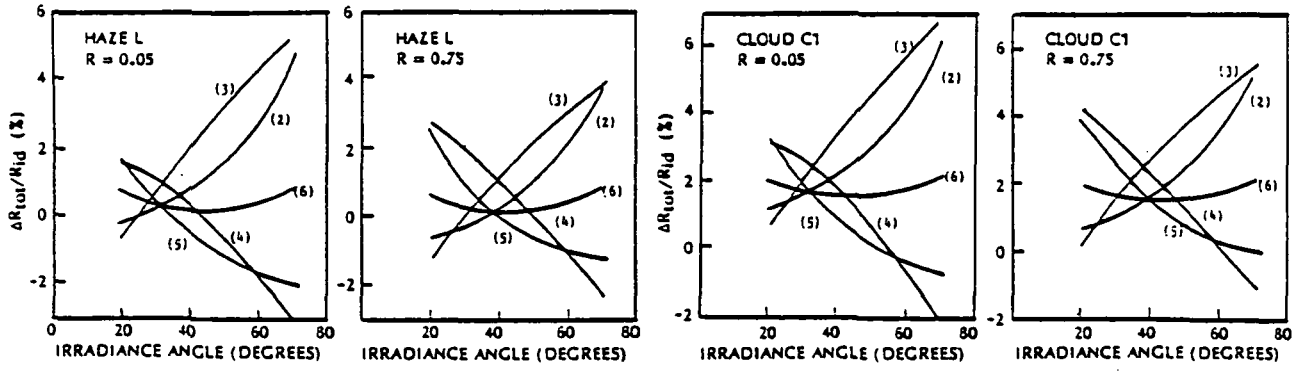

Fig. 6. Expected percentage error in reflectance factor measurement due to scattered irradiance and nonlambertian characteristics of targets. Curves (2) through (6) correspond to surface reflectance models of Fig. 5.

What is τ for these?

2% to 6% under these conditions. The largest measurement errors can be expected for short-wavelength (high atmospheric absorption), low-reflectance targets, larger solar zenith angles, and hazy or cloudy conditions. The average error for $\Delta R_{tot}/R_{id}$ is about 2.3% for R = 0.05 and 1.5% for R = 0.75. However, if the signal ratio of $V_{dir,t}$ to $V_{dir,r}$ is used in the determination of the reflectance factor, the error $\Delta R_{dir}/R_{id}$ is less than 0.4% according to the calculation, assuming that $E_{sky} = 0.2E_{dir}\cos\theta_z$ taking $(1-F_1)$ values from Table 4 (for a shield area 76 cm x 76 cm at a distance of 3 m).

In summary, the reflectance factor measurement can be analyzed more accurately by using the ratios of the two $V_{dir}(\theta)$ terms instead of the two $V_{tot}(\theta)$ terms because (1) the atmospherically scattered irradiance and the nonlambertian characteristic of the measured surfaces have a negligible effect on the measurement, and (2) the effect of the response of the instrument outside its nominal field of view on the measurement is significantly reduced by the subtraction of V_{shad} from V_{tot}.

Field measurement of reflectance factor

We measured reflectance factors on the roof of the Optical Sciences Center, University of Arizona, on November 1, 1983, a cloudless day with high visibility. We used several panels of known reflectance factors as targets, in order to compare them with laboratory measurements. The panels had reflectance properties similar to that of model 2 in Fig. 5. The reflectance factor measured in the laboratory at 45 deg irradiance angle and 0 deg viewing angle, $R(45/0)_{lab}$, was used as the reference to compare the effect of reflectance factor on the measurement error. The relative reflectance factor errors for the direct (ϵ_{dir}) and total (ϵ_{tot}) measurements are, in percent,

$$\epsilon_{dir} = \frac{R_{dir} - R_{lab}}{R_{lab}} \times 100 \qquad \text{and} \qquad \epsilon_{tot} = \frac{R_{tot} - R_{lab}}{R_{lab}} \times 100,$$

where R_{dir} and R_{tot} are the reflectance factors measured in the field with the diffuse component subtracted (R_{dir}) and not subtracted (R_{tot}).

Figure 7 shows the measurement errors relative to the laboratory measurement results. Figure 7a shows that ϵ_{tot} increases with the irradiance angle. The curve is similar to Fig. 6 for reflectance model 2, but the measured error is larger than in Fig. 6. However, ϵ_{dir} is smaller than ϵ_{tot} and does not increase with increasing irradiance angle. As the reflectance factor increases (Figs. 7b through d), the measurement errors ϵ_{tot} and ϵ_{dir} decrease. The ϵ_{tot} is 1% to 3% on average, which is in agreement with the calculated results shown in Fig. 6. However, ϵ_{dir} is less than 1% on average. The results emphasize the need to subtract diffuse irradiance readings from total irradiance readings, particularly for low reflectance targets.

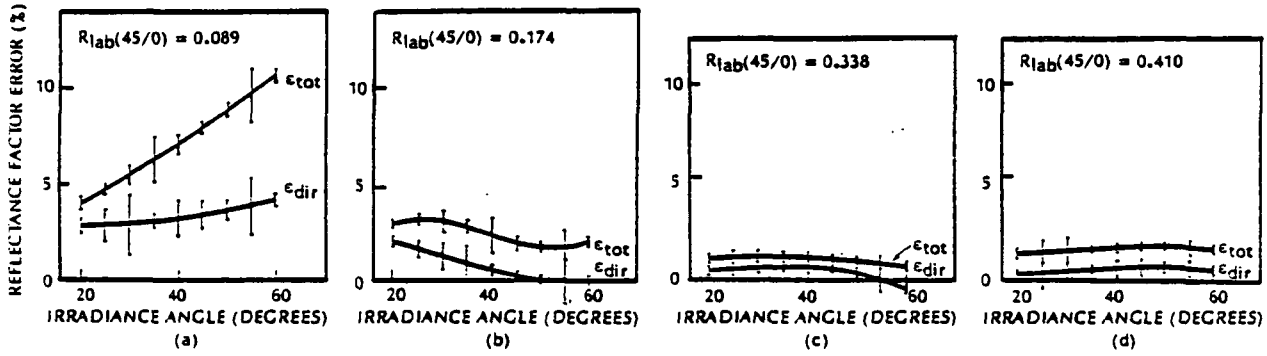

Fig. 7. Percentage error of the reflectance factor in a measurement on November 1, 1983.

Scattered and direct irradiance measurements

The ratio s/d provides a useful way to quantify atmospheric conditions in remote sensing measurements. It may also provide a way to check the assumed atmospheric characteristics used in radiative transfer codes when the latter are used to make spectral signature corrections.

The measurement of s/d with two pyranometers covers the entire wavelength range of the detector's response. However, in many remote sensing applications, multispectral data are required. The spectral measurements of s/d should be made within a short time of each other for accurate intercomparison and analysis. This ratio can be conveniently measured with a multispectral radiometer and a uniform reference panel.

Taking the ratio of Eqs. (6) and (7), considering that $\xi_r(\theta) = 0$, and ignoring $\xi_s(\theta)$, we obtain

$$\frac{V_{shad.r}(\theta)}{V_{dir.r}(\theta)} = \frac{(F_1E_{sky} + Q)R_r(\theta)K_1 + (E_{dir}\cos\theta_z + F_2E_{sky} + Q)R_s(\theta)K_2}{[E_{dir}\cos\theta_z + (1-F_1)E_{sky}]R_r(\theta)K_1 + (1-F_2)E_{sky}R_s(\theta)K_2} . \quad (14)$$

One way to eliminate the second term in the numerator (in the denominator the second term is very small and can be neglected) is to replace the reference panel with a material of extremely low reflectance factor, R_k, but of the same size as the high-reflectance reference. Then $V_{shad.k}(\theta)$ can be calculated by Eq. (7). By connecting the two points $V_{shad.k}(\theta)$ and $V_{shad.r}(\theta)$ and extrapolating to R = 0, as shown in Fig. 8, we can determine the value of n_1, where

$$n_1 = (E_{dir}\cos\theta_z + F_2E_{sky} + Q)R_s(\theta)\,K_2.$$

When a panel with a zero reflectance factor of the same size as the reference panel is viewed by a radiometer, the $V_{shad}(\theta)$ value is exactly the contribution due to the out-of-field-of-view response.

Thus Eq. (14) can be rewritten as

$$\frac{V_{shad.r}(\theta) - n_1}{V_{dir.r}(\theta)} = \frac{F_1E_{sky} + Q}{E_{dir}\cos\theta_z + (1-F_1)E_{sky}} . \quad (15)$$

If n_1 is not subtracted in Eq. (15), the percentage error Δ introduced in the s/d measurement is, from Eq. (14):

$$\Delta = \frac{E_{dir}\cos\theta_z + F_2E_{sky} + Q}{F_1E_{sky} + Q} * \frac{R_s(\theta)K_2}{R_r(\theta)K_1}$$

$$= \frac{1 + F_2(s/d)}{F_1(s/d)} * \frac{R_s(\theta)K_2}{R_r(\theta)K_1} , \quad (16)$$

where $s/d = (E_{sky} + Q)/E_{dir}\cos\theta_z$, which is the ratio of the diffuse irradiance, including skylight and the surround reflection contribution Q, to the direct irradiance.

The percentage error is dependent on the reflectance factor of the surround, the measurement geometry, and the ratio s/d. When the measurement geometry stays unchanged, the measurement error increases with s/d and with the reflectance factor of the surround.

To estimate the effect of the surround on the s/d measurement, we carried out an experiment on March 20, 1984, at the Maricopa Agricultural Center, Arizona, in which two Barnes multiband radiometers were used to make identical measurements in locations with different surrounds. One was placed at the center of a 100-acre field of bare soil and the other at the center of a 100-acre field of wheat. Table 3 lists the average reflectance factor values for the wheat and the bare soil.

According to Eq. (16) and the data in Table 3, we can predict that s/d should be increasingly greater when measured in the bare soil field than when measured in the wheat field for TM bands 1, 2, and 3 because of the higher reflectance factor of bare soil in that wavelength range. However, for TM band 4, the measured s/d should be greater in the wheat field than in the bare soil field owing to the higher reflectance factor for wheat in the IR spectral region. This prediction was confirmed by field measurements, as shown by Fig. 9. For example, at larger zenith angles, the value of s/d is about 5% greater for bare soil than for wheat in band 3 but 20% less in band 4.

It is not difficult to deduce from Eqs. (14) and (16) that

$$\frac{1 + \Delta_{wheat}}{1 + \Delta_{soil}} = \frac{\frac{V_{shad.r}}{V_{dir.r}} \text{ measured in wheat field}}{\frac{V_{shad.r}}{V_{dir.r}} \text{ measured in soil field}} .$$

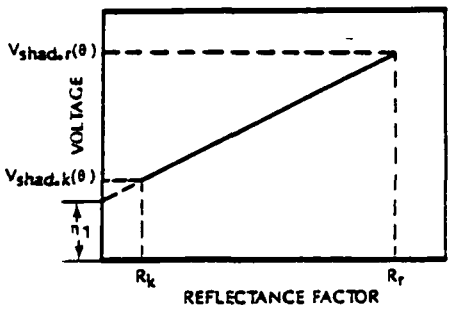

Fig. 8. A method to eliminate the surround effect on the s/d measurement.

Table 3. Average reflectance factors for wheat and bare soil.

Band No.	Wavelength (nm)	Wheat	Soil
1	450–520	0.019	0.058
2	520–600	0.028	0.083
3	630–690	0.017	0.120
4	760–900	0.495	0.181

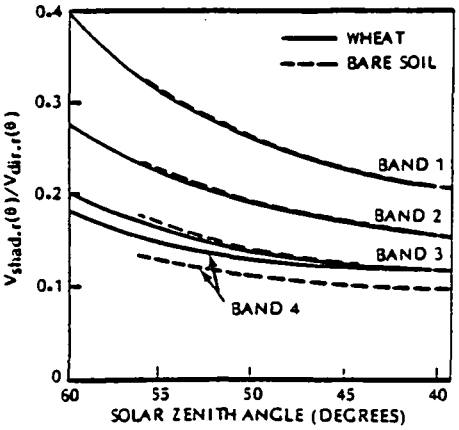

Fig. 9. Surround effect on the s/d measurement in an experiment on March 20, 1984.

Figure 10 shows both the curves for $(1+\Delta_{wheat})/(1+\Delta_{soil})$ calculated for different K_2/K_1 values, as given by Eq. (16) in band 4, and the ratio of $V_{shad.r}/V_{dir.r}$ measured in the wheat field to $V_{shad.r}/V_{dir.r}$ measured in the bare soil field. By comparing the calculated and measured data for different solar zenith angles, we find that the measured ratio lies between K_2/K_1 values of 0.05 and about 0.07, which is higher than the K_2/K_1 value of 0.04 that was determined from the measurement geometry. The discrepancy is probably due to the difficulty of accurately determining K_2/K_1.

Equation (16) suggests that the s/d measurement should be carried out where the surround has a low reflectance factor and/or the reference panel is large enough to make the out-of-field contribution to the radiometer signal negligible.

Setting M equal to $(V_{shad.r}(\theta) - n1)/V_{dir.r}(\theta)$ in Eq. (15), we have

$$M = \frac{F_1(E_{sky} + Q)}{E_{dir}\cos\theta_z + (1-F_1)(E_{sky} + Q)} = \frac{F_1(s/d)}{1 + (1-F_1)(s/d)} \quad (17)$$

and

$$s/d = \frac{M}{F_1 - (1-F_1)M} . \quad (18)$$

The magnitude of F_1 depends on the atmospheric conditions and the measurement geometry (Fig. 11). If we know the scattered radiance distribution $f(\theta,\phi)$ and the geometric measurement parameter α', we can determine F_1 by the equation

$$1-F_1 = \frac{\int_{-\alpha'/\sin\theta_z}^{\alpha'/\sin\theta_z} \int_{\theta_z-\alpha'}^{\theta_z+\alpha'} f(\theta,\phi) \sin\theta \cos\theta \, d\theta \, d\phi}{\int_{0}^{2\pi} \int_{0}^{\pi/2} f(\theta,\phi) \sin\theta \cos\theta \, d\theta \, d\phi} . \quad (19)$$

By measuring atmospheric parameters (atmospheric extinction coefficient, air pressure, temperature, etc.), we can calculate the scattered radiance distribution function $f(\theta,\phi)$ from a radiative transfer model.

The assumption that the scattered radiance is uniformly distributed leads to underestimating the $(1-F_1)$ value because the diffuse radiance is much higher in the region of the solar aureole than in the rest of the sky, especially on hazy or cloudy days (see Fig. 3). The small area of the shield then shades the part of the scattered sky with the strongest radiance peak.

To calculate $(1-F_1)$, the atmospheric models were used as before. The $(1-F_1)$ values are listed in Table 4. These values are for a shield size of 76 cm x 76 cm and for a distance between the midpoint of the reference panel and the shield of 3 m. Table 4 also lists a $(1-F_1)$ value of 0.010 for an assumed uniform diffuse radiance distribution.

The corrected s/d value may now be determined from Eq. (18) using the known F_1 and the measurement data.

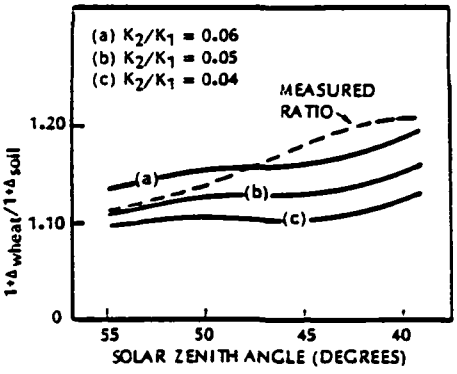

Fig. 10. Ratio of $(1+\Delta_{wheat})/(1+\Delta_{soil})$ as a function of solar zenith angle.

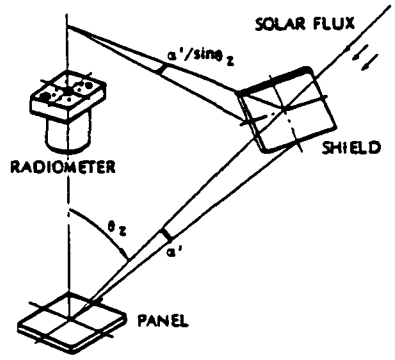

Fig. 11. Calculation geometry for $(1-F_1)$.

Table 4. Scattered skylight shaded coefficient $(1-F_1)$ value.

Irradiance angle (deg)	Haze L	Cloud C1
20	0.158	0.172
30	0.134	0.137
40	0.116	0.108
40	0.116	0.108
50	0.100	0.085
60	0.085	0.065
70	0.067	0.045
Uniform distribution assumption	0.010	

Measurement of atmospheric extinction coefficient

Solar radiometers are used to measure the atmospheric extinction coefficient. They have a narrow field of view (usually 1 to 2 deg), which is pointed at the sun. Readings of direct solar irradiance at the ground are made at known times during the day. The solar zenith angle corresponding to each time of day is calculated and the atmospheric extinction coefficient τ_{ext} is then determined by the Langley plot method.

The measurement of solar irradiance at the ground using a radiometer and a reflectance panel need not involve changing the viewing angle. The measurement geometry was illustrated in Fig. 1. By taking a series of global and diffuse irradiance measurements in rapid succession and at known times from a solar zenith angle of 75 deg to its smallest values that day, we can again determine τ_{ext} by the Langley plot method.

From Eq. (7) we have

$$V_{dir.r}(\theta_z) = \left[E_{dir}\cos\theta_z + (1-F_1)E_{sky}[1 + \xi_r(\theta_z)]\right]R_r(\theta_z)K_1 .$$

Remembering that the term $(1-F_1)$ is small (usually less than 0.1), and assuming that E_{sky} is approximately proportional to $E_{dir}\cos\theta_z$ with a constant* coefficient K_s and that $\xi_r(\theta_z) = 0$, we obtain

$$E_{dir}K_1 = \frac{V_{dir.r}(\theta_z)}{R_r(\theta_z)\cos\theta_z} * \frac{1}{1 + (1-F_1)K_s} . \tag{20}$$

Substituting $E_{dir} = E_{diro}\exp(-\tau_{ext}\sec\theta_z)$ into Eq. (20), where E_{diro} is the exoatmospheric solar irradiance, we have

$$E_{diro}K_1[1 + (1-F_1)K_s] * \exp(-\tau_{ext}\sec\theta_z) = \frac{V_{dir.r}(\theta_z)}{R_r(\theta_z)\cos\theta_z} , \tag{21}$$

and finally

$$\tau_{ext} = -\frac{\Delta\ln\left(\frac{V_{dir.r}(\theta_z)}{R_r(\theta_z)\cos\theta_z}\right)}{\Delta\sec\theta_z} . \tag{22}$$

If $\ln V_{dir.r}(\theta_z)/R_r(\theta_z)\cos\theta_z$ is set as the ordinate and $\sec\theta_z$ as the abscissa, the slope of the regression straight line is exactly the τ_{ext} value. The numerical calculation technique used for the determination of τ_{ext} was that proposed by Harman et al.[11] The reflectance factor value of the reference panel should be measured in the laboratory before and/or after the τ_{ext} measurement.

In comparing the two methods of τ_{ext} measurement, two points should be made. The first is the effect of scattered irradiance on the measurements. Since the solar radiometer has a small field of view, only the atmosphere in the field of view will directly affect the measurements. In the Langley plot, the points that diverge from the straight line owing to occasional atmospheric changes within the field of view of the solar radiometer can be discarded, thus providing a higher correlation coefficient for τ_{ext}. However, when the radiometer measures the reflected radiance, the fluctuations in signal due to irradiance fluctuations in the hemispherical diffuse component may weaken the correlation coefficient of the regression line. Thus the measurement method using a reference panel may not be as accurate as that using a solar radiometer.

The second point is that atmospheric gaseous absorption can be avoided by the appropriate choice of the center wavelengths of the narrow-spectral-band inteference filters used in the solar radiometer.[10] In this case, τ_{ext} is only the scattered extinction coefficient. However, not all field spectroradiometers are designed this way. For remote sensing use, the spectral bands of the field radiometer are usually chosen to match those of space multispectral sensors, which in some cases include atmospheric absorption bands, for example, the 0.8 to 1.1 μm band of the Landsat multispectral scanner systems. So τ_{ext}, determined by the reference panel method, will in some cases include both the scattered and absorption extinction coefficients due to atmospheric gases, especially in the IR where water vapor, carbon dioxide, oxygen, ozone, etc., are strongly absorbing.

To check the accuracy of the reference panel method for determining τ_{ext}, we set up a solar radiometer and a Barnes modular multiband radiometer in the same location in Tucson, Arizona, on September 21, 1983. A $BaSO_4$ panel, the reflectance factor of which had been measured in the laboratory, was used as a reference. Figure 12 shows the results. Note that the two sets of τ_{ext} data are consistent through the visible spectrum but that the reflectance panel method produced a higher τ_{ext} value in the near IR, possibly because of water absorption.

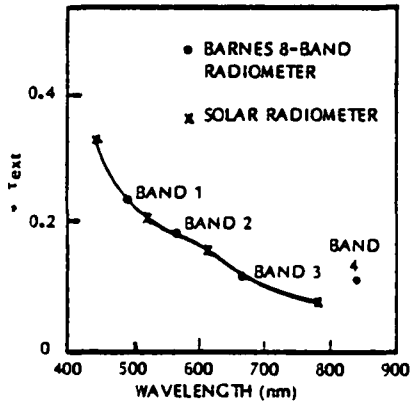

Fig. 12. Comparison of τ_{ext} measurement with a solar radiometer and a Barnes radiometer.

Concluding Remarks

Equations have been derived for use in determining the reflectance factor, the ratio of scattered to diffuse ground irradiance, and the atmospheric extinction coefficient. The equations account for the nonlambertian characteristics of the target, nonuniform sky radiance distributions, reflectance of the surrounding neighborhood, and out-of-field radiance contributions.

*The error introduced by this assumption is not significant. In our summer cloudless measurement, K_s changed less than 10% from sunrise to midday, which leads to an error of less than 1%.

Nonuniform sky irradiance and nonlambertian reflection characteristics give rise to a reflectance factor measurement error of 2% to 6% depending on the angular variation of the reflectance factor and atmospheric conditions. This result is in general agreement with other authors.[7,13] The method proposed in this paper for the measurement of reflectance factors makes this error due to nonuniform sky irradiance and out-of-field effects negligible.

An error on the order of 20% can be encountered even if the shaded readings are taken into account in the determination of reflectance factor, because of the high out-of-field response of a commonly available field radiometer when operated in its mid-IR bands.

A method and a correction procedure were described for the accurate determination of the ratio of scattered to direct (s/d) ground irradiance. The results showed that a multispectral radiometer and a reference panel can give atmospheric extinction coefficients in agreement with solar radiometer data in the visible spectrum. In the IR the results differ, possibly due to water vapor or other absorption in the spectral bands of the radiometer. This procedure should allow τ_{ext} in the visible to be determined by many researchers who have access to a multispectral radiometer and a reference reflectance panel but not to a solar radiometer.

Acknowledgments

The authors acknowledge support provided by NASA grant NAG5-196 and USDA broadform contract number 12-14-5001-38. We also thank Dr. J. A. Reagan of the University of Arizona for the use of a solar radiometer and Drs. B. F. Robinson of Purdue University and D. E. Pitts of Johnson Space Center for the use of a Barnes multiband radiometer.

References

1. B. F. Robinson, R. E. Buckley, and J. A. Burgess, "Performance Evaluation and Calibration of a Modular Multiband Radiometer for Remote Sensing Field Research," SPIE, Vol. 308, pp. 146-156. 1981.

2. K. L. Coulson, Solar and Terrestrial Radiation: Method and Measurement, Academic Press, pp. 129-134, 1975.

3. P. N. Slater, Remote Sensing: Optics and Optical Systems, Addison-Wesley, pp. 180-181, 1980.

4. M. J. Duggin, "The Field Measurement of Reflectance Factors," Photogr. Eng. Remote Sensing, Vol. 46, No. 5, pp. 643-647. 1980.

5. D. S. Kimes, J. A. Kirchner, and W. W. Newcomb, "Spectral Radiance Errors in Remote Sensing Ground Studies Due to Nearby Objects," Appl. Opt., Vol. 22, pp. 8-10. 1983.

6. D. S. Kimes and J. A. Kirchner, "Irradiance Measurement Errors Due to the Assumption of a Lambertian Reference Panel," Remote Sensing Environ., Vol. 12, pp. 141-149. 1982.

7. J. A. Kichner, S. Youkhana, and J. A. Smith, "Influence of Sky Radiance Distribution on the Ratio Technique for Estimating Bidirectional Reflectance," Photogr. Eng. Remote Sensing, Vol. 48, pp. 955-959. 1982.

8. Reference to commercial products does not imply endorsement by the Beijing Institute of Technology, the U.S. Department of Agriculture, or the University of Arizona.

9. J. L. Barker and J. Walker, Personal communication. 1984.

10. J. V. Dave, "A Direct Solution of the Spherical Harmonics Approximation to the Radiative Transfer Equation for an Arbitary Solar Elevation. Part II: Results," J. Atmos. Sci., Vol. 32, pp. 1463-1474. 1975.

11. B. M. Herman, M. A. Box, B. J. Reagan, and C. M. Evans, "Alternate Approach to the Analysis of Solar Photometer Data," Appl. Opt., Vol. 20, pp. 2925-2928. 1981.

12. G. E. Shaw, J. A. Reagan, and B. M. Herman, "Investigations of Atmospheric Extinction Using Direct Solar Radiation Measurements Made with a Multiple Wavelength Radiometer," J. Appl. Meteorol., Vol. 12, pp. 374-380. 1973.

13. B. F. Robinson and L. L. Biehl, "Calibration Procedures for Measurement of Reflectance Factor in Remote Sensing Field Research," SPIE, Vol. 196, pp. 16-26. 1979.

Radiometric Considerations in Remote Sensing

PHILIP N. SLATER

Invited Paper

The need for accurate radiometric data for the verification and use of scene radiation models is emphasized. The radiometric problems associated with reflectance and atmospheric correction field measurements and sensor calibration are reviewed. Estimates are made of the attainable accuracy in each case under favorable conditions. The loss in radiometric accuracy by resampling procedures in digital imagery processing is discussed.

I. Introduction

Coincidental with the development of comprehensive models of the interaction of electromagnetic radiation with the earth's surface and atmosphere, there is a growing interest in the application of radiation models to global earth–atmosphere–ocean studies such as COSPAR's International Satellite Land Surface Climatology Project and NASA's Global Habitability program.

Most scene radiation models described in recent reviews by Bunnik [1] and Smith [2] predict an upward spectral radiance, just above the feature of interest, on the basis of certain input values and then use an atmospheric model to predict the spectral radiance at the aircraft or satellite sensor. For example, in the case of a crop canopy, the input values usually include the leaf spectral reflectance and canopy geometry (leaf orientation and leaf area index, LAI), the soil spectral reflectance, and the geometry of irradiation and viewing. For many applications only the inverted form of this model is relevant: Given the radiance, irradiance, and viewing geometry, what is the constitution (LAI, vigor, etc.) of the canopy? Reference [3] is the latest of several publications by Goel and coworkers in which the result of such a procedure are described, but little other work on scene radiation inversion models has been reported.

The use of satellite-acquired image data with scene radiation models is inextricably dependent on atmospheric correction and sensor absolute radiometric calibration. Unlike computer-aided scene classification, which depends on a statistical analysis of the digital counts in a scene image, usually without correction for the intervening atmosphere, modeling is concerned with determining the radiance of the scene. For this purpose we need to know, first, the output digital counts from the sensor when it is imaging the feature of interest; second, the absolute radiometric calibration of the sensor in order to convert the digital counts to radiance at the entrance pupil of the sensor; and third, the radiance modification introduced by the intervening atmosphere (the atmospheric correction) in order to relate the entrance pupil radiance to the radiance of the ground feature [4]. For verification of models and for purposes of atmospheric correction to an uncertainty of a few percent, we need to be able to measure the bidirectional reflectance of uniform ground areas to an uncertainty of about 1 percent. We also need to be aware of the radiometric errors introduced if the digital image has to be resampled for spectral band and/or map registration purposes.

In this paper, we review the radiometric problems associated with field reflectance and atmospheric correction measurements and with sensor absolute calibration, and estimate the accuracies currently attainable. We then discuss the loss in radiometric accuracy introduced by resampling procedures in digital image processing.

II. Scene Reflectance Measurement

In computer-aided scene classification we use statistical differences among pixel digital counts to distinguish earth surface features. In this context we are usually interested only in relative reflectance values (an exception is multitemporal classification); indeed, the spectral radiant flux reflected by, and characteristic of, the features of interest may be only a small fraction of the total flux at the sensor, depending on the ground reflectance, solar zenith angle, viewing geometry, wavelength interval, and atmospheric conditions. In using models, on the other hand, we are often interested in knowing, or determining, the bidirectional radiance or reflectance distribution function of a surface feature, and we either correct for atmospheric ef-

Manuscript received January 15, 1985; revised February 21, 1985. This work was supported by NASA under Grant NAG 5-196 and under Contract NAS5-27382 and by the USDA under broadform Contract 12-14-5001-38.

The author is with the Committee on Remote Sensing and Optical Sciences Center, University of Arizona, Tucson, AZ 85721, USA.

0018-9219/85/0600-0997$01.00 ©1985 IEEE

fects or consider only the reflected radiance distribution immediately above the surface.

Before we discuss some of the problems in measuring reflectance, it is appropriate to review the definitions and interrelationships among the various ways of describing the reflecting properties of a surface that are relevant to remote sensing.

A. Reflectance Measurement Geometries

Of the nine different geometries that can be used to describe the reflection of radiant flux from a surface [5], fortunately only four are used to any great extent in remote sensing. These are:

1) the directional–hemispherical reflectance factor $R(\theta_i, \phi_i; 2\pi)$
2) the bidirectional reflectance factor $R(\theta_i, \phi_i; \theta_r, \phi_r)$
3) the directional–hemispherical reflectance $\rho(\theta_i, \phi_i; 2\pi)$
4) the bihemispherical reflectance $\rho(2\pi; 2\pi)$

where θ and ϕ are the angle to the surface normal and the azimuthal angle, respectively, and the subscripts i and r refer to incident and reflected angles. It is often important to relate these first four geometries to a fifth description:

5) the bidirectional reflectance distribution function (BRDF) $f(\theta_i, \phi_i; \theta_r, \phi_r)$.

Reflectance is defined as the ratio of the radiant flux reflected from a surface to the radiant flux incident on the surface. In the most general terms, it is the ratio of the radiant flux reflected from a surface into a hemisphere, to the flux incident hemispherically onto the surface; it is entry 4) in the above list: Reflectance factor is the ratio of the radiant flux reflected from a surface to the radiant flux reflected from a lambertian surface of unit absolute reflectance when both measurements are made under identical irradiance and viewing conditions.

The measurement of the directional–hemispherical reflectance factor may be considered the fundamental reflectance measurement because it provides the calibration of reference surfaces used in remote sensing field and laboratory work. Using refinements to the Van den Akker auxiliary sphere method, Venable *et al.* [6] at the National Bureau of Standards (NBS) were able to measure the directional–hemispherical reflectance factor of high-reflectance surfaces with an estimated uncertainty of ± 0.15 percent. Unfortunately, the refined Van den Akker method involves complicated measurement and data-reduction procedures. Measurements of $R(\theta_i, \phi_i; 2\pi)$, or the equivalent $R(2\pi; \theta_r, \phi_r)$, are routinely made in radiometric and colorimetric laboratories by use of a dual-beam spectroradiometer or spectrophotometer [7], [8, pp. 174–180]. These instruments provide a beam of narrow spectral bandwidth that is incident alternately on the surface of interest and on a reference surface whose calibration is traceable to the NBS. The alternative signals from a detector, placed in another port in the sphere, are then ratioed. This ratio, when multiplied by the absolute reflectance of the reference surface, measured using the same irradiance geometry, gives $R(\theta_i, \phi_i; 2\pi)$.

In remote sensing field work, directional–hemispherical and bihemispherical reflectance measurements have been made for reflectance studies and for studies of atmospheric and surface energy budgets [9]–[12]. However, the 2π solid angle collection geometry approximately simulates the averaged response over the total field of view only for wide-field acquisition systems, such as the Advanced Very High Resolution Radiometer. The Landsat Multispectral Scanner System (MSS) and the Thematic Mapper (TM) are better simulated by a bidirectional or hemispherical–directional measurement. Some correctly refer to "conical" in place of "directional" when referring to measurements made with a hand-held radiometer (see, for example, Kimes *et al.* [13]). In most cases, the solid angle subtended by the aperture of the radiometer at the surface of interest is very small, on the order of 10^{-4} sr. In these cases, and certainly for aircraft and spacecraft sensors, "directional" is a sufficiently accurate geometrical description.

The instrument that is usually used to measure the hemispherical–directional reflectance factor is a nadir-viewing, narrow-field (1° to 15°) multiband radiometer. Held typically 1 to 5 m above the ground, it is moved across the feature of interest, and many output voltage readings are taken. These are averaged and ratioed to the output voltage reading obtained when the instrument is viewing a near-lambertian, horizontal reference panel. When data for the reflectance factor of the reference panel have been corrected for the panel's non-lambertian characteristics, the reflectance factor for the unknown surface is determined from

$$R_T(2\pi; 0, 0) = \frac{V_T}{V_R} R_R(2\pi; 0, 0) \tag{1}$$

or, if we make the approximation of neglecting irradiance due to the sky,

$$R_T(\theta_i, \phi_i; 0, 0) = \frac{V_T}{V_R} R_R(\theta_i, \phi_i; 0, 0) \tag{2}$$

where θ_i is the solar zenith angle and the radiometer's optical axis is parallel to the surface normal; V_T and V_R are the voltages from the radiometer (with the dark voltages subtracted) when the instrument is viewing the target and reference, respectively; and $R_R(\theta_i, \phi_i; 0, 0)$ is the reflectance factor of the reference panel with respect to a lambertian surface of unit reflectance.

$R_T(\theta_i, \phi_i; 0, 0)$ for some surfaces can be measured in the laboratory as well as in the field. In this sense, it is more general than $R_T(2\pi; \theta_r, \phi_r)$ because the distribution of diffuse irradiance for an outdoor measurement is difficult to simulate accurately in the laboratory. We will return to this point in the discussion of (9). Fortunately, for a near-lambertian reference panel, $R_p(2\pi; \theta_r, \phi_r)$ and $R_p(\theta_i, \phi_i; \theta_r, \phi_r)$ are very close over the range $40° < \theta_r < 60°$ especially at 50°.

The hemispherical–directional reflectance can be determined in a similar manner by using an upward-looking pyranometer, which views 2π steradians, in place of the reference panel. In this case, the multiband radiometer and the pyranometer have to be accurately calibrated in an absolute sense. The hemispherical–directional reflectance of the target is given by

$$\rho(2\pi; \theta_r, \phi_r) = \frac{L_r(\theta_r, \phi_r)}{L_i(2\pi)} \tag{3}$$

where L_r and L_i are the radiance value readouts for the multiband radiometer and the pyranometer, respectively.

The bidirectional reflectance factor $R(\theta_i, \phi_i; \theta_r, \phi_r)$ is related to the directional–hemispherical reflectance

$\rho(\theta_i, \phi_i; 2\pi)$ of a surface by

$$\rho(\theta_i, \phi_i; 2\pi) = 2\int_0^{\pi/2} R(\theta_i, \phi_i; \theta_r, \phi_r) \sin\theta_r \cos\theta_r \, d\theta_r. \quad (4)$$

Hsai and Weidner [14] have shown that the reflectance of a reference panel can be determined to an uncertainty of 0.5 percent by a numerical integration of (4) if $R(\theta_i, \phi_i; \theta_r, \phi_r)$ is measured in 10° steps form 10° to 60°. The further a surface departs from being lambertian, the greater the number of measurements that must be made.

A complete description of the reflectance properties of a surface is provided by the spectral bidirectional reflectance distribution function (BRDF) $f(\theta_i, \phi_i; \theta_r, \phi_r; \lambda)$, which relates the directional spectral radiance reflected from a surface to the directional spectral irradiance on the surface. BRDF is defined by

$$f(\theta_i, \phi_i; \theta_r, \phi_r) = \frac{dL_r(\theta_i, \phi_i; \theta_r, \phi_r)}{dE(\theta_i, \phi_i)} \quad (5)$$

and has the units of reciprocal steradians; dL_r is the radiance reflected from the surface in the direction θ_r, ϕ_r, and dE is the irradiance incident on the surface in the direction θ_i, ϕ_i. BRDF is related to the bidirectional reflectance factor by

$$R(\theta_i, \phi_i; \theta_r, \phi_r) = \pi f(\theta_i, \phi_i; \theta_r, \phi_r). \quad (6)$$

Also it can be shown that

$$\rho(\theta_i, \phi_i; 2\pi) = R(\theta_i; \phi_i; 2\pi) \quad (7)$$

and

$$\rho(2\pi; 2\pi) = R(2\pi; 2\pi). \quad (8)$$

The rest of this section deals with irradiance and surface effects on field reflectance measurements, shortcomings of instrumentation and measurements, the estimated accuracy of field reflectance measurements, and the need for the comprehensive description of measurement conditions.

B. Irradiance and Surface Effects

The measurement of the reflected flux from both the target and the reference panel is influenced by anisotropy in the hemispherical spatial distribution of irradiance due to atmospheric turbidity and clouds and changes in the solar zenith angle. Kriebel [15]–[17] examined the influence of changes in atmospheric turbidity and solar zenith angle on the radiant flux reflected by vegetated surfaces. He measured the angular distribution of the spectral reflectance of four vegetated surfaces having significantly different canopy structures and used a radiative transfer program to simulate different atmospheric conditions. His results are listed in Table 1 for a wavelength of 0.52 μm. The change in reflectance with change in solar zenith angle is almost wavelength independent whereas the dependence of reflectance on optical depth decreases with increase in wavelength.

Temporal Irradiance Changes: Duggin [11], [18] and Milton [19], [20] have disputed the importance of simultaneity of target and reflectance panel measurements. Undoubtedly, simultaneity is mandatory when clouds can modify the irradiance level between sequential target and panel readings [21]. At large solar zenith angles the ground irradiance changes rapidly with time. Simultaneity in this case is desirable but not necessary because the irradiance change is smoothly continuous and can be accounted for by averaging target measurements taken immediately before and after the panel measurement.

Table 1 Percent Change of the Reflected Radiance Due Either to a Change of the Distribution of the Irradiation by 1° of Solar Zenith Angle or by a 10 Percent Change of the Optical Depth of the Atmosphere, Averaged Over All Directions of Reflection and Over All Distributions of the Irradiation [16]

	Average Change of the Reflected Radiance	
Surface Type	per degree change of the solar zenith angle	per 10-percent change of the optical depth
Savannah	±1.0	±1.6
Bog	±0.9	±0.7
Pasture land	±1.7	±1.0
Coniferous forest	±2.3	±1.5
Average over the four surfaces	±1.5	±1.2

Irradiance fluctuations, reported by Slater [8, p. 315], of 1 to 2 percent at frequencies on the order of 1 kHz, possibly due to fast-moving subvisual cirrus clouds, would affect measurement accuracy only if the radiometer had a fast time response. Most do not. This phemonenon would nevertheless have the effect of increasing the noise in scanner imagery. Fortunately its occurence, at least in the author's experience, seems to be rare.

Non-Lambertian Surface Effects: The combined effect, on the accuracy of reflectance factor measurements, of anisotropic sky irradiance and a non-lambertian target and reference panel has been reported by Kirchner *et al.* [22] and Robinson and Biehl [23]. Their results generally agree with the analytical results of Che *et al.* [24], who modeled several different non-lambertian surfaces and used Dave's [25] haze and cloud models to yield the results listed in Table 2.

Table 2 Maximum Percentage Errors in Hemispherical–Directional Reflectance Factor Measurements for Five Non-Lambertian Surfaces Under Haze and Cloud Conditions [24]

Solar Zenith Angle	Dave Haze 1 Model, λ = 415 nm		Dave Cloud C1 Model, λ = 825 nm	
	$R = 0.05$	$R = 0.75$	$R = 0.05$	$R = 0.75$
20	2 to −1	3 to −1	3 to 0	4 to 0
70	5 to −3	4 to −2	6 to −2	5 to −1

Solar Zenith Angle Effects: The effect of solar zenith angle on reflectance or reflectance factor measurements has been investigated by several workers. Coulson and Reynolds [12] measured bihemispherical reflectance as a function of six vegetation canopies for six discrete wavelengths in the visible and near-infrared. They found that most surfaces showed a maximum bihemispherical reflectance between 70° and 80° that gradually decreased as the solar zenith angle decreased. Egbert and Ulaby [26] measured the spectral hemispherical–directional reflectance factor for many solar zenith angles and nadir and azimuth viewing angles as part of a procedure to determine the best conditions for multiband photography. Kimes *et al.* [13] found that the hemispherical–directional reflectance for lodgepole pine and two grass canopies decreased as the solar zenith angle increased, under clear conditions. In a simulation of the

conditions, they found that the bihemispherical reflectance behaved in the opposite way, in agreement with Coulson and Reynolds. The difference was explained on the basis of the anisotropic BRDF of the simulated canopy. Duggin [27] and Pinter *et al.* [28] found that the effect of solar zenith angle of the bidirectional reflectance factor of several wheat varieties at the same stage of growth depended on the variety. Jackson *et al.* [29] showed, for a single wheat variety, that the effect of solar zenith angle on hemispherical–directional reflectance factor depended on row spacing and orientation, plant height, and canopy cover. Kirchner *et al.* [30] have modeled the conditions of anisotropic BRDF and irradiance distribution to predict directional radiance for a wide range of conditions. Schnetzler [31], using data from Kirchner *et al.*, was able to predict radiance at the entrance pupil of a pointable orbital imager under a wide variety of conditions.

Excellent sources for further information on ground measurement techniques and results are the proceedings of the international colloquia entitled *Spectral Signatures of Objects in Remote Sensing*, edited by Guyot and Verbrugghe [32], [33]. Space does not permit discussion of all the material in these proceedings; the reader is referred in particular to articles by Becker, Guyot, Jackson, Ott *et al.*, Vanderbilt *et al.*, and Verhoef *et al.*

C. Instrumentation and Measurement Shortcomings

Field reflectance measurements are used most extensively in studies of changes in conditions of surface features. In this case, only relative reflectance values are usually required; instrumentation deficiencies, anisotropic irradiance conditions, etc., generally introduce negligible errors in the results. Field reflectance measurements are sometimes compared with laboratory reflectance data or used, as discussed later, as part of the input to a method for determining the in-flight absolute radiometric calibration of sensor systems. In these two cases, and in the verification and use of scene radiation models, accurate absolute reflectance data are usually required.

Robinson and coworkers [7], [23], [34], Collins [35], and Deering and Leone [36] in this country, Ahern *et al.* [37] in Canada, and Bunnik *et al.* [38] in The Netherlands have developed new instruments and advanced the techniques of accurate, convenient, and reliable field reflectance measurements. Their publications should be referred to for descriptions of instrumentation design and of operation and measurement methodology. The following discussion emphasizes some of the problems related to instrumentation and measurement shortcomings.

Avoidance of Effects Due to Sky Anisotropy: To compare field reflectance factor data with laboratory reflectance factor data or to minimize anisotropic sky irradiance effects, a simple approach is to take radiometer voltage readings of the target and reference surfaces when both are globally irradiated and then when both are shaded from direct solar irradiance. If we refer to the target and reference global voltage values as V_{TG} and V_{RG} and the target and reference shaded values as V_{TS} and V_{RS}, then the bidirectional reflectance factor can be obtained from

$$R(\theta_i, \phi_i; 0, 0) = \frac{V_{TG} - V_{TS}}{V_{RG} - V_{RS}} \times R_R(\theta_i, \phi_i; 0, 0) \qquad (9)$$

where $R_R(\theta_i, \phi_i; 0, 0)$ is the reflectance factor of the reference panel with respect to a lambertian surface of unit reflectance. Equation (9) is then a more accurate form of (2).

Che *et al.* [24] used several panels whose reflectance factors were measured in the laboratory and then in the field. The field measurements were made by using global irradiance (sun and hemispherical sky) in conjunction with (1), and then by shading the target and reference panel and using (9). Fig. 1 shows the measurement errors relative to the laboratory measurements. The results show that, for a reflectance factor of about 0.09, the error can be as high as 10 percent but can be reduced to 4 percent by using the shading method. The error shows an increase with solar zenith angle and a decrease with increasing reflectance. The residual error, when (9) is used, is dependent on the geometry of the measurement and the prevailing atmospheric conditions. For example, when the atmospheric aerosol loading increases, the solar aureole increases in size and radiance at the expense of the direct solar irradiance on the ground. The geometry of field measurements under these conditions will differ from a bidirectional laboratory measurement, and the difference between the results is likely to be greater than under low aerosol loading conditions.

These experimental results of Che *et al.* are not in agreement with the predictions of Bauer *et al.* [39], who estimated the measurement uncertainties under conditions of moderate and of very noticeable haze. Admittedly, the haze conditions differed and the assumptions made by Bauer *et al.* regarding typical BRDF values and the uncertainties associated with field measurements may not have applied. Nevertheless, it is not obvious that these differences can

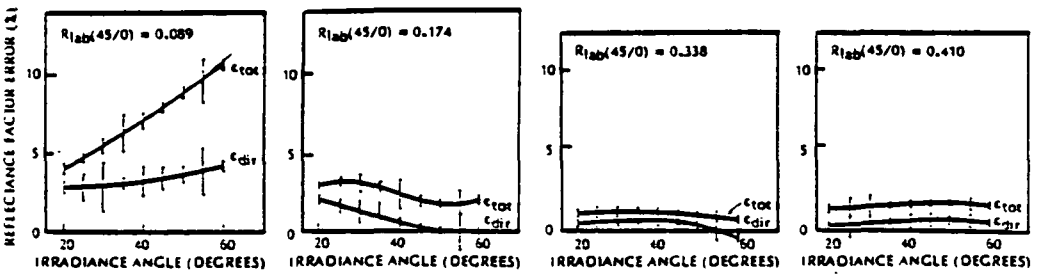

Fig. 1. Percentage error in reflectance factor measurements (from Che *et al.* [24]). Note that the bidirectional reflectance factor measured in the laboratory at 45° irradiance angle and 0° viewing angle was used as the reference.

explain the disagreement. A study should be undertaken to reconcile the differences.

Proximity of Nearby Objects: Duggin [18] has pointed out the need to prevent secondary reflectances from falling onto the measurement areas and to ensure that the upward-looking pyranometer, for measuring global flux, is perfectly horizontal to minimize the integration of flux from reflecting surfaces below the horizon. This last point is, of course, also important in the use of a reference panel.

Kimes *et al.* [40] have investigated the effect of a nearby object on reflectance factor data as a function of the solid angle subtended by the object at the surface to be measured and as a function of the reflectance of the object and solar zenith angle. Both the object and surface were assumed lambertian with the object on the opposite side of the surface from the sun. Dave's [25] clear-sky atmospheric model was used for the calculations. The results, giving the percentage error in the spectral radiance of the surface due to the proximity of the object, are shown in Fig. 2. The

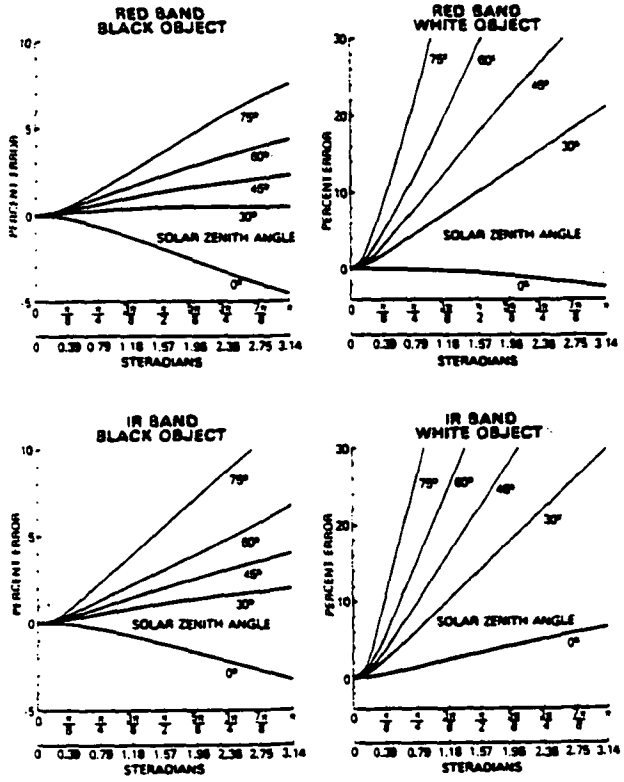

Fig. 2. Simulated percent error of radiance measurement due to the presence of a nearby object (opposite the sun's direction) as a function of solar zenith angle, wavelengths of 0.675 and 0.796 μm, black or white objects, and the solid angle intercepted by the object [40].

errors increase with increase in solar zenith angle and solid angle. The results show that a person in white clothing kneeling 0.5 m from the surface being measured causes an error of 18 percent for a wavelength of about 0.8 μm and a solar zenith angle of 75°. But if the person wears black clothing, the error is less than 2 percent for all solar zenith angles. The error is strongly dependent on the solid angle. So, when making field reflectance measurements, the recommendation is to wear dark clothing and stay away from the surfaces while they are being measured.

Difference Between Actual and Nominal Fields of View: An insidious problem, with at least one multiband radiometer on the market, is that its field of view, when set to be 1° for TM band 5, extends well beyond the nominal field. Che *et al.* [24] measured the field of view and found, for example, that normalized to unity for 0° the response was as high as 0.7 at 2° off-axis. They estimated that, under hazy conditions (a diffuse to direct irradiance ratio of 0.4) and with a surround four times the reflectance of the target, the error in the reflectance factor due to the high out-of-field response would be as high as 20 percent.

Surround Effect on Irradiance: Another insidious problem, related to the above, is the effect of the reflectance of the area surrounding the surface being measured. Che *et al.* [24] observed this effect when determining the ratio of the diffuse to direct irradiance on panels placed at the centers of two 100-acre fields, one of bare soil and the other of wheat. Fig. 3 shows how some of the upward radiance from the surround can be scattered by the atmosphere to be

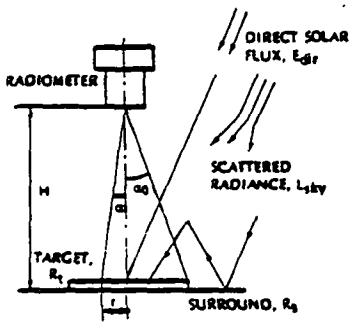

Fig. 3. Measurement geometry with a field spectroradiometer [24].

Table 3 Average Hemispherical–Directional Reflectance Factors for Wheat and Bare Soil [24]

Band No.	Wavelength (nm)	Wheat	Soil
1	450–520	0.019	0.058
2	520–600	0.028	0.083
3	630–690	0.017	0.120
4	760–900	0.495	0.181

incident on the panel being measured. From Table 3, which lists the hemispherical–directional reflectance factors for the two fields for the first four bands of the TM, we can predict that the ratio of diffuse-to-direct irradiance will increase more for the bare soil than for the wheat field with increasing wavelength for the first three TM bands. However, for band 4 the ratio should be greater in the wheat field than in the bare soil field owing to the higher reflectance factor for wheat in the IR spectral region. This prediction is confirmed by the results of the field measurements as shown in Fig. 4. Note that these results also include the out-of-field effect mentioned earlier.

Calibration of Reflectance Factor of Reference Panel: Many investigators calibrate their field reference panels with reference to $BaSO_4$ or Halon powde: pressed according to specifications suggested by the NBS. Some technique descriptions in the literature imply that the authors have

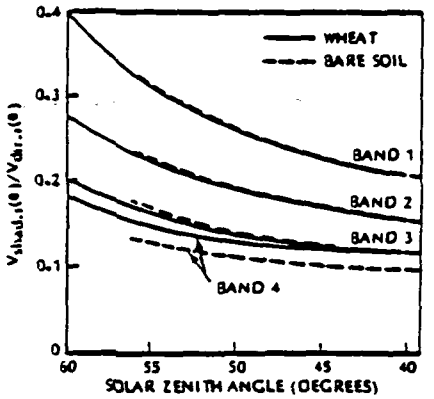

Fig. 4. Effect of the surround in the measurement of the ratio of atmospherically scattered flux to direct solar flux [24].

assumed these pressed powder surfaces to be lambertian and that the directional–hemispherical reflectance has been used in calculating the reflectance factor of the reference surface. A substantial error is incurred if these assumptions are made, as can be seen by reference to Table 4.

Table 4 Values for the Bidirectional Reflectance Factor $R(\theta_i, \phi_i; 0, 0)$ for Halon. Δ is the Difference Between the Quantity Immediately Above and Value of the Directional–Hemispherical Reflectance $\rho(0, 0; 2\pi)$ for Halon

	Angle, θ_i (degrees)						
	10	20	30	40	50	60	70
$R(\theta_i, \phi_i; 0, 0)$	1.135	1.087	1.052	1.021	1.007	0.985	0.960
Δ, percent	14.5	9.7	6.2	3.0	1.6	−0.6	−3.2

Temperature Effects on Radiometer Response: The change in detector response with temperature, particularly in the 1- to 5-μm range, is often a problem. Jackson and Robinson [41] have shown that, although the response of four silicon detectors in a multiband radiometer was nearly independent of temperature, the output from three PbS detectors, in the 1- to 2.5-μm range, decreased linearly with increasing detector temperature at a rate of 4 to 5 percent per kelvin. For a 1 K change in the temperature of a silicon detector, the change in its response was less than 0.25 percent, whereas the change in the response of a PbS detector was 2.5 percent. Jackson and Robinson derived a correction factor that can be used if the detector temperature is known at the time of the measurement.

D. Estimated Accuracy of Field Reflectance Measurements

Bearing in mind the measurement problems described above, the question is: how accurately can we measure the reflectance factor of a surface? The uncertainty in absolute reflectance measurement at the NBS is 0.15 percent. Transferred to a secondary standard or by reference to pressed $BaSO_4$ or Halon powder, the uncertainty is probably 0.5 percent. The calibration of a reference panel with respect to the secondary standard should be within an uncertainty of 1 percent , particularly for near-normal reflectances. Probably 1.5 percent is the lowest uncertainty we can expect to achieve in field reflectance factor measurements. This high accuracy may be achievable only in the measurement of extended flat surfaces with reflectances greater than 0.3 and for small solar zenith angles and a clear and stable atmosphere. The radiometer design to achieve this accuracy should have an extremely well defined field of view and an accurately known departure from linearity. In an effort to improve the precision of field reflectance measurements, the technique described earlier of ratioing direct solar irradiance measurements should be studied further. This method provides the bidirectional reflectance factor of the surface of interest. However, it should be remembered that although the ground irradiance in the case of remotely sensed data collected by aircraft or satellite sensors is mainly directional, there is a hemispherical component that increases with increasing solar zenith angle, ground reflectance, and aerosol loading and with decreasing wavelength. Because of the many factors that influence hemispherical irradiance, it is difficult to relate measurements of $R(2\pi; \theta_r, \phi_r)$ to those of $R(\theta_i, \phi_i; \theta_r, \phi_r)$.

E. Description of Measurement Conditions

The amount of spectral hemispherical–directional or bidirectional reflectance factor data characterizing many different earth-surface features is growing rapidly. Unfortunately, some of these data, particularly some of those collected 10 years ago or earlier, cannot be used reliably because the measurement conditions were not well specified. Accurate and complete documentation of the instrumentation, measurement technique, and measurement conditions is mandatory for the data to be transportable. Those working at the Laboratory for Applications of Remote Sensing (LARS) at Purdue University suggest the following information should accompany reflectance data for crops: air temperature, relative humidity, wind speed and direction, field of view of the spectroradiometer, view angle, latitude, longitude, cloud cover, day of year, time of day (in Coordinated Universal Time), crop species and maturity, row width, leaves per plant, row direction, surface conditions, soil moisture content, leaf area index, and plants per row. In addition, for the reasons mentioned earlier, the irradiance conditions should be described as completely as possible. Ideally this could be done by making 1) spectral measurements of the diffuse to direct ratio of irradiance at the ground, 2) an all-sky scan to determine the spectral radiance anisotropy of the sky, and 3) a measurement of the spectral optical depth. Because a rough estimate of the first two quantities can be made from a knowledge of the spectral optical depth and with the use of an atmospheric radiative transfer program, it is possible that a measurement of the spectral optical depth may suffice.

Finally, the reliability of field reflectance factor data would gain credibility if the method and frequency of calibration of the reference panel were known. Unfortunately, field conditions can cause a rapid reduction in the reflectance of spray-painted $BaSO_4$ panels. In this respect the development by Butner *et al.* [42] of washable painted Halon panels is noteworthy.

III. Atmospheric Correction

There was a flurry of activity in atmospheric correction in the first year of the Landsat program and during the Skylab program, much of which has been reviewed by Slater [8, pp. 288–317]. The activity was caused by concern regarding the magnitude of atmospheric path radiance, that is, atmo-

spherically scattered light that is added to the radiance of the scene. A large component of the path radiance contains no information concerning the scene. An example of its magnitude is that, under clear atmospheric conditions, at a wavelength of 0.55 μm and for a ground reflectance of 0.1, the atmospheric path radiance at the entrance pupil of a satellite sensor is as large as that due to the radiance from the ground.

During the past 10 years, except for a few investigations related to the use of models, little work has been done on atmospheric correction until recently. This can be attributed to the emphasis in the 1970s on the statistical analysis of image data, which did not necessitate correction for the atmosphere, and to the lack of accuracy of the results of those early investigations. The latter was due mainly to three reasons: 1) The atmospheric models were inadequate. For example, they did not account for the multiple scattering and/or the adjacency effect (see later). 2) Because of the difficulty of completely characterizing the atmosphere, the investigator was forced to make many assumptions, which introduced large uncertainties into the result. 3) There was no convenient way to check the accuracy of the results or use them because of the large uncertainty in the in-flight absolute radiometric calibration of the aircraft and spacecraft sensors involved.

A. Correction Methods

Some different attempts to correct for or allow for the atmosphere have been described by Ahern *et al.* [43], Aranuvachapun and LeBlond [44], Dana [45], Doak *et al.* [46], Dozier and Frew [47], Holyer [48], Kowalik *et al.* [49], Kriebel [50], Lyon *et al.* [51], Munday [52], Otterman and Fraser [53], Price [54], Richardson [55], and Watson and Hummer-Miller [56]. Most of these papers are recent and are related to the use of models for analyzing satellite-acquired image data. Among other methods currently in use are the following:

Gordon *et al.* [57] have described a method for the atmospheric correction of Coastal Zone Color Scanner data. Their method uses a Monte Carlo atmospheric radiative transfer model and an algorithm that includes a ratio of the aerosol optical depth at wavelengths of 520 and 550 nm to that at 670 nm, where the reflectance of the ocean is assumed zero. As Aranuvachapun [58] points out, the accuracy of the algorithm relies mainly on the accuracy of this ratio, which is currently not measured by satellite remote sensing. The uncertainty of the method in determining pigment concentration is stated to be 30 to 40 percent over the concentration range 0.08 to 1.5 mg $\cdot$ m^{-3}. In three direct comparisons between ship-measured and satellite-determined values of the water radiance, Gordon *et al.* claim that the atmospheric correction algorithm had an average error of 10 to 15 percent. The method does not require any surface measurements at the time of the satellite overpass.

Castle *et al.* [59] and Kastner and Slater [60] have described a method making use of ground-based measurements at White Sands, NM, to determine the in-flight absolute radiometric calibration of the Landsat Thematic Mapper. The method uses the same type of atmospheric data and radiative transfer code that are needed to provide the atmospheric correction of satellite-sensor acquired data. The determination of the hemispherical–directional reflectance factor of an extended, homogeneous surface feature also depends on a knowledge of the exo-atmospheric solar irradiance [61], the radiance at, and therefore the absolute radiometric calibration of, the sensor, and the angle of incidence of the direct solar flux at the surface. The limitations of the method are that, although it has a low uncertainty (about ± 3 percent), its accuracy may be compromised by the adjacency effect and the difficulty in accounting for the non-lambertian characteristics of an inhomogeneous surround. Analyses of the adjacency effect are referred to in the next section.

Table 5 is an extract of Kastner's [62] preliminary results, which are relevant to atmospheric correction, of a sensitivity analysis of the method for the absolute radiometric calibration of the Landsat TM over White Sands, NM.

Table 5 Results of Sensitivity Analysis for an Atmospheric Correction Method that Uses Ground-Based Atmospheric Measurements [62] (Note that L is the total radiance at the sensor.)

Particle size distribution.	Change in the exponential value, ν, in the Junge particle size distribution from 2.5 to 4 corresponds to a ΔL of 5 to 10 percent, depending on wavelength, in the 2- to 0.45-μm range. The inversion of spectral optical thickness, to provide a known ν value, can reduce this ΔL range by an order of magnitude.
Mie extinction optical thickness.	Under good measurement conditions, reduced Langley plot data can provide τ_{Mie} with an uncertainty such that L can be determined to within 1 percent.
Refractive index.	Calculations show that changing refractive index from 1.5 to $1.5 - 0.01i$ changes L by < 1 percent. The uncertainty in L associated with assuming this value is estimated to be 2 to 5 percent, based on measured index variations at different locations worldwide.
Water vapor.	With τ_{H_2O} measured across a band with a solar radiometer, the uncertainty in L is < 1 percent.
Surround reflectance.	Changing the surface reflectance from 0.35 to 0.7, which surrounds an infinitesimal target of reflectance 0.7, changes L by 2 percent. A Monte Carlo code is needed to determine the adjacency effect introduced by any given surface spatial distribution of radiances.
Ground reflectance.	For a high-reflectance (> 0.5) target such as White Sands, a given uncertainty in ground reflectance gives rise to an equal uncertainty in L. A departure from lambertian characteristics of 5 percent gives rise to a change in L of 1 percent.
Polarization.	Studies [63], [64] need to be extended to determine the influence of scene and atmospheric polarization effects. The polarization introduced by the sensor itself needs to be known from preflight measurements.
Aerosol vertical distribution; ozone; pressure; time.	The aerosol vertical distribution can be assumed, and the other quantities can be determined with sufficient accuracy that their effect on L is negligible.

B. The Adjacency Effect

The adjacency effect, first analyzed by Pearce [65] using a Monte Carlo method and later by Dave [66], describes the influence of atmospheric crosstalk in modifying the radiances of adjacent fields of different radiances. Pearce showed that the effect can extend over large distances. For example, if the TM were to image two semi-infinite planes of reflectances 0.5 and 0.1 at a wavelength of 0.55 μm under normal atmospheric conditions, the radiance of the lower reflectance area, 1 km from the edge, would appear to be

10 percent more than its asymptotic value. Kaufman [67] has recently described the atmospheric effect on the spatial resolution of surface imagery.

Methods for compensating for the adjacency effect have recently been described by Tanre *et al.* [68] and Kaufman and Fraser [69]. Three experiments have been conducted in attempts to verify the adjacency effect. Mekler *et al.* [70] made a laboratory simulation of the atmosphere by suspending latex spheres in water. The measured effect was found to be 20 percent larger than what had been predicted by Pearce [65]. Kaufman *et al.* [71] flew an aircraft in hazy conditions (aerosol optical depth approximately 1.0 at 510 nm) and demonstrated the existence of the effect at a wavelength of 773 nm where the reflectance difference between water and vegetation was high. Dyche [72] showed in a very clear atmosphere (total optical depth 0.3 at 440 nm) that the effect may exist but at a level that is difficult to detect under such good conditions.

Methods for the on-board determination of atmospheric correction factors, which make use of multiple ground views from a pointable sensor, have been suggested by Diner and Martonchik [73] and Slater and Martinek [74]. These suggestions are preliminary and require further development and testing.

IV. Sensor System Calibration

A. Classification of Procedures

Some of the most commonly used procedures for calibrating remote sensing systems are referred to in Fig. 5. The two major divisions in the figure are between relative and absolute calibration and between the static macro-image response and the dynamic micro-image response of the system. This section deals with the absolute calibration of remote sensing systems, and in this context only the static macro-image response will be considered, as is usually the case. In Section V of this paper we will return briefly to the subject of the effect of sensor micro-image response on radiometric fidelity.

The procedures for the absolute calibration of a remote sensing system fall into the three categories shown in the bottom right of Fig. 5. These are described in more detail below.

System Calibration, Preflight Only: In the first category, the absolute calibration of the system is made only before launch; in flight, the calibration is checked by irradiating the focal plane with a radiometrically calibrated source and optical system. The drawback to this procedure is that any change in the transmission of the image-forming optics of the sensor system, caused by the condensation of outgassed contaminants, for example, will be undetected. Furthermore, the on-board calibration system is assumed to be stable through launch and to be unaffected by the vacuum, high-energy-particle irradiation, and zero-g environment at orbital altitudes—an assumption that can lead to error.

The TM and the MSS on Landsat-4/5 are examples of remote sensing systems calibrated only in this manner. Barker *et al.* [75] have estimated the preflight absolute radiometric calibration of the TM to be about ± 10 percent. Norwood and Lansing [76] state that it is no better than ± 6.8 percent. Dinguirard and Maisonneuve [77] have estimated the absolute radiometric calibration of the SPOT/HRVs to be ± 10 percent. The calibration methods employed for TM and SPOT/HRV and their shortcomings have been described in detail by Slater [78].

Laboratory calibrations, in the solar reflected spectral region, are made typically by reference to an integrating sphere that in turn is calibrated against a secondary source traceable to an irradiance scale at a national standards laboratory. In the case of the TM, the irradiance scale at the NBS was transferred successively to a primary lamp, a secondary lamp, an integrating sphere, the TM focal plane, and the TM internal calibrator. The precision with which this transfer was done is illustrated in Fig. 6. Starting with the primary lamp, Barker and coworkers [75] estimated the

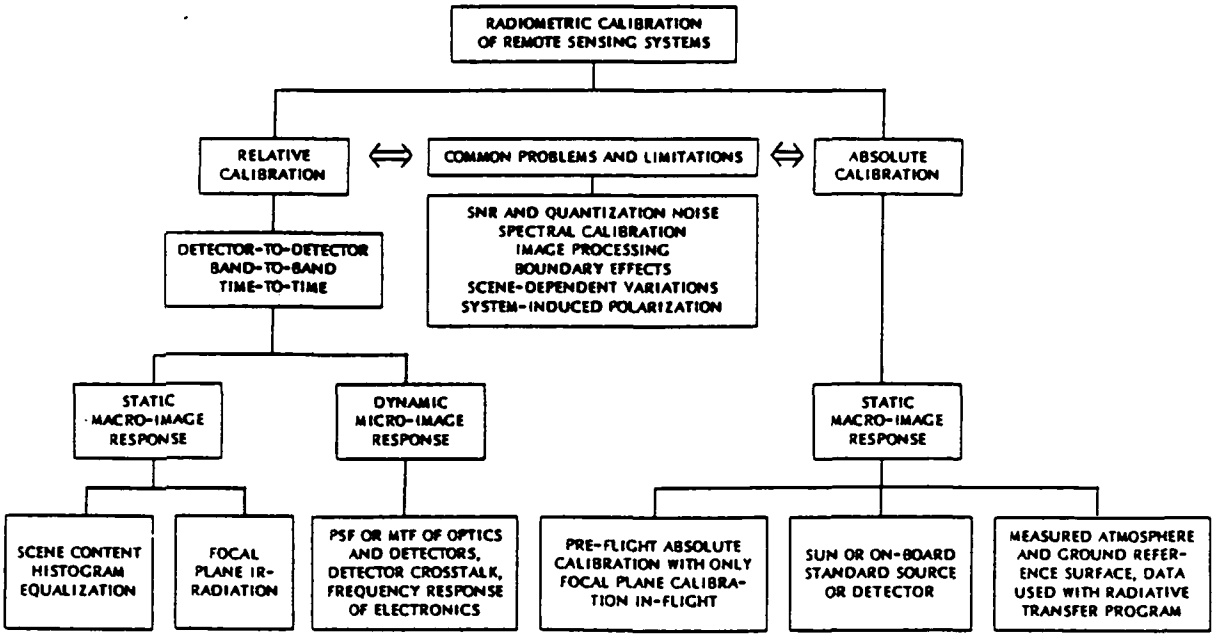

Fig. 5. Classification of radiometric calibration procedures [60].

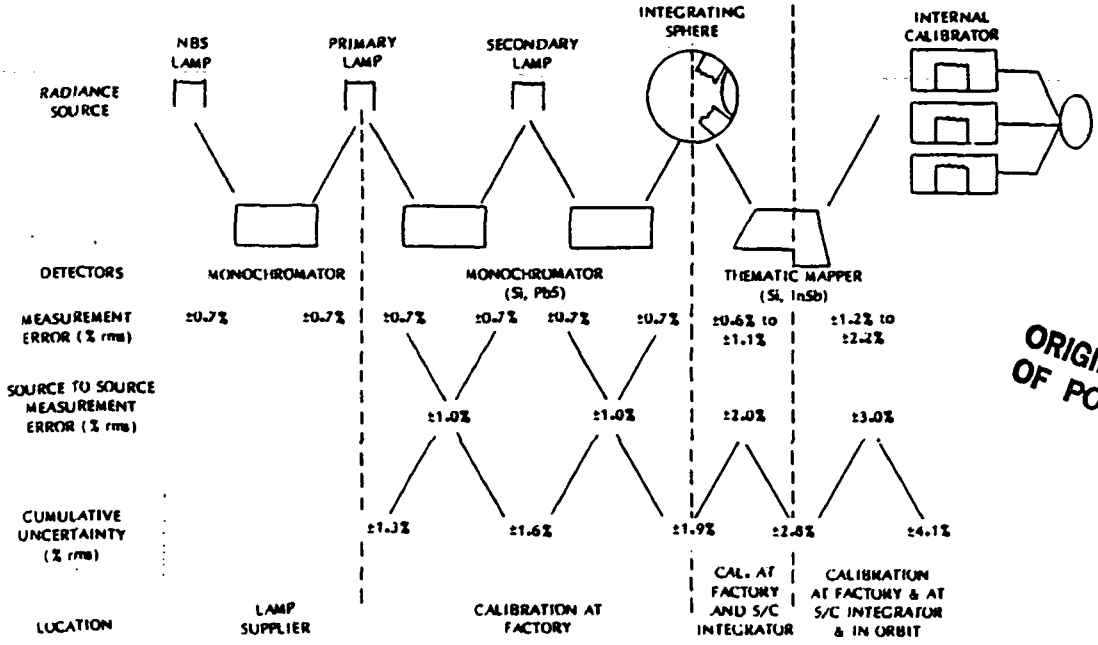

Fig. 6. Precision of transfer of irradiance scale [75].

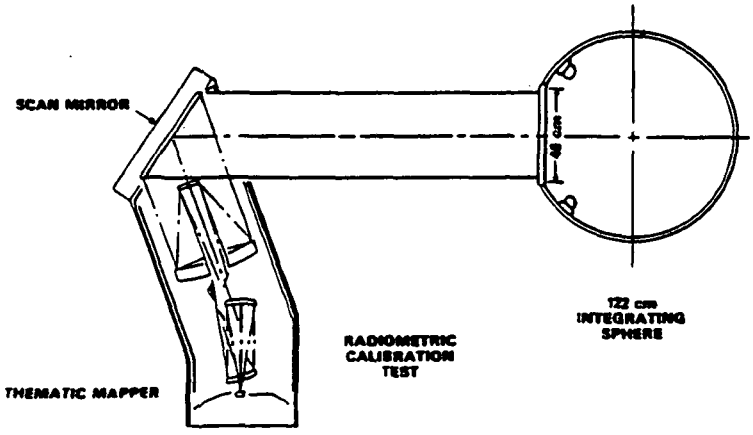

Fig. 7. Arrangement for TM calibration [75].

uncertainties associated with the respective transfers to be 1.3, 1.0, 1.0, 2.0, and 3.0 percent. The root sum of the squares (RSS) of these uncertainties is ±4.1 percent; we emphasize, however, that this is an estimation of the uncertainty in the precision, not of the absolute accuracy of the calibration of the TM internal calibrator. Barker and coworkers report that two different measurement techniques used to calibrate the sphere gave results that differed inexplicably, usually by 2 to 3 percent but at some wavelengths by as much as 7 to 8 percent. These differences coupled with the uncertainty in the knowledge of the NBS irradiance scale (which averages 1.2 percent over the wavelength range 450 to 2500 nm) led Barker and coworkers to estimate an uncertainty in the absolute calibration of the TM internal calibrator at no less than ±6 percent and conservatively at ±10 percent.

The layout of the arrangement used for the calibration of the TM is shown in Fig. 7. A 1.22-m-diameter sphere was required in order to obtain a sufficiently uniform response over the 0.41-m-diameter entrance pupil of the TM. A similar calibration has been done for the SPOT/HRVs using an integrating sphere calibrated by W. A. Hovis of NOAA.

In-Flight Calibration Using the Sun or an On-Board Source: In the second category, the sun or an on-board calibrated source is used to irradiate the focal plane through the image-forming optics. The drawbacks to this approach are the uncertainty in the knowledge of a) the irradiance of the sun above the atmosphere and b) the output of the calibrated source system, for the reasons mentioned earlier. Furthermore, in examples of the use of this procedure (MSSs 1, 2, and 3 and SPOT), the calibration beam passes through only a small portion of the aperture of the system, thus not simulating the actual operation of the system. When imaging the ground, the system entrance aperture is irradiated over its entire area by flux incident over a roughly 3-sr solid angle. In the imaging mode, much more stray light is present in the system and incident on the focal plane. If this additional flux level is unknown, it introduces a substantial uncertainty into the absolute calibration of the system.

In 1972 the sun calibrator system on the Landsat I MSS, which was intended to provide absolute calibration, exhibited a remarkable change in its response. After 21 orbits, the 0.5- to 0.6-μm band calibration had decayed to 7 percent of its preflight value [79]. The other bands showed pronounced but smaller changes. Although Horan *et al.* [79] hypothesized that this was due largely to an unusual amount of contamination occurring in preflight tests, the sun calibrator system has not been used on any of the Landsat MSSs since [80].

In-Flight Calibration with Respect to a Ground Surface: In the third category of absolute calibration, reference is made in flight to a ground area of known spectral radiance. If the atmospheric conditions are measured at the time the sensor system is imaging the known area, these data can be used with an atmospheric radiative transfer program to predict the spectral radiance at the entrance pupil of the sensor. The main uncertainty in this approach is that of determining the refractive index and radial size distribution of atmospheric aerosols well enough. The approach is also limited to scenes having large, uniform areas of high radiance. For example, although many bodies of water are of sufficient size and uniformity, they are not appropriate for calibration purposes because their radiance is too low to provide a calibration of sufficient accuracy or to cover much of the dynamic range of the sensor. Fortunately, some suitable areas do exist, particularly in the arid regions of the world, for example at White Sands, NM. References [59], [60], and [62] describe the method in detail, and the results of a sensitivity analysis of the method are listed in Table 5.

B. Detector-Based Radiometric Calibration

The recent work at the NBS on self-calibrated photodiodes is described only briefly here. For more details about this important advance in radiometric calibration the interested reader is referred to [81]–[84].

The photodiode may be calibrated by either of two differently applied biasing procedures, depending on the wavelength region of interest. At short wavelengths, a negative bias can be applied to remove the recombination centers at the $Si–SiO_2$ interface at the front of the detector. To do this, a temporary contact can be made with the front surface using an electrode immersed in a conducting liquid, or the surface can be exposed to a corona discharge. Recently, an inversion layer photodiode has been developed that obviates the need for a negative front bias [85]. For long wavelengths, a back bias is applied to extend the depletion region to a depth beyond which incident flux penetrates. The experimental procedure is to irradiate the detector with a constant monochromatic flux level and to increase the bias voltage until further increase no longer gives rise to an increase in output signal. For both the short- and the long-wavelength ranges, the internal quantum efficiency saturates at a value extremely close to unity, as shown in Fig. 8. Thus the maximum increase in signal output obtained as a result of biasing can be used to determine the internal quantum efficiency of the detector without biasing, as it will be used in practice.

The external quantum efficiency of the photodiode differs from the internal quantum efficiency owing to reflection losses. These can be reduced to insignificance by making use of four photodiodes according to the geometry

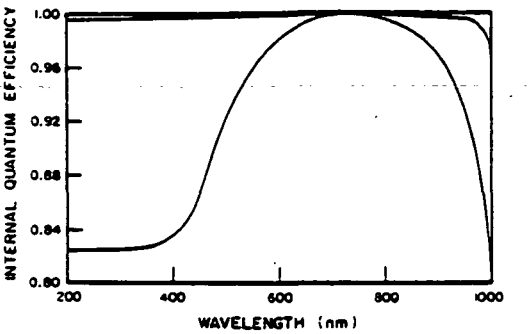

Fig. 8. Typical photodiode internal quantum efficiency without biasing (lower curve) and with biasing (upper curve) [83].

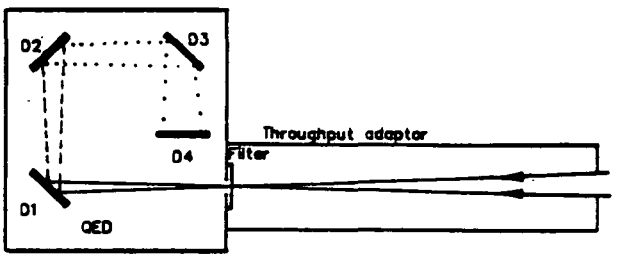

Fig. 9. A four-diode arrangement to minimize specular reflection losses [88].

sketched in Fig. 9. The output signals from the four diodes are summed to provide the signal corresponding to a black detector of overall quantum efficiency that can be assumed to be unity. The second and third diodes specularly reflect the specular reflection from diode 1 to diode 4, which reflects the light back to diodes 3, 2, and 1. The incident flux thereby undergoes seven reflections before leaving the system, and if each reflectance is 10 percent, the final specularly reflected flux is down to 10^{-7} of the initial incident flux level. The diffuse reflectance loss for a clean detector is less than 10^{-3}. The QED four-photodiode package manufactured by United Detector Technology has been specially designed as a unity quantum efficiency detector.

The discussion at the end of this section refers to the use of such a detector for the spectroradiometric calibration of a multispectral imaging sensor. However, as shown in Fig. 8, the unbiased quantum efficiency is wavelength dependent. Because of possible changes in the passband position of spectral filters during space flights of long duration, it may be advisable to use the unity quantum efficiency detector to calibrate a spectrally flat, electrically calibrated pyroelectric radiometer at the 0.1- to 0.2-percent level, and for that to be used for the in-orbit calibration.

Hughes [86] shows that photodiode self-calibration using filtered tungsten radiation, in place of laser radiation, can provide an absolute spectral response scale from 0.4 to 0.8 μm with an uncertainty of less than ±1 percent. The filters used in this work were roughly of 10-nm half-width, which is about a factor of 10 less than those of the MSS and TM. The possibility of extending this filter approach or a monochromator approach to provide a means to calibrate field and flight spectroradiometer instrumentation with an uncertainty in absolute accuracy on the order of ±1 percent appears then to be close to reality [87], [88].

An important requirement for broad-band absolute radiometric calibration is the use of a spectral response normalization procedure that is as nearly independent of the source function as possible. (The source function in the cases considered in this review is the spectral distribution of the sun, the calibration lamp, or the radiance of the scene used as reference.) Fortunately, Palmer and Tomasko [89] have developed a moments normalization method that gives exact results if the source function is quadratic and results that are superior to those of other methods for nonquadratic continuous source functions. Their method has the additional advantage over other normalization procedures of determining both the height of the rectangular function equivalent to the given spectral response and also the wavelength limits. Palmer [90] has applied this moments normalization procedure to specify the effective bandwidths of the Landsat 4 and 5 TMs and MSSs, and Castle *et al.* [59] have used it in their data reduction for TM calibration.

Calibration in the Laboratory and in Orbit: Similar concepts have been proposed [60] for sensor calibration in the laboratory and in orbit. The main difference between them is that an artificial source is used in the laboratory and the sun is used in orbit—simply a matter of convenience and stability in the laboratory case and of convenience and reliability in the latter case. In the laboratory, redundancy is not at a premium and our requirements for a source are simply power, spectral flatness, and stability. We do not need a standard source although an array of standard NBS FEL tungsten halogen lamps could be used. A xenon arc stabilized for minimum arc wander and with a highly stable power supply and a feedback loop would suffice.

The source would be used to irradiate a near-lambertian, near-unit-reflectance, white-surfaced panel perhaps 1 m by 0.5 m in size in front of the system. (An integrating sphere could be used, but it would have to be very large and therefore very inefficient, and uniformity checks can sometimes themselves introduce nonuniformities.) A calibrated radiometer whose area–solid angle product and spectral response are well defined and accurately measured would be used to determine the radiance of the panel in each wavelength band of the sensor. The sensor would image the panel out of focus, but since it is an extended object, its image would have exactly the same irradiance in or out of focus. The arrangement is sketched in Fig. 10.

To avoid problems due to the nonuniform irradiation of the panel, the sensor should be rotated to sequentially irradiate the focal plane with the image of the same small area that is sampled by the radiometer. The reason for a large panel is to simulate the viewing conditions from space

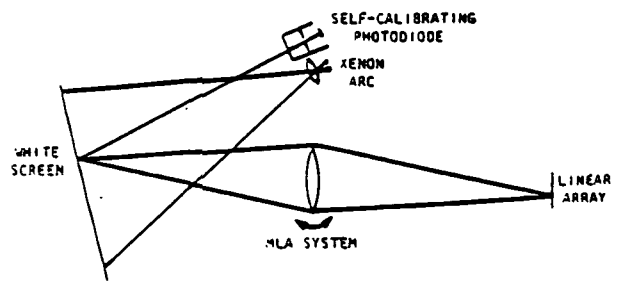

Fig. 10. Factory procedure for absolute spectroradiometric calibration [60].

in which, depending on the baffle design, significant out-of-the-field-of-view stray light could be incident on the image plane to modify the calibration. For this reason it would be worthwhile to conduct at least one calibration using a white panel several meters in diameter. To check for linearity of response, several different irradiance levels on the panel should be used. The irradiance level can be changed conveniently by inserting heat-resistant neutral density filters in front of the stabilized xenon arc source.

If the sensor uses spectral filters to define spectral bands, the wavelength profiles of the spectral filters should be measured by a spectrophotometer using the same *F*-number beam as that for the sensor. If the filters are integral with the array, they should be measured using a double monochromator, again with the sensor *F*-number, before installation in the focal plane. If the sensor is an imaging spectrometer, the wavelength calibration can be made by reference to spectral line sources or sharp cutting spectral filters. For both types of sensor, care should be taken to cover the whole wavelength sensitivity range of the detectors, the off-band suppression being particularly important for detectors with the wide spectral response of silicon.

The procedure proposed here for in-flight calibration is similar to the panel method sketched in Fig. 10, but it uses the sun as the source. The irradiance over the panel will be uniform and known spectrally to better than 1 percent. (Several solar measurement programs are currently being conducted with this accuracy as a goal.) The calibration would be carried out in the few minutes while the spacecraft is sun-illuminated but before it images the sun-illuminated earth. The absolute radiometer containing a self-calibrated detector or an electrically calibrated pyroelectric radiometer would now be needed only to check for any deterioration in the reflectance of the panel owing to exposure to the space environment and short exposures to unattenuated UV and other high-energy radiation from the sun and from space. In this last respect, the panel would usually be stowed in a well-shielded compartment and exposed only during actual calibration checks. Also, when deployed, it would not interfere with normal operation of the system. If a pointing and/or stereo mirror were used, the panel would be viewed in an extreme position of the mirror(s). In this respect it is fail-safe. Keene [91] has determined that the uncertainty of such a calibration procedure could be as low as 1.4 percent.

V. Radiometric Errors in Image Data Collection and Processing

The dynamic micro-image response of remote sensing imaging systems and the radiometric effects of digital image processing are of importance in any pixel-by-pixel analysis procedure. As was indicated in Fig. 5, the dynamic image response includes 1) the system modulation transfer function (MTF), which includes those MTFs due to the imaging optics, the effective size of the detectors, and image smear; 2) the signal-to-noise ratio of the imagery; 3) the electrical frequency response of the system; and 4) aliasing.

A. Radiometric Errors Introduced in Image Data Collection

Several general investigations have been made into this topic, notably a discussion by Norwood [92] on the influence of MTF on the errors in radiance measurements of

different sized ground features, a recent paper by Landgrebe and Malaret [93] on the effects of system noise and the atmosphere on the probability of classification error, and the long-awaited definitive analysis by Park and Schowengerdt [94] on the MTF of sampled imaging systems that accounts for each step in the process of image formation, detection, sampling, and reconstruction. Each of these three references uses the Landsat MSS or TM as an example. In addition, for more detailed system-specific investigations, the reader is referred to a special issue of the IEEE TRANSACTIONS ON GEOSCIENCE AND REMOTE SENSING edited by Salomonson [95], in particular the papers by Anuta *et al.*, Bernstein *et al.*, Markham, and Wrigley *et al.* These refer to analyses of the MSS or TM on Landsat 4 as part of the Landsat image data quality assessment program. A summary of these papers has been compiled by Schueler and Salomonson [96]. The spectral response of sensors has been examined by Markham and Barker [97] and Slater [98], who show that spectrally dependent striping can occur for systems like the MSS due to small departures in the spectral responses of channels within a band.

B. Radiometric Errors Due to Resampling

Analysts who use digital imagery from aircraft or satellite-borne multispectral imaging systems generally purchase it in the processed form, that is, after the image has been radiometrically corrected for striping and resampled to provide systematic distortion correction and registration between spectral bands, or to a specified map projection. For the past 10 years, a cubic convolution method due to Rifman and McKinnon [99] has been used for the resampling of Landsat imagery. Park and Schowengerdt [100] showed that a parametric implementation of cubic convolution is generally superior and can be optimized to the frequency content of the image. In later papers, Schowengerdt *et al.* [101], [102] compared the radiometric errors introduced for different values of the parameter α, the slope of the cubic function at its first crossing. Fig. 11 shows the mean square radiometric error due to sampling and reconstruction as a function of α for digitized aerial photographs and Landsat MSS data. The improvement in choosing $\alpha = -0.5$ instead of the usual $\alpha = -1$ is between 1 and 3 percent, and in all cases the error associated with $\alpha = -0.5$ or -1 is less than that for bilinear reconstruction. Note that the errors are larger for the higher frequency content digitized imagery than for the Landsat MSS imagery, and that in general any resampling error will be worst in the vicinity of image edges.

VI. CONCLUSION

An important aspect of remote sensing is the quantitative determination of earth surface characteristics by spectroradiometric analyses of imagery collected by aircraft and spacecraft sensors. Such analyses are often supported by similar ground-based measurements. We have seen from this review that uncertainties and errors occur, or noise is introduced, in each step in the process of radiative transfer: from the sun to the surface, from the surface to a field radiometer or an aircraft or spacecraft imaging system, through the sensor to the detector, and to a recorded radiance level; and finally, errors are introduced in the data processing step.

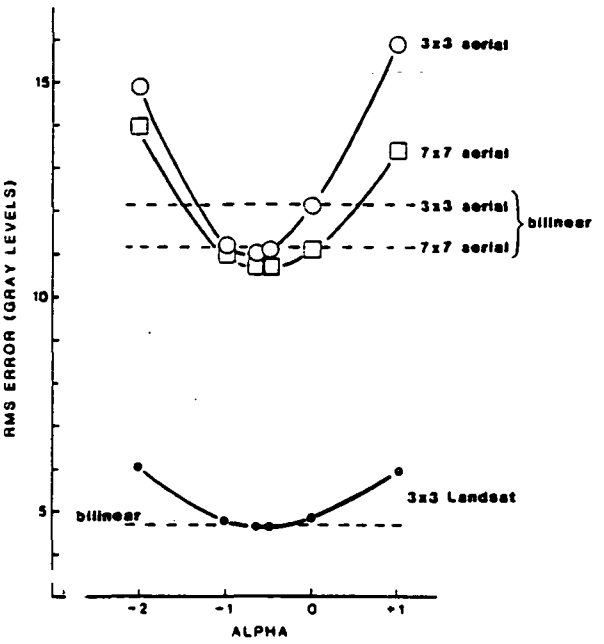

Fig. 11. Mean square radiometric error due to sampling and reconstruction as a function of α for digitized aerial photographs and Landsat MSS data [102].

The accuracy of the verification and exploitation of scene radiation models depends critically on minimizing these various error sources and on completely characterizing the surface irradiance conditions, the surface and atmospheric conditions, the macro- and micro-image calibration of the sensor, and the signal processing techniques employed. More specifically, improvements are needed in 1) simulating the geometry of space imagery with ground measurements, 2) further investigating the bidirectional reflectance factor method for characterizing surface reflectance to avoid sky anisotropy effects, 3) improving ground-based methods for characterizing the atmosphere and thereby correcting remotely sensed data for its effects, 4) devising a method for making atmospheric corrections from orbit, and 5) defining the requirements for, and improving the accuracy of, the absolute calibration of ground-based, aircraft, and space sensors.

Finally, the magnitude of the error introduced by even optimal resampling techniques, such as parametric cubic convolution, is alarmingly high and should be of concern to all interested in the radiometric fidelity of remote sensing data. There is little point in striving for highly accurate sensor calibration and atmospheric correction if the radiometric quality of the processed image data is poor. Those requiring high radiometric accuracy should use unresampled data and, where possible, use pixels that are well removed from high-contrast edges in order to avoid atmospheric and sensor-related degradations that are difficult to account for because of their dependence on the spatial distribution of the surface.

ACKNOWLEDGMENT

The author would like to thank N. Che, R. D. Jackson, C. J. Kastner, J. M. Palmer, A. L. Phillips, and R. A. Schowengerdt for many useful discussions, and R. S. Fraser for his comments on the manuscript.

References

[1] N. J. J. Bunnik, "Review of models and measurements of multispectral reflectance of plant canopies and recommendations for future research," in P. N. Slater, Ed., *SPIE Critical Review of Remote Sensing, Proc. SPIE*, vol. 475, pp. 2–11, 1984.

[2] J. A. Smith, "Matter-energy interaction in the optical region," in R. N. Colwell, Ed., *Manual of Remote Sensing*, 2nd ed. Falls Church, VA: American Society of Photogrammetry, 1983, ch. 3.

[3] N. S. Goel and R. L. Thompson, "Inversion of vegetation canopy models for estimating agronomic variables. V. Estimation of leaf area index and average leaf angle using measured canopy reflectances," *Rem. Sens. Environ.* vol. 16, pp. 69–85, 1984.

[4] P. N. Slater, "The importance and attainment of absolute radiometric calibration," in P. N. Slater, Ed., *SPIE Critical Review of Remote Sensing, Proc. SPIE* vol. 475, pp. 34–40, 1984.

[5] F. E. Nicodemus, J. C. Richmond, J. J. Hsai, I. W. Ginsberg, and T. Limperis, "Geometrical considerations and nomenclature for reflectance," NBS Monograph 160, U.S. Government Printing Office, Washington, DC, SD Cat. No. C13.44:160, p. 52, 1977.

[6] W. H. Venable, Jr., J. J. Hsai, and V. R. Weidner, "Establishing a scale of directional-hemispherical reflectance factor. 1. The Van den Akker method," *J. Res. Nat. Bur. Stand.*, vol. 82, pp. 29–55, 1977.

[7] B. F. Robinson, M. E. Bauer, D. P. DeWitt, L. F. Silva, and V. C. Vanderbilt, "Multiband radiometer for field research," *Proc. SPIE*, vol. 196, pp. 8–15, 1979.

[8] P. N. Slater, *Remote Sensing: Optics and Optical Systems*. Reading, MA: Addison-Wesley, 1980.

[9] V. V. Salomonson and W. E. Marlatt, "Airborne measurements of reflected solar radiation," *Rem. Sens. Environ.*, vol. 2, pp. 1–8, 1971.

[10] R. L. Hulstrom, "Spectral measurements and analyses of atmospheric effects on remote sensor data," *Proc. SPIE*, vol. 51, pp. 90–100, 1975.

[11] M. J. Duggin, "Simultaneous measurement of irradiance and reflected radiance in field determination of spectral reflectance," *Appl. Opt.*, vol. 20, pp. 3816–3818, 1981.

[12] K. L. Coulson and D. W. Reynolds, "The spectral reflectance of natural surfaces," *J. Appl. Meteorol.*, vol. 10, pp. 1285–1295, 1971.

[13] D. S. Kimes, J. A. Smith, and K. J. Ransom, "Vegetation reflectance measurements as a function of solar zenith angle," *Photogram. Eng. Rem. Sens.*, vol. 46, pp. 1563–1573, 1980.

[14] J. J. Hsai and V. R. Weidner, "NBS 45/normal reflectometer for absolute reflectance factor," *Metrologia*, vol. 17, pp. 97–102, 1981.

[15] K. T. Kriebel, "On the variability of the reflected radiation due to differing distribution of irradiance," *Rem. Sens. Environ.*, vol. 4, pp. 257–264, 1976.

[16] ———, "Average variability of the radiation reflected by vegetated surfaces due to differing irradiations," *Rem. Sens. Environ.*, vol. 7, pp. 81–83, 1978.

[17] ———, "Measured spectral bidirectional reflection properties of four vegetated surfaces," *Appl. Opt.*, vol. 17, pp. 253–259, 1978.

[18] M. J. Duggin, "The field measurement of reflectance factors," *Photogram. Eng. Rem. Sens.*, vol. 46, pp. 643–647, 1980.

[19] E. J. Milton, "Does the use of two radiometers correct for irradiance changes during measurement? *Photogram. Eng. Rem. Sens.*, vol. 47, pp. 1223–1225, 1981.

[20] ———, "Field measurement of reflectance factors: A further note," *Photogram. Eng. Rem. Sens.*, vol. 48, pp. 1474–1476, 1982.

[21] M. J. Duggin and T. Cunia, "Ground reflectance measurement techniques: A comparison," *Appl. Opt.*, vol. 23, pp. 3771–3777, 1983.

[22] J. A. Kirchner, S. Youkhana, and J. A. Smith, "Influence of sky radiance distribution on the ratio technique for estimating bidirectional reflectance," *Photogram Eng. Rem. Sens.*, vol. 48, pp. 955–959, 1982.

[23] B. F. Robinson and L. L. Biehl, "Calibration procedures for measurement of reflectance factor in remote sensor field research," *Proc. SPIE*, vol. 196, pp. 16–26, 1979.

[24] N. Che, R. D. Jackson, A. L. Phillips, and P. N. Slater, "The use of field ratiometers in reflectance factor and atmospheric measurements," *Proc. SPIE*, vol. 499, in press.

[25] J. V. Dave, "A direct solution of the spherical harmonics approximation to the radiative transfer equation for an arbitrary solar evaluation. Part II: Results," *J. Atmos. Sci.*, vol. 32, pp. 1463–1474, 1975.

[26] D. D. Egbert and F. T. Ulaby, "Effect of angles on reflectivity," *Photogram. Eng.*, vol. 38, pp. 556–564, 1972.

[27] M. J. Duggin, "Likely effects of solar elevation on the quantification of changes in vegetation with maturity using sequential Landsat imagery," *Appl. Opt.*, vol. 16, pp. 521–523, 1977.

[28] P. J. Pinter, Jr., R. D. Jackson, C. E. Ezra, and H. W. Gausman, "Sun angle and canopy architecture effects on the spectral reflectance of six wheat cultivars," *Int. J. Rem. Sens.*, 1985, in press.

[29] R. D. Jackson, P. J. Pinter, Jr., F. B. Idso, and R. J. Reginato, "Wheat spectral reflectance: Interactions between crop configuration, sun elevation, and azimuth angle," *Appl. Opt.*, vol. 18, pp. 3730–3732, 1979.

[30] J. A. Kirchner, C. C. Schnetzler, and J. A. Smith, "Simulated directional radiances of vegetation from satellite platforms," *Int. J. Rem. Sens.*, vol. 2, pp. 253–264, 1981.

[31] C. C. Schnetzler, "Effect of sun and sensor geometry, canopy structure and density, and atmospheric condition on the spectral response of vegetation, with particular emphasis on across-track pointing," in [32, pp. 509–520].

[32] G. Guyot and M. Verbrugghe, Eds. *Spectral Signatures of Objects in Remote Sensing, No. 5* (Les Colloques de l'INRA, Avignon, France), 674 pp., 1981.

[33] ———, *Spectral Signatures of Objects in Remote Sensing, No. 23* (Les Colloques de l'INRA, Bordeaux, France), 939 pp., 1983.

[34] B. F. Robinson, R. E. Buckley, and M. A. Burgess, "Performance evaluation and calibration of a modular multiband radiometer for remote sensing field research," *Proc. SPIE*, vol. 308, pp. 146–157, 1981.

[35] H. Y. Chiu and W. Collins, "A spectroradiometer for airborne remote sensing," *Photogram. Eng. Rem. Sens.*, vol. 44, pp. 507–517, 1978.

[36] D. W. Deering and P. Leone, "A sphere-scanning radiometer for rapid directional measurements of sky and ground radiance: The PARABOLA field instrument," NASA Tech. Memo 86171, Goddard Space Flight Center, Greenbelt, MD 20771, 1984.

[37] F. J. Ahern, R. J. Brown, K. P. B. Thomson, and K. Staenz, "The CCRS visible-infrared spectroscopy laboratory: Significant results from three years' operation," in [32, pp. 25–40].

[38] N. J. J. Bunnik, W. Verhoef, R. W. de Jongh, H. W. J. van Kasteren, R. H. M. E. Geerts, D. Uenk, H. Noordman, and Th. A. de Boer, "Evaluation of ground-based hot-spot reflectance measurements for biomass determination of agricultural crops," Nat. Aerospace Lab. Rep. NLR MP 84085U, The Netherlands, p. 10, 1984.

[39] M. E. Bauer, L. F. Silva, R. M. Hoffer, and M. F. Baumgardner, "Agricultural scene understanding," Purdue Univ., LARS Contract Rep. 112677, pp. A-18 to A-23, 1977.

[40] D. S. Kimes, J. A. Kirchner, and W. W. Newcomb, "Spectral radiance errors in remote sensing ground studies due to nearby objects," *Appl. Opt.*, vol. 22, p. 8, 1983.

[41] R. D. Jackson and B. F. Robinson, "Field evaluation of the temperature stability of a multispectral radiometer, *Rem. Sens. Environ.*, 1985, in press.

[42] C. L. Butner, J. B. Schutt, and M. C. Shai, "Comparison of the reflectance characteristics of polytetrafluorethylene and barium sulfate paints," *Appl. Opt.*, vol. 23, pp. 1139–1140, 1984.

[43] F. J. Ahern, D. G. Goodenough, S. C. Jain, V. R. Rao, and G. Rochon, "Use of clear lakes as standard reflectors for atmospheric measurements," in *Proc. 11th Int. Symp. on Remote Sensing of the Environment*, pp. 731–755, 1977.

[44] S. Aranuvachapun and P. H. LeBlond, "Turbidity of coastal water determined from Landsat," *Rem. Sens. Environ.*, vol. 11, pp. 113–132, 1981.

[45] R. W. Dana, "Using airborne radiometry to determine atmo-

spheric effects in Landsat data," in *Proc. Amer. Soc. of Photogrammetry Fall Meet.*, pp. 117–129, 1978.
[46] E. Doak, J. Livisay, D. Lyzenga, J. Ott, and F. Polcyn, "Evaluation of water depth techniques using Landsat and aircraft data," ERIM Final Rep. on Contract DMA 800-78-6-0060, 207 pp., 1980.
[47] J. Dozier and J. Frew, "Atmospheric corrections to satellite radiometric data over rugged terrain," *Rem. Sens. Environ.*, vol. 11, pp. 191–205, 1981.
[48] R. J. Holyer, "Comments on 'Turbidity of coastal water determined from Landsat'," *Rem. Sens. Environ.*, vol. 12, pp. 255–258, 1982.
[49] W. S. Kowalik, R. J. P. Lyon, and P. Switzer, "The effects of additive radiance terms on ratios of Landsat data," *Photogram. Eng. Rem. Sens.*, vol. 49, pp. 659–669, 1983.
[50] K. T. Kriebel, "Calibration of the METEOSAT-VIS channel by airborne measurements," *Appl. Opt.*, vol. 20, p. 11, 1981.
[51] R. J. P. Lyon, F. R. Honey, and G. I. Ballew, "A comparison of observed and mode-predicted atmospheric perturbations on target radiance measured by ERTS: Part 1—Observed data and analyses," in *IEEE Conf. Dec. Control, Proc.*, pp. 244–249, 1975.
[52] J. C. Munday, Jr., "Chromaticity of path radiance and atmospheric correction of Landsat data," *Rem. Sens. Environ.*, vol. 13, pp. 525–535, 1983.
[53] J. Otterman and R. S. Fraser, "Earth-atmosphere system and surface reflectivities in arid regions from Landsat MSS data," *Rem. Sens. Environ.*, vol. 5, 247–266, 1976.
[54] J. C. Price, "Estimated surface temperatures from satellite thermal infrared data—A simple formulation for the atmospheric effect," *Rem. Sens. Environ.* vol. 13, pp. 353–361, 1983.
[55] A. J. Richardson, "Relating Landsat digital count values to ground reflectance for optically thin atmospheric conditions," *Appl. Opt.*, vol. 21, pp. 1457–1464, 1981.
[56] K. Watson and S. Hummer-Miller, "A simple algorithm to estimate the effective regional atmospheric parameters for thermal-inertia mapping," *Rem. Sens. Environ.*, vol. 11, pp. 455–462, 1981.
[57] H. R. Gordon, D. K. Clark, J. W. Brown, O. B. Brown, R. H. Evans, and W. W. Broenkow, "Phytoplankton pigment concentrations in the Middle Atlantic Bight: Comparison of ship determinations and CZCS estimates," *Appl. Opt.*, vol. 22, pp. 20–36, 1983.
[58] S. Aranuvachapun, "Variation of atmospheric optical depth for remote sensing radiance calculations," *Rem. Sens. Environ.*, vol. 13, pp. 131–147, 1983.
[59] K. R. Castle, R. G. Holm, C. J. Kastner, J. M. Palmer, P. N. Slater, M. Dinguirard, C. E. Ezra, R. D. Jackson, and R. K. Savage, "In-flight absolute radiometric calibration of the Thematic Mapper," in [95, pp. 251–255].
[60] C. J. Kastner and P. N. Slater, "In-flight radiometric calibration of advanced remote sensing systems," *Proc. SPIE*, vol. 356, pp. 158–165, 1982.
[61] H. Neckel and D. Labs, "Improved data of solar spectral irradiance from 0.33 to 1.25 microns," *Solar Phys.*, vol. 74, p. 231, 1981.
[62] C. J. Kastner, "Absolute radiometric calibration of the Landsat Thematic Mapper," University of Arizona, Tucson, Ph.D. dissertation, in preparation.
[63] K. L. Coulson, "Effects of reflection properties of natural surfaces in aerial photography," *Appl. Opt.*, vol. 5, pp. 905–917, 1966.
[64] P. Koepke and K. T. Kriebel, "Influence of measured reflection properties of vegetated surfaces on atmospheric radiance and its polarization," *Appl. Opt.*, vol. 17, pp. 260–264, 1978.
[65] W. A. Pearce, "A study of the effects of the atmosphere on Thematic Mapper observations," Final Rep. under NASA Contract NAS5-23639, 136 pp., 1977.
[66] J. V. Dave, "Effect of atmospheric conditions on remote sensing of a surface non-homogeneity," *Photogram. Eng. Rem. Sens.*, vol. 46, pp. 1173–1180, 1980.
[67] Y. J. Kaufman, "Atmospheric effect on spatial resolution of surface imagery: Errata," *Appl. Opt.*, vol. 23, pp. 4164–4172, 1984.
[68] D. Tanre, M. Herman, and P. Y. Deschamps, "Influence of the background contribution on space measurements of ground reflectance," *Appl. Opt.*, vol. 20, pp. 3676–3684, 1981.
[69] Y. J. Kaufman and R. S. Fraser, "Atmospheric effects on classification of finite fields," *Rem. Sens. Environ.*, vol. 14, pp. 487–507, 1984.
[70] Y. Mekler, Y. J. Kaufman, and R. S. Fraser, "Reflectivity of the atmosphere-inhomogeneous surface system. Laboratory simulation," submitted to *J. Atmos. Sci.*, 1984.
[71] Y. K. Kaufman, T. W. Brakke, and E. Eloranta, "Field experiment to measure the radiative characteristics of a hazy atmosphere," presented at the Fifth Conf. on Atmospheric Radiation, Oct. 31, 1983, Baltimore, MD, 1983.
[72] D. D. Dyche, "Experimental determination of atmospheric scattering effects on scanner edge response," University of Arizona, Tucson, MS thesis, 1983.
[73] D. J. Diner and J. V. Martonchik, "Atmospheric transmittance from spacecraft using multiple view angle imagery," submitted to *Appl. Opt.*, 1985.
[74] P. N. Slater and S. Martinek, "Multispectral Resource Sampler atmospheric correction study," for ORI, Inc., under NASA sponsorship, 1979.
[75] J. L. Barker, D. L. Ball, K. C. Leung, and J. A. Walker, "Prelaunch absolute radiometric calibration of the reflective bands on the Landsat-4 prototype thematic mapper," in *Proc. Landsat-4 Early Results Symp.* (NASA Goddard Space Flight Center), and personal communication, 1983.
[76] V. T. Norwood and J. C. Lansing, Jr., "Electro-optical imaging sensors," in R. N. Colwell, Ed., *Manual of Remote Sensing*, 2nd ed. Falls Church, VA: American Society of Photogrammetry, 1983, p. 367.
[77] M. Dinguirard and J. M. Maisoneuve, "Dispositif d'etalonnage sur le soleil de la camera HRV du projet SPOT," in *Rassegna Internazionale Elettronica Nucleare ed Aerospaziale* (Rome, Italy, Mar. 7–16, 1980), pp. 1173–1180.
[78] P. N. Slater, "A review of some radiometric calibration problems and methods," in [33, pp. 391–405].
[79] J. J. Horan, D. S. Schwartz, and J. D. Love, "Partial performance degradation of a remote sensor in a space environment, and some probable causes," *Appl. Opt.*, vol. 13, pp. 1230–1237, 1974.
[80] R. F. Nelson, "Sensor induced temporal variability of Landsat MSS data," *Rem. Sens. Environ.*, in press, 1985.
[81] J. Geist, "Quantum efficiency of the p-n junction in silicon as an absolute radiometric standard," *Appl. Opt.*, vol. 18, pp. 760–762, 1979.
[82] J. Geist, "Silicon photodiode front region collection efficiency models," *J. Appl. Phys.*, vol. 51, pp. 3993–3995, 1980.
[83] J. Geist, E. F. Zalewski, and A. R. Shaefer, "Spectral response and self-calibration and interpolation of silicon photodiodes," *Appl. Opt.*, vol. 19, pp. 3795–3799, 1979.
[84] J. Geist and E. F. Zalewski, "The quantum yield of silicon in the visible," *Appl. Phys. Lett.*, vol. 35, pp. 503–506, 1979.
[85] E. F. Zalewski and C. R. Duda, "Silicon photodiode device with 100% external quantum efficiency," *Appl. Opt.*, vol. 22, pp. 2867–2873, 1983.
[86] C. G. Hughes, III, "Silicon photodiode absolute spectral response self-calibration using a filtered tungsten source," *Appl. Opt.*, vol. , pp. 2129–2132, 1982.
[87] S.-M. Lee, "Investigation and extension of self-calibration radiometry," Univ. of Arizona, Tucson, Ph.D. dissertation, 1983.
[88] A. L. Phillips, "Absolute calibration of, and atmospheric measurements using a multiband field spectroradiometer," University of Arizona, Tucson, M.S. thesis, in preparation, 1985.
[89] J. M. Palmer and M. G. Tomasko, "Broadband radiometry with spectrally selective detectors," *Opt. Lett.*, vol. 5, p. 208, 1980.
[90] J. M. Palmer, "Effective bandwidths for Landsat-4 and Landsat D' multispectral scanner and Thematic Mapper subsystem," [95, pp. 336–338].
[91] G. T. Keene, "Improved earth resources sensing instrument," *Proc. SPIE*, vol. 345, pp. 11–22, 1982.
[92] V. T. Norwood, "Balances between resolution and signal to noise ratio in scanner design for earth resources system," *SPIE Proc., Scanners and Imagers for Earth Observations*, vol.

51, pp. 37–42, 1974.
[93] D. Landgrebe and E. R. Malaret, "Noise in remote sensing systems: A model and some results," *IEEE Trans. Geosci. Remote Sensing*, in press, 1985.
[94] S. K. Park and R. A. Schowengerdt, "Image sampling, reconstruction, and the effect of sample-scene phasing," *Appl. Opt.*, vol. 21, pp. 2572–2582, 1982.
[95] V. V. Salomonson, *IEEE Trans. Geosci. Remote Sensing* (Special Issue on Landsat-4), vol. GE-22, pp. 176–338, May 1984.
[96] C. Schueler and V. V. Salomonson, "Landsat image data quality studies," presented at the 25th Plenary Meeting of the Committee on Space Research, Graz, Austria. Submitted to *Adv. Space Res.*, 1985.
[97] B. L. Markham and J. L. Barker, "Spectral characterization of the Landsat-4 MSS sensors," *Photogram. Eng. Rem. Sens.*, vol. 49, pp. 811–833, 1985.
[98] P. N. Slater, "A re-examination of the Landsat MSS," *Photogram. Eng. Rem. Sens.*, vol. 45, 1479–1485, 1979.
[99] S. S. Rifman and D. M. McKinnon, "Evaluation of digital correction techniques for ERTS images," TRW Rep. 20634-6003-TV-02, 1974.
[100] S. K. Park and R. A. Schowengerdt, "Image reconstruction by parametric cubic convolution," *Comp. Vision, Graphics, Image Process.*, vol. 23, pp. 258–272, 1983.
[101] R. A. Schowengerdt, S. K. Park, and R. T. Gray, "Topics in the sampling and reconstruction of two-dimensional images," *Int. J. Rem. Sens.*, vol. 5, pp. 333–347, 1983.
[102] ———, "An optimized cubic interpolator for image resampling," in *Proc. 7th Int. Symp. on Remote Sensing of Environment*, 1983.

Presented as an invited review paper at the 3rd International Colloqium on Spectral Signatures of Objects in Remote Sensing, Les Arcs, France. December 1985.

ABSOLUTE CALIBRATION OF REMOTE SENSING INSTRUMENTS

S. F. Biggar, C. J. Bruegge, B. A. Capron, K. R. Castle, M. C. Dinguirard, R. G. Holm, R. D. Jackson†, Y. Mao, M. S. Moran†, J. M. Palmer, A. L. Phillips, R. K. Savage††, P. N. Slater, S. L. Witman, and B. Yuan

† Agricultural Research Service, USDA, Phoenix, Arizona; †† Atmospheric Sciences Laboratory, White Sands Missile Range, New Mexico. The remaining authors are with the Optical Sciences Center, University of Arizona, AZ 85721.

ABSTRACT

Source-based and detector-based methods for the absolute radiometric calibration of a broadband field radiometer are briefly described. Using such a radiometer, calibrated by both methods the calibration of the integrating sphere used in the pre-flight calibration of the Thematic Mapper was re-determined. The results are presented.

The in-flight calibration of space remote sensing instruments is briefly discussed. A method is described which uses the results of ground-based reflectance and atmospheric measurements as input to a radiative transfer code to predict the radiance at the instrument. A calibrated, helicopter-mounted, radiometer is used to determine the radiance levels at intermediate altitudes to check the code predictions. Results of such measurements for the calibration of the Thematic Mapper on Landsat 5 are described together with an analysis that shows the value of such measurements.

Introduction

To determine ground spectral radiances from the digital counts provided by a multispectral system in a spacecraft or aircraft or to compare data from the same area collected at several different times, we need to make corrections for the atmosphere and we need to know the relationship between the radiance at the entrance pupil of the system within each multispectral band and the output number of digital counts. The latter is called absolute radiometric calibration. Its use in quantitative remote sensing has been discussed by Slater (1, 2).

In this paper, we describe two methods for preflight absolute radiometric calibration of a multispectral system and two methods for inflight calibration. The four methods are fundamentally different. One of the preflight methods is referred to as source-based and the other is detector-based. One of the inflight methods depends on measurements of the spectral hemispherical directional reflectance factor of the ground, and the other makes use of measurements of the spectral radiance of the ground. In both inflight methods the influence of the intervening atmosphere on the measurements has to be taken into account. We will provide examples to compare the different methods.

Source-Based and Detector-Based Pre-Flight Calibration

A. Source-Based

The steps in the source-based calibration of sensors such as the Thematic Mapper and the SPOT HRV are described briefly below with reference to Figure 1. The procedure involves the transfer of calibrations from the source to an integrating sphere and then to the imaging sensor or any broadband radiometer.

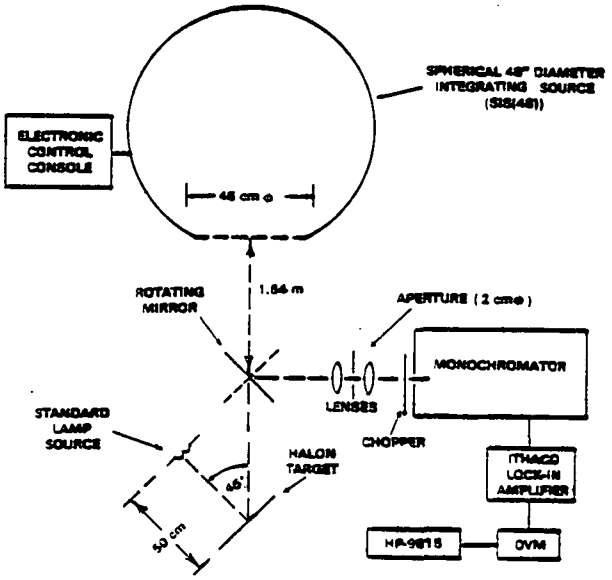

Figure 1. The arrangement for calibrating the integrating sphere and TM at Santa Barbara Research Center.

1. A 1000-W tungsten halogen light source connected to a stabilized power supply is used to irradiate a diffuse reflector. The calibration of the source output and the bidirectional spectral reflectance factor of the diffuser are traceable to a national standards laboratory. The distance from the source to the diffuser (halon in Figure 1) is accurately measured, so the spectral irradiance on the diffuser is accurately known.

2. The integrating sphere, which is calibrated in the first transfer, is arranged such that a monochromator, sampling in 10-nm steps, can alternately sample and compare the sample to the radiance of the diffuser. This is accomplished by rotating the mirror shown in Figure 1 through 90°. The lenses in front of the monochromator are adjusted so that a large fraction of the area of the sphere exit port and the halon surface are sampled by the entrance slit of the monochromator. The aperture is adjusted to limit the cone of radiation passing through the monochromator. Thus the comparison is between spectral radiant flux levels and the spectral radiance of the sphere $L_{\lambda s}$, given by

$$L_{\lambda s} = \frac{\rho(\lambda;0°,45°)}{\pi} E_\lambda \frac{S(\lambda)_s}{S(\lambda)_l} \qquad (1)$$

where $\rho(\lambda;0°,45°)$ is the spectral bidirectional reflectance of the halon; E_λ is the spectral irradiance of the standard lamp; and $S(\lambda)_s$ and $S(\lambda)_l$ are the signals from the monochromator when it is viewing the sphere and the standard lamp, respectively. This procedure is repeated for several sphere output radiance levels achieved by turning on different numbers of lamps inside the sphere. The highest power level is 1.5 kW. The spectral coverage is typically from 0.4 to 2.6 μm using Si and PbS detectors to measure the output of the monochromator. Any departures from linearity in the response of the detector system must be accounted for. Thus the spectral radiance at the exit port of the integrating sphere is known at several levels.

3. The responsivity of the system to be calibrated is determined by aligning it so that its field of view is contained within the area of the exit port of the sphere. The radiance at the exit port of the sphere must not change due to the proximity of the system to be calibrated.

4. The output digital counts or voltages V_n corresponding to each band, n, are recorded for the various radiance levels produced at the port of the sphere.

5. The normalized spectral responses $r(\lambda)_n$ of the system are determined by performing a wavelength scan using a monochromator that irradiates the entrance pupil of the system; $r(\lambda)$ is unitless.

6. The effective radiance measured by the radiometer is given by $\int_\lambda L_\lambda r(\lambda)_n d\lambda$, where the integration is performed over all wavelengths to which the system responds. The relationship between this quantity and V_n for each band compares the total radiance at the entrance pupil of the system to the output voltage or digital counts. This constitutes the absolute radiometric calibration of the system.

B. Detector-Based

Method 1. The steps in one method of detector-based calibration of a broadband radiometer are described as follows:

1. A very stable, high-power tungsten halogen lamp is used to irradiate the entrance slit of a monochromator. The output beam from the monochromator is adjusted to be smaller than the area of a United Detector Technology QED-100 detector of accurately known spectral responsivity, described by Zalewski and Duda (3).

2. A wavelength scan of the monochromator then provides a calibration of its output radiant flux, $\Phi(\lambda)$.

3. The radiometer to be calibrated is inserted into the beam in place of the QED, where again the radiometer detector area must totally encompass the beam. The output voltage $V(\lambda)$ is recorded as a function of wavelength.

4. Applying Palmer's (4) moments normalization method to the ratio $V(\lambda)/\Phi(\lambda)$ provides a measure of the effective bandwidth and responsivity R_n of the radiometer.

5. A peak normalization method is used to determine the effective field of view, which is used to calculate the solid angle, Ω, subtended by the detector at the entrance pupil. A simple measurement of the diameter of the entrance pupil provides the area A.

6. The absolute calibration of the radiometer is given by the relation between L_λ, the spectral radiance at the entrance pupil, and $V(\lambda)$, the voltage out of the radiometer according to

$$L_\lambda = \frac{V(\lambda)}{R_n A \Omega} \qquad (2)$$

Method 2. An alternative detector-based procedure is as follows:

1. The end of a tube with two small circular apertures in it is attached to the front of a QED detector as shown in Figure 2. The geometry of the tube defines the AΩ product mentioned earlier. The filter is removed from the radiometer to be calibrated and placed over the tube.

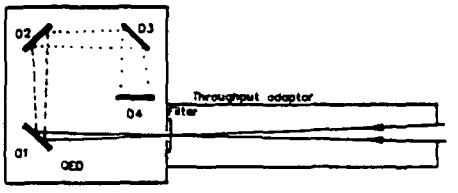

Figure 2. The four-diode QED-100 with throughput adaptor.

2. This QED spectroradiometer is used to measure the radiance of a panel irradiated with a stable, high-power white-light source. The voltage, V, from the detector is recorded.

3. The spectral transmittance of the filter is measured with a spectrophotometer and the moments normalization method is applied to the product $\tau(\lambda)\ R(\lambda)$, where $R(\lambda)$ is the known spectral response of the QED. This gives the normalized responsivity of the filtered QED detector R_n.

4. Applying Equation (2) yields the spectral radiance of the panel.

5. The filter is replaced in the radiometer to be calibrated, and the instrument is directed at the same angle to the panel as was the QED spectroradiometer.

TABLE 1. PERCENTAGE DIFFERENCES IN CALIBRATIONS* BETWEEN:

WAVELENGTH in nm	OSC DETECTOR-BASED (ODB) AND SBRC SOURCE-BASED (SSB) $\frac{SSB-ODB}{ODB}\times 100$	OSC SOURCE-BASED (OSB) AND SBRC SOURCE-BASED (SSB) $\frac{SSB-OSB}{SSB}\times 100$	SBRC MONOCHROMATOR (SM) AND SBRC SOURCE-BASED (SSB), COMPARED AGAINST INTEGRATING SPHERE $\frac{SM-SSB}{SM}\times 100$
440.3	-10.8**	-9.4**	+4.1**
525.4	-2.6	-0.7	+2.9
605.4	-2.9	-0.5	+2.5
662.1	-2.0	+0.8	+2.1
780.7	-1.1***	+1.4	+0.6
861.7	+8.7	+2.5	-1.0

* All the comparisons are for the same radiometer, except for the last column where the radiometer and monochromator were calibrated against the same source and halon diffuser and then both measured the integrating sphere output. The values listed represent the differences between the readings from the two instruments when measuring the sphere output.
** Low signal to noise ratio conditions.
*** Detector heater not working.

6. The relationship between the voltage from the radiometer and the spectral radiance of the panel provides the absolute calibration of the radiometer.

C. Comparison of Results

Table 1 compares source-based and detector-based calibrations using a filter spectropolarimeter described by Castle (5) with a 5° field of view. Some of the calibrations were conducted at the Optical Sciences Center (OSC) of the University of Arizona; others were conducted at Santa Barbara Research Center (SBRC), a division of Hughes Aircraft Company by Witman (6). The integrating sphere and associated equipment (see Figure 1) used in the preflight absolute radiometric calibration of Thematic Mappers 4 and 5 are at SBRC.

The comparisons in Table 1 show that good agreement exists for most of the visible and near infrared wavelengths used. At shorter wavelengths the uncertainty in the measurements increases because of their low signal to noise ratio. This is the reason the first detector-based method described can be used to calibrate only spectroradiometers that use large detectors. The irradiance across the exit slit of the monochromator is low, so to obtain a large signal a long slit is needed.

Inflight calibration by reference to the Earth's surface.

A. Reflectance-Based Methods

The inflight calibration methods considered here utilize simultaneous measurements of the earth's surface and atmosphere and then predict radiance levels at the sensor. The relation of these radiance levels to the digital counts in the image of the measured ground area provides the absolute calibration. The advantage of such measurements is that they are made under the exact conditions the system is operating under and therefore all sources of transmission loss and stray light are accounted for.

Gordon et al. (7) have described a method for the atmospheric correction of Coastal Zone Color Scanner (CZCS) data that can, in conjunction with ocean reflectance measurements, provide a calibration of the sensor. Their method uses a Monte Carlo atmospheric radiative transfer model and an algorithm that includes a ratio of the aerosol optical depth at wavelengths of 520 nm and 550 nm to that at 670 nm, where the ocean reflectance is assumed zero. As Aranuvachapun (8) points out, the accuracy of the algorithm relies mainly on the accuracy of this ratio, which is not currently measured by satellite remote sensing. The uncertainty of the method in determining pigment concentration is stated to be 30 to 40 percent over the concentration range 0.08 to 1.5 mg m^{-3}. In three direct comparisons between ship-measured and satellite-determined values of water radiance, Gordon and associates claim that the atmospheric correction algorithm had an average error of 10 to 15 percent.

Koepke (9), using a radiative transfer program that accounts for multiple scattering in conjunction with ground reflectance data and atmospheric data, performed an inflight calibration of Meteosat I for use in radiation budget studies. Atmospheric water vapor was calculated using data from the nearest radiosonde, and the climatological values of ozone and oxygen were assumed. Ground level barometric pressure defined the Rayleigh optical depth, and aerosol optical depths were derived from visibility data. Four test sites were used: rough ocean, the savanna in Namibia, pastureland in northern Germany, and freshly fallen snow. Bidirectional reflectance data were collected for these sites over a period of several months. Histograms of these areas typically filled less than three columns, and often one column contained 60 per cent of the pixels. We note, however, that Meteosat quantizes data to 6 bits, so for low reflectances a three column spread represents a large variation in reflectance. Nevertheless by using four targets and pointing the sensor into deep space, which fixed the offset point on the counts-versus-radiance curve, Koepke estimated the

uncertainty to be on the order of 6 percent. This resourceful use of colateral data provided a valuable calibration of Meteosat 1. Koepke's estimate of an uncertainty of 6 per cent probably represents a lower limit on the uncertainty of the method because of its dependence on reflectance data that were not collected simultaneously with the Meteosat imagery and the use of visibility estimates that provide only approximate values for optical depths.

During the past three years, we have used this technique several times at White Sands, New Mexico, but we have taken simultaneous ground and atmospheric measurements as the Thematic Mapper acquired images of the ground area. This work has been described by Kastner and Slater (10) and Castle et al. (11). Originally the measurements of the ground were only of its spectral hemispherical directional reflectance. Recently ground level and helicopter measurements of the spectral radiance of the surface have been made. Results of such measurements are shown alongside the reflectance-based results for October 28, 1984 in Figure 3. The conditions at White Sands and the reflectance-based results are listed in Table 2. In Figure 3, the Pre and I.C. bars represent, respectively, the spectral radiance values of the ground determined from the unprocessed digital counts of the image using the preflight calibration (see the comparisons in Table 1) and the internal calibrator updates provided by Barker (12). The Code bar refers to the results of the reflectance-based method, which makes use of a radiative transfer code developed by Herman and Browning (13). The Heli bar represents the radiance at 3,000 m as measured by a spectroradiometer. The M-Heli bar represents modified helicopter results. In this case the ground reflectance used in the code was modified to give a radiance value at 3,000 m that matched that measured by the helicopter, and the results in the bar chart are the corresponding radiances at the top of the atmosphere. The Rayleigh bars represent the radiances at the top of the atmosphere for a Rayleigh atmosphere. Note that the Rayleigh results are within 2 per cent of the result for the no atmosphere case for TM band 1 and within 1 percent for bands 2, 3, and 4.

The results in Figure 3 show anomalously high radiance levels in bands 2 and 4 based on preflight and I.C. calibration data. That the two independent reflectance and radiance-based methods and the Rayleigh case give results that are closely bunched is strong evidence that the preflight and I. C. results are misrepresentative of the calibration of TM on that date. Furthermore, results on other dates (July 8, 1984, May 24, 1985, and August 28, 1985) fail to show this anomaly although there was no change in our measurement methodology, reference panel calibration, and data reduction methods. We have no reason to question the preflight or the internal calibrator gain and offset values themselves; we believe the anomalies are more likely the result of a source of radiance in the atmosphere surrounding the spacecraft, perhaps due to luminescence or ionization phenomena. High energy solar UV or X-ray irradiation could be one cause and the passage of the spacecraft through a gas cloud created by an earlier orbit adjustment has been suggested as another. This last hypothesis is based upon the observed deceleration of the spacecraft as it passes through the region in space

TABLE 2: WHITE SANDS CALIBRATION OF TM ON OCTOBER 28, 1984.

Solar zenith angle Z: 52.068	Latitude: 32 deg 55 min
Solar distance in AU: 0.9932	Longitude: 106 deg 22 min
Junge size distribution: 4.09	Elevation: 1196 m
Aerosol size range: 0.02 to 5.02 μm	Pressure: 663.7 mm
Refractive index: 1.54 - 0.01i	Temperature: 12.4 deg C
Time of overpass: 10:09.1 MST	Relative humidity: 75%
Calculated visibility: 120 km	

Thematic Mapper bands	1	2	3	4
Central wavelength μm	0.4863	0.5706	0.6607	0.8382
Tau Mie	0.1360	0.1027	0.0750	0.0401
Tau Rayleigh	0.1420	0.0739	0.0407	0.0156
Tau ozone	0.0047	0.0198	0.0098	0.0011
Tau water vapor	0.0000	0.0000	0.0000	0.0454
Spectral reflectance	0.4250	0.4830	0.5170	0.5590
Code for zenith angle of 45.00	0.0915	0.0985	0.1086	0.1471
Code for zenith angle of 55.00	0.0731	0.0782	0.0867	0.0861
Eo across band in W/m2.μm	1955.5	1826.9	1545.0	1042.8
Image digital counts	223.25	169.00	161.31	150.50
Preflight cal gains	15.553	7.860	10.203	10.821
Preflight cal offsets	1.8331	1.6896	1.8850	2.2373
IC cal gains for 28 Oct 84	14.211	7.264	9.551	10.427
IC cal offsets for 28 Oct 84	2.2570	2.2160	2.3700	2.3640
Normalized code for Z = 52.068	0.0784	0.0842	0.0931	0.1040
Code TM L in W/m2.sr.μm	155.51	155.87	145.79	109.96
Spectral L from preflight cal	142.36	212.86	156.25	137.01
Spectral L from IC cal	155.51	229.60	166.41	142.07
% (Code-Pre)/Pre	9.2	-26.8	-6.7	-19.7
% (Code-IC)/IC	.0	-32.1	-12.4	-22.6

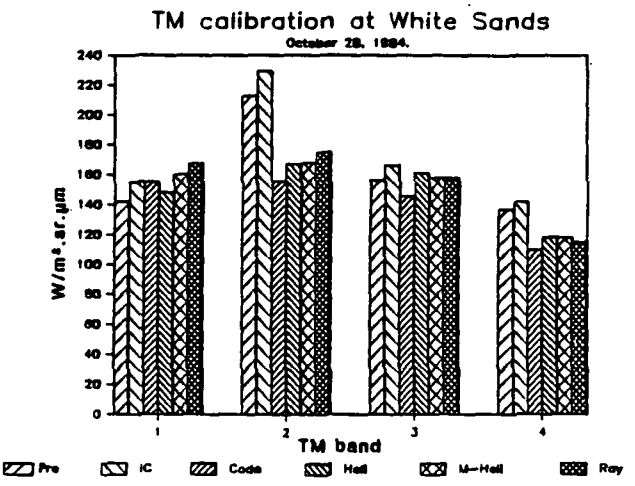

Figure 3. Comparision of results for TM calibration at White Sands, see text.

where the orbit adjustment jets had been previously activated. These decelerations occur for two to three weeks after an orbit adjustment.

The fact that such anomalies were not detected by the internal calibrator is an important reason for using ground-based calibration techniques whenever possible. The following discussion shows that one such technique is easy to implement given a ground reflectance of about 0.5 in each band.

B. Radiance-Based Methods

Figure 3 shows that the radiances as measured at 3000 m above White Sands are about the same as those measured by the Thematic Mapper. This result prompted a more detailed examination of the variation of radiance with altitude as a function of wavelength, reflectance, and visibility.

Starting with the atmospheric conditions of October 28, 1984, at White Sands, and with a solar zenith angle of 35 deg, radiance values were calculated for altitudes between ground level (1196 m at White Sands) and 21,000 m (the operational altitude

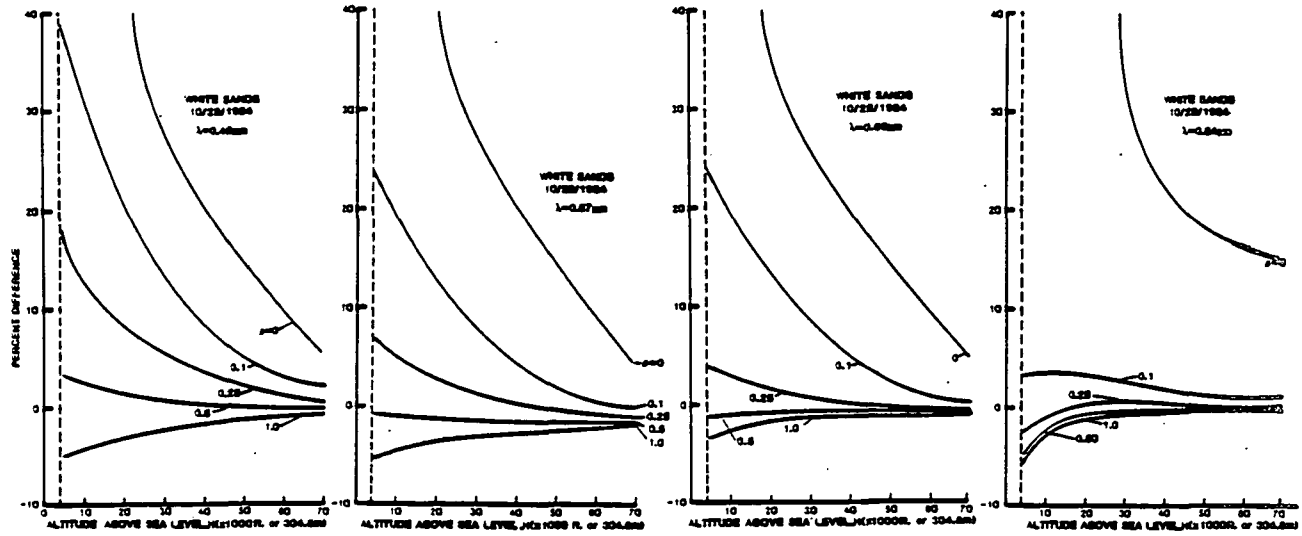

Figure 4. Percentage differences between the radiances at the top of the atmosphere and at intermediate altitudes for the White Sands conditions of October 28, 1984, see Table 2.

above sea level of the NASA U-2 or ER-2 aircraft) and for above the atmosphere. Graphs were then plotted of the percentage difference (the differences between the radiance above the atmosphere and at an intermediate altitude divided by the radiance above the atmosphere, the whole quantity expressed as a percentage) against altitude above sea level. These are shown in Figure 4, for the first four solar reflective TM bands. As anticipated, the results for reflectances less than 0.1 show large percentage differences, but what is intriguing is the sign change in the percentage difference for reflectances between 0.25 and 1.0 for bands 1, 2, and 3 and between 0.1 and 0.25 for band 4. These results show that, for a reflectance of 0.5 and an altitude of 3000 m ASL, the percentage differences are +2.5, -1.0, -1.0, and -2.0 for bands 1, 2, 3, and 4 respectively. This indicates that for the White Sands conditions of 28 October, 1984, helicopter radiance values at an altitude of 3000 m are close to those for space and require only a small correction, which can be made accurately.

With this promising result, the investigation was extended to determine how general this condition might be. Visibilities of 10 and 23 km were considered for a reflectance of 0.5 at all wavelengths. The input values are listed in Table 3, the refractive index was 1.54 - 0.01i in all cases and Junge ν values of 2.9 and 2.6 were used for the visibilities of 10 and 23 km respectively.

TABLE 3. Input Values for Radiative Transfer Calculations

Wavelength μm	τ_{RAY}	τ_{OZ}	τ_{H_2O}	τ_{CO_2}	τ_{MIE} V=10km	τ_{MIE} V=23km
0.49	0.1630	0.0066	0.0	0.0	0.5393	0.2927
0.57	0.0844	0.0277	0.0	0.0	0.4665	0.2657
0.66	0.0466	0.0136	0.0	0.0	0.4089	0.2434
0.84	0.0178	0.0016	0.0335	0.0	0.3303	0.2111
1.64	0.0011	0.0	0.0915	0.0094	0.1766	0.1391
2.22	0.0004	0.0	0.0594	0.0035	0.1374	0.1176

The output plots of percentage difference, as defined earlier, against altitude above sea level are shown as Figures 5 and 6 together with the Rayleigh atmosphere curve for a wavelength of 0.49 μm. The positive difference for λ = 0.49 μm is due to the fact that the large path radiance term contributed more to the total radiance than is lost by the attenuation of the ground reflected term. The other curves show increasing negative differences for altitudes approaching ground level, owing to the heavy aerosol loading in the lower atmosphere. The bowing of the λ = 0.57 μm and 0.66 μm curves at intermediate altitudes is due to reduced path radiance from Rayleigh scattering and the presence of ozone absorption at those altitudes. Note that for an altitude of 3000 m and a visibility of 23 km the percentage differences are +3.0, -1.4, -0.9, -0.8, -2.3, and -1.6 for wavelengths of 0.49, 0.57, 0.66, 0.84, 1.67, and 2.22 μm respectively. Furthermore the percentage differences are less than twice these values for a visibility of 10 km, as can be seen from the remarkable similarity between Figures 5 and 6.

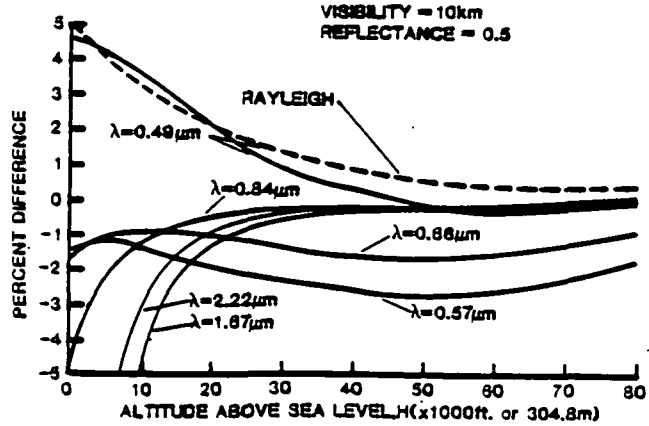

Figure 5. Percentage differences between the radiances at the top of the atmospere and at intermediate altitudes for ρ=0.5 and a visibility of 10 km.

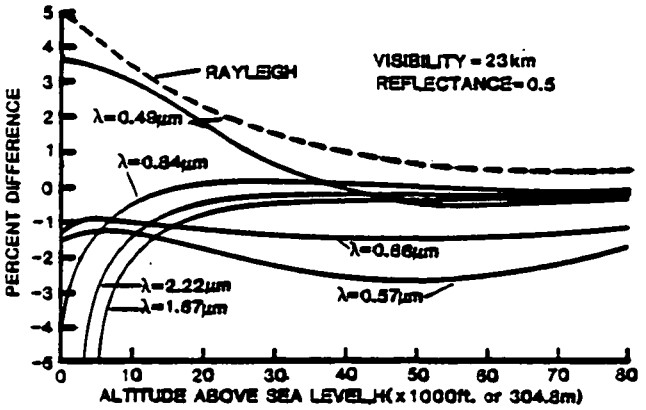

Figure 6. Percentage differences between the radiances at the top of the atmospere and at intermediate altitudes for ρ=0.5 and a visibility of 23 km.

Conclusion

The calibration of imaging and nonimaging broadband radiometers by detector-based and source-based methods needs to be continued to check and refine the accuracy of the former. Although theoretically more accurate, in practice the measurements associated with the detector-based method are sometimes difficult because of low signal to noise ratios and ill-defined radiometer geometries. Further work needs to be done to determine the practical limitations of detector-based calibrations accuracy for broadband radiometers.

The inflight calibrations of several satellite multispectral sensors have shown substantial changes with time. The CZCS has shown what is believed to be a monotonic decrease in response for all wavelengths, with the decrease greater for shorter wavelengths (14). The same is true for TM for the solar reflective bands with the following two exceptions: The mid-IR bands show oscillitory changes (15), and our results for October 28, 1984, show anomalously high responses in bands 2 and 4.

The inflight calibration of satellite sensors by reference to ground reflectance measurements can be conveniently checked by the use of low altitude (3000 m) helicopter radiance measurements. Without correction the latter are within 3 percent of the satellite values for the solar reflective bands of TM, and with correction they are limited by the uncertainty in the absolute calibration of the helicopter radiometer. They do require a ground reflectance of about 0.5 but they are insensitive to atmospheric conditions for a wide range of visibilities above about 15 km. Compared to satellite calibration by reference to high altitude aircraft measurements, the helicopter method enjoys the advantage of lower cost, longer dwell time over the area of interest, and the capability of averaging over a 50 m diameter pixel with a 1 degree field of view instrument from 3000 m altitude.

Again, because of the many difficulties that beset the inflight absolute radiometric calibration of satellite systems, we are not proposing that one method be used to the exclusion of others. Whenever possible, effort should be made to coordinate different but simultaneous measurements over a given site with instruments that have been intercompared in the laboratory. Only by such a concerted effort will we be able to identify systematic errors and reduce them, and be confident of the uncertainties that we ascribe to our calibrations.

Acknowledgments:

We wish to thank L. B. Fulton and J. B. Young of Santa Barbara Research Center for their enthusiastic cooperation in the integrating sphere calibration work. We also wish to thank B. M. Herman for the use of his radiative transfer code, J. A. Reagan for the use of his solar radiometer, and both for useful discussions. The National Aeronautics and Space Administration supported this work at the Optical Sciences Center.

REFERENCES

[1] Slater P N 1984, The importance and attainment of absolute radiometric calibration, in *Proc. SPIE Critical Review of Remote Sensing* 475, 34-40.

[2] Slater P N 1985, Radiometric considerations in remote sensing, *Proc. IEEE* 73(6), 997-1011.

[3] Zalewski E F & Duda C R 1983, Silicon photodiode device with 100% external quantum efficiency, *Appl. Opt.* 22, 2867-2873.

[4] Palmer J M 1984, Effective bandwidths for Landsat-4 and Landsat D' multispectral scanner and Thematic Mapper subsystem, *IEEE Trans. Geosci. Remote Sensing* GE-22, 336-338.

[5] Castle K R 1985, Absolute radiometric calibration of a spectropolarimeter, PhD Dissertation, University of Arizona. 129 pp.

[6] Witman S L 1985, Absolute radiometric calibration of a spherical integrating source, MS Thesis, University of Arizona. In preparation.

[7] Gordon H R et al 1983, Phytoplankton pigment concentrations in the Middle Atlantic Bight: Comparison of ship determinations and CZCS estimates, *Appl. Opt.* 22, 20-36.

[8] Aranuvachapun S 1983, Variation of atmospheric optical depth for remote sensing radiance calculations, *Remote Sens. Environ.* 13, 131-147.

[9] Koepke P 1982, Vicarious satellite calibration in the solar spectral range by means of calculated radiances and its application to Meteosat, *Appl. Opt.* 21, 2845-2854.

[10] Kastner C J & Slater P N 1982, In-flight radiometric calibration of advanced remote sensing systems, *Proc. SPIE* 356, 158-165.

[11] Castle K R et al 1984, In-flight absolute radiometric calibration of the Thematic Mapper, *IEEE Trans. Geosci. Remote Sensing* GE-22, 251-255.

[12] Barker J L 1985, Thematic mapper radiometric and algorithm performance program (TRAPP), personal communication.

[13] Herman B M & Browning S R 1975, The effect of aerosols on the earth-atmosphere albedo, *J. Atmos. Sci.* 32, 158-165.

[14] Hovis W A et al 1985, Aircraft measurement for calibration of an orbiting spacecraft sensor, *Appl. Opt.* 24, 407-410.

Presented at the ISLSCP Conference in Rome, December 1985.

VARIATIONS IN IN-FLIGHT ABSOLUTE RADIOMETRIC CALIBRATION

Philip N. Slater

Optical Sciences Center and
Committee on Remote Sensing
University of Arizona
Tucson, Arizona 85721

ABSTRACT

Variations reported in the in-flight absolute radiometric calibration of the Coastal Zone Color Scanner (CZCS) and the Thematic Mapper (TM) will be reviewed. At short wavelengths, these sensors show a gradual reduction in response while in the mid-IR the TM shows oscillatory variations. One set of measurements made at White Sands, New Mexico shows anomalous results in TM bands 2 and 4.

The results of a reflectance-based and a radiance-based calibration method at White Sands, New Mexico will be described. An analysis of the radiance-based method is presented showing the value of such measurements from helicopter altitudes.

Introduction

It is now well established that the absolute radiometric calibration of satellite remote sensing systems changes with time. The need to know the absolute calibration and methods to obtain it have been described elsewhere (ref. 1,2).

In this paper, we review the variations in the in-flight absolute calibration of the Coastal Zone Color Scanner (CZCS) and the Thematic Mapper (TM). We outline two methods used for in-flight absolute calibration by reference to ground sites, one which utilizes ground spectral reflectance measurements and the other which utilizes ground spectral radiance measurements. An analysis of the radiance-based method is presented showing the value of such measurements from helicopter altitudes.

Variations in Radiometric Calibration

We briefly describe here the variations noted in the calibration of the CZCS and TM. With respect to the CZCS, it is worth noting that Gordon (ref. 3), from an error budget analysis, showed that a 5 percent error in sensor calibration and a 10 percent uncertainty in the exoatmospheric solar irradiance can combine to give rise to errors exceeding 200 percent in the retrieval of water reflectance values. Although the 10 percent uncertainty should perhaps be 1-2 percent, Frohlich (ref. 4), and water reflectances are low making them relatively hard to measure accurately, the point remains that large errors in reflectance measurements can occur due to sensor calibration errors. Gordon showed that, by making simultaneous measurements of aerosol optical thicknesses and water radiance with the satellite measurement of total radiance, the error in determining water reflectance can be reduced by an order of magnitude.

In the summer of 1979, Viollier (ref. 5) compared CZCS derived water reflectance values with measurements made near the surface. He found that the satellite value was less than that of the surface by 3.5 percent at 443 nm and greater than that at the surface by 6.3 and 12 percent at 520 and 550 nm respectively. Viollier comments that Gordon reported corresponding values of -2, +2 and 7 percent at the Fifteenth CZCS NET Meeting but used a different set of calibration constants and exoatmospheric irradiance values.

Gordon et al. (ref. 6) have described a method for the atmospheric correction of (CZCS) data that can, in conjunction with ocean reflectance measurements, provide a calibration of the sensor. Their method uses a Monte Carlo atmospheric radiative transfer model and an algorithm that includes a ratio of the aerosol optical depth at wavelengths of 520 nm and 550 nm to that at 670 nm, where the ocean reflectance is assumed zero. As Aranuvachapun (ref. 7) points out, the accuracy of the algorithm relies mainly on the accuracy of this ratio, which is not currently measured by satellite remote sensing. The uncertainty of the method in determining pigment concentration is stated to be 30 to 40 percent over the concentration range 0.08 to 1.5 mg m^{-3}. In three direct comparisons between ship-measured and satellite-determined values of water radiance, Gordon and associates claim that the atmospheric correction algorithm had an average error of 10 to 15 percent.

By computing the radiance at the satellite from known water radiance values, Gordon et. al (ref. 8) proceeded to force agreement between the

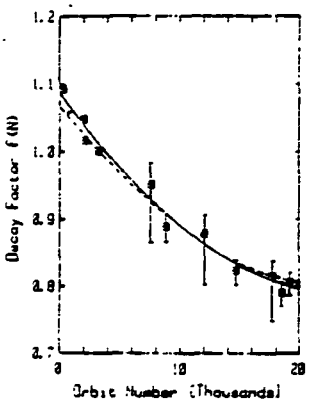

Figure 1. The decay factor with orbit number for the first band of the CZCS, see text (Gordon et al., ref. 8).

sensor-recorded radiance and the computed radiance by adjusting the sensor calibration. Their results are shown in Figure 1 for band 1 of CZCS. The error bars represent the error induced by the uncertainty in the pigment concentration of the water.

Hovis et al. (ref. 9) used the second on-board calibration lamp, used only occasionally, to check the calibration of CZCS after it had been in orbit for 5 1/2 years. They found no measurable change in the calibration, but it is important to note that the calibration lamp checks only the calibration of the focal plane detectors and associated electronics, as is also the case in the Multispectral Scanner System and TM. In comparing CZCS data with those from a calibrated radiometer in a high altitude aircraft, Hovis and associates found a 25 percent degradation in the blue band, centered at 443 nm, after CZCS had been in orbit for four years and seven months. The longer wavelength bands exhibited progressively smaller degradations as shown in Figure 2. Because of the calibration lamp results, the degradation is attributed to a reduction in the reflectances of the telescope optics and the scanning mirror.

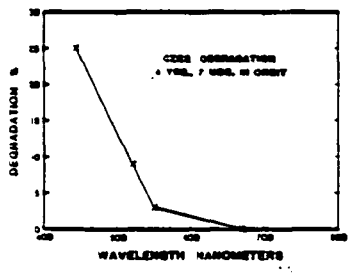

Figure 2. The percentage degradation in the response of the CZCS with time for the first four spectral bands (Hovis et al., ref. 9).

Mueller (ref. 10) has also reported on the change in the calibration gains of the first three channels of the Nimbus-7 CZCS during its first four years of operation. Figure 3 shows the gains for the three channels centered at 443, 520 and 550 nm plotted against year and orbit number. The solid lines are linear regression models and represent the average fits over 20 replications with independent samples of Gaussian random noise. The circles represent decay coefficients calculated for pixels in the central water masses of the northeast Pacific subtropical gyre. The squares are data points generated using the radiometric sensitivity decay correction models of Gordon et al. (ref. 8) with random noise, and the dashed lines are their models. Again the tendencies are as noted by the authors cited earlier, although it is interesting to note the linear fit used by Mueller compared to the quadratic fit used by Gordon et al. (ref. 8).

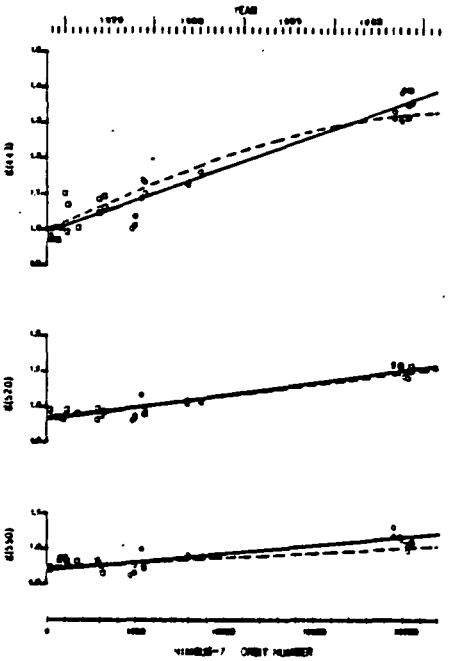

Figure 3. Corrections for the radiometric sensitivity of the CZCS with time for the first three spectral bands (Mueller, ref. 10)

Frequently recorded values for the calibration gains in the solar reflective bands of TM on Landsat 4 have been accumulated by Lee and Barker (ref. 11). Figure 4 compares the pre-launch calibrations with the values from the internal calibrator (IC). Again the results, as for the CZCS lamp-based calibration mentioned earlier, only apply to changes in the focal-plane filters and detectors and the associated electronics. The graphs in Figure 4 are divided into three sections. The left section includes the pre-launch calibration conducted under thermal vacuum conditions. The middle section shows the results of in-orbit IC calibrations during the so-called Scrounge image processing era and the third section shows the results during the Thematic Mapper Image Processing System (TIPS) era. The gains, G, are given from the equation $P = (G \times L) + O$ where P is the observed IC pulse, L is the IC spectral radiance and O is the offset.

The results in Figure 4 show decreases in the apparent gains for band 1 amounting to 7 percent and 13 percent after 500 and 600 days from launch, respectively. Bands 2 and 3 show a similar pattern but with a smaller loss in gain. Band 4 departs from the trend exhibited by bands 1,2 and 3 in showing a gain increase for the last calibration. Bands 5 and 7 show oscillatory changes in gain which are out of phase to start with but then appear to be in phase. The amplitude of the oscillations is about 7 percent.

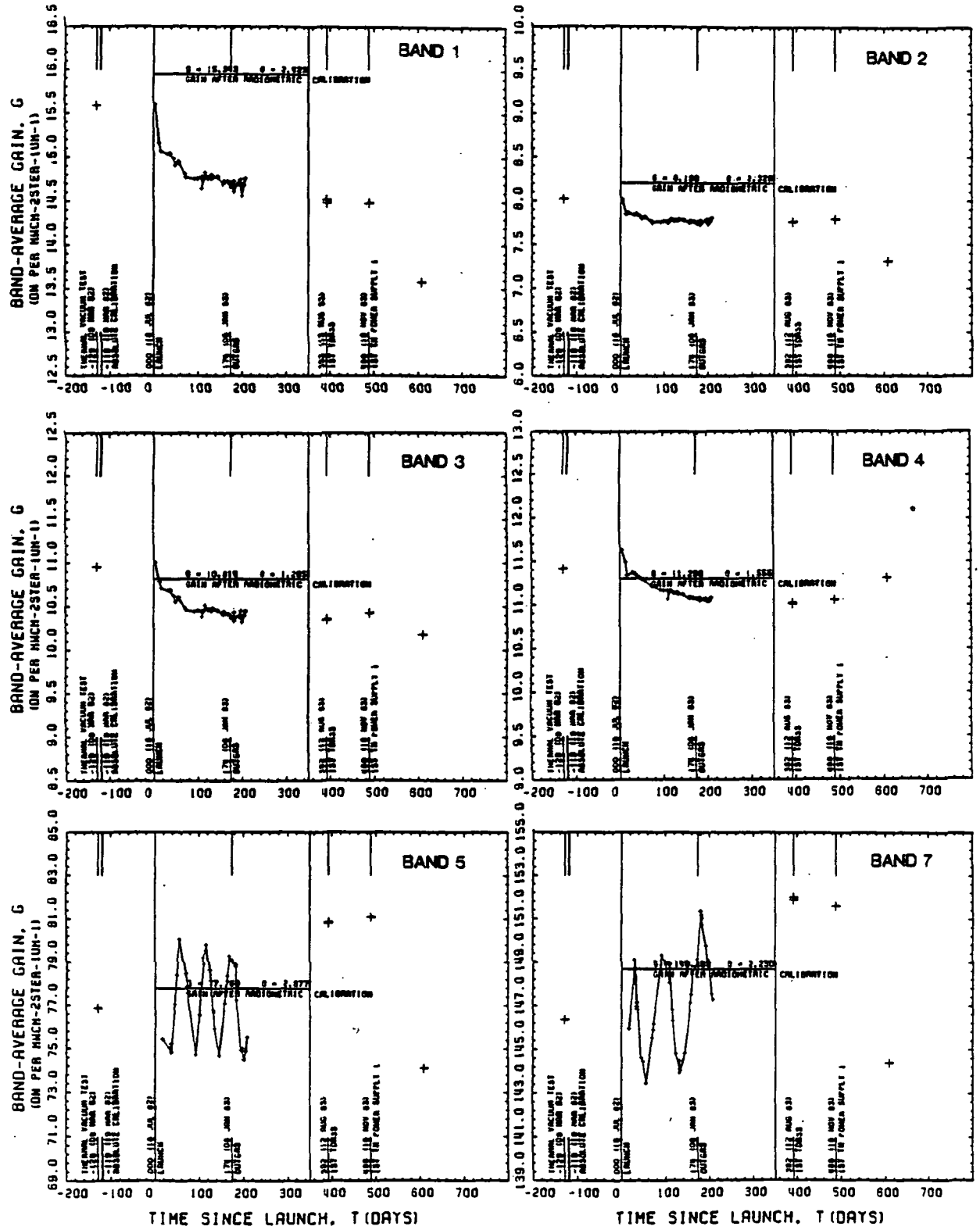

Figure 4. The apparent gain change with time for the solar reflective bands of the TM on Landsat 4. The gain values are in digital numbers per mW/cm² sr um (Lee and Barker, ref. 11).

It must be repeated that these results are only indicative of changes in the filter-detector-electronics part of the system and that superimposed on them should be the changes that occur in the reflectances of the optical components of the telescope and scan mirror.

In-flight calibration by reference to the Earth's surface.

In addition to the work described earlier on the in-flight calibration of the CZCS by reference to know water reflectances, two other reflectance-based calibrations are described here, those of Meteosat and TM. These are followed by a description of a radiance-based calibration method.

A. Reflectance-Based Methods

Koepke (12) using a radiative transfer program that accounts for multiple scattering in conjunction with ground reflectance data and atmospheric data, performed an in-flight calibration of Meteosat I for use in radiation budget studies. Atmospheric water vapor was calculated using data from the nearest radiosonde, and the climatological values of ozone and oxygen were assumed. Ground level barometric pressure defined the Rayleigh optical depth, and aerosol optical depths were derived from visibility data. Four test sites were used: rough ocean, the savanna in Namibia, pastureland in northern Germany, and freshly fallen snow. Bidirectional reflectance data were collected for these sites over a period of several months. Histograms of these areas typically filled less than three columns, and often one column contained 60 per cent of the pixels. We note, however, that Meteosat quantizes data to 6 bits, so for low reflectances a three column spread represents a large variation in reflectance. Nevertheless by using four targets and pointing the sensor into deep space, which fixed the offset point on the counts-versus-radiance curve, Koepke estimated the uncertainty to be on the order of 6 percent. This resourceful use of colateral data provided a valuable calibration of Meteosat 1. Koepke's estimate of an uncertainty of 6 per cent probably represents a lower limit on the uncertainty of the method because of its dependence on reflectance data that were not collected simultaneously with the Meteosat imagery and the use of visibility estimates that provide only approximate values for optical depths.

During the past three years, we have used this technique several times at White Sands, New Mexico, but we have taken simultaneous ground and atmospheric measurements as the Thematic Mapper acquired images of the ground area. This work has been described by Kastner and Slater (13) and Castle et al. (14). Originally the measurements of the ground were only of its spectral hemispherical directional reflectance. Recently ground level and helicopter measurements of the spectral radiance of the surface have been made. Results of such measurements are shown alongside the reflectance-based results for October 28, 1984 in Figure 5. The conditions at White Sands and the reflectance-based results are listed in Table 1. In Figure 5, the Pre and IC bars represent, respectively, the spectral radiance values of the ground determined from the unprocessed digital counts of the image using the pre-flight calibration and the internal calibrator updates provided by Barker (11). The Code bar refers to the results of the reflectance-based method, which makes use of a radiative transfer code developed by Herman and Browning (15). The Heli bar represents the radiance at 3,000 m as measured by a spectroradiometer. The M-Heli bar represents modified helicopter results. In this case the ground reflectance used in the code was modified to give a radiance value at 3,000 m that matched that measured by the helicopter, and the results in the bar chart are the corresponding radiances at the top of the atmosphere. The Rayleigh bars represent the radiances at the top of the atmosphere for a Rayleigh atmosphere. Note that the Rayleigh results are within 2 per cent of the result for the no atmosphere case for TM band 1 and within 1 percent for bands 2, 3, and 4.

TABLE 1: White Sands Calibration of TM on October 28, 1984.

Solar zenith angle Z: 52.068	Latitude: 32 deg 55 min
Solar distance in AU: 0.9932	Longitude: 106 deg 22 min
Junge size distribution: 4.09	Elevation: 1196 m
Aerosol size range: 0.02 to 5.02 μm	Pressure: 663.7 mm
Refractive index: 1.54 - 0.01i	Temperature: 12.4 deg C
Time of overpass: 10:09.1 MST	Relative humidity: 75%
Calculated visibility: 120 km	

Thematic Mapper bands	1	2	3	4
Central wavelength μm	0.4863	0.5706	0.6607	0.8282
Tau Mie	0.1360	0.1027	0.0750	0.0401
Tau Rayleigh	0.1420	0.0739	0.0407	0.0156
Tau ozone	0.0047	0.0198	0.0098	0.0011
Tau water vapor	0.0000	0.0000	0.0000	0.0454
Spectral reflectance	0.4250	0.4830	0.5170	0.3590
Code for zenith angle of 45.00	0.0915	0.0985	0.1086	0.1471
Code for zenith angle of 55.00	0.0731	0.0782	0.0867	0.0861
Eo across band in W/m2.μm	1955.5	1826.9	1545.0	1042.8
Image digital counts	223.25	169.00	181.31	150.50
Preflight cal gains	15.353	7.860	10.203	10.821
Preflight cal offsets	1.8331	1.6896	1.8850	2.2373
IC cal gains for 28 Oct 84	14.211	7.264	9.351	10.427
IC cal offsets for 28 Oct 84	2.2570	2.2160	2.3700	2.3640
Normalized code for Z = 52.068	0.0784	0.0842	0.0931	0.1040
Code TM L in W/m2.sr.μm	155.51	155.87	145.79	109.36
Spectral L from preflight cal	142.36	212.86	156.25	137.01
Spectral L from IC cal	155.51	229.60	166.41	142.07
% (Code-Pre)/Pre	9.2	-26.8	-6.7	-19.7
% (Code-IC)/IC	.0	-32.1	-12.4	-22.6

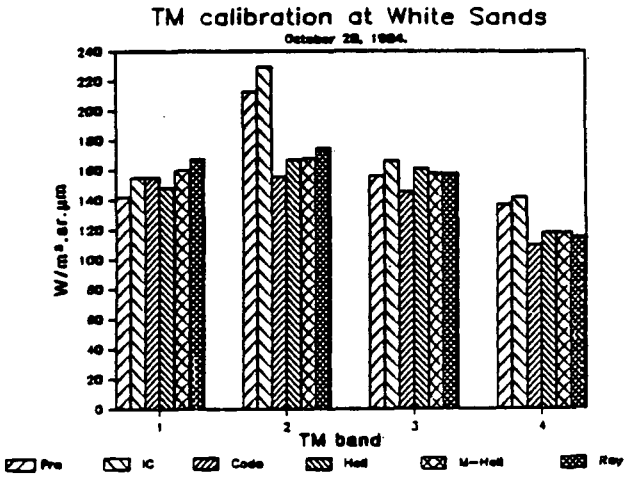

Figure 5. Comparision of results for TM calibration at White Sands, see text.

The results in Figure 5 show anomalously high radiance levels in bands 2 and 4 based on pre-flight and IC calibration data. That the two independent reflectance and radiance-based methods and the Rayleigh case give results that are closely bunched is strong evidence that the pre-flight and IC results are misrepresentative of the calibration of TM on that date. Furthermore, results on other dates (July 8, 1984, May 24, 1985, and August 28, 1985) fail to show this anomaly although there was no change in our measurement methodology, reference panel calibration, and data reduction methods. We have no reason to question the pre-flight or the internal calibrator gain and offset values themselves; we believe the anomalies are more likely the result of a source of radiance

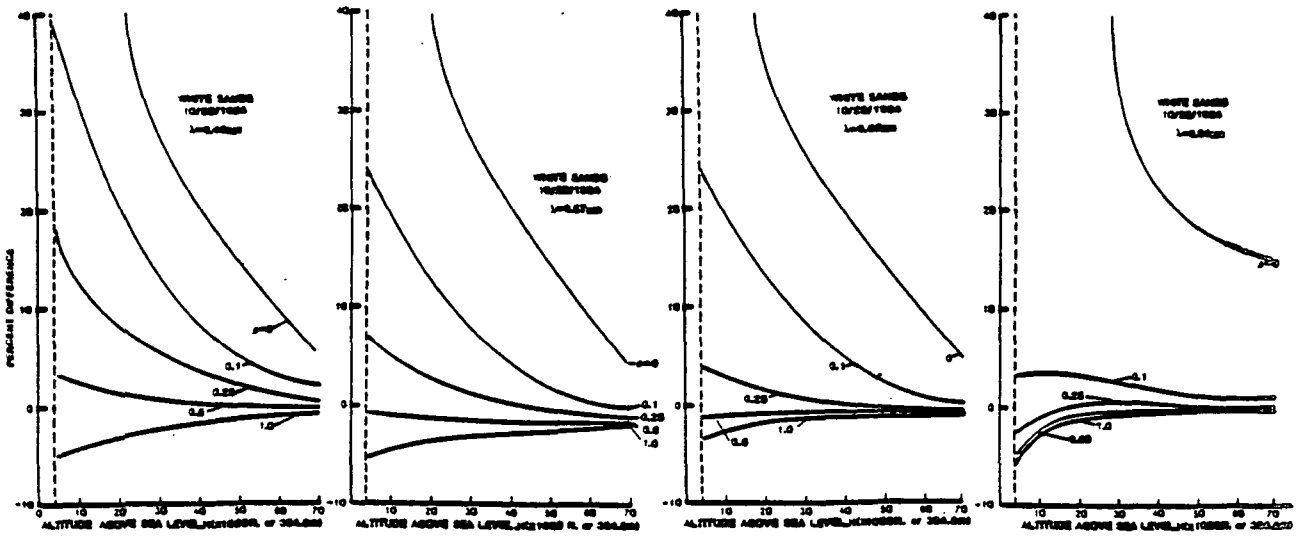

Figure 6. Percentage differences between the radiances at the top of the atmosphere and at intermediate altitudes for the White Sands conditions of October 28, 1984, see Table 1.

in the atmosphere surrounding the spacecraft, perhaps due to luminescence or ionization phenomena. High energy solar UV or X-ray irradiation could be one cause and the passage of the spacecraft through a gas cloud created by an earlier orbit adjustment has been suggested as another. This last hypothesis is based upon the observed deceleration of the spacecraft as it passes through the region in space where the orbit adjustment jets had been previously activated. These decelerations occur for two to three weeks after an orbit adjustment.

The fact that such anomalies were not detected by the internal calibrator is an important reason for using ground-based calibration techniques whenever possible. The following discussion shows that one such technique is easy to implement given a ground reflectance of about 0.5 in each band.

B. Radiance-Based Methods

Figure 5 shows that the radiances as measured at 3000 m above White Sands are about the same as those measured by the Thematic Mapper. This result prompted a more detailed examination of the variation of radiance with altitude as a function of wavelength, reflectance, and visibility.

Starting with the atmospheric conditions of October 28, 1984, at White Sands, and with a solar zenith angle of 35 deg, radiance values were calculated for altitudes between ground level (1196 m at White Sands) and 21,000 m (the operational altitude above sea level of the NASA U-2 or ER-2 aircraft) and for above the atmosphere. Graphs were then plotted of the percentage difference (the differences between the radiance above the atmosphere and at an intermediate altitude divided by the radiance above the atmosphere, the whole quantity expressed as a percentage) against altitude above sea level. These are shown in Figure 6, for the first four solar reflective TM bands. As anticipated, the results for reflectances less than 0.1 show large percentage differences, but what is intriguing is the sign change in the percentage difference for reflectances between 0.25 and 1.0 for bands 1, 2, and 3 and between 0.1 and 0.25 for band 4. These results show that, for a reflectance of 0.5 and an altitude of 3000 m ASL, the percentage differences are +2.5, -1.0, -1.0, and -2.0 for bands 1, 2, 3, and 4 respectively. This indicates that for the White Sands conditions of 28 October, 1984, helicopter radiance values at an altitude of 3000 m are close to those for space and require only a small correction, which can be made accurately.

With this promising result, the investigation was extended to determine how general this condition might be. Visibilities of 10 and 23 km were considered for a reflectance of 0.5 at all wavelengths. The input values are listed in Table 2, the refractive index was 1.54 - 0.01i in all cases and Junge ν values of 2.9 and 2.6 were used for the visibilities of 10 and 23 km respectively.

The output plots of percentage difference, as defined earlier, against altitude above sea level are shown as Figures 7 and 8 together with the Rayleigh atmosphere curve for a wavelength of 0.49 um. The positive difference for λ = 0.49 um is due to the fact that the large path radiance term contributed more to the total radiance than is lost by the attenuation of the ground reflected

TABLE 2. Input Values for Radiative Transfer Calculations

Wavelength um	τ_{RAY}	τ_{O2}	τ_{H_2O}	τ_{CO_2}	V=10 km τ_{MIE}	V=23 km τ_{MIE}
0.49	0.1630	0.0066	0.0	0.0	0.5393	0.2927
0.57	0.0844	0.0277	0.0	0.0	0.4665	0.2657
0.66	0.0466	0.0136	0.0	0.0	0.4089	0.2434
0.84	0.0178	0.0016	0.0335	0.0	0.3303	0.2111
1.64	0.0011	0.0	0.0915	0.0094	0.1766	0.1391
2.22	0.0004	0.0	0.0594	0.0035	0.1374	0.1176

term. The other curves show increasing negative differences for altitudes approaching ground level, owing to the heavy aerosol loading in the lower atmosphere. The bowing of the λ = 0.57 um and 0.66 um curves at intermediate altitudes is due to reduced path radiance from Rayleigh scattering and

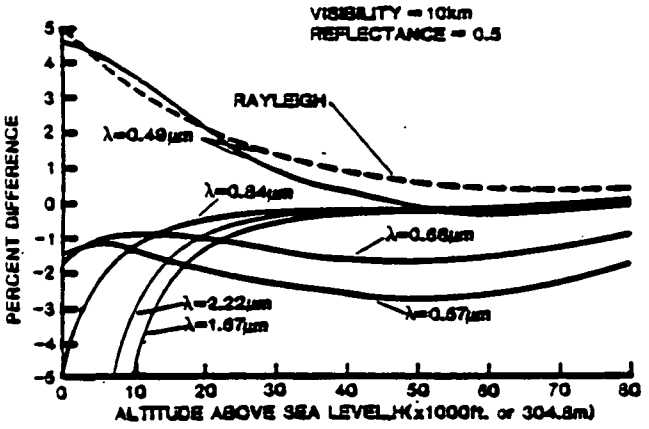

Figure 7. Percentage differences between the radiances at the top of the atmosphere and at intermediate altitudes for ρ=0.5 and a visibility of 10 km.

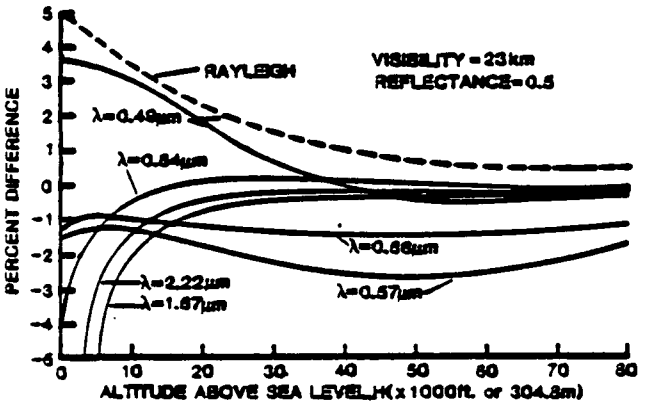

Figure 8. Percentage differences between the radiances at the top of the atmosphere and at intermediate altitudes for ρ=0.5 and a visibility of 23 km.

the presence of ozone absorption at those altitudes. Note that for an altitude of 3000 m and a visibility of 23 km the percentage differences are +3.0, -1.4, -0.9, -0.8, -2.3, and -1.6 for wavelengths of 0.49, 0.57, 0.66, 0.84, 1.67, and 2.22 um respectively. Furthermore the percentage differences are less than twice these values for a visibility of 10 km, as can be seen from the remarkable similarity between Figures 7 and 8.

Conclusion

The in-flight calibrations of several satellite multispectral sensors have shown substantial changes with time. The CZCS has shown what is believed to be a monotonic decrease in response for all wavelengths, with the decrease greater for shorter wavelengths. The same is true for TM for the solar reflective bands with the following two exceptions: The mid-IR bands show oscillitory changes, and our results for October 28, 1984, show anomalously high responses in bands 2 and 4.

That the degradation in response of the CZCS was not detected by the on-board calibration system and our anomalous results for TM were not detected by the IC is evidence of the desirability of using some calibration procedure that involves imaging the Earth's surface and applying atmospheric corrections.

The in-flight calibration of satellite sensors by reference to ground reflectance measurements can be conveniently checked by the use of low altitude (3000 m) helicopter radiance measurements. Without correction the latter are within ±3 percent of the satellite values for the solar reflective bands of TM, and with correction they are limited by the uncertainty in the absolute calibration of the helicopter radiometer. They do require a ground reflectance of about 0.5 but they are insensitive to atmospheric conditions for a wide range of visibilities above about 15 km. Compared to satellite calibration by reference to high altitude aircraft measurements, the helicopter method enjoys the advantage of lower cost, longer dwell time over the area of interest, and the capability of averaging over a 50 m diameter pixel with a 1 degree field of view instrument from 3000 m altitude.

Again, because of the many difficulties that beset the in-flight absolute radiometric calibration of satellite systems, we are not proposing that one method be used to the exclusion of others. Whenever possible, effort should be made to coordinate different but simultaneous measurements over a given site with instruments that have been intercompared in the laboratory. Only by such a concerted effort will we be able to identify systematic errors and reduce them, and be confident of the uncertainties that we ascribe to our calibrations.

Acknowledgments

I wish to thank many colleagues for their contributions to our program on satellite sensor calibration, and the National Aeronautics and Space Administration who supported this work at the Optical Sciences Center.

References

[1] Slater P N 1984, The importance and attainment of absolute radiometric calibration, in *Proc. SPIE Critical Review of Remote Sensing* 475, 34-40.

[2] Slater P N 1985, Radiometric considerations in remote sensing, *Proc. IEEE* 73(6), 997-1011.

[3] Gordon H R 1981, Reduction of error introduced in the processing of coastal zone color scanner-type imagery resulting from sensor calibration and solar irradiance uncertainty, *Appl. Opt.* 20, 207-210.

[4] Frohlich C 1983, Data on total and spectral irradiance: comments, *Appl. Opt.* 22, 3928.

[5] Viollier M 1982, Radiometric calibration of the Costal Zone Color Scanner on Nimbus 7: a proposed adjustment, *Appl. Opt.* 21, 1142-1145.

[6] Gordon H R et al 1983, Phytoplankton pigment concentrations in the Middle Atlantic Bight: Comparison of ship determinations and CZCS estimates, *Appl. Opt.* 22, 20-36.

[7] Aranuvachapun S 1983, Variation of atmospheric optical depth for remote sensing radiance calculations, *Remote Sens. Environ.* 13, 131-147.

[8] Gordon H R et al 1983, Nimbus 7 CZCS: reduction of its radiometric sensitivity with time, *Appl. Opt.* 22, 3929-3931.

[9] Hovis W A et al 1985, Aircraft measurement for calibration of an orbiting spacecraft sensor, *Appl. Opt.* 24, 407-410.

[10] Mueller J L 1985, Nimbus-7 CZCS: confirmation of its radiometric sensitivity decay through 1982, *Appl. Opt.* 24, 1043-1047

[11] Lee Y & Barker J L (1984) Thematic mapper radiometric and algorithm performance program (TRAPP), available courtesy J L Barker at *NASA Goddard Space Flight Center.*

[12] Koepke P 1982, Vicarious satellite calibration in the solar spectral range by means of calculated radiances and its application to Meteosat, *Appl. Opt.* 21, 2845-2854.

[13] Kastner C J & Slater P N 1982, In-flight radiometric calibration of advanced remote sensing systems, *Proc. SPIE* 356, 158-165.

[14] Castle K R et al 1984, In-flight absolute radiometric calibration of the Thematic Mapper, *IEEE Trans. Geosci. Remote Sensing* GE-22, 251-255.

[15] Herman B M & Browning S R 1975, The effect of aerosols on the earth-atmosphere albedo, *J. Atmos. Sci.* 32, 158-165.

Survey of Multispectral Imaging Systems for Earth Observations

PHILIP N. SLATER

Committee on Remote Sensing and Optical Sciences Center, University of Arizona, Tucson, AZ 85721

Fifty-six multispectral imaging systems are described in terms of their instantaneous fields of view, spectral bands, fields of view, and number of quantization levels. These systems have been used during the past decade for earth resources studies from aircraft or spacecraft, or are currently in the proposal or design and development stage.

Introduction

An increasing interest worldwide in research and applications studies in remote sensing, together with the development of new types of optical detectors and systems, has led to a recent proliferation of multispectral imaging systems[1] for use on aircraft and spacecraft. Most of these systems are experimental, their purpose being to determine the optimum selection of spectral bands and the spatial and radiometric resolutions suitable for different research and applications studies.

The purpose of this paper is to provide a listing of these systems as a convenient reference for remote sensing investigators and systems engineers. For space systems, the listing includes, to the author's knowledge, all past and present systems and those planned for the future. With respect to airborne systems the listing is not exhaustive. For example, military systems, such as forward-looking infrared systems, are not included, nor are multispectral video cameras, which are becoming increasingly popular for aerial remote sensing in the visible and near infrared. Also, when improvements have been made to a particular system, only the latest model is described.

In addition to the references cited in the listing, there are several general references worthy of note. Due (1982) describes in considerable detail many military and civilian systems, both past and present, among them the AVHRR-2, M^2S, Landsat MSS, S-192, TM, and VISSR, which are listed in the appendix. (The acronyms are defined in the appendix.) Doyle (1984) and the Landsat Data Users Notes (1982) describe the status of space remote sensing plans worldwide for scanners, film cameras, and microwave sensors. Slater (1980) describes in detail many past and present space systems. Holmes (1984) discusses several advanced sensor systems.

Many authors have suggested spectral bands for earth observation purposes, among them the following: Begni (1982) describes the rationale for the choice of the SPOT HRV bands; Cihlar et al. (1984) describe the choice for Radarsat; and Colvocoresses (1979) describes the choice for Mapsat. Stoner and Baumgardner (1980) discuss the location of bands most

[1] For the purpose of this survey, the term "multispectral imaging system" includes any optical system that scans the object or image surface electromechanically or electronically in more than one wavelength interval. It excludes photographic film cameras and nonimage-forming spectroradiometers.

52 Vanderbilt Ave., New York, NY 10017

0034-4257/85/$3.30

suitable for soil classifications. Siegrist and Schnetzler (1980) discuss the location of bands for geological applications. Wiersma and Landgrebe (1979) discuss the location of bands suitable for vegetation monitoring. Tucker (1978) lists the desirable bands for vegetation monitoring in order of priority.

Vane et al. (1982) summarize the recommendations in some of the published literature and in the Multispectral Resource Sampler (MRS) workshop, described in the ORI Report (1979), regarding the spatial and spectral requirements for future sensor systems. Cox (1982) summarizes discussions of the Multispectral Imaging Science Working Group convened by NASA, which included a Botanical Sciences Team, a Geographic Sciences Team (including panels on land use and land cover, geomorphology, and cartography), a Hydrologic Sciences Team, a Workshop for Lithologic Mapping, an Imaging Science Panel, and an Information Science Panel.

System Characteristics

The appendix lists the multispectral imaging systems and satellites for earth observations as well as spectral band recommendations of science working groups concerned with the definition of future systems. The listing includes references to publications that describe these systems or recommendations in detail or to the individuals who supplied the information.

The following comments relate to the Appendix:

1. Thirteen countries and the European Space Agency (ESA), have been or are involved in the development of one or more of the systems.
2. Of the 56 systems listed, 11 are no longer in use, 23 are currently in use, and 22 are proposed or in the design and development phase.
3. Of the 56 systems, 32 are spacecraft systems, of which three are primarily meteorological systems, 23 are aircraft systems, and 1 has been used both as an aircraft and a spacecraft system.
4. Of the 56 systems, 24 are mechanical scanners, 20 are pushbroom scanners using linear detector arrays, 5 are television systems (four of which use vidicons and one of which uses an area detector array); 5 are imaging spectrometers using area detector arrays; and 2 are spin-scan systems.

Discussion

All numerical data listed in the appendix should be taken as nominal or projected values. Depending on the system and the source reference, however, they may be accurately measured quantities. In some cases the systems are in the planning stage and may change substantially before fabrication. The reader should refer to the listed references to obtain further details and to form an opinion on the reliability of the data quoted in the references.

This survey shows that many different kinds of multispectral imaging systems are now available for research and application purposes in remote sensing, and that the number, availability, and improved performance of linear and area arrays of detectors, using mainly CCD and CID readouts, has encouraged several groups to explore their application as

aircraft and spacecraft remote sensing systems.

The advantages of using these detectors are that a scanning mirror is no longer required, the system can be pointed for stereo imaging or for more frequent imaging of a given area, and the integration time and therefore the signal-to-noise ratio and radiometric sensitivity are higher than for the equivalent mechanical scanner.

The shortcomings of silicon CCDs and CIDs are that their long-wavelength cutoff is 1.1 μm and, unless carefully selected, they exhibit large nonuniformities in response and noise properties. However, improvements in the yields of high performance CCDs and CIDs and the production of IRCCDs are subjects of substantial research and development activity. So, although few linear or area CCD or CID systems are currently in use, we can expect them to rival the worldwide data output of mechanical scanners, both in volume and spectral coverage, by the end of the decade.

In addition to those persons mentioned in the references as having provided information on certain systems, I should like to thank K. J. Ando, W. L. Barnes, C. D. Mason, and M. S. Maxwell for their inputs and comments, and acknowledge financial support from NASA grant NAG 5-196.

Appendix: List of Multispectral Imaging Systems and Satellites for Earth Observations, and Spectral Band Recommendations of Science Working Groups Concerned with the Definition of Future Systems

AADS-1260 Daedalus airborne multispectral scanner. The AADS series of mechanical scanners is commercially available for airborne use; referenced here is the 11-band system. IFOV 2.5 mr, field of view 86°, 8-bit quantization. Spectral bands: 0.38–0.42, 0.42–0.45, 0.45–0.50, 0.50–0.55, 0.55–0.60, 0.60–0.65, 0.65–0.69, 0.70–0.79, 0.80–0.89, 0.90–1.1, 10.4–12.5 μm (Daedalus Enterprises, Inc.).

AADS-1268 This is an extensively modified version of AADS-1260 (above) for use as a Thematic Mapper (see TM) simulator. The IFOV can be selected to be 2.5 or 1.25 mr with field of view 86° or 43°, respectively. Spectral bands: 0.42–0.45, 0.45–0.52, 0.52–0.60, 0.605–0.625, 0.63–0.69, 0.695–0.75, 0.76–0.90, 0.91–1.05, 1.55–1.75, 2.08–2.35, 8.5–13 μm. Note that the thermal band is wider than that of the Thematic Mapper and that there are four additional bands (Daedalus Enterprises, Inc.).

AEROS-A Advanced Earth Resources Observational Satellite-A, proposed for 1986 launch financed by Space America. The payload consists of two 4-band linear array sensors, one looking 22.5° forward and 5° starboard, the other 22.5° aft and 5° port. The 0.63–0.69 μm band

in the former and the 0.6–0.7 μm band in the latter will have a 45-m IFOV and a 149-km swath; the other bands will have an 80-m IFOV and a 165-km swath. The second sensor will image the same ground swath as the first but one day later, providing stereo data with a base-to-height ratio of 0.83 and a height resolution of 104 m. The orbit is that of Landsats 1-3 (see Landsat). 8-bit quantization, 18-Mb/s bandwidth using X-band. Spectral bands: 0.45–0.52, 0.52–0.6, 0.63–0.69, 0.76–0.9 μm for the forward looking sensor and 0.433–0.53, 0.54–0.56, 0.6–0.7, 0.7–0.8 μm for the aft looking sensor (Lowndes, 1983).

AIS — Airborne Imaging Spectrometer. This system was recently built and tested at the Jet Propulsion Laboratory for measurements in the 1.2–2.4 μm range. IFOV 2 mr, field of view 3.6°, 8-bit quantization. A 32×32 detector area array is stepped four times during data collection to provide 128 bands in the in-track direction, each having 10-nm bandwidth (Vane et al., 1983).

AMSS — Australian Multispectral Scanner System. (The system is actually known as MSS, but AMSS is used here to avoid confusion with Landsat MSS.) A mechanical scanner for aircraft use under development in Australia, primarily for ocean color studies. IFOV 4 mr, field of view 40°, 8- or 10-bit quantization. Spectral bands: 0.345–0.395, 0.43–0.45, 0.45–0.47, 0.47–0.48, 0.49–0.51, 0.51–0.53, 0.53–0.55, 0.68–0.69, 0.975–1.025 μm (Cartwright, 1983).

ASAS — Advanced Solid-state Array Spectroradiometer. Modification of an existing aircraft system by NASA Johnson Space Center to include a 512×32 CID array in the focal plane of a grating spectrometer that will provide 32 contiguous spectral bands 14-nm wide covering the range 0.40 to 0.85 μm or 0.50 to 0.95 μm. The IFOV will be 0.34 or 0.854 mr, the field of view 10° or 25°, and there will be 12-bit quantization with variable gain and offset before quantization. The system is designed to map chlorophyll, determine chlorophyll profiles, and study ocean surface effects. The spectral bands for this system are to be determined (Stewart and Buntzen, 1982).

AVHRR-2 — Advanced Very High Resolution Radiometer. A 5-band mechanical scanner system on a NOAA meteorological satellite. IFOV 1.1 km, field of view $\pm 56°$, inclination 98.9°, orbit altitude 862 km, repeat coverage interval 12 h. To map cloud cover, surface, and cloud top temperatures, land–water boundaries, and snow and ice coverage. Spectral bands: 0.58–0.68, 0.725–1.0, 3.55–3.93, 10.2–11.3, 11.5–12.5 μm (Due, 1982; Schneider and McGinnis, 1982).

AVIRIS — Airborne Visible-InfraRed Imaging Spectrometer. A mechanical scanner imaging spectrometer capable of operating in as many as 224 spectral bands in the 0.4 to 2.4 μm region. Under construction at the Jet Propulsion Laboratory as an airborne research instrument for development of new data analysis methodologies for use with imaging spectrometer data. IFOV 1.0 mr, field of view 30°, 10-bit quantization, data rate 15 Mb/s (Vane et al., 1984).

Bhaskara-2 — An Indian system launched on 20 November 1981 that consisted of a 2-band TV camera system with 1-km IFOV. Eccentric orbit varying between 514 and 557-km altitude at 50° inclination. Spectral bands: 0.54–0.65 and 0.75–0.85 μm (Doyle, 1984).

BST — Botanical Science Team, a group of 21 participants convened by NASA in 1982 to recommend research activities and parameters for future sensors. Recommended spectral bands: 0.54–0.56, 0.65–0.67, 0.84–0.86, 1.52–1.74, 2.08–2.32, 3.5–3.9, 10.5–12.5 μm (Cox, 1982).

CAESAR — CCD Airborne Experimental Scanner for Applications in Remote sensing. A modular CCD pushbroom system in the development phase at the National Aerospace Laboratory NRL and at the Institute of Applied Physics TPD, both in the Netherlands. IFOV 0.3 mr, field of view 25°, 12-bit quantization. Capability of 54° forward look for canopy and water studies. Spectral bands: 0.405–0.415, 0.51–0.53, 0.535–0.565, 0.555–0.575, 0.62–0.64, 0.655–0.685, 0.675–0.695, 0.77–0.80, 0.825–0.875 μm (Bunnik, 1984b).

CBML/CSIRO — A modular mechanical 15-channel scanner for aircraft use being developed by Carr Boyd Minerals Limited and the Commonwealth Scientific and Industrial Research Organization, Australia. IFOV 5 mr, field of view 90°. Can be used in an active mode using a laser. Prototype band selections: 0.45–0.55, 0.55–0.6, 0.65–0.7, 0.83–0.87, 0.93–0.97, 1.55–1.65, 1.98–2.08, 2.13–2.23, 2.3–2.4, 7.75–8.75, 8.75–9.35, 9.25–10.25, 10.75–11.25, 11.75–12.25 μm (Lyon, 1983).

CZCS — Coastal Zone Color Scanner. A 6-band mechanical scanner orbited on Nimbus 7 on October 1978 in a 955-km circular, sun-synchronous orbit. IFOV 800-m, swath 1600-km, 8-bit quantization. Modifications to the system are being studied with the anticipation of orbiting a modified 8-band unit on the TIROS-N series (NOAA-H and/or I). The Tiros system may have a 980-m IFOV. For determining global oceanic chlorophyll concentration and diffuse attenuation coefficients and sediment transport in coastal zones. Spectral bands for Tiros and Nimbus systems: 0.43–0.45, 0.48–0.50, 0.51–0.53,

0.55–0.57, 0.58–0.60, 0.66–0.68, 0.75–0.79, 0.84–0.89 μm (Barnes, 1983).

FILE — Feature Identification and Location Experiment. A 2-band CCD system flown on the second Shuttle. The system consisted of two filtered CCD area array cameras, each array consisting of 100×100 detectors. The IFOV was 1×0.75 km and the field of view 17° by 23°. The orbit was circular at an altitude of 255 km with a period of 1 hr 29 m 40 s. Data were collected on 12–14 November 1981. Spectral bands: 0.64–0.66 and 0.84–0.86 μm (Silverton et al., 1982).

FLD — Fraunhofer Line Discriminator. A variable single-band, aircraft, mechanical scanner for detecting solar-stimulated luminescence. Operates in Fraunhofer absorption lines, typically H_α at 656.3 nm, Na at 589.0 nm, Mg at 518.4 nm, H_β at 486.1 nm, Ca at 422.7 nm. Uses Fabry-Perot filter with < 0.1-nm halfwidth. IFOV 1°, field of view 37° (Hemphill, 1981; Slater, 1980; Watson and Theisen, 1981).

FLI — Fluorescence Line Imager. A programmable spectroscopic imaging system with five two-dimensional CCD array sensors operating in a pushbroom mode being designed by Moniteq Ltd. of Canada for delivery in January 1985 to the Canadian Department of Fisheries and Oceans and to be flown in an aircraft of the Canada Centre for Remote Sensing. The FLI can operate over the range 0.42 to 0.81 μm with 1.9-nm bandwidths and a choice from 256 spectral channels. Eight spectral bands can be used in two configurations, one for general chlorophyll mapping (A) and one for studying fluorescence line properties (B). IFOV 1 mr. Each sensor covers about 15° to give a total field of view of 73°, 12-bit quantization. Typical spectral bands: 0.433–0.453 (A&B), 0.510–0.530 (A), 0.540–0.560 (A&B), 0.633–0.644 (A), 0.66–0.671 (A&B), 0.671–0.682 (A&B), 0.682–0.685 (B), 0.685–0.690 (B), 0.708–0.714 (A&B), 0.746–0.754 (A), 0.772–0.790 (B) μm (Edel, 1982; Gower, 1982).

Fragment-2 — 8-band mechanical scanner orbited as part of the Meteor spacecraft payload (see Meteor), by the USSR. IFOV 80 m, swath width 85 km. Spectral bands: 0.40–0.80, 0.50–0.60, 0.60–0.70, 0.70–0.80, 0.70–1.1, 1.2–1.3, 1.5–1.8, 2.1–2.4 μm (Avanesov et al., 1981).

HCM — Heat Capacity Mapper. A 2-band mechanical scanner used on a U-2 in support of the HCMR (see below). IFOV 2.8 mr, field of view 90°. Spectral bands: 0.51–0.89 and 10.44–12.52 μm (Price, 1984).

HCMR — Heat Capacity Mapping Radiometer. A 2-band mechanical scanner launched 26 April 1978 into nearly sun-synchronous 620-km circular orbit at 97.6° inclination, repeat coverage interval 16 days. IFOV 0.5 km in visible, 0.6 km in IR, swath width 716 km. Equatorial crossing times 0230 and 1330. Spectral bands: 0.55–1.1 and 10.5–12.5 μm (Price, 1978; Slater, 1980).

HRV — High Resolution Visible. Two HRV systems, which are CCD pushbroom scanners, are under construction for the French Centre National d'Etudes Spatiales in association with Belgium and Sweden. The HRV systems will be launched on SPOT (see SPOT). Each HRV will operate in 3 spectral bands with an IFOV of 20 m or 1 panchromatic band with an IFOV of 10 m. Each covers a 60-km swath with 8-bit quantization. Pointing mirror to $\pm 27°$ cross-track can provide stereo or repeat coverage interval at least every 5 days. Data rate 48 Mb/s for both HRV systems, transmitted in X-band. Spectral bands: 0.50–0.59, 0.61–0.68, 0.79–0.89 μm. Panchromatic band: 0.51–0.73 μm (Midan et al., 1982).

IRS — Indian Resources Satellite, see LISS.

JERS-1 — Japanese Earth Resources Satellite. Proposed by the Japanese Science and Technology Agency for a Launch in 1989–90, it is a linear array stereo camera with 30-m IFOV and four spectral bands between 0.51 and 1.1 μm. No further details are available (Doyle, 1984).

Landsat — A NASA program and five associated satellite instrument payloads. The first payload launched on 23 July 1972 (then called the Earth Resources Technology Satellite and now Landsat-1), included a multispectral Return Beam Vidicon (RBV) system, a four-band Multispectral Scanner System (MSS), and a Data Collection System (DCS). (See the Landsat Data Users Handbook, 1979.) Landsat-2, launched on 22 January 1975, contained instruments with the same nominal characteristics as Landsat-1. Landsat-3, launched on 5 March 1978, contained a two-camera panchromatic RBV system and an MSS with a fifth band in the thermal infrared. Landsats 1, 2, and 3 were inserted into a circular, near-polar orbit at a nominal altitude of 919 km, with an inclination of 99.11°, a period of 103.27 min, a repeat coverage interval of 18 days, and an equatorial crossing time of nominally 9:30 a.m. (the crossing times could change by an hour during the system's lifetime). Landsat-4, launched in July 1982, contains an MSS with similar characteristics to MSS 1 and 2. It also

contains the 7-band Thematic Mapper but no RBV camera or DCS. The circular orbit is at an altitude of 705 km, inclination is 98.2°, repeat coverage interval is 16 days, and the equatorial crossing time is 0945 ± 15. Landsat-5, identical to Landsat-4, was launched in March 1984 (Landsat Data Users Notes, 1982).

LAPR-II — Linear Array Pushbroom Radiometer. A pushbroom airborne system built and currently under test at NASA Goddard Space Flight Center. IFOV 1.54 mr, field of view 42.5°, 10-bit quantization. There are four lens-detector modules in the system. A filter wheel allows for the selection of 1 of 6 bandpasses per module in flight. The system is pointable through ±45° both in-track and across-track. Spectral bands: 0.40–0.42, 0.45–0.52, 0.49–0.51, 0.52–0.60, 0.54–0.56, 0.63–0.69, 0.67–0.69, 0.71–0.73, 0.73–0.75, 0.76–0.90, 0.78–0.80, 0.84–0.86, 0.88–0.90, 0.93–0.95 μm (Irons et al., 1982).

LISS — Linear Imaging Self-Scanned sensors, three of which are to be flown on the Indian Resources Satellite (IRS-1A), planned launch date 1985–86. LISS-1 will have four spectral bands in the visible and near IR, an IFOV of 73 m, and a swath of 148 km. Two LISS-2 systems will cover adjacent swaths 74-km wide with IFOVs of 37 m in four spectral bands. IRS-1A will be placed into a 904-km sun-synchronous orbit with a 99° inclination, and repeat coverage will be obtained every 22 days. S-band and X-band telemetry. Plans call for the sensors on IRS-1B to provide IFOVs of 15 to 20 m and those on IRS-2 to include middle and thermal IR bands (Doyle 1984).

M^2S — Modular Multiband Scanner. An 11-band airborne mechanical scanner built by Bendix Corp. IFOV 2.5 mr, field of view 100° ± 10°. Spectral bands: 0.38–0.44, 0.44–0.49, 0.49–0.54, 0.54–0.58, 0.58–0.62, 0.62–0.66, 0.66–0.70, 0.70–0.74, 0.77–0.86, 0.97–1.06 μm, and a band of filter-selectable width at approximately 11 μm (Due, 1982).

M-7 — University of Michigan Scanner. A 12-band airborne mechanical scanner used extensively during the Corn Blight Watch experiment in 1971. The scanner has been the property of the Environmental Research Institute of Michigan since 1973 and has been modified several times since 1971. IFOV 2 mr, field of view 90°. Included 17 bands, only 12 of which could be used at one time. Spectral bands: 0.33–0.35, 0.46–0.49, 0.48–0.51, 0.50–0.54, 0.52–0.57, 0.54–0.60, 0.58–0.65, 0.61–0.71, 0.72–0.92, 1.0–1.4, 1.5–1.8, 2.0–2.6, 9.3–11.7 μm (Lowe, 1975; Landgrebe, 1981).

Mapsat — An orbital mapping system, proposed by the U.S. Geological Survey, that can operate in a 3-band multispectral or a panchromatic stereoscopic CCD pushbroom mode. Orbital characteristics are those of Landsats 1, 2, and 3 (see Landsat). Imaging proposed in an epipolar orbit to facilitate stereo compilation. Mixed resolution, the finest being an IFOV of 10 m, 8-bit quantization. Swath width 60 to 185 km depending on imaging mode for bandwidth not to exceed 48 Mb/s. Nadir and $\pm 23°$ viewing to obtain 20-m contours. Spectral bands: 0.47–0.57, 0.57–0.70, 0.76–1.05 μm (Colvocoresses, 1979, 1982; Snyder, 1982).

MEIS-II — Multispectral Electro-optical Imaging Spectrometer. An airborne pushbroom CCD system built in 1982 by Macdonald Dettwiler and Associates Ltd., for the Canada Centre for Remote Sensing. A modular 5-band system with future expansion to 8 bands including IR. Output IFOV (after resampling) 0.71 mr, input IFOV 0.53 mr, 13-μm detectors. Field of view 50° for 24.6-mm lens, 8-bit quantization. Real time resampling to provide band-to-band pixel registration to $\pm 1/8$ pixel. Real time dark current subtraction and relative radiometric calibration. Spectral bands: 0.45–0.52, 0.50–0.60, 0.52–0.60, 0.60–0.70, 0.63–0.69, 0.70–0.80, 0.76–0.90, 0.80–1.1 μm (Hrebenyk, 1982; Macdonald Dettwiler and Associates).

MEOSS — Multispectral Electro Optical Stereo Scanner, a system under study by Deutsche Forschungs- und Versuchsanstalt für Luft und Raumfahrt (DFVLR), West Germany, and India. Five CCD linear arrays are located across the focal plane of a Hasselblad camera using a Zeiss Biogon lens of 61-mm focal length. This arrangement will provide two forward, two aft, and one vertical view of the ground. Depending on the arrays and lens chosen, the IFOVs will be 67 or 150 m and the swath 180 or 350 km. The system will be placed in orbit by the Indian Rohini launch vehicle in April 1985 at an altitude of 400 km and at a 44° inclination. Telemetry bandwidth 12.3 Mb/s. Spectral bands: 0.5–0.6, 0.6–0.7, 0.7–0.8 μm (Doyle 1984).

MESSR — Multispectral Electronic Self-Scanning Radiometer. Two 4-band CCD pushbroom MESSRs are being built by Nippon Electric Co., Inc., as part of the payload for the Japanese Marine Observation Satellite I to be launched in 1986. Sun-synchronous circular orbit, altitude 909 km, inclination 99.1°. Time of descending node between 10 and 11 a.m. IFOV 50 m, swath for both MESSRs combined is 200 km, 6-bit quantization, data rate 8 Mb/s for each system. Spectral bands: 0.51–0.59, 0.61–0.69, 0.72–0.80, 0.8–1.1 μm (Matsumoto, 1981; Ishizawa et al., 1980).

Meteor — An earth observation and meteorology spacecraft orbited by the USSR in June 1980. Eccentric orbit between altitudes of 589 and 678 km with a 90° inclination. Payload contained 5 multispectral systems: MSU-M and MSU-S (together referred to as RTVK), MSU-E and MSU-SK (together referred to as BIK-E), and Fragment-2. Refer to each for further details (Sidorenko, 1981).

Meteosat — A European Space Agency geostationary meteorological spin-scan radiometer located at longitude 0°. East-to-west scan provided by spacecraft rotation round an axis parallel to earth's axis, south-to-north scan provided by small stepping mirror. First system launched in November 1977; second system launched in May 1981; four additional launches planned for the 1980s. From 36,000-km altitude the IFOV is 2.5 km in the visible and near-IR band and 5 km in the IR bands. 6-bit quantization in spectral bands: 0.5–1.0 and 5.7–7.1 μm, and 8-bit in the 10.5–12.5 μm band (Jouan, 1982).

MLA/STS — A Multispectral Linear Array system for the Space Transportation System under development at NASA Goddard Space Flight Center for shuttle flights in the late 1980s. The system has six spectral bands in the 0.45–1.65 μm region: 0.46–0.48, 0.54–0.56, 0.66–0.68, 0.87–0.89, 1.23–1.25, 1.64–1.66 μm. IFOV is 15 m in the first four bands, 30 m in the last two. Swath width is 30 km. The system provides 8-bit quantization with a data rate of 48 Mb/s. Along-track pointing achieved using a steerable mirror, across-track pointing (of $\pm 45°$) achieved by rolling the shuttle (Barnes and Salomonson, 1983).

MOMS — Modular Opto-electronic Multispectral Scanner. A CCD pushbroom system built by Messerchmitt-Bolkow-Blohm for the Shuttle Pallet Satellite (SPAS-01) and flown in July 1983 on the Space Transportation System-7 (STS-7). A two-band system expandable to four bands for subsequent flights, IFOV 20 m, field of view 140 km from shuttle altitude of 296 km; 7-bit quantization. Spectral bands: 0.575–0.625 and 0.825–0.975 μm (Hofmann et al., 1982).

MOS — Marine Observation Satellite, see MESSR.

MRS — Multispectral Resource Sampler. A workshop involving 70 attendees representing user interests met in 1979 to suggest requirements for a new orbital earth resources research system. Spectral bands: 0.36–0.40, 0.40–0.42, 0.41–0.43, 0.43–0.45, 0.44–0.46, 0.48–0.50, 0.53–0.55, 0.54–0.56, 0.58–0.62, 0.59–0.61, 0.66–0.68, 0.67–0.69, 0.73–0.78, 0.74–0.76, 0.76–0.78, 0.78–0.82, 0.84–0.90 μm (ORI Report, 1979).

MSS — Multispectral Scanner System. Five mechanical scanner systems have been orbited as part of the Landsat program (see Landsat). IFOV 76 m for MSS 1 to 3 and 80 m for MSS 4 and 5, swath width 185 km, 6-bit quantization, data rate 15 Mb/s. Spectral bands: 0.5–0.6, 0.6–0.7, 0.7–0.8, 0.8–1.1 μm (Due, 1982; Landsat Data Users Handbook, 1979; Lansing and Cline, 1975; Norwood et al., 1972; Markham and Barker, 1983; Slater, 1979).

MSU-M — A 4-band television system on the Meteor spacecraft (see Meteor). IFOV 1.7×1 km, field of view 1930 km. Spectral bands: 0.50–0.60, 0.60–0.70, 0.70–0.80, 0.80–1.0 μm (Selivanov and Tuchin, 1981).

MSU-S — A 2-band television system on the Meteor spacecraft (see Meteor). IFOV 240 m, field of view 1380 km. Spectral bands: 0.50–0.70 and 0.70–1.1 μm (Selivanov and Tuchin, 1981).

MSU-SA (or SK) — A 4-band conical image scanner on the Meteor spacecraft (see Meteor). IFOV 170 m, field of view 600 km. Spectral bands: 0.50–0.60, 0.60–0.70, 0.70–0.80, 0.80–1.0 μm (Selivanov et al., 1981).

MSU-VA (or E) — A 3-band system using electronically scanned arrays on the Meteor spacecraft (see Meteor). IFOV 30 m, field of view 30 km. Spectral bands: 0.50–0.70, 0.70–0.80, 0.80–1.0 μm (Selivanov et al., 1981).

MULTIFADS — Multispectral Fast Area Digitizing Scanner, a system comprising four filtered cameras each using 128×128 area arrays as detectors, under development for aircraft use in New Zealand. The system operates in the snapshot mode with an IFOV of 0.35°, field of view of 35°, 8-bit quantization. Spectral bands: 0.5–0.6, 0.6–0.7, 0.7–0.8, 0.8–1.1 μm (Hodgson et al., 1981).

NS-001 — An 8-band airborne mechanical scanner thematic mapper simulator system flown from NASA Johnson Space Center during 1978 to 1981 and now from NASA Ames Research Center in an NC-130 aircraft. IFOV 2.5 mr, field of view 100°. Spectral bands: 0.45–0.52, 0.52–0.60, 0.63–0.69, 0.76–0.90, 1.0–1.3, 1.55–1.75, 2.08–2.35, 10.4–12.5 μm.

OCE — See OCS.

OCM — Ocean Color Monitor. A 13-band CCD pushbroom system proposed by the European Space Agency. Sun-synchronous orbit altitude 777 km, equatorial crossing time 11 a.m., inclination 99°, repeat coverage interval of 3 days. IFOV 800 m (with 200 m a design goal), field of view 80°, 11-bit quantization. Data rate 20.8 and 2.5 Mb/s for IFOVs of 200 and 800 m, respectively. Spectral bands: 0.39–0.41, 0.435–0.455, 0.51–0.53, 0.555–0.575, 0.63–0.65, 0.675–0.695, 0.77–0.8, 0.99–1.05, 1.5–1.7, 3.5–3.9, 8.25–8.75, 10.3–11.3, 11.5–12.5 μm.

OCS (I-III) — Ocean Color Scanner. Three 10-band mechanical scanners flown in different configurations by NASA Goddard Space Flight Center on a U-2, a Lear Jet, and the Shuttle. [The Shuttle system is referred to as the Ocean Color Experiment (OCE) and uses eight slightly different bands than the OCS.] IFOV 3.5 mr, field of view 90°, 10-bit quantization. Spectral bands: 0.455–0.475, 0.485–0.505, 0.515–0.535, 0.546–0.566, 0.577–0.597, 0.609–0.629, 0.642–0.662, 0.673–0.693, 0.727–0.749, and 0.763–0.783 μm modified to 0.498–0.518, 0.528–0.548, 0.560–0.580, 0.588–0.608, 0.620–0.640, 0.655–0.675, 0.683–0.703, 0.717–0.737, and 0.822–0.842 μm (Kim et al., 1980).

OCTS — Ocean Color and Thermal Scanner, a Japanese mechanical scanner for a post-1992 proposed launch of MOS-2. IFOV 1 km, swath 1400 km. Spectral bands: 0.43–0.45, 0.5–0.53, 0.54–0.58, 0.65–0.67, 0.75–0.79, 10.5–11.5, 11.5–12.5 μm.

Push-broom — A 4-band airborne pushbroom scanner built by CNES. System can be rotated by $\pm 26°$ to provide lateral stereo. Each band uses a single 1728 detector linear array with a choice of lenses of focal lengths 55, 32, or 18 mm. IFOV 0.24, 0.41, or 0.72 mr, field of view 22.6, 37.9, or 62.9°, respectively. 10-bit quantization. Selectable spectral bands in the range 0.4–1.1 μm. CNES uses a set that nominally matches that of the SPOT/HRV. Mid-IR bands are planned. (Laporte, 1981; Begni, 1983).

Radarsat — The primary payload proposed by the Canada Centre for Remote Sensing is a C-band synthetic aperture radar. The secondary payload proposed comprises three optical sensors: a high resolution (10 m) and a low resolution (1000 m) subsystem, and a cloud sensor. Only the former is described here. From an altitude of 1000 km the IFOV will be 10 m and the swath 100 km. The NE$\Delta\rho$ will be 0.1% of full scale with 10-bit quantization. A mirror will provide cross-track pointing to $\pm 43°$. Initial data rate is 448 Mb/s. The data will be compressed before transmission. The seven spectral bands tenta-

tively proposed are: 0.43–0.45, 0.51–0.53, 0.54–0.56, 0.64–0.69, 0.80–0.90, 1.55–1.75, 2.08–2.35 μm (Cihlar et al., 1984).

RBV — Return Beam Vidicon. Three differently filtered return beam vidicon cameras were boresighted on Landsat-1 and -2 to provide multispectral imagery. Only a small amount of data was collected on Landsat-1 because of an electrical difficulty, and it was found that the imagery from the MSS was preferred from a radiometric standpoint. The multispectral system was replaced on Landsat-3 by a panchromatic system of half the IFOV. The multispectral RBV had an IFOV of about 70 m and a swath of 185 km. Spectral bands: 0.475–0.575, 0.58–0.68, 0.69–0.83 μm (Landsat Data Users Handbook, 1979; Slater, 1980).

S-192 — A 13-band conical scanner flown as part of the Earth Resources Experiment Package on Skylab. Data were collected from May 25, 1973, to February 8, 1974. Circular orbit altitude 435 km, inclination 50°, repeat coverage every 5 days. IFOV 87 m, swath width 11°. Spectral bands: 0.41–0.46, 0.46–0.51, 0.52–0.56, 0.56–0.61, 0.62–0.67, 0.68–0.76, 0.78–0.88, 0.98–1.08, 1.09–1.19, 1.20–1.30, 1.55–1.75, 2.10–2.35, 10.2–12.5 μm (Due, 1982; Abel and Reynolds, 1974).

SISEX — Shuttle Imaging Spectrometer Experiment, proposed by Jet Propulsion Laboratory for a late 1980s Shuttle flight. The system has 128 contiguous spectral bands in the 0.4 to 2.5-μm region with 10-nm spectral resolution in the 0.4 to 1.0-μm region and 20-nm spectral resolution in the 1 to 2.5-μm region. IFOV 30-m, swath width 12.1 km from 250-km altitude. $\pm 20°$ cross-track and $\pm 45°$ pointing along-track obtained by means of steerable mirrors. The system provides 8-bit quantization and an initial data rate of 103 Mb/s reduced with on-board editing to 50 Mb/s (Wellman et al., 1983).

SPOT — Système Probatoire d'Observation de la Terre. The SPOT satellite is a multimission platform to be first launched by an Ariane-2 launcher in 1985 and placed in a circular sun-synchronous orbit of 832-km altitude and 98.7° inclination. Payload will consist of two HRV systems (see HRV). Equatorial crossing time will be 10:30 a.m.

STIMS — Shuttle Thermal Infrared Multispectral Scanner. A pushbroom version of TIMS proposed by JPL as a Shuttle experiment for 1988. IFOV 30-m, swath 12-km, 8-bit quantization. Spectral bands: 8.2–8.6, 8.6–9.0, 9.0–9.4, 9.4–10.2, 10.2–11.2, 11.2–12.2 μm (Kahle, 1984).

Supercyclope — A 4-band airborne mechanical scanner for the middle and thermal IR built by the Société Anonyme de Télécommunication (SAT). Focal length 145 mm, IFOV 1.72 mr, field of view 90°. Analog output. Spectral bands: 3.6–4.3, 7.3–8.3, 8.4–9.5, 9.5–11.3 μm (Begni, 1983).

SWIR-LAPR — Short Wave InfraRed Linear Array Pushbroom Radiometer. A single-band aircraft system with three in-flight commandable spectral filters used at NASA Goddard Space Flight Center for geological studies. IFOV 5 mr, field of view 18.5°. Spectral filters: 1.0–1.5, 1.61–1.69, 2.14–2.30 μm (Mason, 1984).

TERS — Tropical Earth Resources Satellite, a joint Indonesia-Netherlands program. The sensor is a three spectral band system of 20-m IFOV and panchromatic band of 10-m IFOV with a swath of 100 km. High equatorial orbit, altitude 1680 km, 0° inclination, providing 2.5-day repeat coverage. Use of a pointing mirror can increase frequency to a few repeated acquisitions each day, a capability that is desirable for regions frequently covered by cloud. A thermal IR sensor has also been suggested to provide a 100-m IFOV over a 100-km swath. NE$\Delta\rho$ 0.5%, NEΔT 0.5 K at 300 K, 8-bit quantization. Spectral bands: 0.49–0.59, 0.61–0.685, 0.75–0.835, 10.4–12.5 μm with a panchromatic band from 0.49–0.685 μm (Bunnik, 1984a).

TIMS — Thermal Infrared Multispectral Scanner. A 6-band mechanical scanner delivered by Daedalus as the AADS 1285 TIMS System to NASA-NSTL Earth Resources Laboratory in 1982. IFOV 2.5 mr, field of view 76.6°, 8-bit quantization. NEΔT between 0.09 and 0.32 K at 300 K, depending on spectral band. Spectral bands: 8.2–8.6, 8.6–9.0, 9.0–9.4, 9.4–10.2, 10.2–11.2, 11.2–12.2 μm (Kahle and Goetz, 1983).

TM — Thematic Mapper. A 7-band mechanical scanner orbited by NASA with MSS-4 and -5 as part of the Landsat-4 and -5 payloads in July 1982 and March 1984, respectively. Sun-synchronous circular orbit, altitude 705 km, inclination 99.1°, equatorial crossing time 9.45 a.m., repeat coverage interval every 16 days. IFOV 30 m (except for band 6, which is 120 m), swath 185 km, 8-bit quantization, data rate 85 Mb/s. Spectral bands: 0.45–0.52, 0.52–0.60, 0.63–0.69, 0.76–0.90, 1.55–1.75, 2.09–2.38, 10.4–12.5 μm (Engel and Weinstein, 1982; Slater, 1980).

U-2 TMS — Thematic Mapper Simulator flown on a U-2 or an ER-2 aircraft at 20-km altitude by NASA Ames Research Center. Of the 11 spectral

bands available, 7 are the same as those for the Thematic Mapper. IFOV 1.3 mr, field of view 43°, 8-bit quantization.

VISSR — Visible-Infrared Spin-Scan Radiometer. A 2-band spin-scanned system in geostationary orbit providing images every 30 min. System is on the Synchronous Meteorological Satellites (SMS 1 and 2), the Geostationary Operational Environmental Satellites (GOES 1, 2, and 3), and Japan's Geostationary Meteorological Satellite (GMS 1 and 2). IFOV 0.025×0.021 mrad, field of view $18° \times 20°$. Spectral bands: 0.55–0.75 and 10.5–12.5 μm (Due, 1982).

VTIR — Visible and Thermal Infrared Radiometer. A Japanese system to be part of the Marine Observation Satellite (see MOS) payload for measuring sea surface temperature. Visible band, 0.5–0.7 μm, has IFOV of 0.9 km; three bands in the IR, 6–7, 10.5–11.5, and 11.5–12.5 μm, have IFOV of 2.7 km. Swath width 500 km. NE $\Delta T \leqslant 0.5$ K at 300 K (Ishizawa, 1981).

References

Abel, I. R., and Reynolds, B. R. (1974), Skylab multispectral scanner (S-192)—Optical design and operational imagery, *Opt. Eng.* 13:292–298.

Avanesov, G. A., Glazkov, V. G., Ziman, Ya. L., Ignatenko, S. A., Kurmanaliev, T. I., Murav'ev, V. M., Rozhavskii, E. I., Tarnopol'skii, V. I. Fuks, V. I., and Shcherbakov, V. V. (1981), Fragment multispectral scanner system, *Sov. J. Remote Sensing* 5:726–741.

Barnes, W. L. (1983), NASA Goddard Space Flight Center, U.S.A. Personal communication.

Barnes, W. L., and Salomonson, V. V. (1983), Studies of optical and biological properties of terrestrial land cover using multispectral linear array technology, *Proc. Pecora VIII Sympos.* 340–354.

Begni, G. (1982), Selection of the optimum spectral bands for the SPOT satellite, *Photogr. Eng. Remote Sens.* 48:1613–1620.

Begni, G. (1983), CNES, Toulouse, France. Personal communication.

Bunnik, N. J. J. (1984a), National Aerospace Laboratory NLR, Amsterdam, The Netherlands. Personal communication providing a report on TERS: A joint Indonesian-Netherlands Tropical Earth Resources Satellite Programme.

Bunnik, N. J. J. (1984b), Personal communication providing flier on CAESAR published by National Aerospace Laboratory, NLR, Amsterdam, The Netherlands.

Cartwright, D. G. (1983), Department of Defence, Salisbury, Australia. Personal communication.

Cihlar, J., O'Neil, R., Ahern, F., and Till, S. (1984), Optical sensor for Radarsat, *8th Canadian Symposium on Remote Sensing*, pp. 49–62.

Colvocoresses, A. P. (1979), Proposed parameters for Mapsat, *Photogr. Eng. Remote Sens.* 45:501–506.

Colvocoresses, A. P. (1982), An automated mapping satellite system (Mapsat), *Photogr. Eng. Remote Sens.* 48:1585–1591.

Cox, S. C. (1982), Executive summary, the Multispectral Imaging Science Working

Group: Final Report, Working Group Reports.

Daedalus Enterprises, Inc., P.O. Box 1869, Ann Arbor, MI 48106.

Doyle, F. J. (1984), Review of earth observation satellite programs, *2nd International Colloquium on Spectral Signatures of Objects in Remote Sensing, Bordeaux, France*, Les Colloques de l'INRA No. 23, pp. 889–898.

Due, C. T. (1982), Optical-Mechanical, Active/Passive Imaging Systems—Volume II, Report number 153200-2-T(II), ERIM, Infrared Information and Analysis Center, P.O. Box 8618, Ann Arbor, MI 98107.

Edel, H. R. (1982), Government of Canada Fisheries and Oceans, Ottawa, Ontario, Canada K1A OE6. Personal communication.

Engel, J. L., and Weinstein, O. (1982), The thematic mapper—An overview, *1982 International Geoscience and Remote Sensing Symposium*, Munich, Germany, Vol. 1, WP-1.

Gower, J. F. R. (1982), Inst of Ocean Sciences, Patricia Bay, Sidney, B. C., Canada. Personal communication.

Hemphill, W. R. (1981), Cooperative role of NASA and the Geological Survey in the development of techniques to measure luminescence. In *Workshop on Applications of Luminescence Techniques to Earth Resources Studies*, (Hemphill, W. R., and Settle, M., Eds.), pp. 9–11, Lunar and Planetary Institute, Tech. Rept. 81-03, 3303 NASA Road 1, Houston, TX 77058.

Hodgson, R. M., Cady, F. M., and Pairman, D. (1981), A solid-state airborne sensing system for remote sensing, *Photogr. Eng. Remote Sens.* 47:177–182.

Hofmann, M., Laucht, H., and Meissner, D. (1982), The Modular Optoelectronic Multispectral Scanner (MOMS) System performance and first results, *1982 International Geoscience and Remote Sensing Symposium*, Munich, Germany, Vol. 1, WP-2.

Holmes, R. A. (1984), Advanced sensor systems: Thematic mapper and beyond, *Remote Sens. Environ.* 15:213–221.

Hrebenyk, B. W. (1982), MEIS II: An operational multispectral airborne pushbroom scanner, *Proc. Am. Soc. Photogram.* Fall Technical Conf.

Irons, J. R., Smith, J. C., Blaine, L. R., and Finkel, M. W. (1982), A plan for the characterization, calibration and evaluation of LAPR-II, NASA Tech. Memo 83915, p. 12.

Ishizawa, Y. (1981), The Japanese MOS and LOS Program, *Proc. 15th International Symposium on Remote Sensing of Environment, Ann Arbor, Mich.* Available from Environmental Research Institute of Michigan.

Ishizawa, Y., Kuramasu, R., Kuwano, R., and Nagura, R. (1980), Multispectral electronic self-scanning radiometer for MOS-1. XXXI Congress International Astronautical Federation IAF '80, Tokyo, Japan, B-91.

Jouan, J. (1982), MATRA, Toulouse, France. Personal communication.

Kahle, A. B. (1984), Jet Propulsion Laboratory, Pasadena, CA. Personal communication.

Kahle, A. B., and Goetz, A. F. H. (1983), Mineralogic information from a new airborne thermal infrared multispectral scanner, *Science* 222:24–27.

Kim, H. H., McClain, C. R., Blaine, L. R., Hart, W. D., Atkinson, L. P., and Yoder, J. A. (1980), Ocean chlorophyll studies from a U-2 aircraft platform, *J. Geophys. Res.* 85:3982–3990.

Landgrebe, D. A. (1981), Analysis technology for land remote sensing, *Proc. IEEE* 60:628–642.

Landsat Data Users Handbook (revised) (1979), U.S. Geol. Survey, EROS Data Center, Sioux Falls, SD 57198.

Landsat Data Users Notes (1982), International land satellite programs, 24:4–6. U.S. Geol. Survey, EROS Data Center, Sioux Falls, SD 57198.

Lansing, J. C., Jr., and Cline, R. W. (1975), The four- and five-band multispectral scanners for Landsat, *Opt. Eng.* 14:312–322.

Laporte, M. (1981), Characteristiques principales du push broom aeroporte, CNES Project Report, N 81/023.

Lowe, D. S. (1975), Imaging and nonimaging sensors, In *Manual of Remote Sensing*, (R. G. Reeves, Ed.).

Lowndes, J. C. (1983), Space America to launch stereoscopic earth sensor, *Aviation Week Space Technol.* 87–89.

Lyon, R. J. P. (1983), Stanford University, CA Personal communication including letter from J. L. Daniels, Director of CBML.

Macdonald Dettwiler, and Associates, Ltd., 3751 Shell Road, Richmond, B.C., Canada V6X 2Z9.

Markham, B. L., and Barker, J. L. (1983), Spectral characterization of the Landsat-4 MSS sensors, *Photogr. Eng. Remote Sens.* 49:811–833.

Mason, C. D. (1984), Goddard Space Flight Center, U.S.A. Personal communication of update of Code 900 Instrument Catalog of 30 Systems.

Matsumoto, K. (1981), Development of marine observation satellite-1. *AAS 19th Goddard Memorial Symposium*, AAS-81-060.

Midan, J. P., Reulet, J. F., Giraudbit, J. N., and Bodin, P. (1982), The SPOT HRV Instrument, *1982 International Geoscience and Remote Sensing Symposium*, Munich, Germany.

Norwood, V. T., Fermelid, L. R., and Tadler, G. A. (1972), Multispectral Scanner System for ERTS. Final Report, NASA contract NAS5-11255, Hughes Aircraft Co.

ORI Report (1979), Multispectral Resource Sampler (MRS) Workshop, Summary of workshop held May 31–June 1, 1979, at Colorado State University.

Price, J. C. (1978), *Heat Capacity Mapping Mission User's Guide* (Revised 1980), Goddard Space Flight Center, Greenbelt, MD.

Price, J. C. (1984), U.S. Department of Agriculture, Beltsville, Md., U.S.A. Personal communication.

Schneider, S. R., and McGinnis, D. F. (1982), The NOAA/AVHRR: A New Satellite Sensor for Monitoring Crop Growth. Proc. 8th International Symposium on Machine Processing of Remotely Sensed Data, Purdue University, Indiana, pp. 281–290.

Selivanov, A. S., and Tuchin, Yu. M. (1981), Onboard radio/TV system for. earth resources studies, *Sov. J. Remote Sens.* 5:704–712.

Selivanov, A. S., Tuchin, Yu. M., Naraeva, M. K., and Nosov, B. I. (1981), An experimental earth-survey data acquisition system, *Sov. J. Remote Sens.* 5:713–719.

Sidorenko, A. V. (1981), Materials of New Experimental Project under the Meteor-Priroda Program, *Sov. J. Remote Sens.* translation date 1983. Harwood Academic c/o STBS, P.O. Box 197, London WC2N 4DE, U.K.

Siegrist, A. W., and Schnetzler, C. C. (1980), Optimum spectral bands for rock discrimination, *Photogr. Eng. Remote Sens.* 46:1207–1215.

Silverton, W. E., Jr., Wilson, R. G., Bullock, G. F., and Schappell, R. T. (1982), Feature identification and location experiment, *Science* 218:1031–1033.

Slater, P. N. (1979), A re-examination of the Landsat MSS, *Photogr. Eng. Remote Sens.* 45:1479–1485.

Slater, P. N., (1980), *Remote Sensing Optics and Optical Systems*, Addison-Wesley, Reading.

Snyder, J. P. (1982), Geometry of a mapping satellite, *Photogr. Eng. Remote Sens.* 48:1593–1602.

Stewart, S. E., and Buntzen, R. R. (1982), A solid state spectroradiometer for ocean remote sensing, *IEEE Proc. Oceans '82*, Washington, D.C.

Stoner, E.R., and Baumgardner, M.F. (1980), Physiochemical site and bidirectional reflectance factor characteristics of uniformly moist soils, Laboratory for Applications of Remote Sensing, Purdue University, Technical Report 111679.

Tucker, C. J. (1978), A comparison of satellite sensor bands for vegetation monitoring, *Photogr. Eng. Remote Sens.* 44:1369–1380.

Vane, G., Billingsley, F. C., and Dunne, J. A. (1982), Observational parameters for remote sensing in the next decade, *SPIE Proc.* 345:52–65.

Vane, G., Chrisp, M., Enmark, H., Macenka, S., and Solomon, J. (1984), Airborne visible/infrared imaging spectrometer (AVIRIS): an advanced tool for earth remote sensing, *Proc. IEEE, 1984 International Geoscience and Remote Sens. Symp.*, in press.

Vane, G., Goetz, A. F. H., and Wellman, J. B. (1983), Airborne imaging spectrometer: a new tool for remote sensing, *Proc. IEEE, 1983 International Geoscience and Remote Sens. Symp.*, IEEE Cat. No. 83CH 1837-4.

Watson, R. D., and Theisen, A. F. (1981), Electronic and Optical Modification of the Engineering Model FLD, and the Evolution of Peripheral Equipment. In *Workshop on Applications of Luminescence Techniques to Earth Resources Studies*, (W. R. Hemphill and M. Settle, Eds.), pp. 15–18, Lunar and Planetary Institute, Tech. Rept. 81-03, 3303 NASA Road 1, Houston, TX 77058.

Wellman, J. B., Goetz, A. F. H., Herring, M., and Vane, G. (1983), A shuttle imaging spectrometer experiment for the late 1980s, *Proc. IEEE National Telesystems Conference*, IEEE Cat. No. 83CH2975-2:286–292.

Wiersma, D. J., and Landgrebe, D. A. (1979), The analytical design of spectral measurements for multispectral remote sensor systems, Laboratory for Applications of Remote Sensing, Purdue University, IN, Technical Report 122678 TR-EE 79-B.

Received 28 June 1984; accepted 24 September 1984

Absolute Calibration of Field Reflectance Radiometers

Ray D. Jackson
USDA Agricultural Research Service, U. S. Water Conservation Laboratory, Phoenix, AZ 85040
Philip N. Slater
Committee on Remote Sensing and Optical Sciences Center, University of Arizona, Tucson, AZ 85721

ABSTRACT: A method is described whereby field reflectance radiometers can be calibrated in an absolute sense using equipment available at most agricultural or environmental research locations. A radiometer is positioned directly above a calibrated standard reflectance panel that is horizontal to the Earth's surface. The sun's direct beam is separated from the total by measuring the total, shading the panel with a nontransparent shield held between the sun and the panel, measuring the diffuse component, and subtracting the diffuse from the total. These measurements are repeated periodically from shortly after sunrise to near solar noon. A graph of the logarithm of the radiometer response to the direct beam versus the secant of the solar zenith angle (known as a Langley plot) yields the spectral-extinction optical thickness of the atmosphere as the slope and the logarithm of the exoatmospheric irradiance divided by the calibration factor as the intercept. Calibration factors for two radiometers were within 10 percent of those obtained by other methods, indicating that this technique is a viable method for the absolute calibration of field radiometers.

INTRODUCTION

SMALL, LIGHTWEIGHT, RADIOMETERS that measure radiation in the reflected solar portion of the electromagnetic spectrum are currently being used to obtain spectral data for environmental and agricultural research projects. For the most part, these radiometers are used in conjunction with a reference reflectance panel made from flat metal plates coated with highly reflecting substances such as $BaSO_4$ (Robinson and Biehl, 1979) or Halon (Schutt *et al.*, 1981). With a calibrated reflectance panel, the reflectance factors of targets can be calculated by dividing the target radiance by the panel radiance, if the radiances from both surfaces are measured at nearly the same time. For some purposes, however, it is necessary to quantitatively measure the radiance reflected from targets. For example, the calculation of the net amount of radiation absorbed by a plant canopy can be made if the irradiance at, and the reflected radiance from, the canopy are known (Jackson *et al.*, 1985). To accomplish this using reflectance radiometers, calibration factors for each channel of the radiometer must be known.

Calibration factors for some radiometers are available from their manufacturer, whereas other radiometers are delivered uncalibrated. Calibration procedures are best carried out in well equipped optical laboratories. Such facilities are not ubiquitous, and are essentially unavailable to a number of researchers who routinely use small field radiometers. In the absence of a precise laboratory calibration, a field calibration procedure would be of benefit. This report describes a field procedure for the calibration of reflectance radiometers using equipment already available at most environmental research stations.

METHOD

The proposed method is an adaptation of a technique for determining the solar constant from ground based measurements (Shaw *et al.*, 1973; Slater, 1980). For any solar zenith angle (θ_z), the spectral irradiance on a surface perpendicular to the direct solar incident flux is,

$$E_\lambda = E_{\lambda o} e^{-\tau(\lambda)\sec\theta_z} \quad (1)$$

where $E_{\lambda o}$ is the exoatmospheric irradiance (the spectral irradiance outside the Earth's atmosphere on a plane one astronomical unit from the sun and perpendicular to the incidence flux), and $\tau(\lambda)$ is the spectral-extinction optical thickness at the wavelength λ.

Observations of E_λ are made with a radiometer for several zenith angles from just after sunrise to near solar noon on a single day. It is assumed that $\tau(\lambda)$ remains constant during the measurement period, and that the radiometer output signal is linear with respect to input radiant energy. The graph of $\ln(E_\lambda)$ versus $\sec(\theta_z)$, known as a Langley plot, will be linear if the assumptions are sufficiently met. The slope of the line is the spectral-extinction optical thickness, and the intercept is the natural logarithm of the exoatmospheric irradiance. The solar zenith

PHOTOGRAMMETRIC ENGINEERING AND REMOTE SENSING,
Vol. 52, No. 2, February 1986, pp. 189–196.

0099-1112/86/5202-189$02.25/0

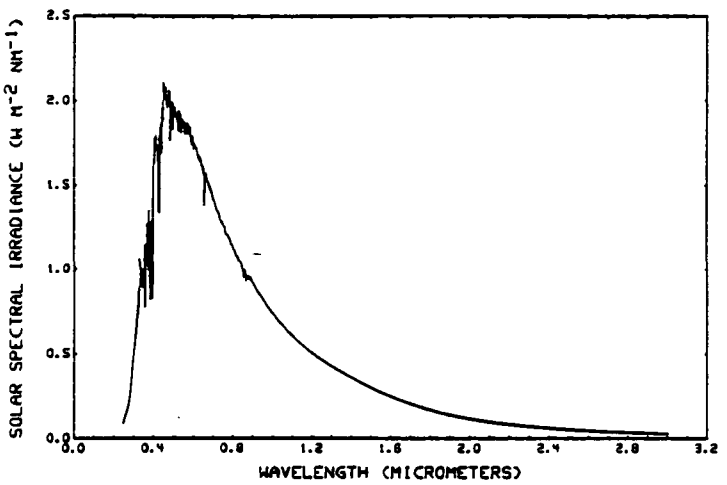

FIG. 1. Solar spectral irradiance at the top of the atmosphere.

angle can be directly measured, but it is readily calculated from a time measurement and the ephemeris of the sun (List, 1958, Table 169).

The irradiance (E_λ) can be measured by pointing a radiometer, having a field of view that just includes the solar disk, directly at the sun. The irradiance is the produce of an output voltage (V) times a calibration factor (c).

For an uncalibrated radiometer, Equation 1 becomes

$$Vc = E_{\lambda o} e^{-\tau(\lambda)\sec\theta_z} \quad (2)$$

If $\ln(V)$ is plotted versus $\sec\theta_z$, the slope is $-\tau(\lambda)$ and the intercept is $\ln(E_{\lambda o}/c)$. If $E_{\lambda o}$ is known, the calibration factor (c) is

$$c = E_{\lambda o}/e^{A} \quad (3)$$

where A is the intercept of the Langley plot.

Equation 2 requires that V be in response to the direct solar incident flux. A radiometer having a field of view (FOV) of 3° pointed directly at the sun would see less than 2 percent diffuse radiation (Shaw *et al.*, 1973). With field radiometers such as the Exotech Model 100-A* and the Barnes 12-1000 Modular Multispectral Radiometer (MMR)*, the available FOV's are 1° and 15°. Using a 1° FOV, alignment of the radiometer optics with the solar beam would require precision solar tracking equipment. Using a 15° FOV would allow a significant portion of diffuse radiation to reach the detector.

An alternate procedure is to measure the direct radiant flux reflected from a horizontal panel of known reflectance. This removes the stringent field of view requirement and allows radiometers having any field of view less than, say, 20° to be calibrated. Fields of view larger than about 20° would require either an excessively large standard reflectance panel or placement of the radiometer close to the panel. The latter condition could cause errors by the instrument blocking a significant amount of diffuse radiation and/or re-reflecting radiation from the panel.

The procedure depends upon the assumption that the standard reflectance panel is a perfect lambertian reflector. This requirement can be approximated if the reflectance of the panel is accurately known at all illumination angles that may be encountered during field measurements.

The evaluation of $E_{\lambda o}$, the corrections necessary for the reflectance panel to approximate a perfect lambertian reflector, and experimental procedures are discussed in the following sections.

Exoatmospheric Irradiance

Data for solar spectral irradiance at the top of the atmosphere were obtained for the wavelength interval from 0.33 to 1.25 μm from Neckel and Labs (1981), for 1.25 to 2.95 μm from Pierce and Allen (1977), and for wavelengths below 0.33 μm from Slater (1980). The data were interpolated to yield values for each nanometre between 0.25 and 3.0 μm (Figure 1).

Response functions for the four Exotech bands and the seven reflectance bands of the Barnes 12-1000 MMR are shown in Figure 2. Response function data are usually found in the radiometer instruction manual. The Exotech simulates the four Landsat multispectral scanner system (MSS) bands and the

* Trade names and company names are included for the benefit of the reader and imply no endorsement of the product or company by the U. S. Department of Agriculture or the University of Arizona.

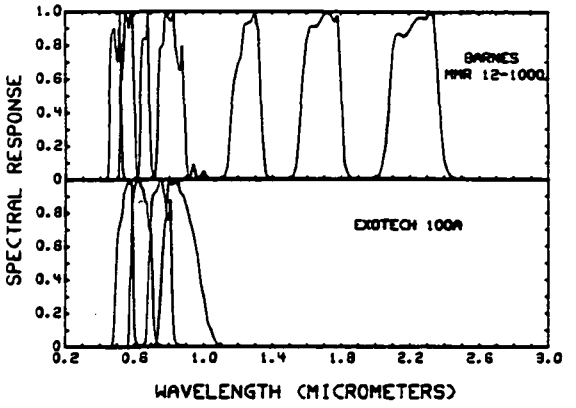

FIG. 2. Spectral response functions for two field radiometers.

MMR simulates the six solar reflective Landsat Thematic Mapper (TM) bands. The MMR also has a band at 1.15 to 1.30 μm. Nominal wavelength intervals for the two instruments are given in Table 1.

The exoatmospheric irradiance within the wavelength interval (the symbol $E_{\lambda o}$ will now apply to the WLI) for each band of the two instruments was obtained by summing the product of the irradiance (Figure 1) and the response functions (Figure 2) for each radiometer band of interest. The results are presented in Table 1. The data are for the mean Earth-sun distance. $E_{\lambda o}$ varies with the square of the Earth-sun distance, differing by about 7 percent between January and July. The values for $E_{\lambda o}$ given in Table 1 can be corrected to the actual Earth-sun distance by dividing them by the square of the radius vector of the Earth (r) for each measurement day. Tabular values of the radius vector are available (List, 1958, Table 169), but they can be approximated using the relation (Gurney and Hall, 1983)

$$r = 1 + 0.0167\sin[2\pi(D - 93.5)/365] \quad (4)$$

where D is the day of year. With this correction, and dividing by π to put the calibration factor in terms of radiance per volt, Equation 3 becomes

$$c = E_{\lambda o}/(r^2 e^{\wedge}\pi) \quad (5)$$

with c having units of W m^{-2} sr^{-1} V^{-1}.

When ephemeris tables are used to calculate the solar zenith angle, the solar time must be noted at the precise time that the measurements are made. An uncertainty in the time measurement of about 10 s would cause an error of about 0.1 percent in the zenith angle calculation for angles less than 75° (Thomason *et al.*, 1982).

Reflectance Panel

Reflectance factor data for a panel painted with $BaSO_4$ was provided by LARS, Purdue University (L. L. Biehl, personal communication). Reflectance factor data for 10 and 20° incidence angles were interpolated to yield data at 15° for each band of the Exotech and the MMR (Table 1). Panel reflectance factors were measured as a function of incidence angle from 15 to 75° using a device that allowed the panel to be held at a known angle to the sun's rays. With the MMR radiometer positioned about 1 m above and perpendicular to the panel, a measurement of the direct solar radiation was made (using a shading technique described in the following section). Subsequently, the incidence angle was changed and

TABLE 1. NOMINAL WAVELENGTH INTERVALS (WLI), EXOATMOSPHERIC IRRADIANCE WITHIN THE SPECIFIED WLI OF THE EXOTECH MODEL 100-A AND THE BARNES 12-1000 MMR RADIOMETERS, AND $BaSO_4$ PANEL REFLECTANCE FACTORS AT θ_z = 15° FOR EACH WLI.

Radiometer	Band	Nominal wavelength (μm)	Exoatmospheric irradiance (W m^{-2})	Panel reflectance factor
Exotech				
	1	0.5 – 0.6	167.6	0.942
	2	0.6 – 0.7	188.2	0.936
	3	0.7 – 0.8	157.3	0.929
	4	0.8 – 1.1	197.5	0.914
Barnes MMR				
	1	0.45 – 0.52	112.4	0.948
	2	0.52 – 0.60	134.4	0.941
	3	0.63 – 0.69	72.2	0.935
	4	0.76 – 0.90	145.0	0.922
	5	1.15 – 1.30	69.1	0.897
	6	1.55 – 1.75	49.9	0.855
	7	2.05 – 2.30	22.0	0.757
	8	10.5 – 12.5	–	–

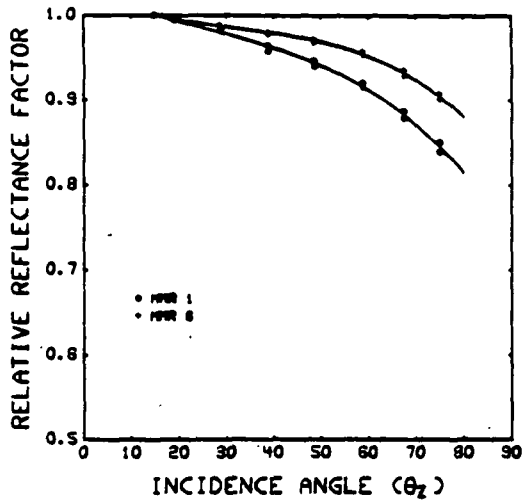

FIG. 3. Relative reflectance factors of a $BaSO_4$ panel as a function of incidence angle for two bands of a field radiometer.

the measurement repeated. Relative reflectance factors were calculated as the ratio of radiometer output voltage to the voltage at 15°. The choice of 15° as the the reference angle was dictated by the fact that, for smaller incidence angles, the radiometer shadowed the panel. A measurement sequence for eight incidence angles required about 15 minutes.

Values of relative reflectance factors for the $BaSO_4$ panel as measured by MMR radiometer bands 1 and 6 are shown in Figure 3. Data for MMR bands 2 to 5 are intermediate to those shown, and those for MMR-7 are slightly higher than for MMR-6. Third degree polynomial equations were statistically fit to the data for each MMR band. The lines in Figure 3 indicate how well the data from two measurements were represented by the equations. Equations for MMR bands 2, 3, and 4 were used as representative for similar bands of the Exotech.

The reflectance factor of the panel at any zenith angle $R(\theta_z)$ is the product of the reflectance factor at 15° and the relative reflectance factor. In practice, the polynomial approximations of the relative reflectance factor data (Figure 3) were used in the calculations.

Because the panel was kept horizontal during the measurements, instead of perpendicular to the solar beam as required by Equation 1, the voltage that would result if the standard reflectance panel were a perfect lambertian reflector held perpendicular to the sun's rays is approximated by

$$V = V_h/[R(\theta_z)\cos\theta_z] \quad (6)$$

which is the value of V to be used in the Langley plots. The term V_h is the radiometer voltage when viewing a horizontal panel.

If radiometer gain settings are other than 1 during measurements, the voltage should be adjusted to represent a gain of 1. The output from the PbS detectors (Bands 5 to 7) of the MMR are ambient temperature sensitive. A procedure to adjust the output to a reference temperature was described by Jackson and Robinson (1985). The Langley plot for bands 5 to 7 of the MMR will not be linear if the temperature effect is not compensated for.

Measurement of Direct Solar Radiation

The direct component of the irradiance can be separated from the total by measuring the total, shading the panel with a nontransparent shield held between the sun and the panel, and measuring the diffuse component, with the direct component being the difference between the total and the diffuse. The use of a shading device (which should be held at as great a distance from the panel as practical) blocks a portion of the sky, reducing the amount of diffuse radiation that strikes the panel by a small amount. The error caused by the use of the shade and the error caused by the time difference between measurements of the total and the diffuse can be minimized by holding the shield so that the shaded area is to the side of the panel while the total irradiance is measured, then moved sideways to shade the panel for the diffuse measurements, then moved back to the original position for another total irradiance measurement. The before and after total irradiance measurements are averaged to yield a value corresponding to nearly the same time as that when the diffuse measurements were made. By holding the shield the same distance from the panel during all measurements, the portion of the sky blocked by the object is similar, thus reducing the error caused by its use. For a detailed discussion of this type of measurement see Che *et al.* (1985).

Measurement Procedure

An Exotech and a Barnes MMR (serial no. 119) were mounted side-by-side at the end of a rotatable boom which held the instruments about 1.7-m above a 1.2 by 1.2-m $BaSO_4$ painted horizontal panel. Outputs from the two radiometers were recorded using a portable data acquisition and storage device that also noted the time of measurement. Measurements were made on six dates, 19 November 1983, 15 December 1983, 13 April 1984, and 8, 10, and 20 June, 1984, beginning shortly after sunrise and continuing periodically until about an hour before solar noon. A 1.3 by 1.3-m flat shield mounted at the end of a 3.5-m pole was used to shade the panel during measurements of diffuse radiation. The measurement sequence was total (sunlit panel), diffuse (shaded panel), and total.

When the measurements were completed, the data were downloaded to a computer. The voltage data

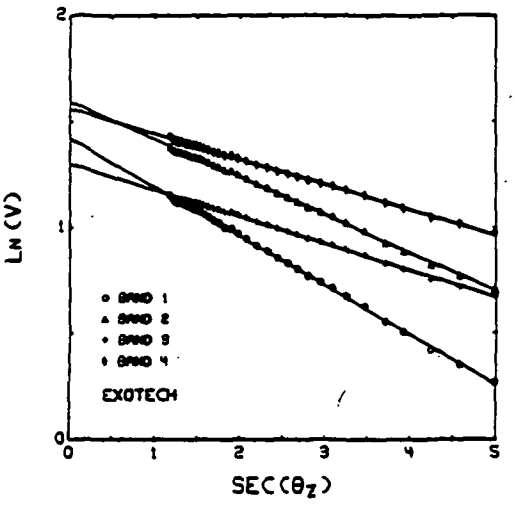

FIG. 4. Langley plots for the four Exotech bands. Data were taken on 13 April 1984.

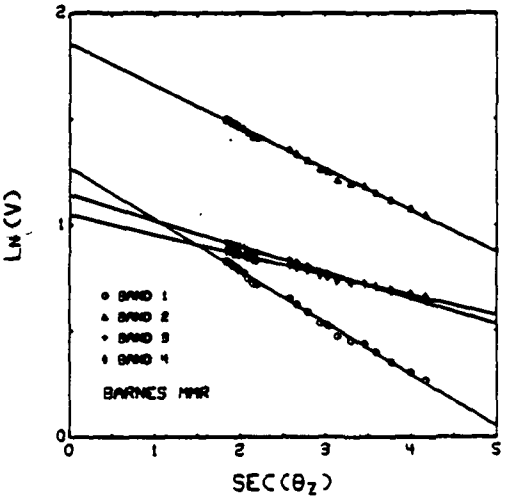

FIG. 5. Langley plots for MMR bands 1 to 4. Data were taken on 15 December 1983.

were, when necessary, adjusted to a gain of 1 and the ambient temperature sensitive channels adjusted to a reference temperature of 25°C (Jackson and Robinson, 1985). For each channel on each radiometer at each measurement time, the two total (sunlit) data were averaged and the diffuse subtracted to yield a voltage value (V_h) due to direct radiation at the time of the diffuse measurement (the time at which θ_z was calculated). Using θ_z, the relative reflectance factor was calculated using the appropriate polynomial equations (see discussion of Figure 3), the panel reflectance factors at 15° were taken from Table 1, and the voltage V_h was adjusted to V using Equation 6. Plots of $\ln(V)$ versus $\sec(\theta_z)$ were made

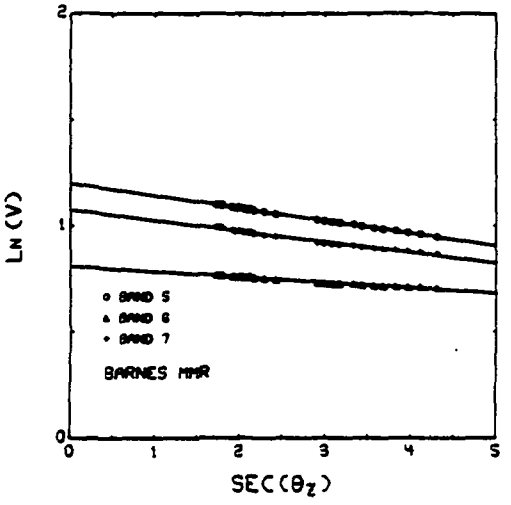

FIG. 6. Langley plots for MMR bands 5 to 7. Data were taken on 19 November 1983.

to obtain the intercept A which, when used in Equation 5, yielded the calibration factors.

RESULTS AND DISCUSSION

Representative Langley plots for eleven bands and for three measurement dates are shown in Figures 4 to 6. In all cases the data are linear, a necessary but not sufficient condition for the underlying assumptions to be met. Reagan *et al.* (1984) showed by model simulations that a linear relation can result when the spectral-extinction optical thickness varies temporally. This emphasizes the necessity of making measurements under clear, stable weather conditions.

If the temperature correction had not been made to the PbS detector outputs for MMR bands 5 to 7, the data would have been markedly non-linear, being concave downward.

The calibration factors for the two instruments are given in Tables 2 and 3. Table 2 includes the calibration factors for the Exotech as furnished by the manufacturer. The percent difference between the company measured and the Langley plot results range from −4.0 percent for band 2 to 9.6 percent for band 3. There were no data available with which the MMR calibration factors (Table 3) could be directly compared.

A secondary comparison was made with a second MMR (S# 116) at White Sands, New Mexico on 28 October 1984. Langley plots of the data provided a calibration factor for the first four MMR bands. These data, along with the means for bands 1 to 4 of MMR S# 119 from Table 3, are presented in Table 4. Also included are calibrations for bands 1 and 3 for MMR S# 116 from a laboratory-based procedure (Phillips, 1985). The detector temperature was not monitored

TABLE 2. CALIBRATION FACTORS FOR THE EXOTECH MODEL 100-A DETERMINED FROM LANGLEY PLOTS AND RESPONSE FUNCTIONS GIVEN IN THE MANUFACTURERS INSTRUCTION MANUAL. ALL CALIBRATION FACTORS HAVE UNITS OF $W\ M^{-2}\ SR^{-1}\ V^{-1}$.

Date of measurement	Band 1	2	3	4
19 Nov 83	12.5	11.8	13.6	13.5
15 Dec 83	12.1	11.5	13.3	13.4
13 Apr 84	12.8	12.1	13.6	13.1
08 Jun 84	12.0	11.6	13.3	13.2
10 Jun 84	13.2	12.5	14.1	13.9
20 Jun 84	13.6	12.7	14.2	13.7
Mean (SD)	12.7 (0.6)	12.0 (0.5)	13.7 (0.4)	13.5 (0.3)
Company calibration	12.7	12.5	12.5	12.9
Percent difference	0	−4.0	9.6	4.7

TABLE 3. CALIBRATION FACTORS FOR THE BARNES MMR 12-1000 S#119 DETERMINED FROM LANGLEY PLOTS AND RESPONSE FUNCTIONS GIVEN IN THE MANUFACTURERS INSTRUCTION MANUAL. ALL CALIBRATION FACTORS HAVE UNITS OF $W\ M^{-2}\ SR^{-1}\ V^{-1}$.

Date of measurement	Band 1	2	3	4	5	6	7
19 Nov 83	10.8	7.16	7.77	17.0	6.78	7.26	2.45
15 Dec 83	10.4	6.91	7.58	16.7	6.72	7.00	2.41
13 Apr 84	11.2	7.04	8.09	17.0	6.59	6.94	2.40
08 Jun 84	10.4	6.62	7.83	16.7	6.91	7.10	2.41
10 Jun 84	11.4	7.13	8.37	17.4	7.26	7.39	2.48
20 Jun 84	11.5	7.16	8.34	17.2	7.00	7.23	2.44
Mean	11.0	7.00	8.00	17.0	6.88	7.15	2.43
SD	0.5	0.21	0.32	0.3	0.24	0.17	0.03

TABLE 4. COMPARISON OF CALIBRATION FACTORS FOR 4 BANDS OF TWO MMR RADIOMETERS AND FIELD AND LABORATORY CALIBRATIONS FOR 1 BANDS OF ONE RADIOMETER. THE FACTORS HAVE UNITS OF $W/M^{-2}\ SR^{-1}\ V^{-1}$.

Date of measurement	Band 1	2	3	4
SN#119	11.0	7.00	8.00	17.0
SN#116 (field)	9.8	13.5*	7.72	17.0
SN#116 (lab)	10.3	–	7.57	–

*The internal gain adjust was changed from the factory setting.

for S# 116, precluding the calculation of calibration factors for bands 5 to 7. On this radiometer, the gain on band 2 had been internally adjusted from the factory setting, invalidating any comparison of that band. For the following comparison we make the assumption that, because S# 116 and S# 119 were made at the same time, their calibration factors are similar (for bands 1, 3, and 4).

The calibration factors for these two instruments differed by 12 percent in band 1, by 3.6 percent in band 3, and were identical for band 4. The factors for both instruments are reasonably close to the laboratory-based calibration of bands 1 and 3. These data support the premise that the Langley plot method is a viable means of obtaining calibration factors using field data.

The spectral-extinction optical thickness (τ), being the slope of the Langley plots, is readily obtained from the same data as the calibration factors. This parameter is a measure of the extent to which the atmosphere scatters and absorbs the irradiance within the spectral bands of the MMR. Values of τ for each of the eleven bands are given in Table 5. Differences between the six measurement dates are evident, with 8 June 1984 having the highest values. Two days later the next to lowest values for the six days were recorded. Although both days were cloud-free, 10 June apparently had less atmospheric contaminants than did 8 June. Che *et al.* (1985) presented a detailed discussion of the measurement of τ using a field radiometer and a calibrated reflectance panel.

The data and the standard deviations of the cal-

C-2

TABLE 5. VALUES OF THE SPECTRAL-EXTINCTION OPTICAL THICKNESS (τ) OBTAINED FROM SLOPES OF LANGLEY PLOTS FOR SEVEN BANDS OF THE BARNES MMR S#119 AND THE FOUR EXOTECH BANDS.

Date of measurement	Band 1	2	3	4	5	6	7
Barnes MMR							
19 Nov 83	0.211	0.169	0.105	0.074	0.059	0.025	0.050
15 Dec 83	0.243	0.197	0.122	0.095	0.086	0.049	0.087
13 Apr 84	0.286	0.239	0.157	0.122	0.094	0.054	0.072
08 Jun 84	0.353	0.292	0.195	0.149	0.116	0.067	0.095
10 Jun 84	0.225	0.185	0.112	0.089	0.074	0.031	0.063
20 Jun 84	0.233	0.190	0.117	0.089	0.079	0.039	0.068
Exotech							
19 Nov 83	0.165	0.123	0.078	0.072			
15 Dec 83	0.187	0.140	0.096	0.095			
13 Apr 84	0.232	0.179	0.127	0.120			
08 Jun 84	0.298	0.229	0.164	0.153			
10 Jun 84	0.181	0.133	0.092	0.089			
20 Jun 84	0.183	0.136	0.093	0.090			

ibration factors given in Tables 2 and 3 indicate that the method is reasonably precise. The variation between the six measurements does not appear to be related to time nor to the degree of atmospheric scattering (Table 5).

The accuracy of the measurement depends upon the accuracy of the exoatmospheric irradiance data and the reflectance data for the standard panel. Errors in $E_{\lambda o}$ will cause a proportional error in c. The most probable error in exoatmospheric irradiance within the wavelength interval as given in Table 1 would be in the response functions used in the calculation of the values. These functions could be determined for a particular instrument using equipment available in most optics laboratories.

If the reflectances of the standard panel are in error by a multiplicative amount, the calibration factors will be in error by the negative of that amount. Thus, if the relative reflectance of the panel is known with sufficient accuracy, but the reference reflectance at 15° is in error, the calibration factors can be easily corrected when the true reflectance values are known. If the relative reflectances are in error, the Langley plots may not be linear.

Equations 1 and 2 are expressions of Beer's law which was derived for monochromatic radiation. Thomason *et al.* (1982) showed that less than 0.1 percent error would result from using a 0.01-μm wavelength interval. The wavelength intervals used ranged from 0.06 to 1.1 μm. However, a twenty-fold larger error (2 percent) can be tolerated in the field method discussed here.

CONCLUDING REMARKS

The Langley plot technique is a viable field method for absolute radiometric calibration at the 10 percent level. Requirements are that the reflectance of a standard panel be known as a function of incidence angle, and that the exoatmospheric irradiance be known for the wavelength interval of each channel of the radiometer. The method is rather simple to implement but requires several hours to obtain one set of calibration factors.

ACKNOWLEDGMENTS

The assistance of C. E. Ezra and A. L. Phillips during the course of these experiments is gratefully acknowledged.

REFERENCES

Che, N., R. D. Jackson, A. L. Phillips, and P. N. Slater, 1985. The use of field radiometers in reflectance factor and atmospheric measurements, *Soc. Photo-Optical Instrum. Eng.*, 499:24–33.

Gurney, R. J., and D. K. Hall, 1983. Satellite-derived surface energy balance estimates in the Alaskan Sub-Artic, *J. Climate and Applied Meteorol.* 22:115–125.

Jackson, R. D., and B. F. Robinson, 1985. Field evaluation of the temperature stability of a multispectral radiometer. *Remote Sens. of Environ.*, 17:103–108.

Jackson, R. D., P. J. Pinter, Jr., and R. J. Reginato, 1985. Net radiation calculated from remote multispectral and ground station meteorological data. *Agric. and Forest Meteorol.* (in press).

List, R. J., 1958. *Smithsonian Meteorological Tables*, Smithsonian Institution, Wash. D. C., p. 527.

Neckel, H., and D. Labs, 1981. Improved data of solar spectral irradiance form 0.33 to 1.25 μ. *Solar Physics* 74:231–249.

Pierce, A. K., and R. G. Allen, 1977. The solar spectrum between 0.3 and 10 μm. In O. R. White (ed.), *The Solar Output and its Variation*, Colorado Assoc. Univ. Press, Boulder, Colo., pp. 169–192.

Phillips, A. L., 1985. *Absolute calibration of, and atmospheric measurements using, a multiband field spectroradiometer.* M. S. Thesis, Optical Sciences Center, University of Arizona, Tucson, Ariz.

Reagan, J. A., I. C. Scott-Flemming, B. M. Herman, and R. M. Schotland, 1984. Recovery of spectral optical depth and zero-airmass solar spectral irradiance under conditions of temporally varying optical depth. *Proc. IGARSS'84 Symposium*, Strasbourg 27-30 Aug. 1984, pp. 455–459.

Robinson, B. F., and L. L. Biehl, 1979. Calibration procedures for measurement of reflectance factor in remote sensing field research. *Soc. Photo-optical Instrum. Eng.* 196:16–26.

Schutt, J. B., Holben, B. N., Shai, C. M., and Henninger, J. H., 1981. Reflectivity of TFE—a washable surface—compared with that of $BaSO_4$. *Appl. Opt.* 20:2033–2035.

Shaw, G. E., J. A. Reagan, and B. M. Herman, 1973. Investigations of atmospheric extinction using direct solar radiation measurements made with a multiple wavelength radiometer. *J. Applied Meteorol.* 12:374–380.

Slater, P. N., 1980. *Remote Sensing: Optics and Optical Systems*. Addison-Wesley Pub. Co., Reading, Mass.

Thomason, L. W., B. M. Herman, R. M. Schotland, and J. A. Reagan, 1982. Extraterrestrial solar flux measurement limitations due to a Beer's law assumption and uncertainty in local time. *Appl. Optics* 21:1191–1195.

(Received 28 March 1985; accepted 12 June 1985; revised 9 August 1985)

Forum

Comments on Evaluations of Simulated SPOT Data

The August 1985 issue of *Photogrammetric Engineering and Remote Sensing* contained a number of articles evaluating products from the 1983 SPOT Simulation Campaign. Because conclusions from the simulation pertain also to the utility of the satellite data, it is appropriate to clarify differences between the simulation and satellite data which may affect some applications.

The paper by Ackleson and Klemas discusses the utility of the simulation data for discriminating water masses, emphasizing the low noise content of the simulation data. However, the simulation data have lower noise content than is to be expected from the satellite data; e.g., Saint and Weill (1984) present noise values for the three 20-m channels (S1, S2, and S3) and the panchromatic channel (P).

Radiometric Noise	S1	S2	S3	P
SPOT (Nominal) NeΔL	0.14	0.15	0.11	0.15
Simulation NeΔL	0.05	0.05	0.03	0.05

Radiometric noise is given in mW $cm^{-2}sr^{-1}\mu m^{-1}$)

"The simulations are in this respect significantly better than real data, but this can be taken into account by using the calibration coefficients on the CCTs to compute the noise equivalent digital count corresponding to the noise and quantization levels of SPOT." This computation requires knowledge of the satellite calibration coefficients, as described by Price (1984). However, in the author's experience with two scenes, the calibration coefficients are not correct in the simulation data sets. Thus, the conversion to satellite equivalent data is problematic. The difference between simulation and satellite data is expected to be most significant in cases similar to that studied by Ackleson and Klemas having low surface reflectivities.

In addition, Ackleson and Klemas state that "It is anticipated that banding will not be a problem within the operational SPOT data because of the linear array configuration of the sensor." However, the simulation data again present an optimistic picture, as the simulation data were obtained by a Daedalus scanner with a single detector per channel, with scanning by means of a rotating mirror, while the SPOT satellite sensor will have some thousands of detectors. It is likely that minor residual banding will remain after calibration, unless special techniques are used (Bernstein *et al.*, 1985). For data which have not been geometrically corrected, this effect will be present as vertical striping associated with the pushbroom scan of the sensor along the satellite track.

Several authors, e.g., DeGloria, have carried out photointerpretation of the imagery produced in conjunction with the SPOT Simulation Campaign. Several caveats apply to the availability of such satellite products:

- Although the simulation imagery included 10-metre multispectral image products produced from the high resolution aircraft data, the 10- and 20-metre satellite data will not be coregistered by the satellite instruments. This task must fall to the user or to the SPOT Corporation, at least until the launch of SPOT 3 and 4, which will acquire 10- and 20-m data in registered form. In contrast, the planned Landsats 6 and 7 will be able to acquire 15-m panchromatic data coregistered with the multispectral 30-m data.

(continued on page 211)